Construction and Calibration of the Laser Alignment System for the CMS Tracker

Von der Fakultät für Mathematik, Informatik und Naturwissenschaften
der Rheinisch-Westfälischen Technischen Hochschule Aachen
zur Erlangung des akademischen Grades eines Doktors der Naturwissenschaften
genehmigte Dissertation

vorgelegt von

Diplom–Physiker
Roman Adolphi

aus Aachen

Diese Dissertation ist auf den Internetseiten der Hochschulbibliothek online verfügbar.

Zusammenfassung

Am europäischen Kernforschungszentrum CERN (Genf, Schweiz) befindet sich der CMS Detektor (Compact Muon Solenoid) an einer der vier Proton-Proton Wechselwirkungszonen des Beschleunigers LHC (Large Hadron Collider) im Bau. Der innere Spurdetektor des CMS Experimentes wird mit einem Durchmesser von $2.4\ m$ und einer Länge von $5.4\ m$ bei seiner Fertigstellung der weltweit größte Silizium-Detektor sein. Zum Nachweis von geladenen Teilchen wird eine aktive, ca. 200 m^2 große Fläche von insgesamt etwa 15000 Silizium-Streifen-Modulen zur Verfügung gestellt, die auf einer modularen mechanischen Tragestruktur befestigt sind. Die Verwendung von Kohlefasermaterial ist eine optimale Voraussetzung, um mechanische Stabilität bei $-10^o C$ Betriebstemperatur in einem $4\ T$ Magnetfeld zu gewährleisten.

Zur präzisen Vermessung der einzelnen Teilchenspuren ist die genaue Kenntnis der Spurkammergeometrie notwendig. Neben der mechanischen Montagegenauigkeit größerer Detektoreinheiten und deren vermessungstechnischer Überprüfung liefert das Laser-Alignment-System (LAS) die Grundlage zur effizienten Spurrekonstruktion. Durch das in die Spurkammer intergrierte Laser-Alignment-System können die Positionen der Elemente der Tragestruktur auf der Skala von 100 μm festgestellt werden. Relative Bewegungen einzelner Komponenten können in der Größenordnung von 10 μm kontrolliert und überwacht werden.

Die Planung, das Design und die Verifizierung der Zuverlässigkeit eines optischen Systems dieser Komplexität für die räumliche Ausrichtung eines Silizium-Detektors in der Größenordnung der CMS Spurkammer – unter der Voraussetzung minimaler Beeinflussung des Detektordesigns und Vermeidung zusätzlicher externer Referenzstrukturen – ist eine neue wissenschaftliche Herausforderung. Die Entwicklung eines Laser-Alignment-Systems zur Rekonstruktion der CMS Spurkammergeometrie, die Realisierung unter Berücksichtigung der bestehenden Anforderungen, die Integration in den CMS Detektor und die Bestimmung der Leistungsfähigkeit des optischen Systems werden in der vorliegenden Arbeit beschrieben.

Das Prinzip der Positionsbestimmung basiert auf der Tatsache, daß Silizium im infraroten Wellenlängenbereich teilweise transparent ist. Der absorbierte Anteil eines Laserstrahls erzeugt ein Signal im jeweiligen Silizium-Streifen-Modul, womit dessen Position rekonstruiert werden kann, und der transmittierte Anteil stellt die optische Verbindung zur nächsten Detektorlage her. Ausgehend von den Ergebnissen der Untersuchungen der Eigenschaften von Laserdioden sowie den Tests von Lichtleitfasern und Steckern wurden die Systemkomponenten von der Laserquelle bis zum Detektor definiert.

Detailierte Studien bezüglich der Verwendung von Strahlteilern und geeigneten Test-aufbauten zur Vermessung der von ihnen ausgesandten kollinearen Strahlen wurden durch-geführt. Im Rahmen sowohl der geometrischen als auch der optischen Anforderungen wur-de eine Strahlteilerkonstruktion entwickelt, die auf dem Polarisationsprinzip beruht. Die Genauigkeit, mit der die Kollinearität der ausgehenden Strahlen gemessen wurde, war besser als 50 μrad, und es konnte gezeigt werden, daß unter den experimentellen Bedin-gungen in CMS die relative Position beider Strahlen konstant bleibt.

Die Schnittstelle zwischen dem LAS und dem Spurdetektor stellen die Silizium-Align-ment-Sensoren dar, die sowohl zum Teilchennachweis als auch zur Laserpositionsbestim-mung dienen. Zur Verbesserung der optischen Eigenschaften wurde eine Anti-Reflex-Schicht auf der Rückseite der Sensoren unter Gewährleistung gleichbleibender elektri-scher Eigenschaften aufgetragen. Die experimentellen Ergebnisse der Transmissions- und Reflexionsmessungen von Alignment-Sensoren in einem speziell entwickelten Testaufbau stimmten mit den Modellrechnungen überein und bestätigten die hohe optische Qualität der Sensoren.

Mit Hilfe einer Laserdiode und der Datenauslese der Signale in Silizium-Streifen-Modulen in einer Anordnung gemäß der Geometrie einer Endkappe (TEC) des Spurdetek-tors wurde das Funktionsprinzip überprüft und die räumliche Modulauflösung gemessen. Für fast alle Modulpositionen innerhalb der Endkappe konnte die Laserstrahlposition bei Relativbewegung der Module in der Größenordnung der Spezifikation von 10 μm rekonstruiert werden. Zusätzlich konnte gezeigt werden, daß die Brechung des Strahls vernachlässigbar ist.

In einem bereits fertig montierten Sektor der Endkappenstruktur der Spurkammer wurden die Daten des LAS mit denen aus einer fotogrammetrischen Vermessung vergli-chen. Die Rekonstruktion der Endkappengeometrie mittels der Laserstrahlen gelang mit einer Präzision von besser als 100 μm, und durch den übereinstimmenden Vergleich mit den Ergebnissen der fotogrammetrischen Vermessung konnte die optische Positionsanalyse des LAS bestätigt werden.

Die hohen Anforderungen an die Implementierung und an die Leistungsfähigkeit des Laser-Alignment-Systems erforderten während der Entwicklung, Konstruktion und Kali-bration die Lösung von unterschiedlichen Fragestellungen und Problemen. Die dadurch gesammelte Erfahrung kann als Grundlage für weitere Anwendungen bei der Ausrichtung von Spurkammern und Teilchendetektoren dienen.

Abstract

The CMS detector (Compact Muon Solenoid) is under construction at one of the four proton-proton interaction points of the LHC (Large Hadron Collider) at CERN, the European Organization for Nuclear Research (Geneva, Switzerland). The inner tracking system of the CMS experiment consisting of silicon detectors will have a diameter of 2.4 m and a length of 5.4 m representing the largest silicon tracker ever. About 15000 silicon strip modules create an active silicon area of 200 m^2 to detect charged particles from proton collisions. They are placed on a rigid carbon fibre structure, providing stability within the working conditions of a 4 T solenoid magnetic field at $-10^o C$.

Knowledge of the position of the silicon detectors at the level of 100 μm is needed for an efficient pattern recognition of charged particle tracks. Metrology methods are used to survey tracker subdetectors and the integrated Laser Alignment System (LAS) provides absolute positioning of support structure elements to better than 100 μm. Relative movements of the components are resolved and monitored at the 10 μm scale.

A robust and reliable optical system able to measure and control the large CMS tracker geometry with high accuracy has been developed and validated. The design and construction of such a system, fully integrated in the silicon tracker, avoiding external reference structures in order to have minimal impact on the tracker layout and consisting of radiation hard and non-magnetic components represents a new scientific challenge. The construction and integration of the LAS fulfilling the requirements, as well as its calibration and performance are described in this thesis.

The working principle is based on the partial transparency of silicon for light wavelengths in the near infrared region. The absorbed part of the laser beam generates a signal in the corresponding silicon strip module serving to reconstruct its position. The transmitted part reaches the subsequent module layer generating an optical link between the two layers.

Investigation of the light generation and distribution led to a definition of the optical components and their optimization for Laser Alignment purposes. Laser diodes have been qualified as light sources and singlemode optical fibres, terminated by special connectors, distribute the light to the CMS tracker detector.

The beamsplitting device, a key component of the LAS light distribution inside the CMS tracker, has been studied in detail. The challenge of splitting one collimated beam into two back-to-back beams inside a small available volume has been solved by using the polarization principle. Special test setups were developed to determine the collinearity of the two outgoing beams with a precision better than 50 μrad and it has been shown that their relative orientation remains constant under working conditions.

The interface between the tracker and the LAS is given by the silicon sensors which are responsible both for particle detection and for the determination of the position of the laser spot. An anti-reflex-coating has been applied on the backside of all alignment sensors to improve their optical properties without deterioration of their tracking performance. A test setup has been developed to simultaneously study the transmission and reflection properties of the alignment sensors. The results are in good agreement with calculations and confirm the high optical quality of the sensors.

The working principle of the optical alignment has been verified and the resolution of the laser spot was measured in a test setup with alignment modules arranged according to the CMS tracker endcap (TEC) geometry. For almost all laser spot positions in the TEC, relative module movements at the level of 10 μm were reconstructed. In addition, it has been shown that refraction effects are negligible.

Data from Laser Alignment in one TEC sector has been compared with TEC survey measurements. The reconstruction precision of better than 100 μm obtained by two laser beams was independently confirmed by the metrology data, thus validating the performance of the optical alignment.

The stringent requirements imposed on the implementation and performance of the Laser Alignment System necessitated the solution of a variety of problems and led to the accumulation of considerable experience in the alignment of particle tracking detectors by optical means.

Inhaltsverzeichnis

Inhaltsverzeichnis

Preface

The trend of High Energy Physics collider experiments is to reach higher center-of-mass energies. This goes along with larger detectors to be able to reconstruct physics events with high accuracy.

An optical alignment system has been incorporated in the inner tracking system (tracker) of the CMS experiment for the future Large Hadron Collider at CERN, able to provide an absolute and relative positioning knowledge of the tracker components to support reliable track reconstruction. The silicon modules of the tracking system are also used to detect the light from appropriately arranged laser beams.

This thesis deals with the research, development, and implementation of the optical Laser Alignment System (LAS) and presents its performance under the operating conditions of the CMS tracker.

The first chapter introduces the physics motivation, the collider machine, the CMS detector, and describes the tracker in detail.

The second chapter starts with the purpose and goals of the LAS and proceeds to define its layout as obtained from a series of requirements and constraints.

One important optical component, the beamsplitting devices, are the subject matter of chapter 3. Their functionality and properties are described and results of quality measurements are presented.

The optimization of the CMS sensors for laser alignment purposes is discussed in chapter 4. Experimental data of their optical properties are compared to simulations, based on an extended model for transmission calculations through layered media.

The LAS performance is the content of chapter 5. The laser spot reconstruction accuracy has been determined experimentally and refraction effects analysed. The first sector assembled in one of the tracker endcaps has been aligned by means of the LAS and the results are compared to data from survey measurements.

Chapter 6 summarizes all obtained results in a compact form and gives an outlook for the remaining issues.

Inhaltsverzeichnis

2

1. Introduction

In High Energy Physics the fundamental constituents of matter as well as their interactions are studied. Scattering experiments consisting of particle accelerator rings and detectors surrounding the collision points analyse phenomena at the sub-atomic scale ($\leq 10^{-15}\ m$).

All present knowledge is formulated in the Standard Model, which is in agreement with all experimental results, including high precision measurements at the large e^+e^- collider LEP [1].

1.1. The Standard Model of Particle Physics

1.1.1. Basic Concept

The Standard Model (SM) is a $SU(3)_C \otimes SU(2)_L \otimes U(1)$ gauge quantum field theory, which describes fermionic matter and its interaction through the exchange of boson field quanta [2].

In case of the electroweak interaction ($SU(2)_L \otimes U(1)$), these are the massive bosons W^+, W^-, Z^0 and the massless photon γ, whereas the exchange of massless gluons is responsible for the strong interaction ($SU(3)_C$) described by Quantum Chromodynamics (QCD).

Bosons are characterized by an integer spin in units of $\hbar$. Fermions have half integral spin and are divided into three generations of leptons

$$\begin{pmatrix} \nu_e \\ e \end{pmatrix}_L \quad e_R \qquad \begin{pmatrix} \nu_\mu \\ \mu \end{pmatrix}_L \quad \mu_R \qquad \begin{pmatrix} \nu_\tau \\ \tau \end{pmatrix}_L \quad \tau_R \tag{1.1}$$

and quarks

$$\begin{pmatrix} u \\ d' \end{pmatrix}_L \quad u_R\ d_R \qquad \begin{pmatrix} c \\ s' \end{pmatrix}_L \quad c_R\ s_R \qquad \begin{pmatrix} t \\ b' \end{pmatrix}_L \quad t_R\ b_R \tag{1.2}$$

with left-handed doublets $\left(T_3 = \pm\frac{1}{2}\right)$ and right-handed singlets ($T_3 = 0$) of the weak isospin T_3. The asymmetry between left (L) and right (R) follows from the parity violation of the weak interaction. Neutrinos $\nu_{e,\mu,\tau}$ have electric charge $Q = 0$, the other leptons $Q_{e,\mu,\tau} = -1$ and in the quark sector $Q_{u,c,t} = +\frac{2}{3}$ and $Q_{d,s,b} = -\frac{1}{3}$.

Leptons do not participate in the strong interaction, whereas quarks interact both electroweakly and strongly. Quarks are triplets under the ($SU(3)_C$) group and carry an additional charge called color, which is also a property of the gluon octet [3]. Since the QCD coupling α_S is large at large distances (small momentum transfers), quarks are confined inside color neutral hadrons. α_S gets small for large momentum transfers leading

to asymptotically free quarks [4] and allowing the calculation of cross-sections for the production of massive particles at LHC [5].

To keep the electroweak interaction universal, the mass eigenstates (d, s, b) are rotated by the unitary CKM matrix $\mathbf{V}$ to obtain the electroweak interaction eigenstates, (d', s', b') [6].

$$\begin{pmatrix} d' \\ s' \\ b' \end{pmatrix}_L = \begin{pmatrix} V_{ud} & V_{us} & V_{ub} \\ V_{cd} & V_{cs} & V_{cb} \\ V_{td} & V_{ts} & V_{tb} \end{pmatrix} \begin{pmatrix} d \\ s \\ b \end{pmatrix}_L \tag{1.3}$$

Gauge theories with massless gauge bosons including a spontaneously broken symmetry [7] for the gauge boson mass generation are renormalizable. In the unification of the weak and the electromagnetic theory, the Higgs mechanism [8] has been implemented into the GSW-Model [9] to generate masses for the $W^\pm$, Z^0 as well as for the fermions via Yukawa-couplings to the Higgs field proportional to the fermion mass.

In addition, the Higgs boson H^0, a scalar spin 0 particle, serves to preserve unitarity by regularizing cross-sections at high energies.

1.1.2. Experimental Verification and Limits

The Standard Model has been extensively checked experimentally, especially with the high precision data of LEP. Several discoveries in the last few decades are consistent with the theoretical description. A few examples are given below.

- Observation of the J/ψ-particle, a $c\bar{c}$ resonance with mass 3097 MeV [10], as well as the heavier 9460 MeV $b\bar{b}$ resonance [11].

- Discovery of the top quark at the $p\bar{p}$ collider Tevatron by D0 and CDF [12].

- Experimental observation of the neutral (NC) electroweak current [13], and of the $W^\pm$, Z^0 bosons [14] with masses as predicted by GSW theory.

- Three jet events measured at the e^+e^- collider PETRA at DESY and thus the identification of gluons [15].

- CP-violation measured in K- and B-decays [16].

- Confirmation of three generations, measured on the Z^0 resonance at LEP and SLAC [17].

The Higgs mechanism is the only sector of the SM, that remains experimentally unverified. The Higgs mass m_{H^0} is not predicted by the theory. A lower limit has been measured by LEP [18] and an upper bound is given by loop corrections, as shown in the Feynman diagram 1.1 [1], resulting in

$$114.4 \ GeV < m_{H^0} < 207 \ GeV$$

Despite all its success the SM is not regarded to be the final theory, because several open issues are not solved, e.g.
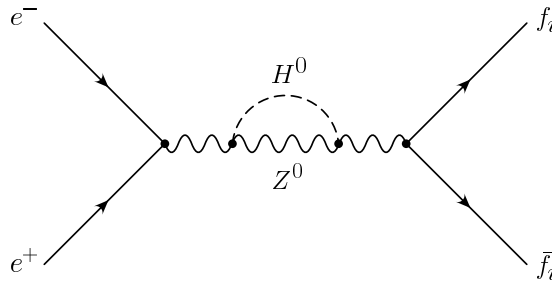
Abbildung 1.1.: The higher order Feynman diagram shows the Higgs boson correction on the Z^0 resonance. The dependence of the correction on the m_{H^0} mass is only logarithmic and leads to an upper bound on the Higgs mass. The correction on the electroweak coupling is larger, the smaller m_{H^0} is.

- It still has a large number of parameters.

- QCD and the electroweak theory are not unified in a Grand Unified Theory (GUT).

- Hierarchy problem: Since logarithmic divergencies are absorbed into a redefinition of physical parameters (renormalization), the Higgs mass corrections increase quadratically with the cutoff parameter Λ. At the GUT scale ($\Lambda \approx 10^{15}\ GeV$) this leads to a fine tuning problem to preserve a physical Higgs mass of $\mathcal{O}(100\ GeV)$.

- Gravity is not included.
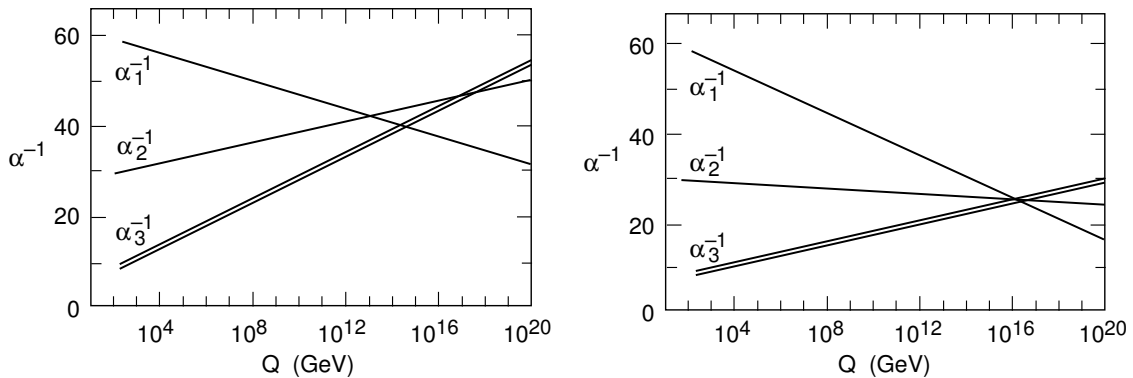
(a) Without SUSY the extrapolation of the inverse coupling constants α_1 ($U(1)$), α_2 ($SU(2)$), and α_3 ($SU(3)$) as functions of the energy scale Q does not lead to a unification (meeting at a single point), even when including a large error on α_3 (double lines).

(b) The same diagram based on the SUSY extension of the SM unifies the different forces at the GUT scale.

Abbildung 1.2.: Unification of the coupling constants at large energy scales [2].

Supersymmetry (SUSY) is at present the most favored concept to unify QCD and electroweak theory at the GUT scale (see figure 1.2), as well as to solve the hierarchy

problem by introduction of supersymmetric partners [19] to the SM particles. It also offers the possibility of incorporating gravity into a common framework, called Supergravity (SUGRA).

1.2. The Large Hadron Collider

To provide a closer look into the constituents of matter and their interactions, a small wavelength, i.e. high energy, is needed.

$$E = pc = \frac{hc}{\lambda} \qquad p \gg m \tag{1.4}$$

In a synchroton ring, particles are forced on circular trajectories by dynamic magnetic dipole fields. The particle momentum $|\vec{p}|$ is hence constrained by the orbit radius R of the ring.

$$R = \frac{|\vec{p}|}{q|\vec{B}|} \tag{1.5}$$

When accelerated, charged particles lose energy by emitting synchroton radiation. The energy loss per orbit, ΔE, is inverse proportional to the fourth power of the particle mass and therefore protons instead of electrons are used to reach the TeV energy scale.

$$\Delta E \sim \gamma^4 \qquad \gamma = \frac{E}{m} \qquad \left(\frac{m_e}{m_p}\right)^4 \approx 6 \times 10^{-14} \tag{1.6}$$

A new accelerator ring, the Large Hadron Collider (LHC) [20], is under construction at CERN[1] inside the tunnel with a circumference of 26.7 km, where the LEP ring was installed. It will provide pp collisions by two counter-rotating beams, each with 7 TeV energy, resulting in a center-of-mass energy of $\sqrt{s} = 14$ TeV, at four different collision points, where the following four LHC experiments are located (see also figure 1.3):

- **ATLAS**   A Toroidal LHC AparatuS [22]
  This is one of the general purpose detectors. All such detectors surround the interaction region with tracking, calorimetry, and muon detectors. ATLAS has a large stand-alone muon spectrometer for excellent muon measurement, a liquid argon and a hadronic tile calorimeter providing a good jet and missing energy reconstruction, and an inner tracking system inside a solenoidal magnetic field of 2 T.

- **ALICE**   A Large Ion Collider Experiment [23]
  LHC will also be used for heavy-ion interactions to study the physics of nuclear matter at high energies.

- **CMS**   Compact Muon Solenoid [24]
  In contrast to ATLAS, the design of CMS is compact. Apart from a good muon measurement, CMS emphasizes high resolution of electron and photon energies as well as precise tracking inside a 4 T solenoidal magnetic field.

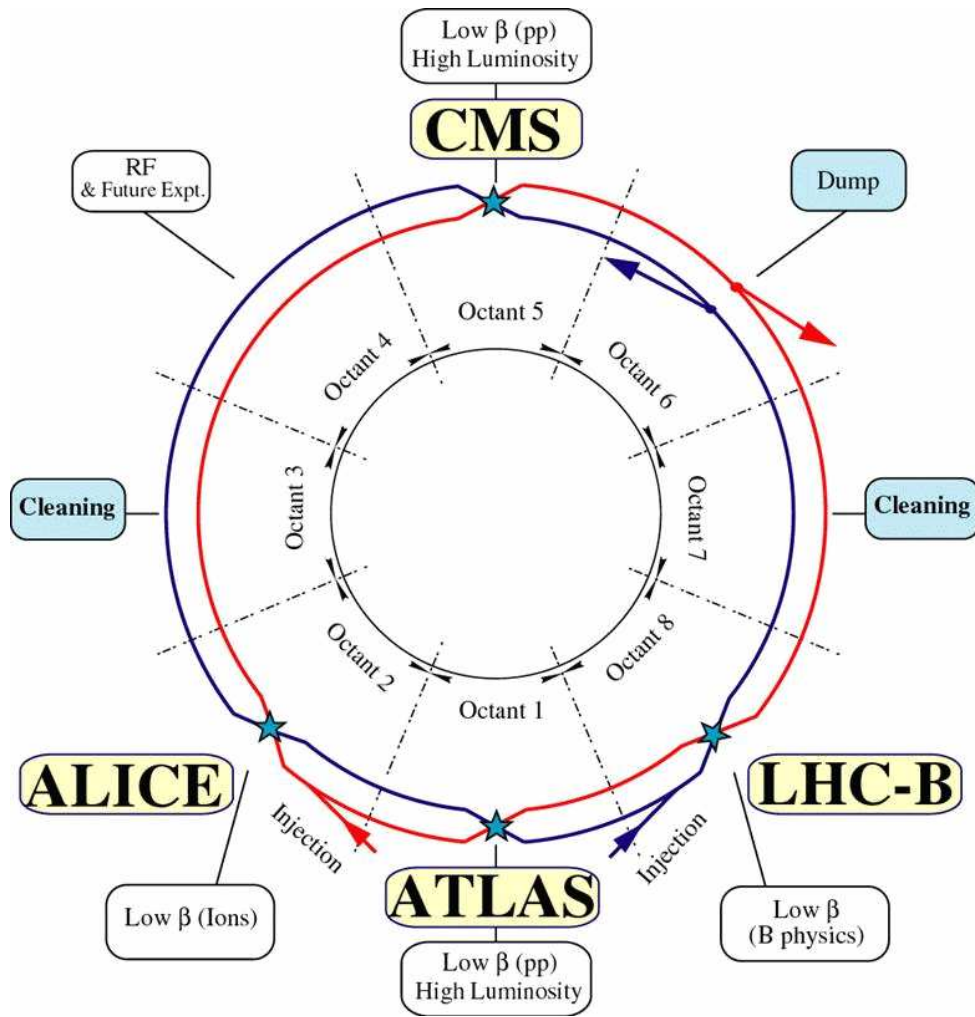[1]Centre Européen pour la Recherche Nucléaire [21]

Abbildung 1.3.: Layout of the Large Hadron Collider LHC with its four experiments [20].

- **LHCb**   Large Hadron Collider beauty experiment [25]
  This experiment is dedicated to precise measurement of CP violation in B meson decays.

Superconducting 8.4 T magnets and radio frequency (RF) cavities, cooled by a cryogenics system, bend and accelerate the proton beams, which are organized in bunches, as illustrated in figure 2.15 [26]. Each bunch will contain $\approx 10^{11}$ protons. With a bunch spacing of 25 ns, there is a bunch crossing rate of 40 MHz at the four interaction points.

For a process with cross-section σ, the event rate $\dot{N}$ is given by

$$\dot{N} = \mathcal{L}\, \sigma \tag{1.7}$$

where $\mathcal{L}$ is the machine luminosity. The LHC will start operation with relatively low luminosity, $\mathcal{L} \approx 10^{33}\ cm^{-2}s^{-1}$, followed by a high luminosity phase of $\mathcal{L} \approx 10^{34}\ cm^{-2}s^{-1}$. An overview of expected LHC event rates for various reactions can be obtained from figure 1.4 [27].
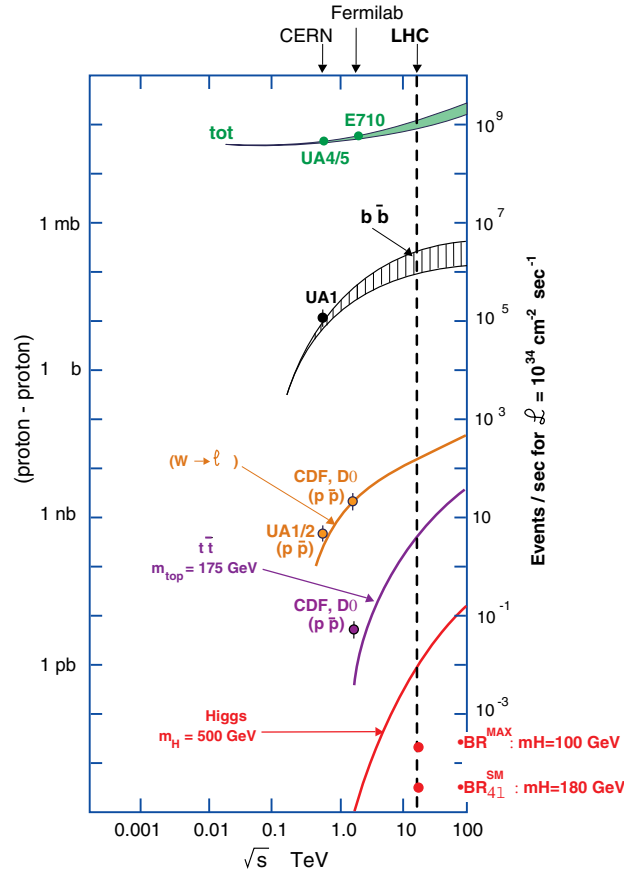
Abbildung 1.4.: Comparison of different cross-sections and event rates at Hadron Colliders [27]. The elastic *pp* cross-section will be used to measure the luminosity at LHC within 2 % and in addition processes like $Z^0 \to \mu^+\mu^-$ with large statistics are convenient for a first estimation as well as suitable for luminosity monitoring [28].

The LHC environment places stringent requirements on detectors and their electronics. They have to resist

- a hadronic fluence of $\Phi = 3 \cdot 10^{14}/cm^2$

- and a γ irradiation dose of $D_\gamma = 1.5 \cdot 10^5 \ Gy$

Therefore all materials used in the detectors have to be tested under these conditions.

1.2.1. Physics at the Large Hadron Collider

The LHC proton-proton physics can be divided into the analysis of Standard Model processes as well as searches for new phenomena, e.g. SUSY [27], [29].

LHC will be a top and bottom quark factory, e.g. production of $8 \cdot 10^6 \ t\bar{t}$ pairs per year at low luminosity. It is possible to achieve a precise measurement of top quark properties as well as those of other particles, for example the W-boson width [30]. Also the enormous
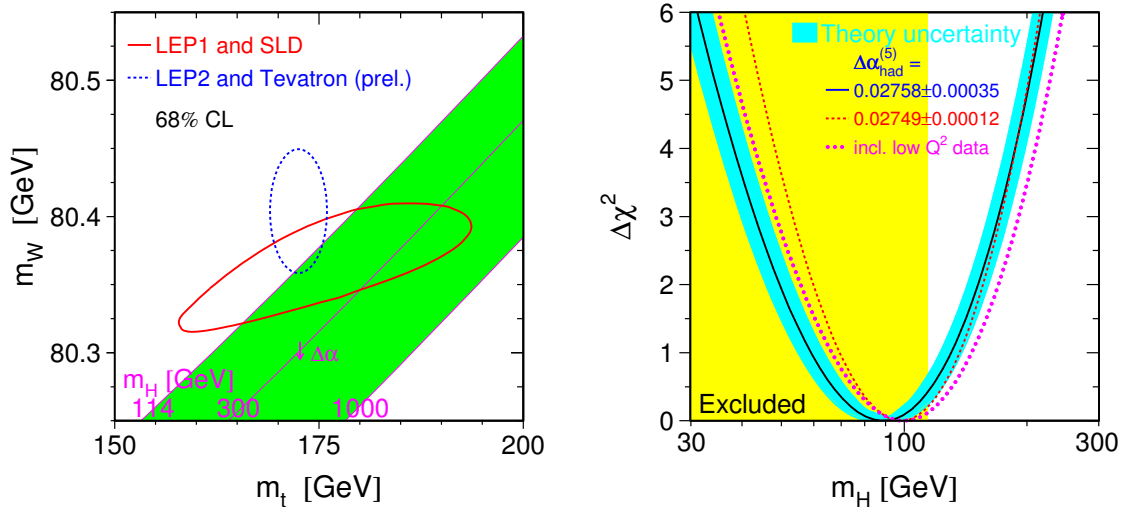
(a) Precise measurements of m_W and m_t give constraints on the SM Higgs boson mass [1].

(b) $\Delta\chi^2$-distribution from high Q^2 precision electroweak measurements [1] as function of m_{H^0}.

Abbildung 1.5.: It follows from LEP, SLD, CDF, and D0 experimental results, that a light SM Higgs boson is preferred. If interpreted in the theoretical framework of the SM, the result is a $\Delta\chi^2$ minimum at $89\ GeV$ with experimental errors of $+42\ GeV$, $-30\ GeV$ at $68\ \%$ confidence level [1].

numbers of B-hadrons allow looking for rare decays. For example, in some SUSY models the measurement of the branching ratio of $B_s^0 \to \mu^+\mu^-$ is proportional to $(\tan\beta)^6$ and would have a value larger by three orders of magnitude compared to the SM prediction. This would be a signature for new physics [33].

An important task of LHC is the discovery of the Higgs boson. As the plot 1.5(b) suggests, a light SM Higgs boson is preferred [17]. Figure 1.6 shows the cross-section for the various Higgs production mechanisms and the branching ratios for Higgs decays as functions of its mass m_{H^0} [31]. For small values ($m_{H^0} \leq 135\ GeV$) the decay into two photons, $H^0 \to \gamma\gamma$, offers a very characteristic signature, despite its extremely small branching ratio.

Production via vector boson fusion (see figure 1.6) followed by decay into two τ leptons, $H^0 \to \tau\tau$, is another promising discovery channel [32]. The by far most frequent decay mode $H^0 \to b\bar{b}$ is hard to exploit due to the enormous QCD jet background. This decay would lead to a 4 b-jet final state for a Higgs produced in association with a $t\bar{t}$ pair, $gg, q\bar{q} \to t\bar{t}H^0$, as illustrated in figure 1.6.

A tracking detector with excellent b-tagging capability might then be able to identify a signal in this channel. For heavier Higgs bosons, decays into W^+W^- and Z^0Z^0 pairs becomes predominant and greatly facilitates discovery.
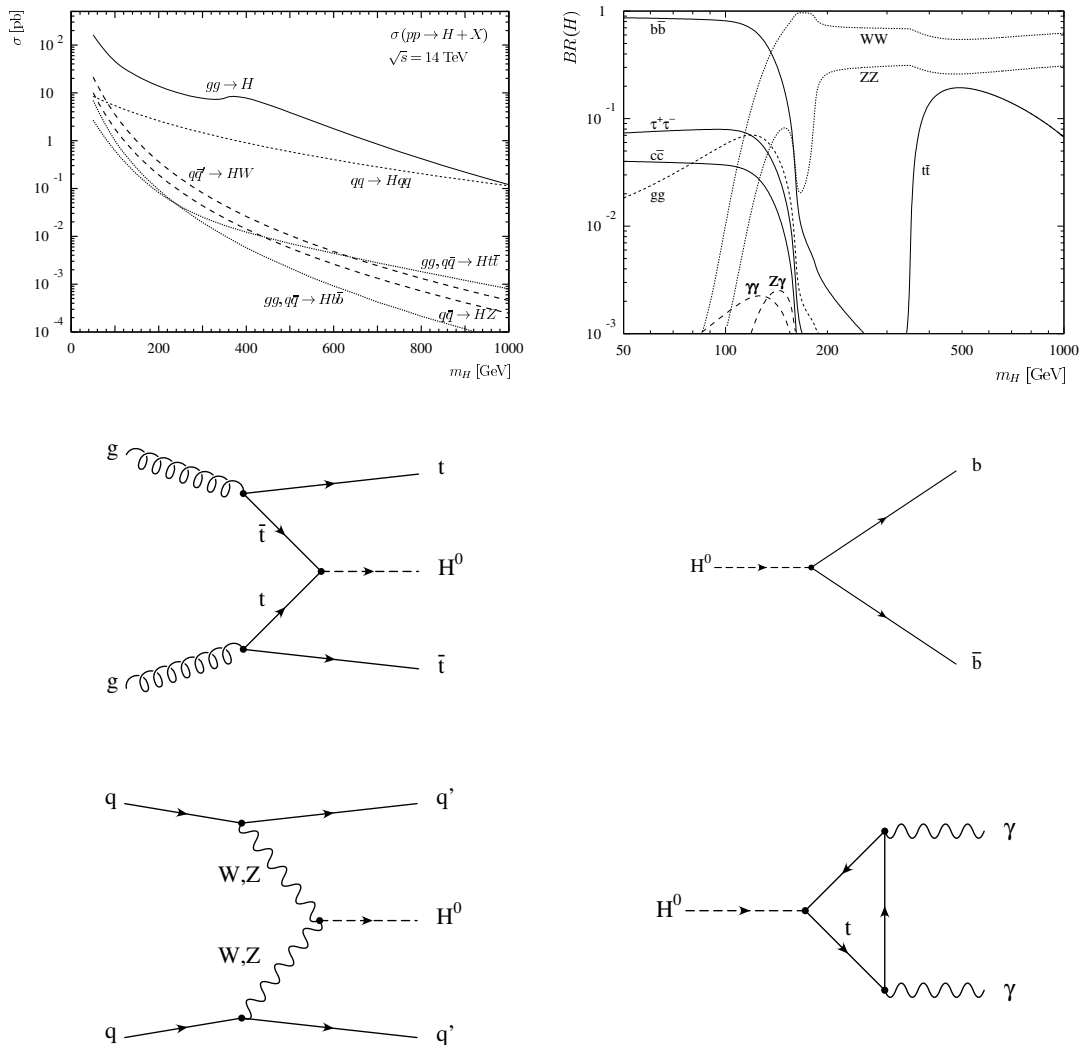
Abbildung 1.6.: Higgs production cross-sections (*left*) and decays (*right*) as a function of m_{H^0} [31]. The Feynman-diagrams on the left show first the production in association with a $t\bar{t}$ pair, $q\bar{q} \to t\bar{t}H^0$, and second the vector-boson-fusion, $qq \to qqH^0$ (q' denotes the production by exchange of a $W^\pm$, whereas the quark flavour is not changed by a Z^0). Those on the right side illustrate the decay into a $b\bar{b}$ pair, $H^0 \to b\bar{b}$, as well as the decay into two photons via a top quark loop, $H^0 \to \gamma\gamma$.

1.3. The Compact Muon Solenoid

As mentioned above, CMS is a multipurpose detector (see figure 1.7) for the study of pp collisions at the LHC [24]. Providing almost 4π coverage, its task is to analyse all decay products originating from the pp interaction region point and to reconstruct physics events as completely as possible. CMS has a cylindrical geometry with a diameter of 14.6 m in

Very-forward Calorimeter

Superconducting Solenoid

Silicon Tracker

Pixel Detector

Preshower

Hadronic Calorimeter

Electromagnetic Calorimeter

Muon Detectors

Compact Muon Solenoid
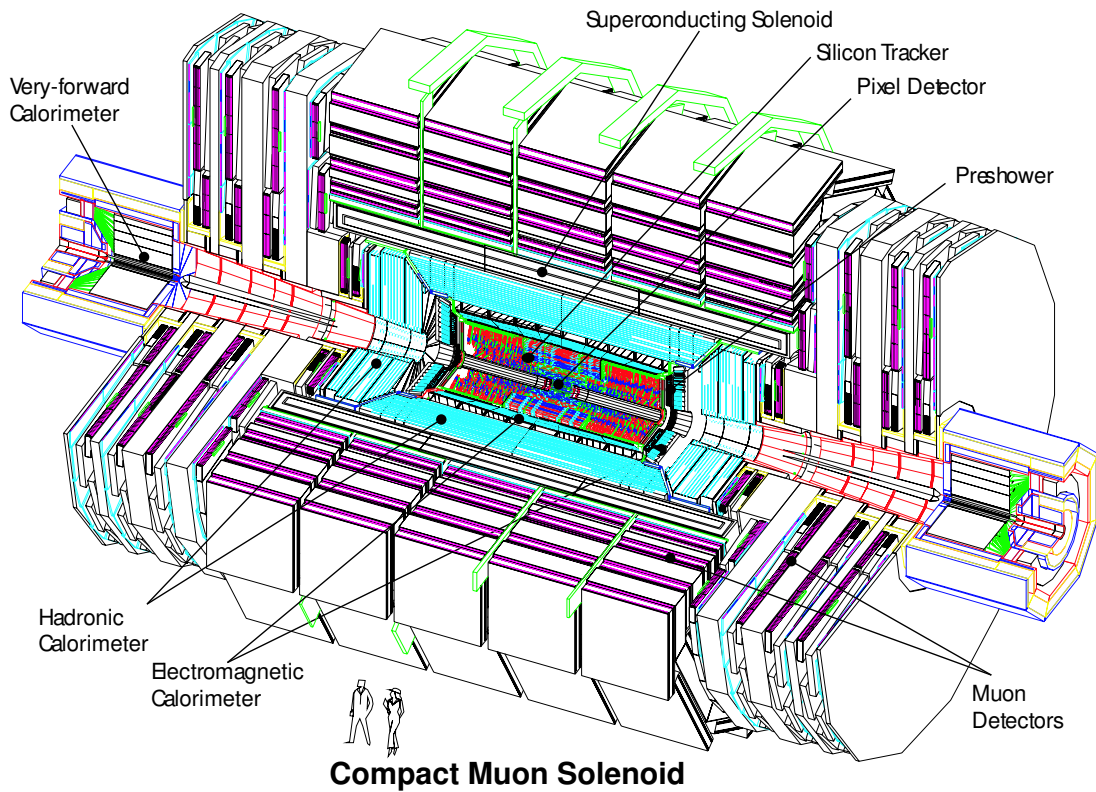
Abbildung 1.7.: Layout of the CMS detector [24].

the barrel region and is closed by endcaps. The overall length will be 22 m, and the weight around 12500 t.
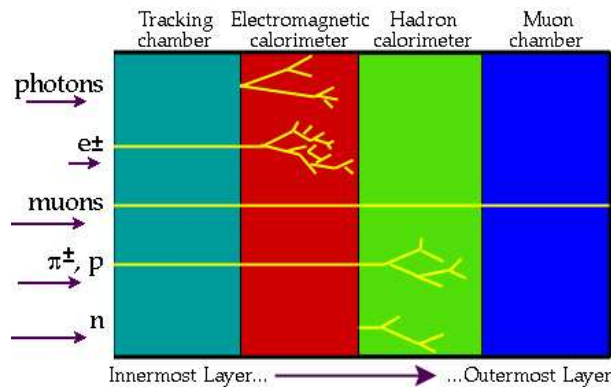
Abbildung 1.8.: Principle of particle identification in multipurpose detectors [34].

In CMS a superconducting coil generates a solenoidal 4 T magnetic field, in which the central tracker as well as both calorimeters are placed. The iron return yoke is instrumented with four layers of muon chambers.

Common for all multipurpose detectors is the working principle illustrated in the figure 1.8. Photon and electron energies are measured by the electromagnetic calorimeter, whereas the hadronic energy is mainly obtained by the hadron calorimeter. Muons are

identified by chambers in the outermost detector layers. Their momenta, as well as those of other charged particles, are measured in the tracker, placed inside the magnetic field.

Hence the construction is divided into several sub-detectors, each of them responsible for detection of special particles.

1.3.1. The Muon System

The largest part of the CMS detector is the muon system. It is designed to identify muons with pseudorapidity $|\eta| \leq 2.4$, to determine their charge and to measure their momentum in combination with the central tracker. It consists of

- DT:
  Drift Tubes in the barrel region

- CSC:
  Cathode Strip Chambers in the endcap area

- RPC:
  Resistive Plate Chambers in both regions for fast level 1 trigger signals [35].

An efficient muon measurement with a good momentum resolution is essential for reconstruction of various processes, e.g. $H^0 \rightarrow ZZ^* \rightarrow \mu^+\mu^-\mu^+\mu^-$.
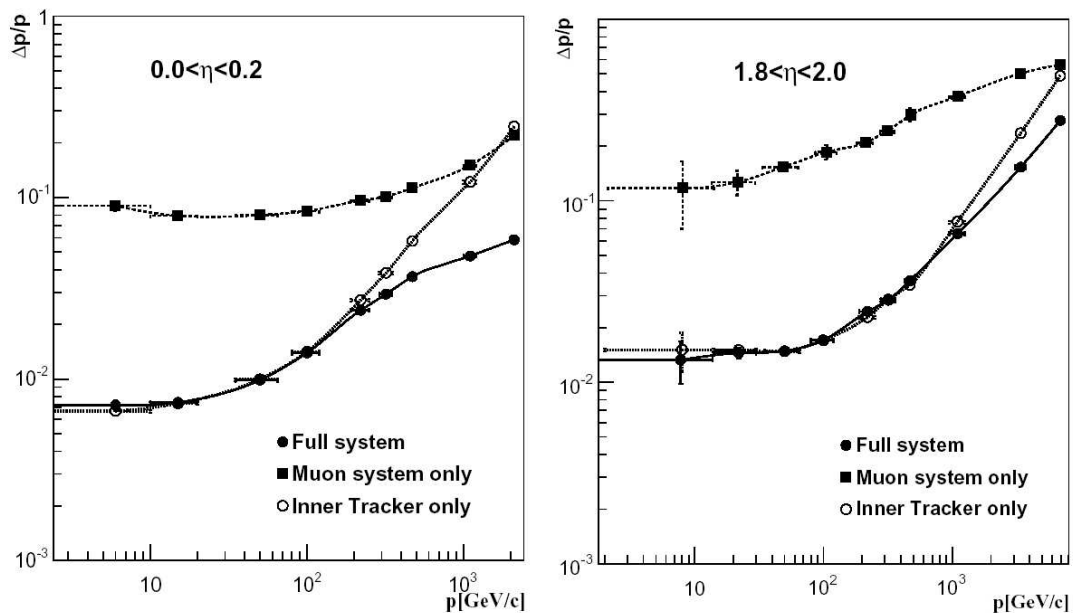
Abbildung 1.9.: p_T resolution of the muon system and the tracker alone as well as both combined together in the central (*left*) and forward region (*right*) [29]. For momenta less than 100 GeV, the full detector simulation shows a resolution of better than 1 %.

There are two main contributions to the relative measurement error of the transverse momentum [2]

$$\frac{\Delta p_T}{p_T} = \left(\frac{\Delta p_T}{p_T}\right)_{res} \oplus \left(\frac{\Delta p_T}{p_T}\right)_{ms} \tag{1.8}$$

multiple scattering (ms) and trajectory uncertainty (res), which includes alignment errors. They can be estimated to be

$$\left(\frac{\Delta p_T}{p_T}\right)_{res} = \frac{7\ \sigma_x\ p_T}{L^2\ 0.3\ B} \approx 6 \cdot 10^{-3}\ \frac{\sigma_x}{mm}\ \frac{p_T}{GeV} \sim p_T \cdot \sigma_x \qquad (1.9)$$

and

$$\left(\frac{\Delta p_T}{p_T}\right)_{ms} = \frac{0.016}{L\ 0.3\ B}\ \sqrt{\frac{X}{X_0}} \approx 0.013\ \sqrt{\frac{X}{X_0}} \sim const. \qquad (1.10)$$

The single point resolution σ_x depends on detector granularity and can be improved by detector alignment. X is the distance measured in units of the radiation length X_0, B the magnetic field and L the trajectory chord (see appendix B).

As it can be seen from figure 1.9 a stand-alone muon system provides in the barrel region a resolution varying from 8 % to 20 %, which becomes worse in the forward region. For $p_\mu \leq 100\ GeV$ the muon momenta are measured by the tracker up to $\frac{\Delta p}{p} \approx 1$ %, before the influence of the linear term in (1.9) increases.

To identify muons, a matching of inner tracker and muon system tracks is required over the full momentum range and for $p_\mu \geq 100\ GeV$, a joint fit of matched tracks can improve the momentum resolution. As described later, a special optical link has been developed to align the tracker with respect to the muon system.

1.3.2.   The Calorimeter System

Inside the solenoid magnet of about 6 m diameter, two calorimeters measure the energy of particles.
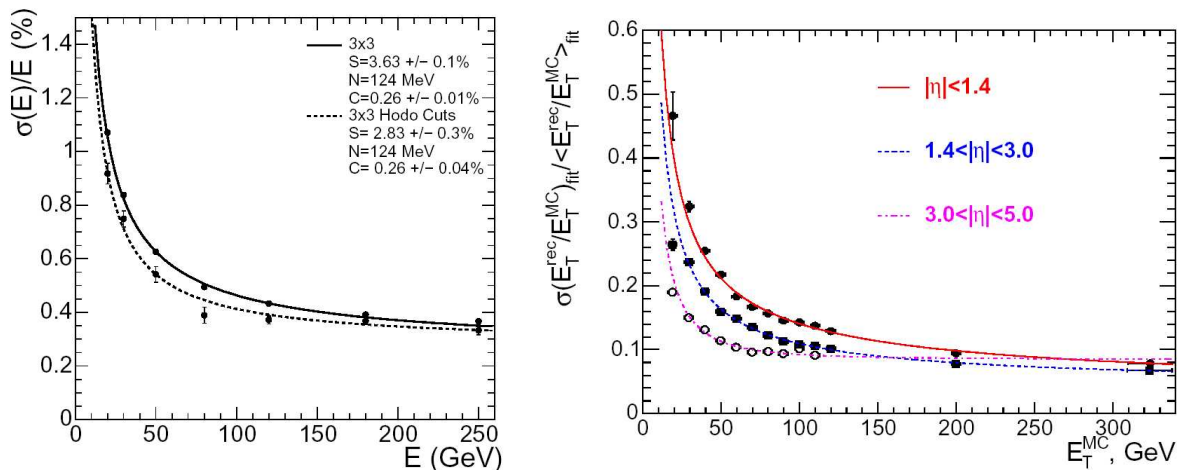
ECAL

The CMS electromagnetic calorimeter, ECAL, is composed of lead tungstate crystals, $PbWO_4$. The design can be kept compact, since $PbWO_4$ is a dense material ($\rho = 8.3\ g\ cm^{-3}$). The crystals have a $22 \times 22\ mm^2$ front face and a length of 23 cm, which corresponds to 25.8 X_0. The scintillation time is in the order of the LHC bunch crossing rate and the light yield is amplified by silicon avalanche photo diodes (APD). The small Moliere radius of 2.2 cm allows a good separation between adjacent showers.

Especially for low Higgs masses $m_{H^0} \leq 150\ GeV$, the decay channel $H^0 \to \gamma\gamma$ plays an important role due to its clear signature. Its identification requires good energy resolution, which is provided by the ECAL and can be described by

$$\frac{\sigma_E}{E} = \frac{S}{\sqrt{E}} \oplus \frac{N}{E} \oplus C$$

with a stochastic term S, noise N and constant term C. The resolution is shown as a function of energy in diagram 1.10(a) [29]. For electrons/positrons or photons with $E \geq 50\ GeV$ the ECAL provides a resolution better than 0.5 %.

(a) ECAL resolution as function of electron energy. Details about the parameters can be found in [29].

(b) HCAL resolution as function of particle energy in different detector regions.

Abbildung 1.10.: Calorimeter resolution [29].

HCAL

The showers of strongly interacting particles, like pions, kaons, protons or neutrons, are contained inside the hadronic calorimeter HCAL. To provide good hermeticity, very forward calorimeters are placed close to the beampipe covering the range from $3.0 \leq |\eta| \leq 5.0$, see figure 1.7.

In the HCAL brass absorber plates are interleaved with $3.7\ mm$ thin plastic scintillators tiles, which are read out by wavelength-shifting fibres (WLS) in the barrel and endcap region. In the forward calorimeter quartz fibres are embedded in a steel absorber matrix and the emitted Cerenkov light is guided by fibres to photomultipliers.

The performance of the HCAL is shown in diagram 1.10(b), where the jet transverse energy resolution is plotted versus the simulated transverse energy for different detector regions.

The curves show the typical $1/\sqrt{E}$ behaviour and for high particle energies, $E_T \geq 50\ GeV$, $10-20\ \%$ resolution can be achieved, depending on the detector region.

1.4. The CMS Tracking System

1.4.1. The Pixel Tracker

To be able to reconstruct primary and secondary vertices with a resolution of $10\ \mu m$ in $r\varphi$ and $20\ \mu m$ in z, 66 million silicon pixels with a size of $100 \times 150\ \mu m^2$ are arranged in larger units close to the beampipe around the interaction point (IP, $z = 0$), as shown in figure 1.12(a).

There are three layers in the barrel region, with radii of 4.4 cm, 7.3 cm, 10.2 cm, and two discs on each z side, $|z| = 34.5\ cm, 46.5\ cm$ for a total of $\approx 1\ m^2$ active area [29].

The alignment of the pixel vertex detector with respect to the silicon strip tracker will be done by using reconstructed tracks. No internal optical alignment is implemented in this device.
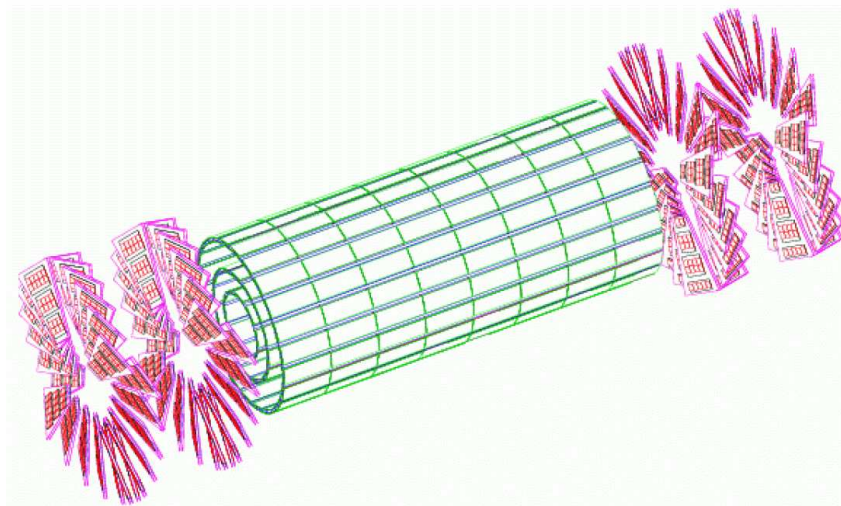

Abbildung 1.11.: The layout of the pixel vertex detector, the innermost part of the tracker [29].

## 1.4.2. The Silicon Microstrip Tracker

A 3D drawing, figure 1.12(a), of the CMS Silicon Microstrip Tracker (SST) as well as the rz-view, figure 1.13, illustrate the general layout. The SST is divided into sub-detectors: tracker inner barrel (TIB), tracker outer barrel (TOB), two tracker inner discs (TID), and two tracker endcaps (TEC). The SST has to provide:

1. Precise track measurement
   A good impact parameter and momentum resolution is needed. It relies on high quality track reconstruction for low and high p_T tracks.

2. Fast detector response
   The LHC bunch crossing rate of 40 MHz has to be resolved.

3. Low material budget
   It is essential to minimize the amount of material in front of the ECAL. Furthermore, all materials used in the tracker must be radiation hard.

With about 200 m^2 of active silicon in 15148 modules it is currently[2] the largest silicon tracker with a cylindrical size of 2.4 $m \times 5.4\ m$. The working environment will be inside a 4 T magnetic field and the construction is cooled down in a dry N_2 atmosphere to -10^oC operating temperature to minimize silicon radiation damage effects.

---

[2]in the year 2006

1. Introduction
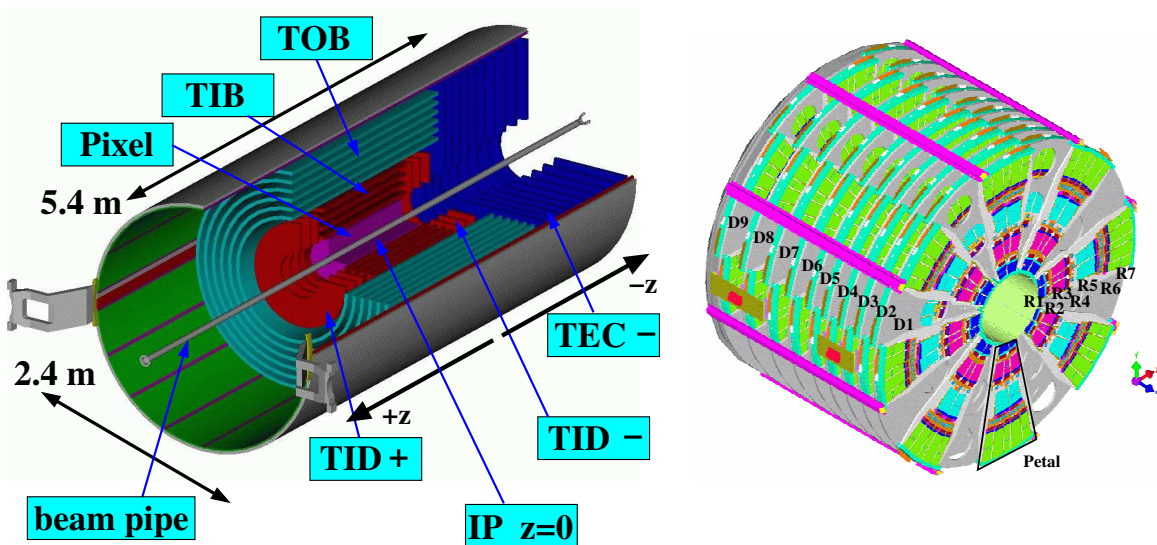
(a) 3D view of the SST. It has a cylindrical design with a diameter of 2.4 m and a length of 5.4 m.

(b) Layout of one tracker endcap, TEC. It consits of 9 discs, $D1, \ldots, D9$. Modules are mounted on petals in a ring structure from the innermost layer $R1$ to the outermost $R7$.

Abbildung 1.12.: The Silicon Strip Tracker [36].

In the detailed rz cross-section of the tracker in figure 1.13, the silicon sensor positions are shown and the corresponding pseudorapidity η is indicated.

The sensors in the barrel are rectangular with strips parallel to the z-axis, whereas in the endcaps wedge-shaped geometry has been used and the strip direction is perpendicular to the z-axis. The pitch p, defined as the distance between two neighbouring strips, varies in the radial direction from 80 μm to 205 μm.

Thin sensors, $d = 320 \; \mu m$, are mounted inside a radius of $r \leq 600 \; mm$, i.e. the TIB area and TEC rings R1 to R4. To compensate for the increase in noise due to a larger strip length, thick sensors, $d = 500 \; \mu m$, are used in the TOB region and in TEC rings R5 to R7. To obtain a position measurement along the strips, double sided modules, consisting of two single sided ones mounted back-to-back with a stereo angle of 5.7^o, are placed on several layers in the barrel and also in R1, R2, R5 in the endcaps [36].

The CMS silicon sensor design (see figure 1.14) is optimized for operations in the LHC radiation environment ([51], [52]).

It consists of n-type bulk silicon with $320 \pm 20 \; \mu m$ and $500 \pm 20 \; \mu m$ thickness. On the junction side heavily doped p^+ implants are capacitatively coupled to aluminium strips, with the dielectricum in between being a multilayer (insulating layer) of SiO_2/Si_3N_4 with a thickness of 1.1 μm. Wire bonds to the AC pads are used for signal readout.

The p^+ implant width w is smaller than the aluminium strip width. The metal overhang on each side is of the order of 15 % to improve breakdown behaviour. For all sensors,
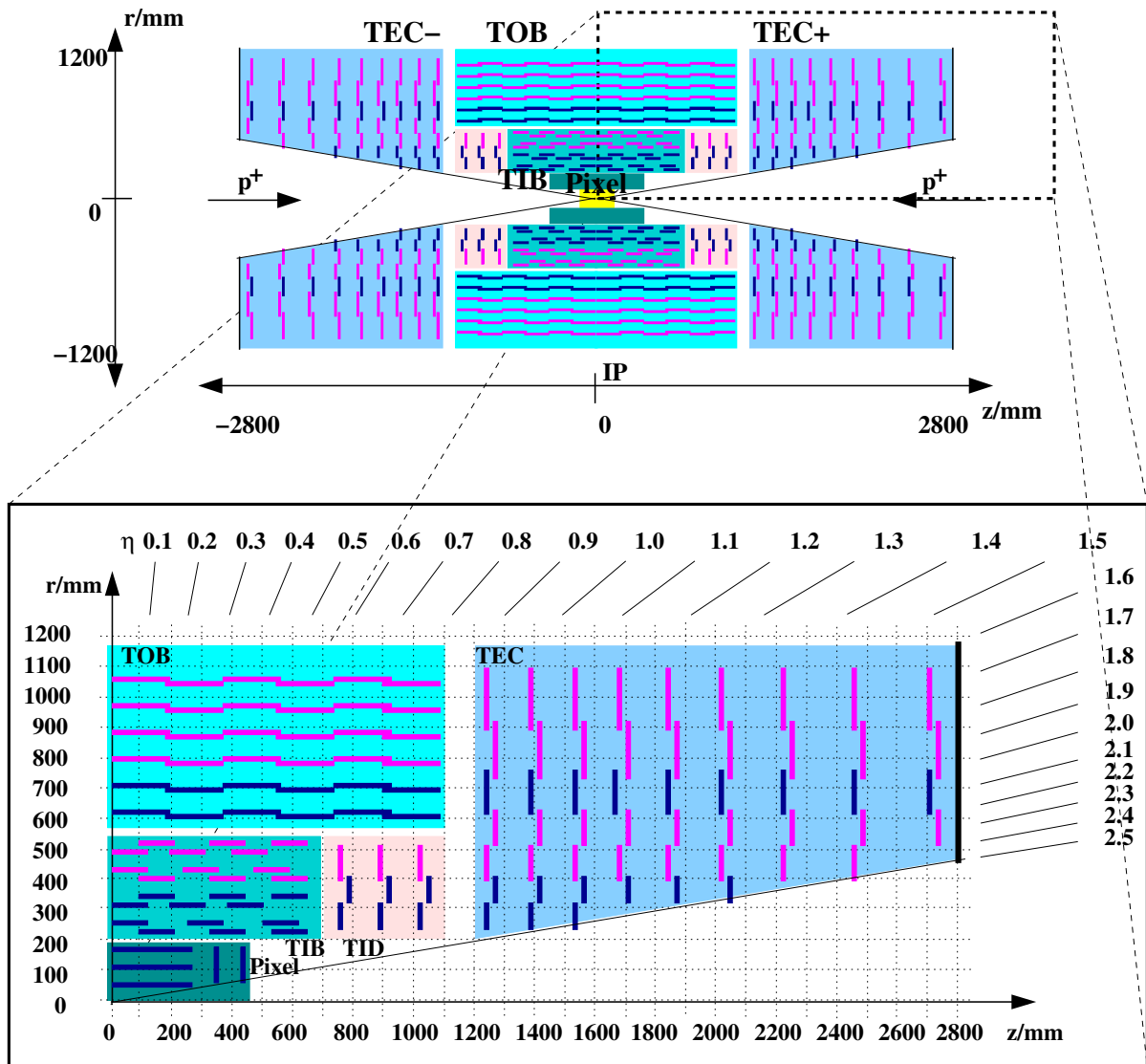
Abbildung 1.13.: *rz*-view of the SST with one quarter in detail. The positions of the silicon modules in TIB/TID, TOB and TEC are indicated. The double sided modules are marked in dark blue. The bulkheads are located at $z = \pm 2800\ mm$.

the ratio $\frac{w}{p} = \frac{1}{4}$ is fixed to keep the strip capacitance constant. To guarantee a good ohmic contact to the metal electrode on the backplane a small n^+ implant is used [52].

With a bias voltage $V_{bias} > 0$ on the backplane, the sensor works as a reverse-biased strip-shaped (p^+ implantation) diode. If a minimal ionizing particle (MIP) crosses the detector, electrons e^- and holes h^+ drift in the electric field to the electrodes, e^- to the backplane and h^+ to the junction side, where the segmentation delivers the spatial information. The induced charge is capacitatively read out and the signal amplified by the APV chips, each of them having 128 channels.

bias ring ⟍ guard ring   wire bond ⟍   bias resistor
                                           DC pad   AC pad

aluminium strip

oxide
(thin layers of
SiO$_2$ and Si$_3$N$_4$)

n$^+$-ring

p$^+$-implants below
bias and guard ring

p$^+$-strips

w   p

n-bulk

p$^+$-implants below
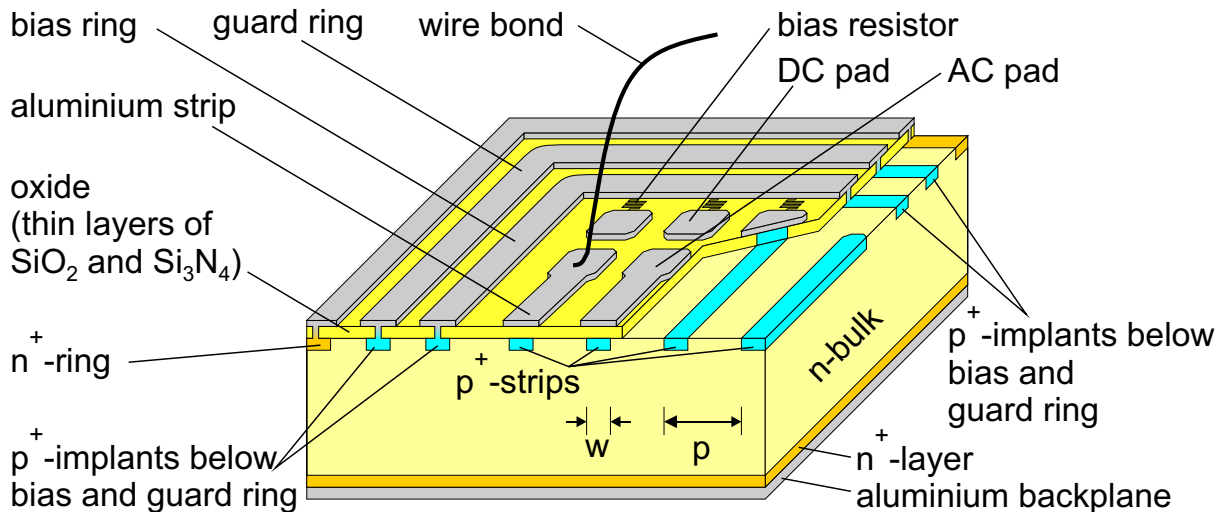bias and
guard ring

n$^+$-layer
aluminium backplane

Abbildung 1.14.: CMS microstrip sensor, 3D view [65].

The Tracker Mechanical Support Structure

The construction is modular in order to be able to build elements in different laboratories and to facilitate maintenance. It is made of carbon fibre composite materials, which have a large radiation length and at the same time large mechanical stability.

TIB, TID, TOB, and TEC are further subdivided into several elements, which carry finally the active components: silicon strip sensors of different shape, size, and thickness, according to their position in the tracker. A complete overview of the modular mechanical design is shown in figure 1.15, separately for the barrel and the endcap region:

- Two endcaps, TEC+ and TEC-, each consisting of 9 discs. The TIB and the TOB are built out of 4 and 6 cylindrical layers, respectively.

- There are 8 front and 8 back petals on each TEC disc with trapezoidal silicon modules arranged in ring geometry. In the TOB, the rods, each carrying 6 single or double sided rectangular modules, are inserted into appropiate openings of the support wheels. Strings of modules comprise the TIB half-shells, which are fixed to the support flanges. The TID consists of 3 rings of modules mounted on carbon fibre discs, which are attached to the outer TIB flanges (see appendix A).

- Silicon sensors and readout components of the detector modules are glued on carbon fibre frames.

The Tracker Performance

The measurement accuracy for the transverse impact parameter Δd_0 as well as the transverse momentum resolution $\frac{\Delta p_T}{p_T}$ are shown in diagram 1.16 as functions of the pseudorapidity η. Due to the increase in the amount of traversed material and to lever arm variations the resolution quality decreases for larger pseudorapidity values, starting at $\eta = 1.6$. In the barrel region $\frac{\Delta p_T}{p_T} \approx 1 - 2\,\%$ is achieved. The momentum error increases in the endcap

Barrel **Endcap**

subdetectors

TEC+, TEC−
TIB, TOB
in half barrels

flange, wheel, disc

9 discs in TEC
4 wheels in TOB
4 flanges in TIB

rod, shell, petal

8 front, 8 back petals
on TEC discs
4 layers of shells in TIB
6 layers of rods in TOB

modules

string structure in TIB
6 modules on rods in TOB
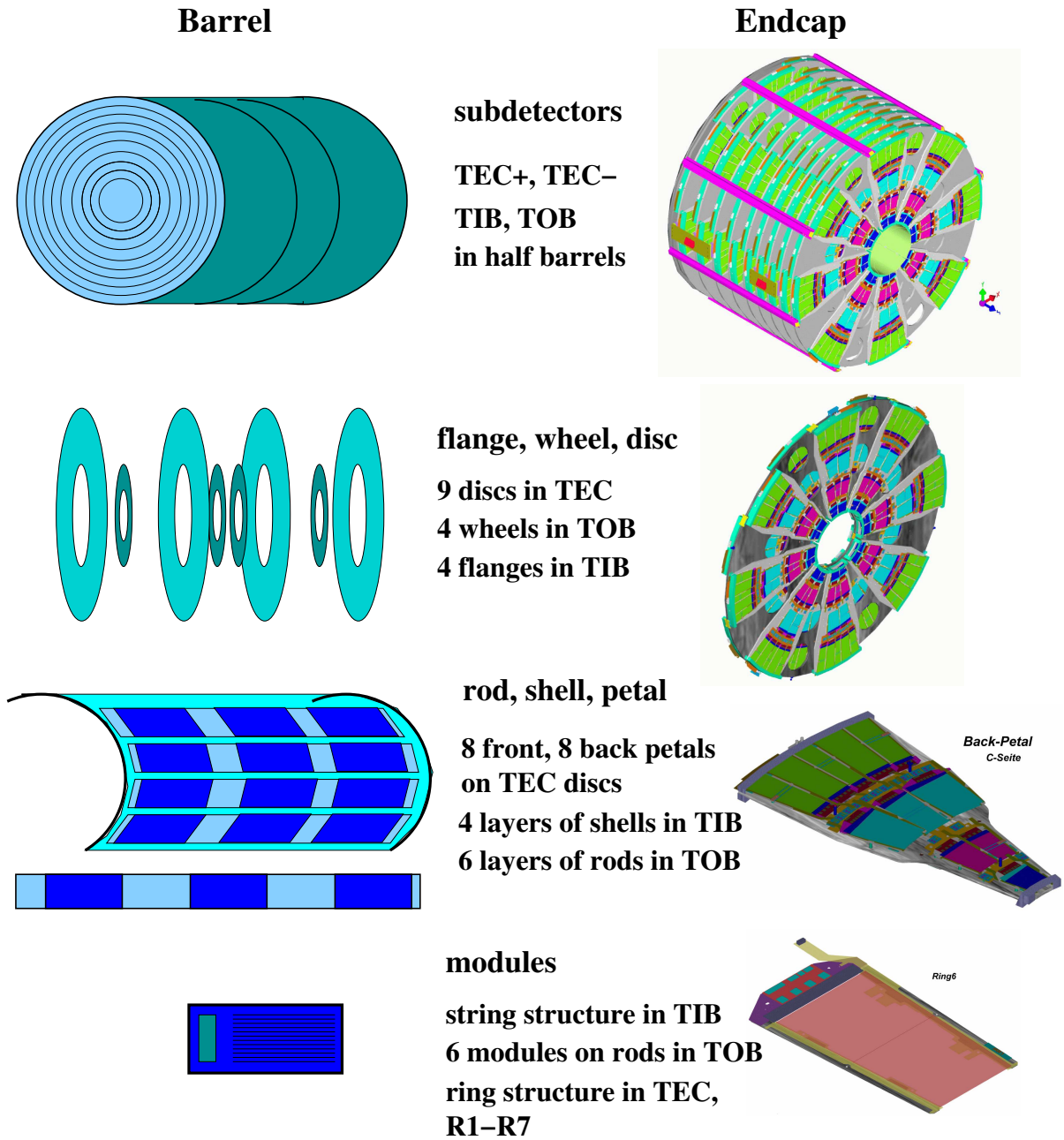**ring structure in TEC,**
R1−R7

Abbildung 1.15.: The different mechanical substructures of the SST are ordered according to their size
[36]. A collection of photographs of the tracker elements is shown in appendix A.

region, especially for high p_T muons. The Δd_0 resolution is nearly independent of η and
varies from 10 μm for high p_T muons to 100 μm for muons of low p_T.

Accurate knowledge of the absolute sensor positions is essential for successful track
reconstruction. Simulations have shown that the correct assignment of hits to tracks de-
pends on the precision of a pre-aligned detector as provided by survey measurements and
by the Laser Alignment System [29] [37].

The single hit resolution is given by the error of a uniform distribution $\frac{p}{\sqrt{12}}$, where
p denotes the pitch and varies from 23.1 μm to 59.2 μm. If the particle charge shared
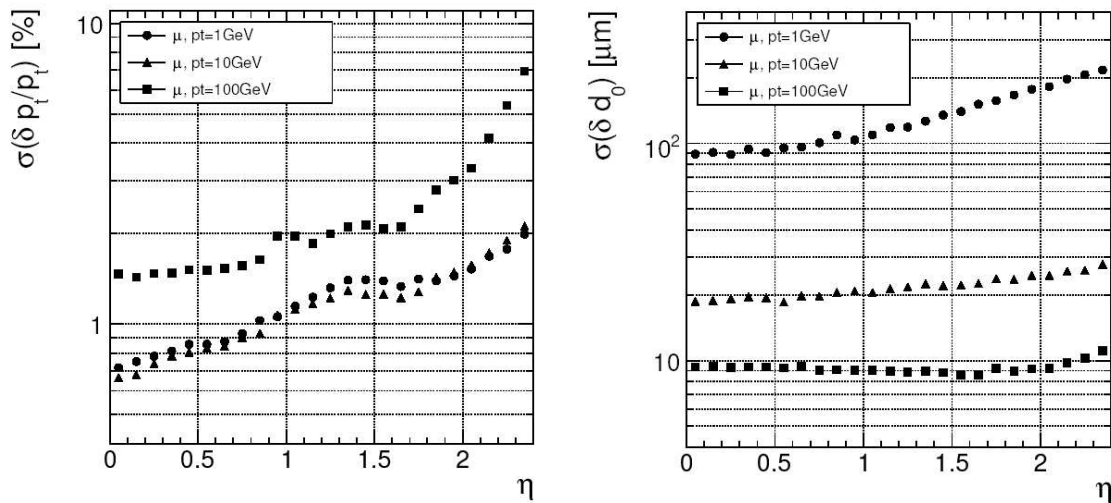
(a) The p_T resolution as a function of η and muon momenta. For low p_T it is around 1 %, but also depends on the region of measurement in the detector.

(b) The transverse impact parameter shows a nearly η independent behaviour and resolution down to 10 μm are envisaged for large momenta. Simulations of low muon momenta give impact parameters of less precision.

Abbildung 1.16.: The tracker performance [29].

among several adjacent strips, then the positional accuracy is improved because of the analogue tracker readout.

Knowledge of the absolute sensor positions must be more precise than the intrinsic resolution of the silicon sensors if the tracking capabilities of the SST are to be realized. Sensor alignment by tracks is needed to determine the absolute positions at the 10 μm scale.

2. Description of the CMS Tracker Laser Alignment System

To realize the potential of the CMS tracker, a precise knowledge of the position of the silicon modules is essential. Given the intrinsic sensor resolution (23.1 μm to 59.2 μm), an alignment accuracy of better than 10 μm is desired for all detector elements. Such an accuracy can be reached only by using a large number of reconstructed tracks.

The strategy for the alignment of the CMS tracker involves three steps [29]:

1. Mechanical construction precision and survey:
   All support structures are constructed in a mechanically precise way and are checked by standard survey methods, e.g. 3D measuring machines. For the large subdetector elements (TIB, TOB, and TEC) this precision amounts to a few hundred microns, while their relative positioning upon assembling the tracker will be accurate to a few millimeters.

2. Laser Alignment System (LAS):
   To guarantee stable and efficient pattern recognition for tracks, the position of the subdetectors should be known to about 100 μm [38]. The LAS will align the TIB, TOB, and the two TECs with respect to each other within 100 μm.

3. Alignment with tracks:
   A large sample of reconstructed tracks will be used to achieve the final accuracy of 10 μm. Studies and recent developments are summarized in [29].

2.1. Purpose of the LAS

2.1.1. Goals of the CMS Tracker Laser Alignment

The LAS is integrated in the CMS tracker and has to accomplish the following tasks:

Internal Tracker Alignment

As noted above, the first goal of the LAS is to align the tracker subdetectors (TIB, TOB. 2 TECs) with respect to each other to an accuracy of 100 μm in order to guarantee track pattern recognition and fast online reconstruction, so that track data can be used in High Level Trigger (HLT) decisions. This is essential in the CMS trigger scheme, which is organized in several levels [39]. The dataflow from an initial bunch crossing rate of

$40\ MHz$ is reduced by hardware triggers to $100\ kHz$ and further decreased to $100\ Hz$ by software High Level Triggers.

Following alignment based on large samples of offline reconstructed tracks, the detector will be known at the 10 μm scale. Hence relative movements of the carbon fibre support structure have to be monitored with the same accuracy. Such movements may be due to thermal stresses, since the tracker will be cooled down to -10^oC, or to switching on and off the 4 Tesla magnetic field. Therefore, the second goal of the LAS is the monitoring of these time-dependent effects at the 10 μm level.

Since the LAS is integrated in the tracker and uses the tracker sensors for the detection of the laser rays, it offers the advantage of being always available, before, during and after physics runs.

External Alignment to the Muon System

The third goal of the LAS is the etablishment of a common coordinate system for the tracker and the muon chambers via an optical link.

Laser beams with defined positions and directions in the internal tracker coordinate frame are detected in the muon system, thus determining the position of these CMS subdetectors with respect to each other. Tiltmeters are used in both subdetectors to determine their relative φ positioning by measuring their orientation with respect to gravity.

2.1.2. Alignment Objects

As an example of the precision with which objects are mounted on the tracker mechanical substructures, the data for the TEC are collected in the table below. In the column specification the range Δ of placement uncertainties is given according to [40] and in the column data the measured $RMS_{x,y}$ values are collected [41].

TEC mounting precision		
	specification	data
elements	Δ	$RMS_{x,y}$
	μm	μm
sensor $\rightarrow$ module	± 10	10
module $\rightarrow$ petal	$\pm 50 - 100$	25
petal $\rightarrow$ disc	$\pm 100 - 200$	60
disc $\rightarrow$ TEC CS	$\pm 100 - 500$	50

Tabelle 2.1.: Design specification for the TEC mechanical mounting precision. The internal TEC coordinate system (TEC CS) will be defined in section 2.4. Important to note is that the range Δ is used in the column specification whereas the RMS values are shown in the column data. The measured placement accuracy of 60 μm in the row petal versus disc was obtained by measuring the petal inserts in the disc coordinate frame [41].

If the absolute disc positions are reconstructed by the LAS to within 100 μm, then the sum of the other error contributions

$$10 \ \mu m \oplus 20 \ \mu m \oplus 50 \ \mu m \approx 50 \ \mu m \ll 100 \ \mu m \tag{2.1}$$

justifies the approximation that the measured laser spots in the modules represent the disc positions. Also for the inner and outer barrel, the placement accuracy of silicon modules within each subdetector is 50 μm. Hence follows, that the objects to be optically aligned are the discs, wheels, and flanges [53], see figure 1.15.

The parameters that are reconstruced by the LAS are discussed in section 2.4.

2.2. Requirements and Design Considerations

All tracker components have to be radiation hard, non-magnetic, light and mechanically stable. In addition to these general properties, further design considerations have to be taken into account in realizing the optical alignment system.

2.2.1. Concept

- Minimal impact on tracker layout
  Only a few optical components are additionally integrated into the tracker. The same silicon modules that detect the passage of charged particles are used as well to readout the induced laser signals. This necessitates a modification of the appropiate sensors so that they are transparent for laser light.

- No external reference frame
  All elements of the LAS are mounted directly on the tracker support structure to allow a direct alignment without need for an external reference structure.

- Redundancy
  The actual state of the tracker has to be reconstructed by a redundant amount of module readings. Thus the number of measurements must be greater than the number of parameters.

- Near infrared lasers
  The bandgap of Si is 1.12 eV, equivalent to a photon wavelength of $\lambda = 1107 \ nm$. Stable lasers in the near infrared region have to be used in order to achieve light transmission adequate to reach successive layers of silicon sensors, combined with sufficient absorption to generate signals inside the sensors. Due to the timing characteristics of the readout system, the laser must work in pulsed mode.

- Support online track reconstruction
  To reduce the dataflow by HLT, a pre-aligned detector is fundamental for pattern recognition algorithms and the LAS has to be integrated into the CMS DAQ.

- High resolution
  A good laserspot resolution is required to be able to monitor the structure. This assumes straight rays with gaussian profiles on each layer and minimal refraction effects.

- Minimal costs
  Research and development of new high precision optical alignment tools has to be combined with an affordable budget.

2.2.2. Working Principle

The proposed technique is based on the transmission (T) and absorption (A) behaviour of silicon. The absorbed part of the light generates a signal proportional to the intensity absorbed in the silicon strip module, whereas the transmitted part reaches the next module layer. The reconstruction of the laser spot profile provides the module position.
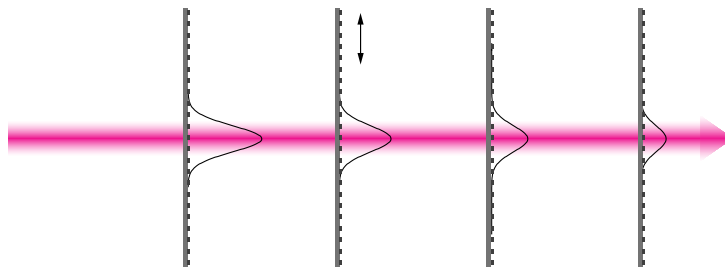
Abbildung 2.1.: Illustration of the working principle.

Reflection (R) should be minimized to have smaller losses and less interference. Preparatory measurements on one of the first silicon sensors show the dependence of T and R on the light wavelength, figure 2.2. It can be seen that a large fraction of the incoming light is reflected at the silicon-air-interface. Improvements regarding this behaviour are discussed in chapter 4.

The choice of wavelength has to take into account the amplitude of the signal generated in the silicon modules and the available power of the laser sources. After crossing a module, the intensity is reduced by a factor $\approx 4 - 5$, limiting the amount of modules that can be consecutively traversed.

The requirement of a gaussian signal profile on each layer is important in order to be able to reconstruct the beam position precisely. Proving the final working principle was therefore a large step towards the realisation of the optical hardware, as discussed in chapter 5 (figure 5.4).

Experience with the successful implementation and operation of a similar system has been obtained in the AMS experiment, where the wavelength was $\lambda = 1083 \ nm$ and a reconstruction accuracy of the laser spot position of $\leq 10 \ \mu m$ has been achieved [42].
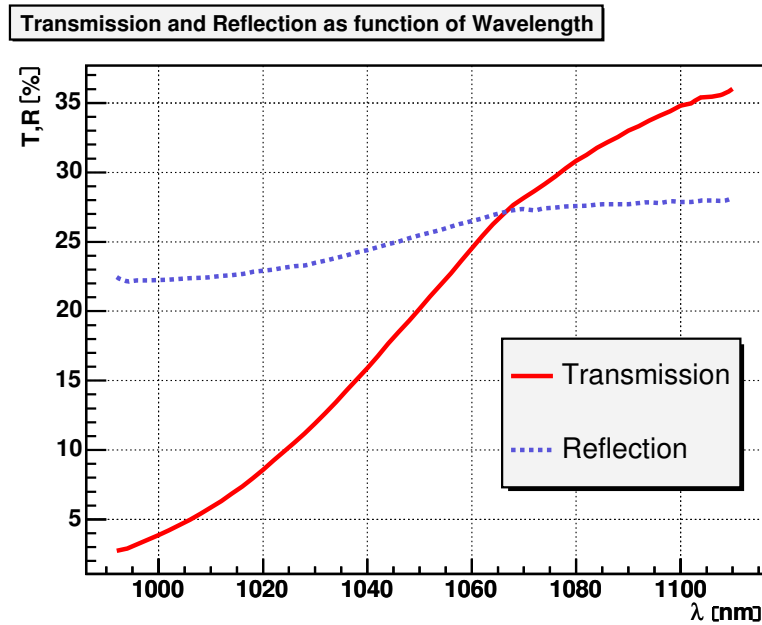
Transmission and Reflection as function of Wavelength

Abbildung 2.2.: Measured T and R values of a first sensor prototype as a function of wavelength λ.

2.3. General Layout

The LAS layout that has been incorporated into the CMS tracker, is illustrated in figure 2.3. The four rays shown correspond to the following different tasks.

- Internal TEC alignment ($8 \times$ ray 2, ray 3)
  Starting from the bulkhead at $z = \pm2800 \ mm$, the laser light is distributed by monomode fibres to optical devices, called beamsplitters (BS), where it is collimated and split into two back-to-back beams. Ray 2 is in R6 at the radius $r_{R6} = 840 \ mm$, while ray 3 is in R4 at $r_{R4} = 564 \ mm$. A detailed description of the beamsplitters will be given in chapter 3.
  The BS for rays 2 and 3 are both mounted on D6 of the TEC in an arrangement with 8-fold azimuthal symmetry and distribute the light towards disc D1 and disc D9. The rays hit the eight back petals on each TEC disc (see figure 2.11(b)). Front petals are aligned by using tracks in the region of azimuthal overlap between front and back petals.

- TEC+ to TEC- and barrel (TIB, TOB) alignment ($8 \times$ ray 4)
  As shown in figure 2.3, fibres are guided from the bulkhead along the TEC to enter the volume between TOB and TEC, where they are coupled to BS mounted on 8 alignment tubes (AT) at $r_{R4} = 564 \ mm$ on the $+z$ side. At this point half of the intensity goes to the barrel region as well as to the other endcap (TEC-) and half enters the first 5 discs of TEC+. 8 AT without BS are placed on the $-z$ side.
  The azimuthal segmentation of TIB, TOB, and the two TECs is different. Therefore it is not always possible to use the same TEC R4 alignment module for ray 4 as well as for ray 3. Depending on the AT position in $r\varphi$ (see figure 2.7) the left,

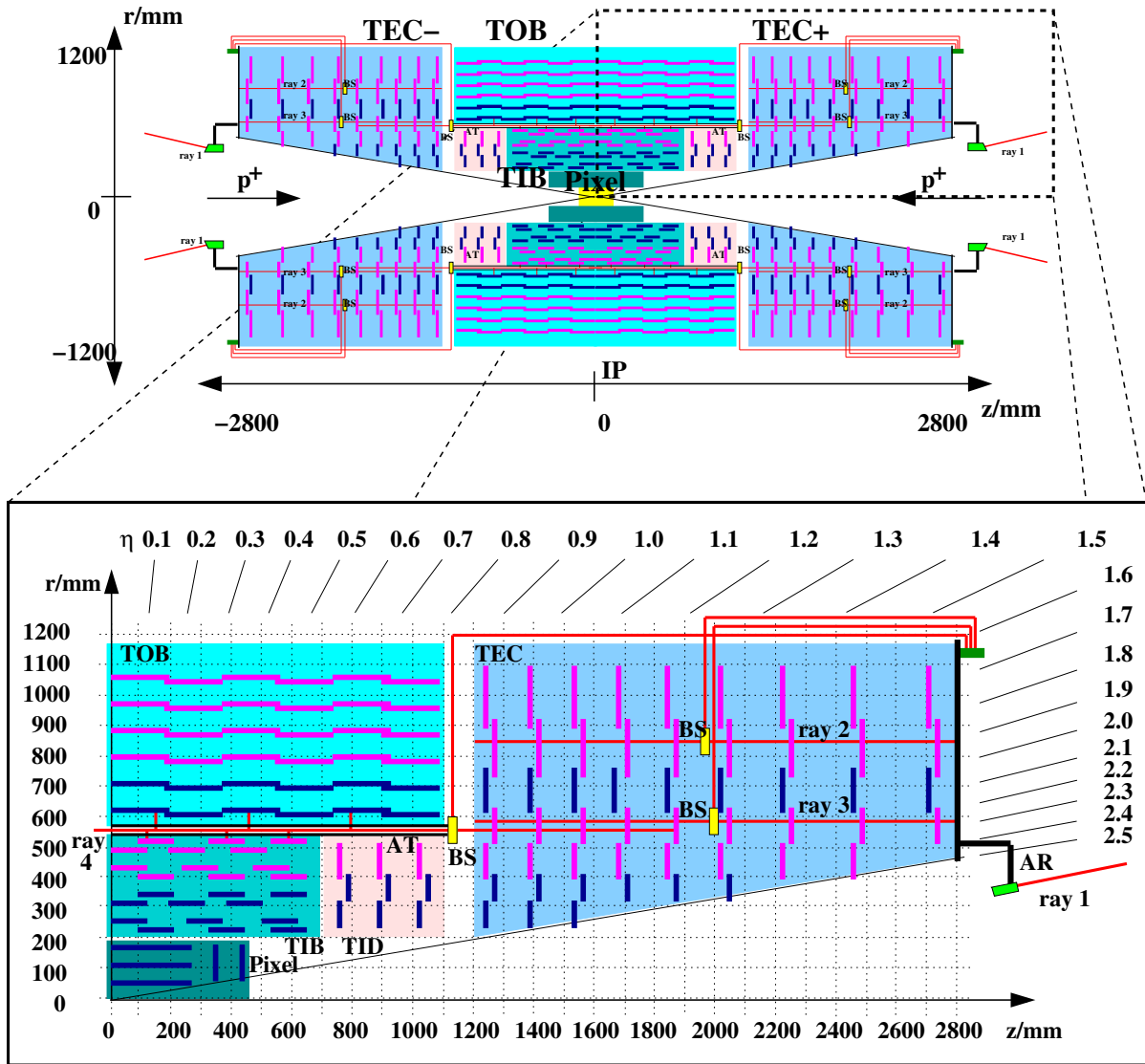## 2. Description of the CMS Tracker Laser Alignment System

Abbildung 2.3.: Zoom into one quarter of the CMS tracker inclusive the LAS components. In comparison to figure 1.13, only a few elements according to the concept have been added: beamsplitters BS and alignment tubes AT for light distribution and the alignment ring AR for the optical link to the muon system.

middle or right R4 module on the TEC back petal is hit by ray 4. For the sake of uniformity and logistic simplification, all TEC back petals are equipped with one R6 and three R4 alignment modules. To avoid interferences between ray 3 and ray 4 the corresponding laser diodes are fired sequentially.

Every AT has six mirrors, three reflecting the laser light to the TIB and three to the TOB. Since there are no radial lines of sight available in the barrel region, the optical alignment reaches only the innermost layer of TOB and the outermost layer of TIB, which are both regarded as solid bodies.

The relative orientation of both endcaps with respect to each other and to the barrel support elements is measured by ray 4.

- Optical link to the muon system (6 × ray 1)
  Since there are no direct lines of sight ($\eta_{ECAL} > \eta_{Tk}$) from the tracker to the muon system, a special interface is needed. An alignment ring (AR) is placed outside the tracker volume in the $\eta \geq 3$ region and sends 6 laser beams to the muon system, according to the 6-fold symmetry. It is rigidly coupled by pillars to the tracker support structure and can be removed during pixel installation.

Excluding the link system, there are $2 \times (2 \times 8)$ rays in the two endcaps and an additional 8 in the barrel, resulting in a total of 40 rays for the internal tracker alignment.

The LAS can be divided into subsystems of laser light generation, distribution, and detection.

2.3.1. Laser Sources
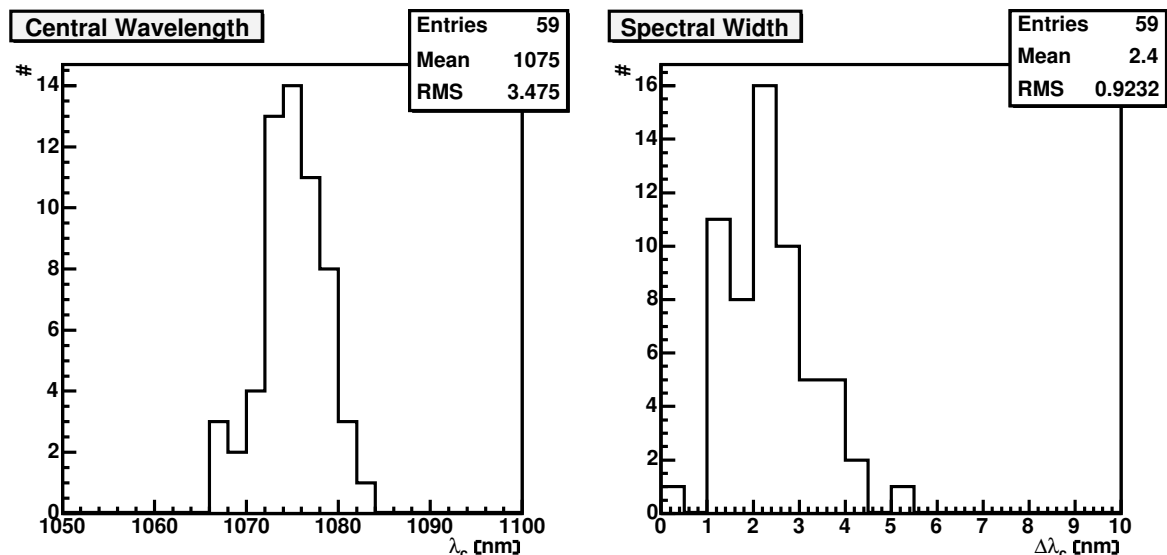
Abbildung 2.4.: Laser diodes have been chosen as light sources for the LAS.

As explained in appendix C, results of laser diode power estimation experiments have shown that the 40 laser diodes (LD), one per ray, must have an output power of at least $10 \ mW$, in agreement with earlier calculations [43].

Furthermore interference effects can be reduced by a small coherence length, which corresponds to laser sources with a spectral width $\Delta\lambda \geq 0.5 \ nm$ [44]. To be consistent with the CMS DAQ system, the laser diodes have to work in pulsed mode and should be triggered within a few ns.

Finally, including spares, 60 laser diodes with the follwing properties have been procured [45].

- Wavelength: $\overline{\lambda} = 1075 \pm 3.5 \ nm$

- Spectral Width: $\overline{\Delta\lambda} = 2.4 \pm 0.9 \ nm$

2. Description of the CMS Tracker Laser Alignment System
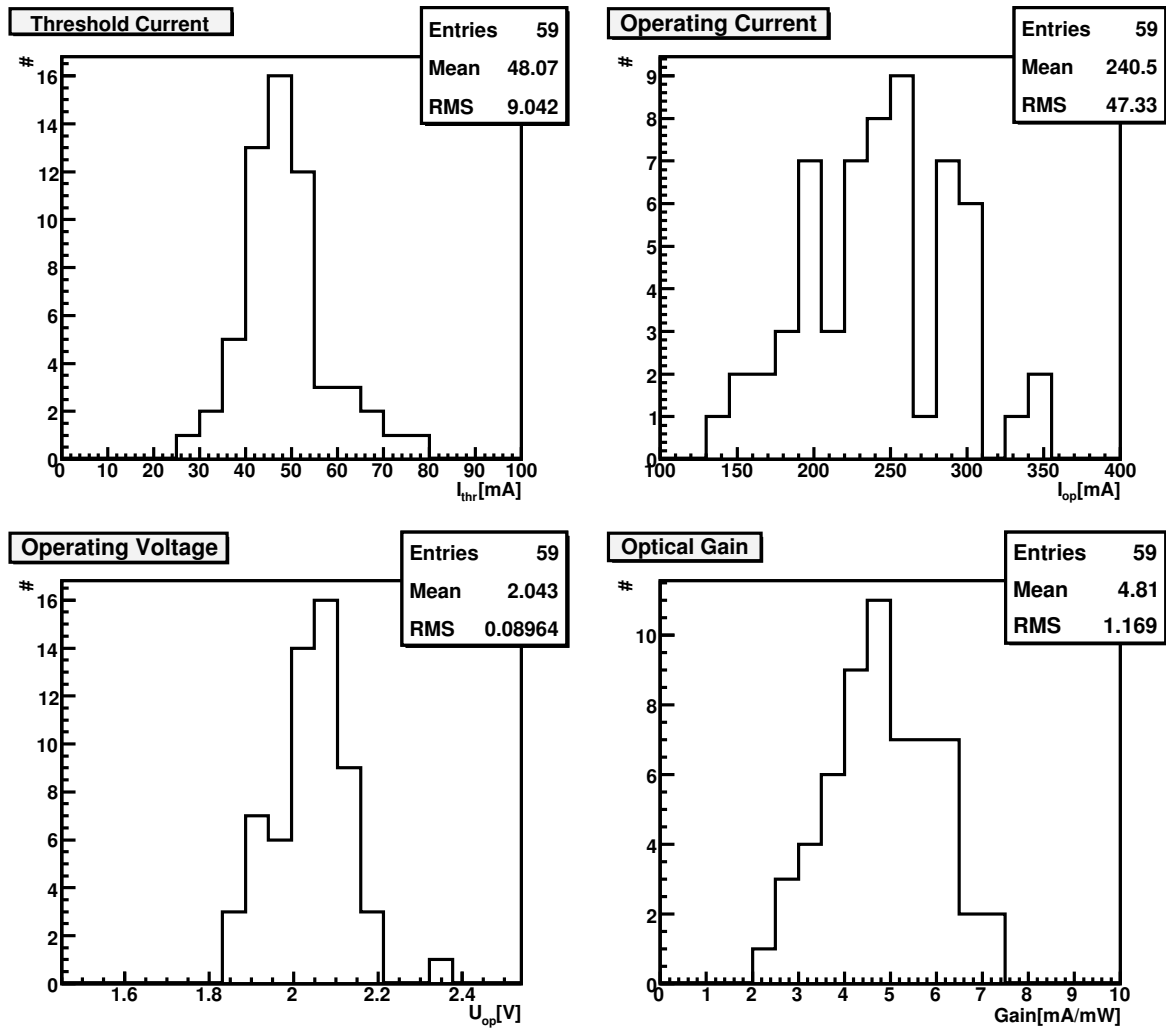

Abbildung 2.5.: Histograms of different LD properties.

- Threshold Current: $I_{thr} = 48.1 \pm 9.0\ mA$

- Operating Current at $P = 40\ mW$: $I_{op} = 240.5 \pm 47.3\ mA$

- Operating Voltage: $U_{op} = 2.04 \pm 0.09\ V$

- Optical Gain, the relation between the electrical input ($I = I_{op} - I_{thr}$) (mA) and optical power output P (mW): $4.8 \pm 1.2\ \frac{mA}{mW}$. Because the operating voltage is constant ($U_{op} \approx 2\ V$) and the relation between I and P can be linearly approximated, the LD output power is controlled by the operating current.

The laser light generation units are housed inside a control area, called USC55, which is spatially separated from the CMS experimental hall USX, as shown in appendix D.

2.3.2. Light Distribution

From each laserdiode in USC55 (see figure D.1), singlemode optical cables guide the light by internal total reflection to the TEC bulkheads, where they are coupled to shorter cables connected with the beam optics. Special non-magnetic connectors of type FC/PC, provide mechanically stable and optically efficient coupling and terminate the cables at both ends. More information is given in appendix E.

The beam splitting optics are placed inside cutouts in D6 of the TEC (see figure 2.6) as well as on the $+z$ alignment tubes. The latter are inserted in the TOB inner cylinder at $r_{R4} = 564\ mm$ and their orientation in φ is defined by a precision flange, as indicated in the figure 2.7. Details are discussed in chapter 3.
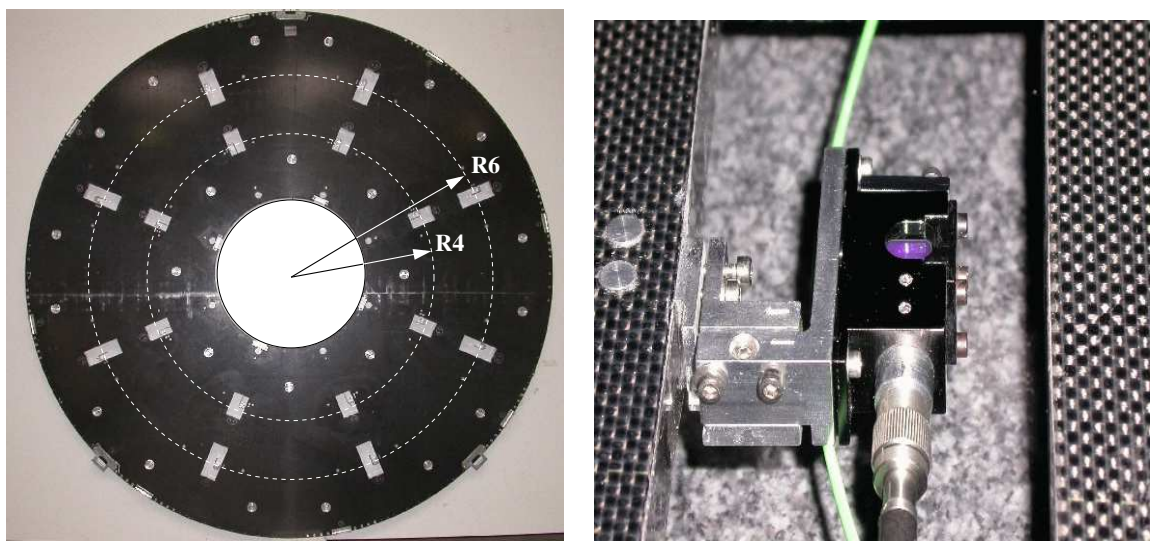
(a) TEC D6. Eight BS positions in $r_{R4} = 564\ mm$ and 8 in $r_{R6} = 840\ mm$ are indicated.

(b) BS mounted inside D6, view from D7.

Abbildung 2.6.: Beamsplitter positions and mount in the TEC.

From both endcaps of the tracker, the optical link to the muon system starts with the alignment ring. This is a rigid carbon fibre structure with diameters $d_{in} = 480\ mm$ and $d_{out} = 730\ mm$. It is rigidly connected to the TEC and two tiltmeters measure its orientation with respect to gravity (see figure 2.8).

As shown in figure 2.9, the laser beams cover a distance of $\approx 5\ m$ in radial direction. Starting from collimators at the tracker bulkhead ($z = 2.8\ m$), the beams travel along the line of sight in the $\eta = 3$ region to a link disc ($z = 6.6\ m$, $r = 0.6\ m$), where they are reflected by semi-transparent mirrors to the muon system. Additional collimators placed on the link disc serve to position it with respect to the light detectors in the muon system as well as the light sources on the AR. Since the muon chambers have an internal resolution of 100 μm precision and reproducibility in mounting the AR must be better than 20 μrad.

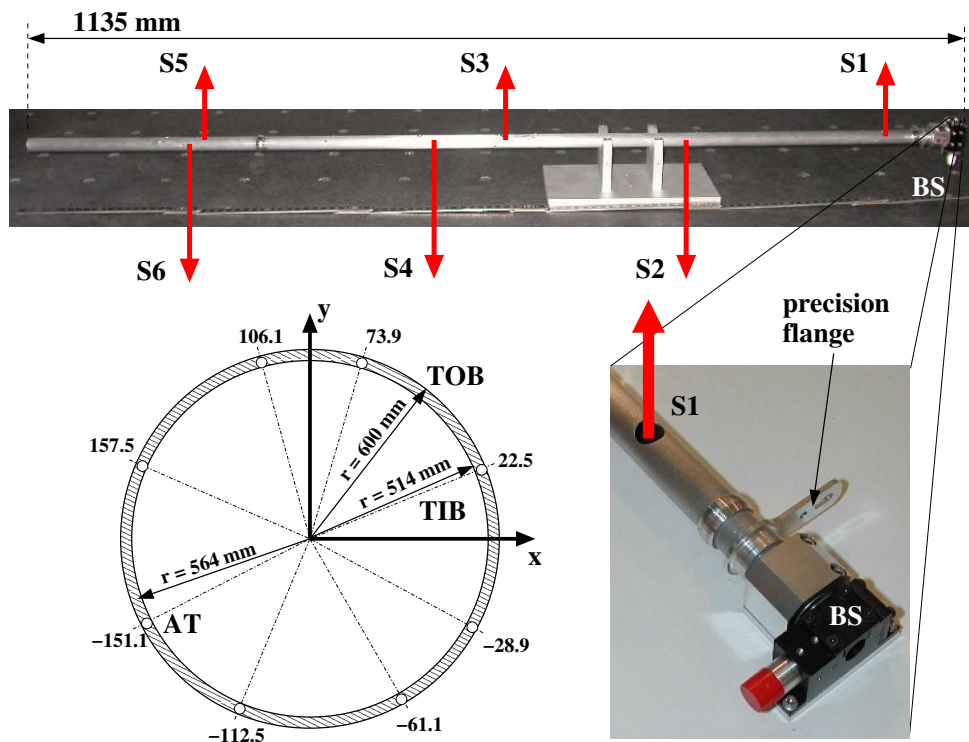## 2. Description of the CMS Tracker Laser Alignment System

Abbildung 2.7.: Alignment tube (AT) and positions of the beams to the TIB/TOB as well as the $r\varphi$ mount positions of the AT in the inner TOB envelope. The AT distributes 3 beams each to TIB and TOB by semitransparent mirrors inside. A precision flange is used for the orientation of the AT with respect to a precision pin on the TOB structure.
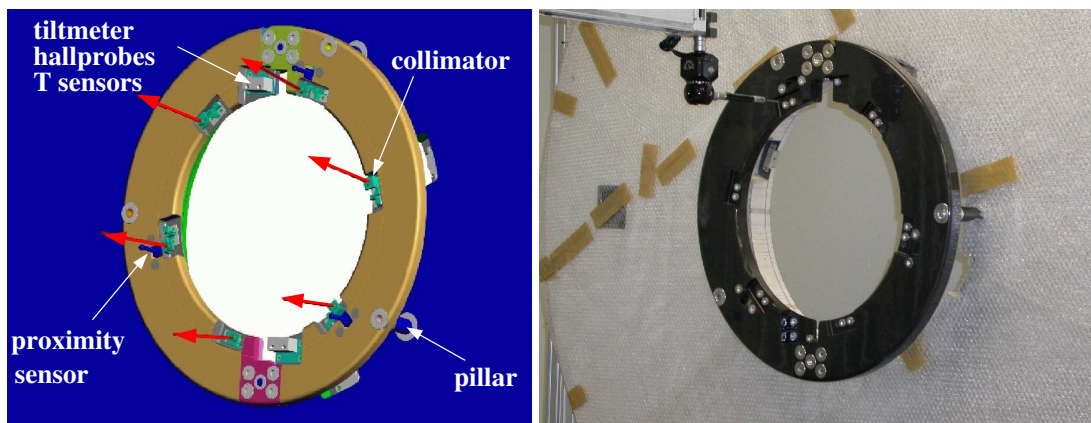

Abbildung 2.8.: Design of the alignment ring (AR). There are 6 collimators, emitting light of $\lambda = 670$ nm, two 2D tiltmeters, two 2D Hall probes, two temperature sensors, and three proximity sensors mounted on each AR.

The link system was tested during the cosmic challenge and magnet test at CERN. Laser beams from collimators placed on the AR, hit mirrors on the link disc and were detected by sensors (MS sensors) mounted on the muon system. One of the laser spot signals is shown in figure 2.10. Since it is within the dynamic range of the sensitive area of the sensors (30×30 mm^2), a relative positioning of both subsystems can be provided.

The observation of laser signals in the muon system originating from the tracker confirms the feasibility and working principle of the link system. More information about the link system is available from the CMS muon alignment group [50].
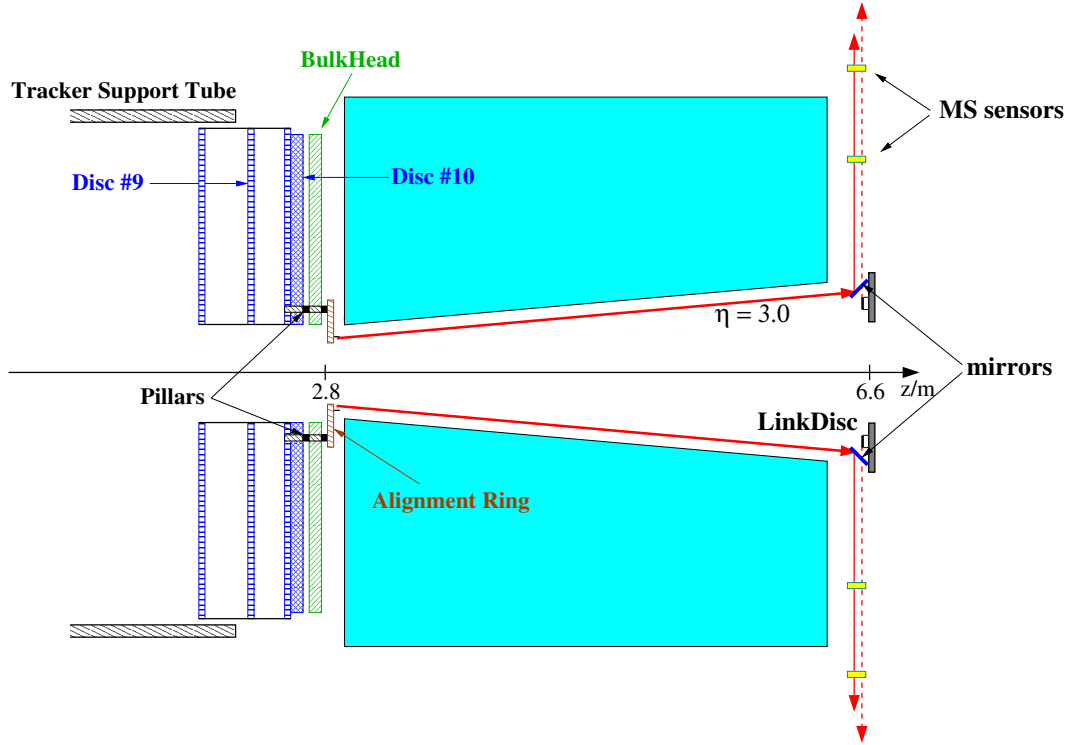

Abbildung 2.9.: The optical link between the tracker and the muon system is built using a line of sight in the $\eta = 3$ region to a special link disc [50].
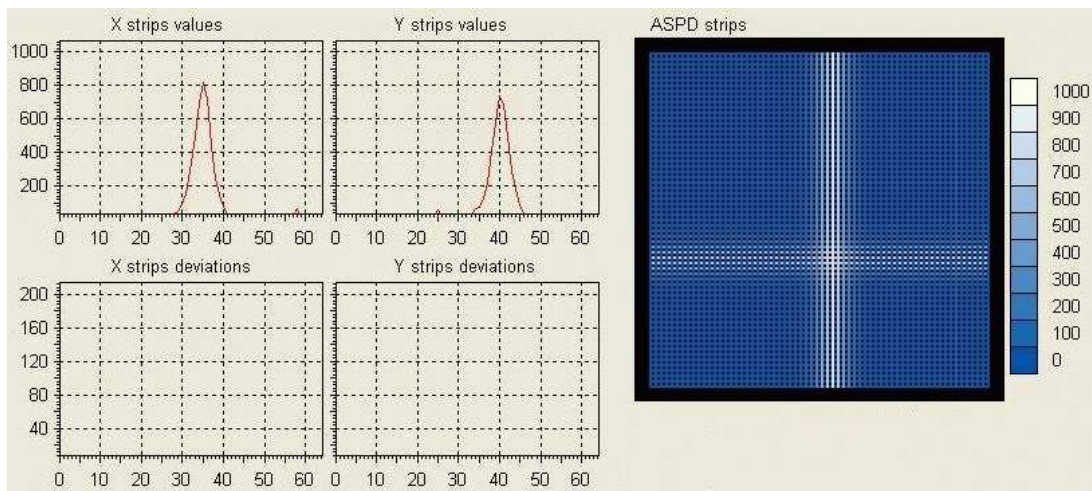

Abbildung 2.10.: Laser signal from the optical link measured by an alignment sensor of the muon system [50].

2.3.3. Signal Detection

Laser beams in the TEC will travel through every back petal (BP) at the R4 and R6 positions indicated in figure 2.11(b). Holes of 10 mm diameter in the corresponding petal and disc positions provide a line of sight for the laser beams. The laser beam spots are measured by the silicon modules.
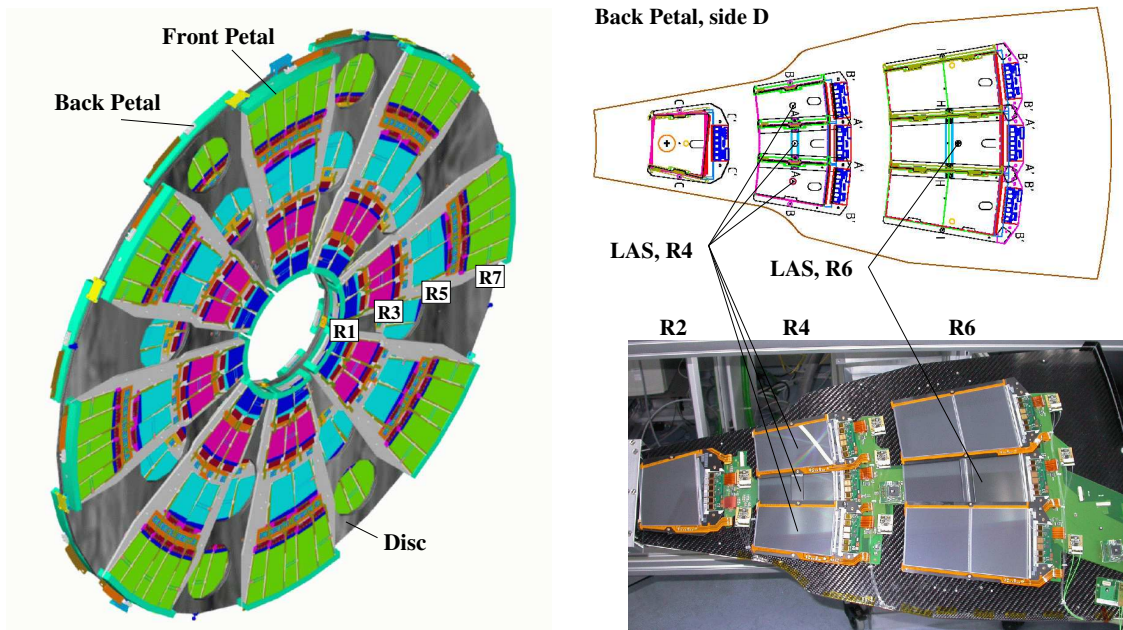
(a) TEC disc with front (FP) and back (BP) petals. Silicon modules belonging to R1, R3, R5 and R7 are mounted on the front side of all FP and BP, while those forming R2, R4 and R6 are mounted on the petal back side.

(b) Back side of a BP. The Laser Alignment spots are measured by silicon modules on all BP at the indicated positions.

Abbildung 2.11.: TEC discs and petals are made out of carbon fibre, having holes for the laser beams in R4 and R6. Petals and modules have been arranged to provide complete coverage in $r\varphi$.

For LAS purposes the module manufacturing process has been changed with a mask covering the circular laser sector for all alignment sensors to keep this zone aluminium free while sputtering the backplane, see figure 2.12.

It has been checked that the effect on the electric field distribution is negligible and that the sensors have the same operation properties as those with a complete aluminium backplane. To avoid distortions of the laser beam profile while crossing a silicon sensor, both sides have been mirror polished by the vendor.

The R4 as well as the R6 alignment modules have 512 strips. The analogue read out is performed by APV chips (APV 0, 1, 4, 5), placed on hybrids[1] glued on the carbon fibre frames.

[1]To have one hybrid design, APV 2 and APV 3 are put on the hybrids only for sensors with 768 strips.
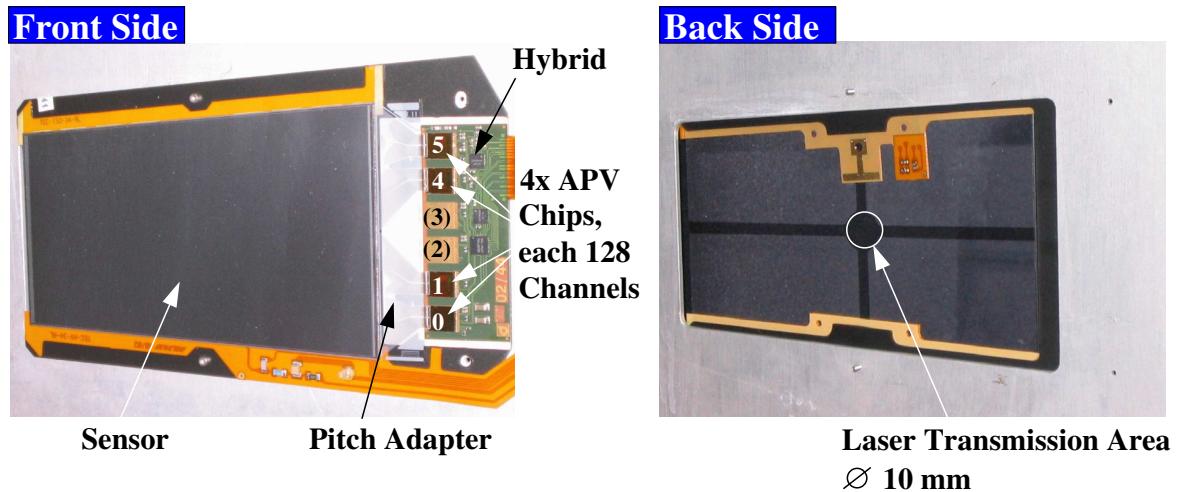
Abbildung 2.12.: CMS TEC R4 alignment module. The 4 APV readout chips, as well as the modification on the backside for laser light transmission, are indicated.

The laser zone involves the border channels of APV 1 and APV 4 and therefore this region will be particularly discussed later. In the standard layout, there are 480 TEC R4 and 160 TEC R6 alignment modules needed.

2.4. Performance

Detailed Monte Carlo simulation studies on the LAS performance have been done in [53], [44] and [54]. The simulations start with the definition of

- the alignment objects

- the geometrical parameters, to be reconstructed by the LAS

The overall alignment scheme consits of the following sequence of steps.

1. Ray 2 and ray 3 are used to align optically the nine discs in each TEC with respect to each other with 100 μm accuracy. Since they are parallel to the z-axis, rotations around this axis (R_z), as well as displacements in x (Δ_x) and y (Δ_y) are the parameters, which can be reconstructed by the LAS.

2. Reconstructed tracks are then used to determine the relative module positions in each TEC with 10 μm precision.

3. Ray 4 is used to reconstruct the relative positions of the objects TEC+, TEC-, the four TOB wheels and the four TIB flanges with 100 μm accuracy. Starting from TEC+ as a reference system and regarding it as one solid body, rotations R_x and R_y of TEC- are added to the list of geometrical parameters, in addition to Δ_x, Δ_y and R_z for the barrel.

4. Track data in the barrel as well as in the barrel/endcap transition zone are used to do the final relative alignment of barrel to endcap modules at the 10 μm level.

5. The tracker is then known at the ≈ 10 μm scale and monitored by the LAS with the same precision. The optical link to the muon chambers is used to align the tracker and muon system coordinate frames.

2.4.1. Reconstruction Model

The model describing the reconstruction of the geometry performed by the LAS is based on χ^2-minimization. Here it is explained in detail using the internal alignment of a TEC as an example [53].

In the endcap the alignment objects are 9 discs and there are 2×8 axial laser beams. In principle there are 3 displacements $(\Delta_x, \Delta_y, \Delta_z)$ and 3 rotations (R_x, R_y, R_z), but since laser beams are parallel to the z-axis, the LAS is only sensitive to $(\Delta_x, \Delta_y, R_z)$.

Due to the fact that the laser position itself is unknown, two parameters have to be added for each beam: $(\Delta_{r\cdot\varphi}, \Delta\Theta_{C,D6})$. There are the azimuthal displacement $\Delta_{r\cdot\varphi}$ of the laser beam and its tilt $\Delta\Theta_{C,D6}$ with respect to D6, equivalent to the orientation of the beamsplitter mounting inside D6[2].

A straight line, representing the laser beam, is fixed in the middle at one point P of a disc with known point precision $\Delta_{r\cdot\varphi}$ and orientation $\Delta\Theta_C$ with respect to this disc. Since the coordinates of this line are measured by one-dimensional radial strips only changes perpendicular (index: C, cross) to the strips can be determined. In principle the straight line consists of two rays originating at P and the error in considering them as a single line is given by the two collinearity angles θ_C, θ_P defined in the BS coordinate system, where, as explained above, only θ_C is measurable.

Using a coordinate system in which D1 and D9 are fixed, the assumption of a placement accuracy of $\sigma_{p,r\cdot\varphi} = 50$ μm for modules on the disc and a laser spot resolution of $\sigma_{res} = 10$ μm leads to a total measurement error given by $\sigma_{exp} = \sigma_{p,r\cdot\phi} \oplus \sigma_{res} \approx 50$ μm.

On each of the nine discs the $r \cdot \varphi$ coordinate of the 2×8 laser spots is measured by the alignment modules and results in a total of $m = 2 \times 8 \times 9 = 144$ measurements. The number of reconstructed parameters is $n = 3 \times 7 + 2 \times 16 = 53$, with $(\Delta_x, \Delta_y, R_z)$ for D2 to D8 and $(\Delta_{r\cdot\varphi}, \Delta\Theta_{C,D6})$ for ray 2 and ray 3. Since $m > n$ it follows that the endcap alignment system is highly redundant [53].

In the model the χ^2 function is defined in the usual way:

$$\chi^2 (p_1, \ldots, p_n) = \sum_{i=1}^{m} \left(\frac{R^i_{exp} - R^i_{th}}{\sigma^i_{exp}} \right)^2 \tag{2.2}$$

with

- R_{exp} is the set of measurements, e.g. module readings for beam R4 in D3.

- $R_{th} = f(p_1^v, \ldots, p_n^v)$, where $(p_1^v, \ldots, p_n^v)$ is the set of theoretical parameters. R_{th} are the values predicted by the reconstruction model for the position of the laser

---

[2]compare figure 2.6(b)

beam spot, e.g. beam R6 in D4. Starting from a set of initial values, for example $(p_1^0 \ldots p_n^0) \equiv (0 \ldots 0)$, the parameters are varied v times, until the changes in χ^2 are insignificant.

- σ_{exp} is the measurement accuracy, e.g. the collinearity of a BS.

Using a linear approximation for the rotation matrices (e.g. $\sin x \approx x$) the model leads finally to a set of parameters $R_{th}^{min} = (p_1, \ldots, p_n)$, for which the χ^2 function in the n-dimensional space is minimal. A simple example of the method is given in appendix F.

In a first version of this model [53], a misalignment scenario of displacements by $\pm 1 \ mm$ and rotations of $\pm 3 \ mrad$, has been simulated.

For each misalignment Monte-Carlo scenario straight tracks from the interaction point were distributed uniformly in the TEC and their hits in the silicon sensors were computed and fitted to a straight line for each track. The residuals before and after alignment corrections are shown in figure 2.13.

Comparing the width of the two distributions shows the improvement given by use of the LAS. Residuals are reduced from $1 \ mm$ to $30 \ \mu m$, confirming the working principle of the applied geometrical reconstruction model. The precision of the reconstructed geometry is comfortly better than $100 \ \mu m$.

A more complex model ([54]) takes into account detailed properties of the optical devices (e.g. BS, fibres), known from laboratory experience, as well as the characteristics of silicon modules, readout components etc., and has been implemented into the CMS software framework [29].

For the optical alignment of the barrel and the two endcaps with respect to each other, the experimental error for the geometry reconstruction depends in addition on the placement accuracy of the silicon modules on the uncertainty in the orientation of the alignment tubes ($\sigma_{\varphi_{AT}}$), which is mechanically defined by a precision flange.

The error contribution to the geometry reconstruction of both endcaps and the barrel relies besides the modules placement accuracy mainly on the alignment tube orientation $\sigma_{\varphi_{AT}}$ and is mechanically defined by a precision flange.

Two important consequences for the optical hardware follow from Monte-Carlo simulations of the LAS performance:

- Beamsplitter:
  The collinearity angle θ_C has to be known with a $50 \ \mu rad$ precision. The BS sits in the center of the TEC. With the TEC length of $l \approx 2 \ m$ and the measurement accuracy $\sigma_{exp} = 50 \ \mu m$ this leads to a precision for the beam collinearity of $\sigma_{\theta_C} = \frac{\sigma_{exp}}{1m} = 50 \ \mu rad$.

- Alignment tube:
  The error on the φ_{AT} orientation has to be less than $\sigma_{\varphi} = 1.5 \ mrad$, a less stringent requirement than that for the BS. For a distance of $\approx 50 \ mm$ to the TIB and TOB modules, this gives $1.5 \ mrad \cdot 50 \ mm < 100 \ \mu m$ and fulfills the resolution requirement of $100 \ \mu m$.

Entries	70000
Mean	0.02081
RMS	1.175
χ^2 / ndf	693.9 / -3
Constant	477.3 ± 3.0
Mean	0.03502 ± 0.00633
Sigma	1.155 ± 0.004

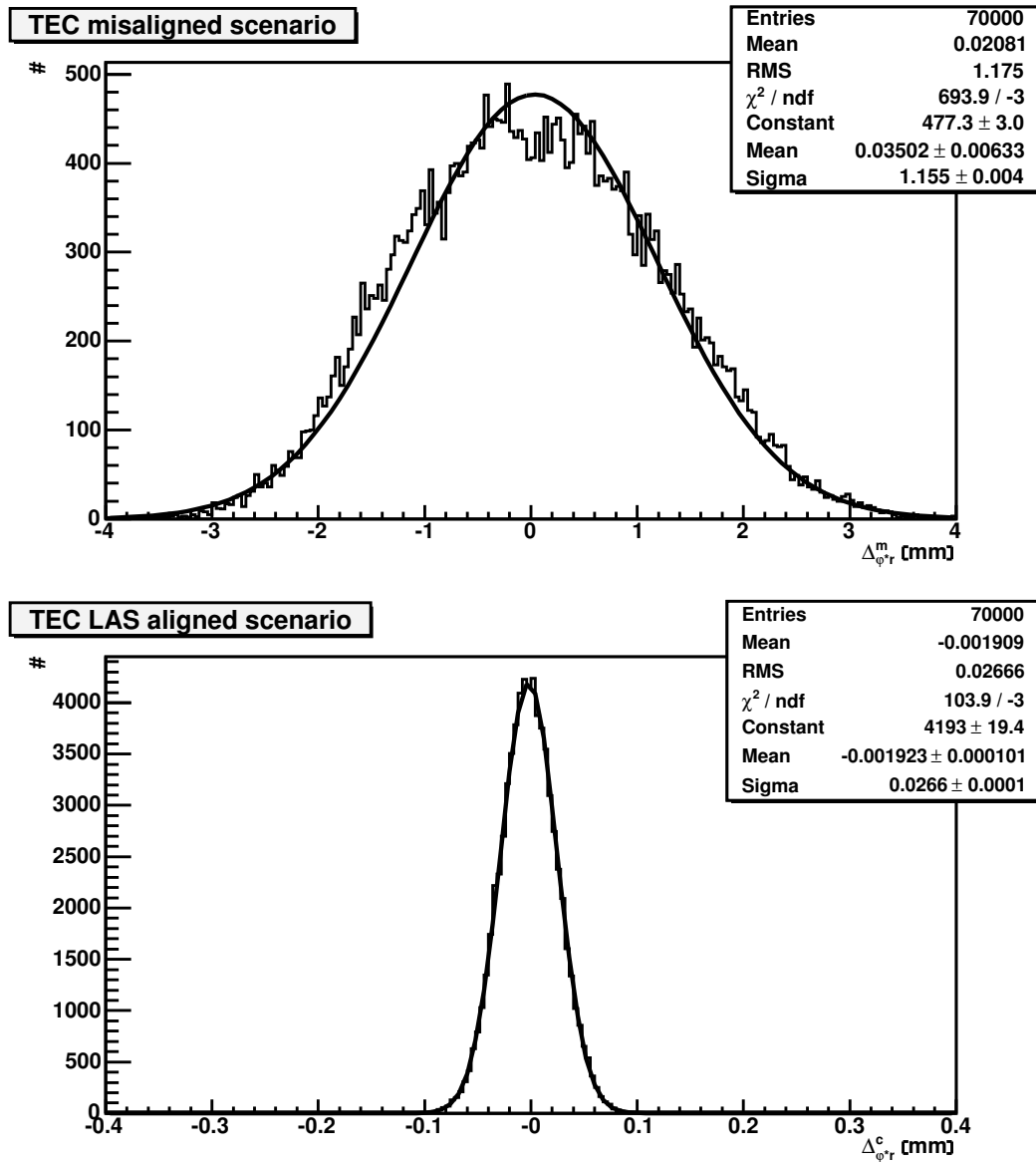| Entries	70000
Mean	-0.001909
RMS	0.02666
χ^2 / ndf	103.9 / -3
Constant	4193 ± 19.4
Mean	-0.001923 ± 0.000101
Sigma	0.0266 ± 0.0001

Abbildung 2.13.: Simulation of TEC LAS performance. In the upper diagram the track residuals $\Delta_{r\varphi}^{m}$ are shown without alignment corrections by using ray 2 and ray 3. The lower diagram illustrates the improvement after optical alignment, $\Delta_{r\varphi}^{c}$, from $\sigma_{NoLAS} = 1.2\ mm$ to $\sigma_{LAS} = 0.03\ mm$.

2.4.2. CMS DAQ Integration

LAS Electronics

Laser light pulses are generated by the laser diodes, distributed by monomode fibres to optical devices inside the CMS tracker and detected by silicon strip modules. Therefore the time at which the lasers are fired has to be properly defined and it must be ensured that the laser signals are read out and processed by the tracker electronics[3].

---

[3]A compact overview of the readout and control architecture is given in [55].
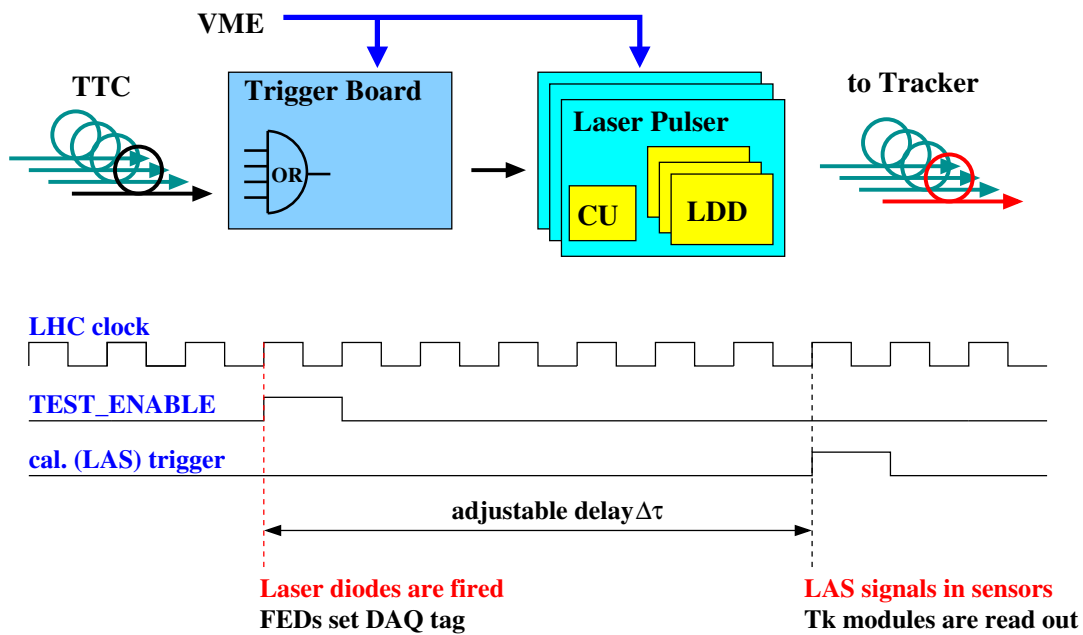
Abbildung 2.14.: Block diagram of the LAS electronics and trigger scheme. The firing of the laser diodes is synchroneous to the LHC clock and their signal is read out by the tracker modules after an adjustable delay $\Delta\tau$.

As shown in the figure 2.14, this leads to two interfaces of the LAS with the CMS Trigger and Data Acquisition (DAQ) Systems (TriDAS), [39]:

1. Trigger Scheme
   The timing, trigger and control (TTC) information is distributed by the global LHC TTC system [56] with calibration signals issued on channel B, the TTC B line.
   Upon reception of a global calibration pattern (0010), TTC TEST_ENABLE, which is synchronous to the LHC clock of 40 MHz, all 40 laser diodes are fired.

2. Signal Readout
   The electrical signals from the APV readout chips are converted and transmitted along analogue optical fibres to a Front-End Driver (FED) [57], where they are digitized and processed further according to the trigger decision.
   The FED recognizes the same TTC B (0010) signal and writes it into the DAQ header to declare the next event as LAS event. This event is readout upon reception of the subsequent, LHC clock synchronous, calibration trigger, following the TEST_ENABLE command. Several adjustable delay stages $\Delta\tau$ in the LAS electronics allow a precise timing of the laser pulses arriving at the silicon modules.
   The DAQ filter unit recognizes the header tag given by the FED and routes the LAS event to the calibration data as well as to the online laser alignment processing.

Block diagram 2.14 shows the modular design of the laser system control, which consists of two main devices:

- Trigger Board (TB)
  The TB is a 9U VME card with 4 optical inputs and 2 TTL outputs. The TTC B

commands on the inputs are decoded by 4 TTCrq cards connected in a logical OR, each for one of the 4 tracker partitions (TEC+, TEC-, TIB, TOB).
Upon reception of TEST_ENABLE two trigger pulses are generated at the first TB output: a non-delayed TTL trigger pulse and a subsequent one, after a programmable delay.

- Laser Pulser (LP)
There are 8 laser diode devices (marked as LDD in figure 2.14) on the laser pulser VME board. On each of them the parameters delay, duration and intensity of the laser diode are controlled by a separate programmable unit (CU), which also monitors temperature and provides a laser interlock. The CU has a memory sufficient up to 100 triggers. Laser intensity variations for successive triggers can thus be monitored and the signal can be adjusted to assure that it reaches the appropiate module layers.

Run Scenarios

The FED runs either in raw data or in zero suppression mode. Further processing like subtraction of pedestal and common-mode noise as well as cluster finding is applied in the zero suppression mode, which is the default mode during physics runs [58].
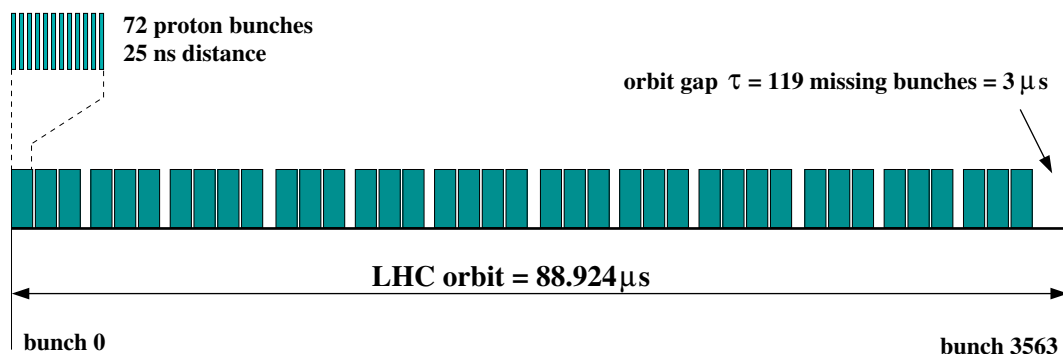
Abbildung 2.15.: LHC beam structure [26].

The LAS requires raw data for laser spot reconstruction and it is possible to program the FED into this mode for special dedicated alignment and calibration runs before and after physics running.

To monitor the tracker during physics data taking, it is possible to take LAS events in the orbit gap $\tau \approx 3\ \mu s$, marked in the LHC beam structure scheme (figure 2.15). If in every hundred beam cycles a calibration trigger is received, this would lead to a 100 Hz trigger rate, given by the LHC orbit time of 89 $\mu s \approx 0.1\ ms$. Collection of 100 LAS triggers would then result in a complete picture of the tracker in 1 s. If such events, taken during physics running, are needed, further investigations of how to handle the LAS data in the zero suppression format have to be carried out.

3. Beamsplitters

Beamsplitting optics are incorporated inside the TEC D6 to divide the incoming laser beams. There are two main reasons why such an optic device is needed.

1. LD power
   As it has been shown by estimates of the power of the laser diodes (appendix C), the integration of a BS in the TEC center (D6) decreases the required power by three orders of magnitude ($W \rightarrow mW$). Near infrared LD in the mW range are available and enough signal can be generated in each TEC by accumulating statistics even without tuning the intensity on individual discs.

2. Resolution
   Each additional traversed TEC disc means also a convolution of an additional diffraction pattern. By use of BS in D6, the influence on resolution is reduced by a factor of two, as will be discussed in chapter 5.

3.1. Layout and Functionality

Research on the design of the BS was carried out and several models were tested in cooperation with Optics Laboratories [60]. Beam splitting based on deflection, as in figure G.1 (appendix G), had the advantage to be able to control and adjust the relative position of both outgoing beams by wedge prisms. Intensity sharing was also easy without relying on special light properties. However, it was impossible to implement this design within the geometrical limit, defined by the disc thickness of 16 mm.

The challenge of providing beam collimation and separation perpendicular to the plane defined by D6 has been met by using the polarization principle.

As illustrated in figure 3.1(b), the incoming beam, consisting of both s and p polarizations, is collimated onto a 45° inclined surface, on which the s-polarized part of the laser light is completely reflected. The p fraction continues, traverses a $\frac{\lambda}{4}$-plate and is reflected by a mirror. After a second traversal of the $\frac{\lambda}{4}$-plate, the light is s-polarized and is completely reflected on the other side of the 45° inclined surface. The result are two parallel back-to-back beams with s polarization.

3.1.1. Properties

The BS has an overall size of $46 \times 16 \times 24$ mm and a weight of 29.67 g. The mechanical support structure is made of aluminium and the optical components consist of fused silica.

3. Beamsplitters
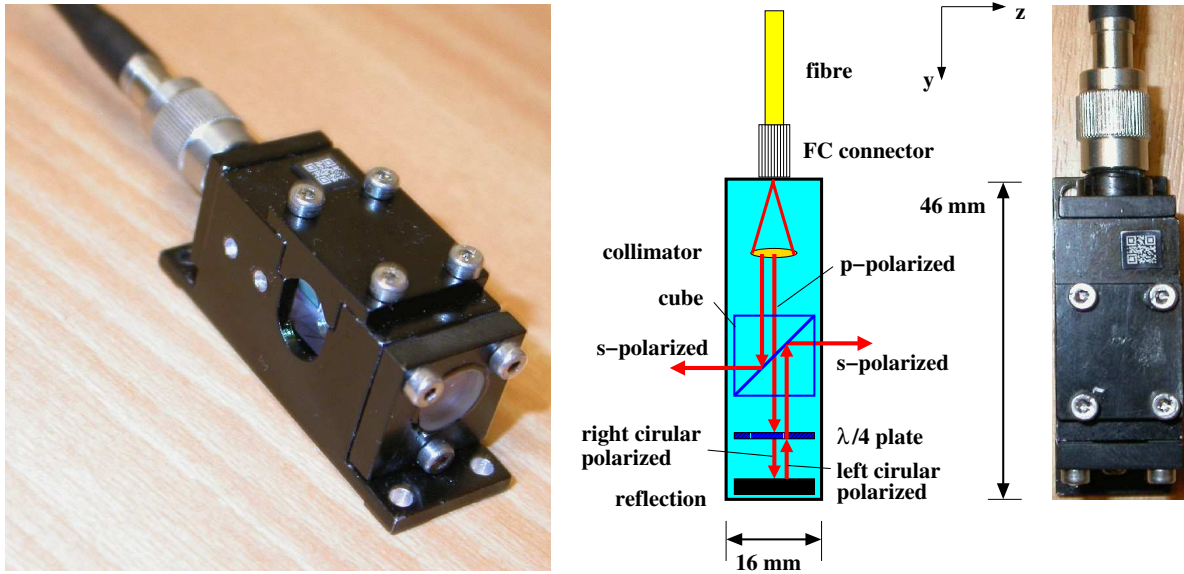
(a) Picture of final BS type   (b) Illustration of the BS working principle

Abbildung 3.1.: Size and explanation of the beam splitting device.

With respect to the plane of incidence, there are perpendicular s (TE) and parallel p (TM) electrical field components and the wave propagation is different according to equations (H.34) and (H.35) (appendix H).

This has been used in the polarization cube embedded in the BS, whose diagonal surface has a coating consisting of 31 layers. In the wavelength range of the used laser diodes, $\lambda = 1075 \pm 3.5 \ nm$, this special coating is transparent for p and reflects the s polarized light.

All components of the BS (shown in figure 3.1) can be operated in a temperature environment from -35^oC to 70^oC and are individually discussed in the following.

1. Collimator
   The fibre is coupled to the BS via a connector of type FC/PC providing a very rigid connection. The connector ferrule is in the focal plane of the lense, which results in a collimated ray. Properties of the collimator lens are given below.

   - Paraxial focal length: $10 \ mm$
   - Diameter: $5.0 \ mm$
   - Centering with respect to the optical axis: $< 1'$
   - Central thickness: $1.6 \pm 0.2 \ mm$
   - Surface regularity: $\leq \frac{\lambda}{4}$ @ $633 \ nm$
   - Coating: both sides of the lense have an anti-reflex-coating for $\lambda = 1064 \ nm$, $R < 0.25 \ \%$, as shown in diagram 3.2 (details in appendix G).
   - Material: fine annealed bubble selected fused silica

BS, ARC on collimator lens, polarization cube and λ/4 plate
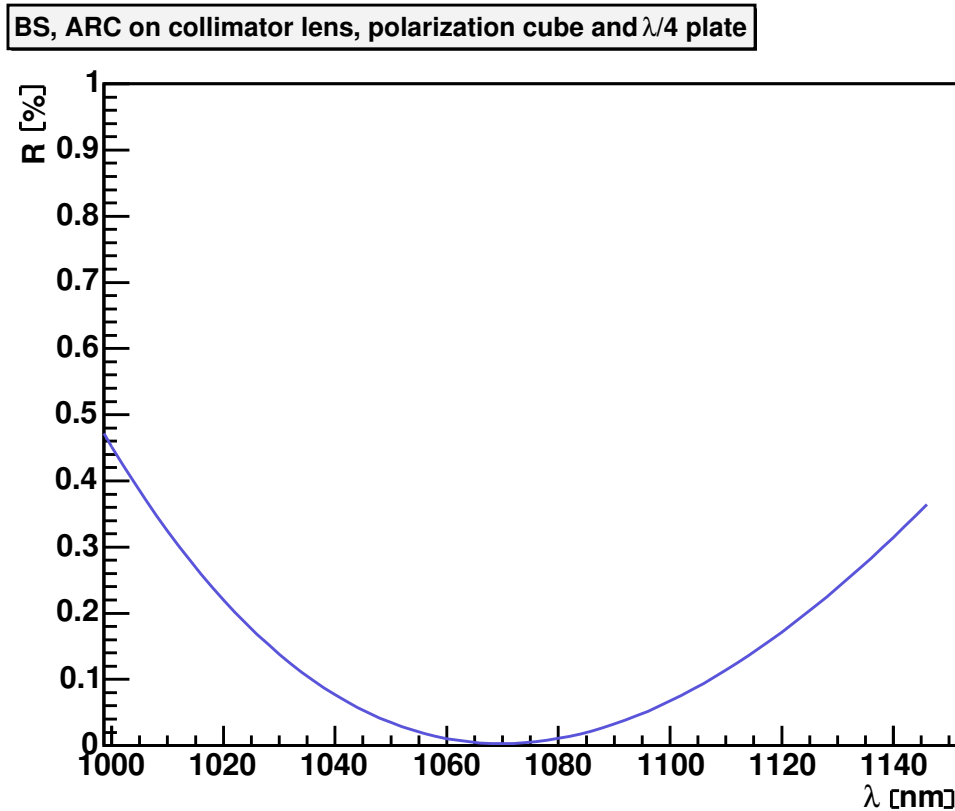
Abbildung 3.2.: Reflection as function of wavelength. The surface anti-reflex-coating of all BS components was optimized for infrared applications.

2. Beamsplitter Cube

- Size: $10 \times 10\ mm$
- Beam deviation: $< 1'$
- Surface flatness: $\frac{\lambda}{10}$ @ $633\ nm$
- Material: fine annealed bubble selected fused silica
- Cement joining the two BS cube prisms: NOA 61 (Norland), UV curing cement

On top of each outer cube surface the same anti-reflex-coating as for the collimator lens has been applied to optimize the transition zone from air to fused silica.

To gain a good separation between the s- and p- polarized light components, a special coating of 31 layers alternating between high (Ta_2O_5, $n = 2.05$) and low (SiO_2, $n = 1.46$) refractive index materials has been developed and put on the diagonal contact surface of two prisms. Details about the optical thickness of each layer is given in appendix G.

The effect of the coating was calculated by using the matrix formalism of appendix H and the result can be seen in figure 3.3. It is obvious, that optimal separation has been achieved in the near infrared from $\lambda = 1050\ nm$ to $\lambda = 1100\ nm$, the working wavelength range of the LAS. With this coating only the component of p

polarization is transmitted while the s component is completely reflected to -z. This is valid for both directions $\pm y$ (figure 3.1(b)), because the coating is symmetric. Therefore, the component reflected back from the mirror, being s-polarized by two traversals of the $\frac{\lambda}{4}$-plate, also gets reflected at the cube, but now in the opposite direction +z.
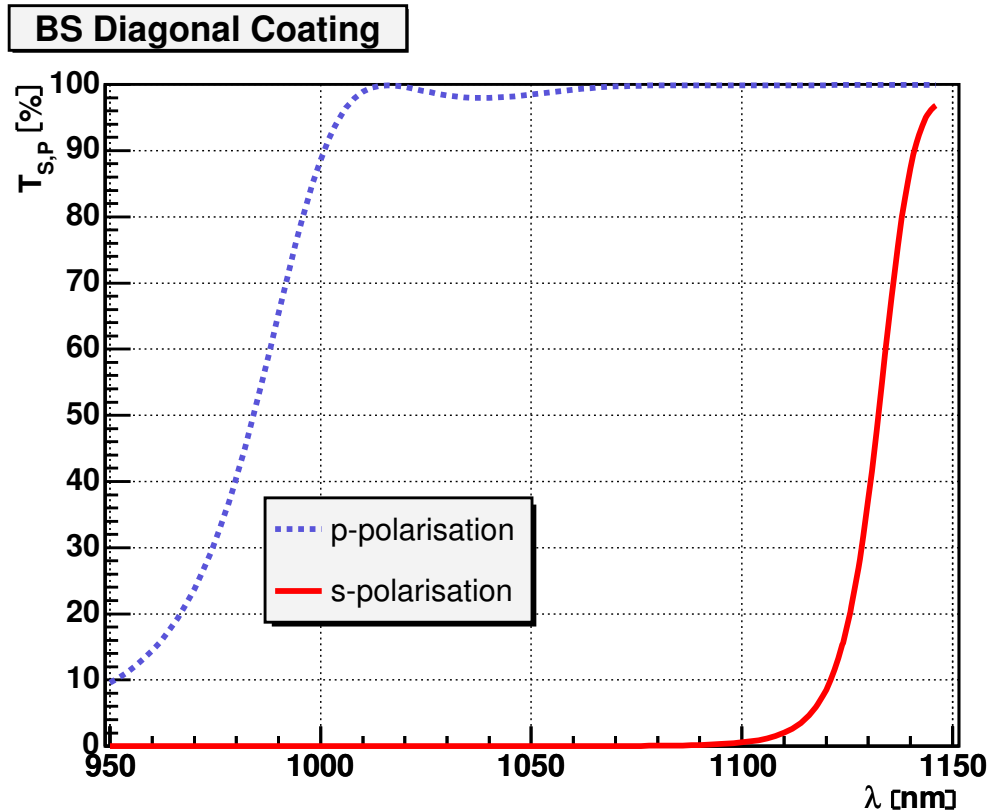

Abbildung 3.3.: Transmission of the special beamsplitter coating for s- and p-polarized light as a function of wavelength. A separation of both polarizations is achieved in the desired infrared region [60]. Details about the coating are given in appendix G.

3. $\frac{\lambda}{4}$ retardation plate

- Diameter: 10 mm
- Optimal wavelength: $\lambda = 1064\ nm$
- Parallelism: 0.5″
- Material: crystal quartz
- Coating: on both sides same as for the lens and cube surfaces (figure 3.2)

In the correct 45° orientation with respect to the beam splitting cube, the p linear polarization is converted into right circular polarization.

In the opposite direction, the light reflected from the mirror is left circularly polarized because of a phase shift of π and becomes s linearly polarized after the second pass through the $\frac{\lambda}{4}$ retardation plate.

4. High Reflection Mirror

- Diameter: $8.0 \ mm$
- Surface flatness: $\frac{\lambda}{10}$ @ $633 \ nm$
- Material: fine annealed bubble selected fused silica

A stack of 29 layers alternating between high (Ta_2O_5, $n = 2.05$) and low (SiO_2, $n = 1.46$) refractive index materials, all of the same optical thickness $\frac{\lambda}{4 \ n}$, has been put on top of a fused silica plate to generate a highly reflective mirror over a wide wavelength range. The reflection coefficient as a function of λ is shown in figure 3.4 (see also appendix G).

The mirror converts right circular into left circular polarized light.
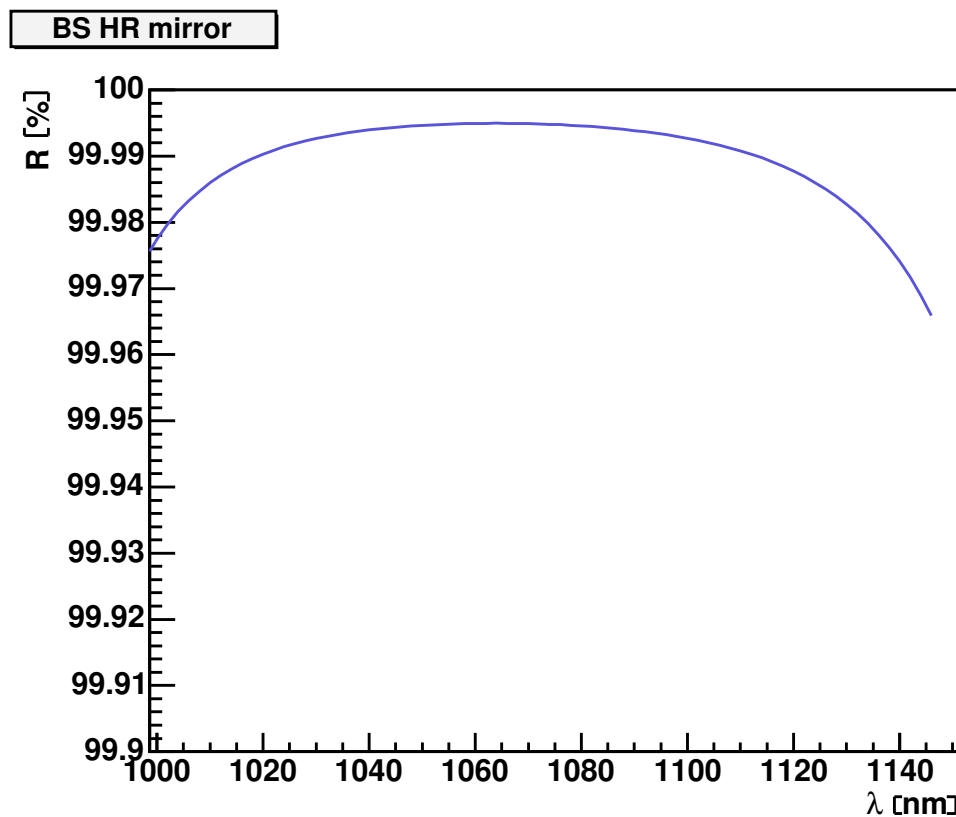
Abbildung 3.4.: A stack of high and low refractive index materials on the mirror surface results in light reflection without intensity losses.

3.1.2.   Irradiation Tests

One of the important requirements for the optical devices is their radiation hardness in the tracker environment.

In earlier studies testing different glass substrates, several components have been irradiated to the γ-ray dose and neutron fluence expected for 10 years of CMS operation [61].

3. Beamsplitters

As in these tests, beamsplitters, optical fibres, connectors, as well as separate $\frac{\lambda}{2}$-plates have been positioned in an irradiation device and exposed to a Co^{60} γ-ray source. The distance was $44-56\ mm$ and the dose between $80000-130000\ Gy$. The irradiation time was $2807\ min \approx 46\ h$ at room temperature [62].

In addition all devices have been exposed to a neutron radiation source, with the following parameters:

- Thermal neutrons
  $\bar{E} = 0.025\ eV$, flux: $2.5 \cdot 10^{11} \frac{n}{cm^2 s}$

- Fast neutrons
  $\bar{E} = 1.0\ MeV$, flux: $5.0 \cdot 10^{10} \frac{n}{cm^2 s}$

For the 30 min. irradiation time this corresponds to $4.5 \cdot 10^{14} \frac{n}{cm^2}$ ($9.0 \cdot 10^{13} \frac{n}{cm^2}$) of thermal (fast) neutrons.

The BS properties have been measured before and after these tests and show neither color changes of the optical components nor changes in their polarising and attenuation characteristics.

The color of the connector ferrules changed to dark brown, but no losses in transmission and no performance decrease of the irradiated fibres has been observed after all tests. In conclusion the beamsplitters, fibres, connectors, and retardation plates have been qualified for operation in the CMS tracker environment.

3.2. Collinearity Measurements

In the LAS the TEC laser beams are assumed to be straight lines from D1 to D9. Since beamsplitters are located at D6 and distribute rays in two opposite directions, a kink is introduced. Two angles, θ_C (xz plane) and θ_P (yz plane), are defined between these beams in the local BS coordinate system, as illustrated in figure 3.5.

The angular orientation of the BS in R4 and R6 with respect to the module strips is always the same and is described by the angles θ_P and θ_C.

As discussed before, θ_P involves displacements parallel to the strips and cannot be measured by the silicon sensors, whereas θ_C involves displacements perpendicular (cross) to the strips. Providing a line of sight inside the TEC from D1 to D9 determines the allowed θ_C range to be less than 3 $mrad$. From simulations (chapter 2) it follows that θ_C has to be known with an accuracy of $\Delta\theta_C = 50\ \mu rad$ to reconstruct the TEC structure in the order of $100\ \mu m$.

$$\theta_C \quad < \quad 3\ mrad \tag{3.1}$$
$$\Delta\theta_C \quad < \quad 50\ \mu rad \tag{3.2}$$

In the laboratory both angles have been measured simultaneously and the data for each individual BS allows to correct the introduced non-collinearity within the calibration error.

Besides the geometrical requirement that the BS should fit within the 16 mm thickness of the TEC discs, the main concern in the development of beamsplitting devices was to guarantee a measurement precision better than 50 μrad for θ_C.
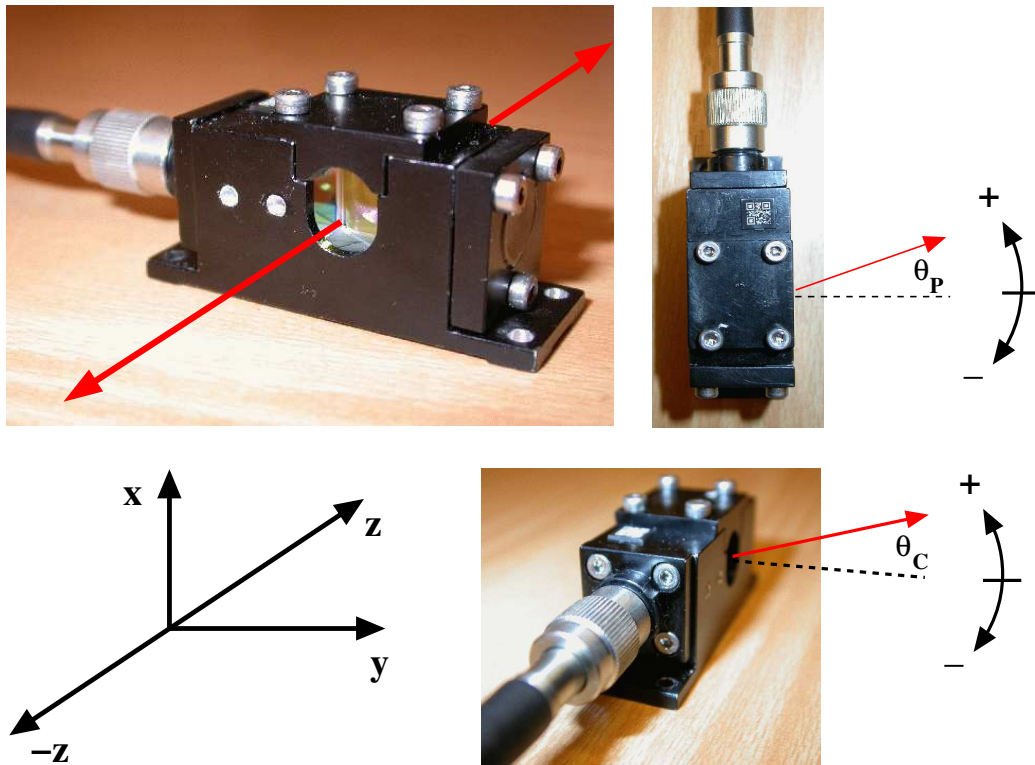
Abbildung 3.5.: The local BS coordinate system and the two angles θ_P and θ_C.

In the BS design collinearity is defined by the position of the incoming fibre in the xz plane. As shown in figure 3.18, a shift in the xz plane results in an incoming angle θ different from 45° and leads in total to a deviation, which is three times larger.

It was found that the reproducibility in θ_C resulting from repeated disconnection and re-coupling of the fibre to the BS was in the order of 100 μrad. Therefore, to achieve a constant ferrule position a definite assignment of each optical fibre to a particular BS was made and after combining both their connection was never disturbed.

To be able to know the relative orientation of both beams outgoing from the BS to within 50 μrad, a test setup was developed to measure the collinearity angle with a much better precision.

3.2.1. Test Setup

In the test setup a CCD camera mounted on a servomotor on a granite table was used to detect the two different rays, beam 1 and beam 2 originating from one beamsplitter BS as illustrated in figure 3.6.

With the help of a retroreflector it is possible to measure the relative position of the two beams as a function of the distance z between the BS and the CCD camera. For all z positions the CCD measured the x and y coordinates of both laser spots. Finally a linear fit was performed to the coordinate differences between the two beams $\Delta x(z)$ and $\Delta y(z)$.

In comparison to the required spot resolution, the 2 μm movement error of the servomotor was negligible. The advantage of the chosen measurement method was its indepen-

3. Beamsplitters
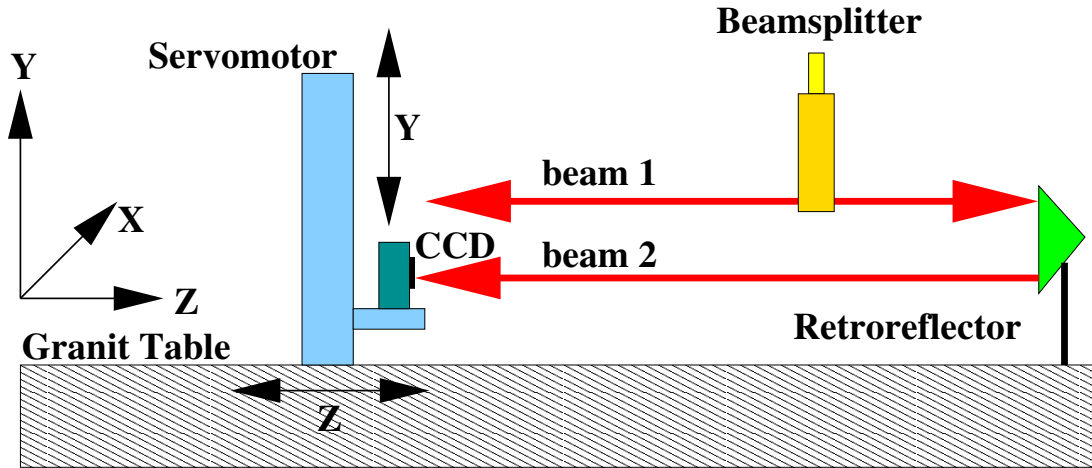
Abbildung 3.6.: Setup to measure the BS collinearity.

dence from an external coordinate system, since only the relative position of beams was determined.

For each collinearity data set the following actions were performed:

1. Mount the BS in a specific position (see figure 3.8).

2. Define the initial CCD distance in y of the two beam spots at the starting z position.

3. Start at a distance $z_0 = 50\ mm$ to the BS and measure the x and y coordinates of both beam spots by performing a 2D gaussian fit to the CCD pixel data.

4. Repeat this measurement at six different z positions $(z_i, i = 1, \ldots, 6)$ spaced by $50\ mm$.

5. For every z position calculate $\Delta x = x_{beam1} - x_{beam2}$ and $\Delta y = y_{beam1} - y_{beam2}$.

6. The slope of $\Delta x = f(z)$ and $\Delta y = g(z)$ gives directly the collinearity angles θ_C and θ_P respectively.

The properties of all components used in the setup are given below. The quadratic sum of all errors gives the measurement accuracy and is in the order of 10 μrad, significantly less than the precision $\Delta\theta_C = 50\ \mu rad$ with which the collinearity angle must be known.

- CCD
  The pixel size is $7.6 \times 8.3\ \mu m^2$ with the pixels arranged in a 844×576 array, equivalent to an area of $6.4 \times 4.8\ mm^2$. For purposes of analysis, the array size was modified by software to 80×52.

  Digitization is done by an 8-bit ADC $(0 - 255)$. To obtain an appropiate error estimate noise data have been taken by recording 100 events and plotting the distribution of the RMS values for each pixel. Figure 3.7 shows this distribution with the ADC range normalized to one. Thus the mean value of the noise corresponds to $0.74\ ADC$ units.

46

CCD error distribution

Entries	4159
Mean	0.002822
RMS	0.0003461
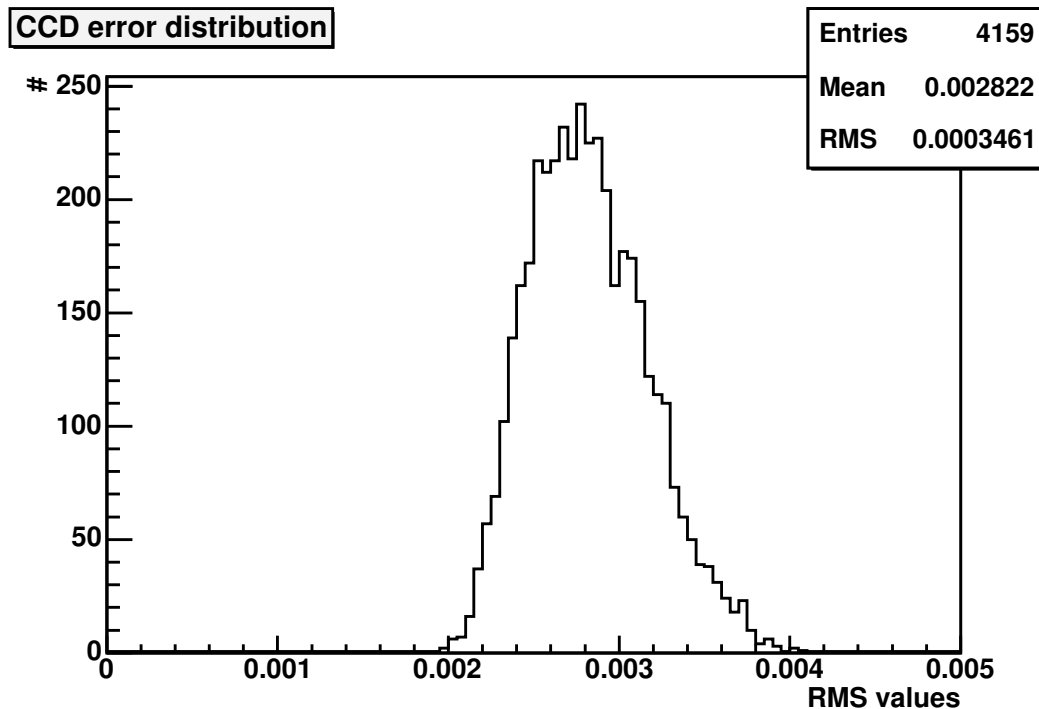
Abbildung 3.7.: CCD camera noise distribution. The 8-bit ADC range was normalized to one and therefore the mean value corresponds to 0.74 ADC units.

- Servomotor
  The servomotor used is a LIMES 150 by the company OWIS [63]. It has a DC 500/ DSC 1000 encoder, a DC-motor step width of 0.4 μm and a step reproducibility over the full range of ≈ 40 cm of 2 μm.

- Retroreflector
  A solid uncoated glass retroreflector 02CCG007 by the company Melles Griot [64] has been integrated in the setup to reflect the incoming beam back on itself by total internal reflection. The specified deviation is $180^o \pm 2''$ leading to an error of less than 10 μrad. It has a diameter of 50 mm and a height of 37.5 mm.

Collinearity data has been taken for each given BS orientation (P_{11}, P_{12}, P_{13}, P_{14}, P_{21}, P_{22}, P_{23}, P_{24}) (see figure 3.8). Apart from the sign of the slope, P_{11} is equivalent to P_{13} and $P_{12} \widehat{=} P_{14}$, $P_{21} \widehat{=} P_{23}$, $P_{22} \widehat{=} P_{24}$ respectively. The modification from front (P_{1k}) to back positions (P_{2k}, $k \in (1, .., 4)$) means exchanging the roles of beam 1 and beam 2.

The integration of 8 independent measurements in one setup allows an easy testing procedure. Besides that, data reproducibility can be checked by repeatedly measuring θ_P and θ_C in all 8 different BS mounting positions. The distribution of the measured values provides immediately the reproducibility accuracy $\Delta\theta_{C,P}$.

Mounting of the BS in the test setup is identical to the way it is done in the TEC. The BS itself has a three point support and its mounting is defined by precision holes on the backside, with pin counterparts on the special BS mounting structure, see figure 3.9.
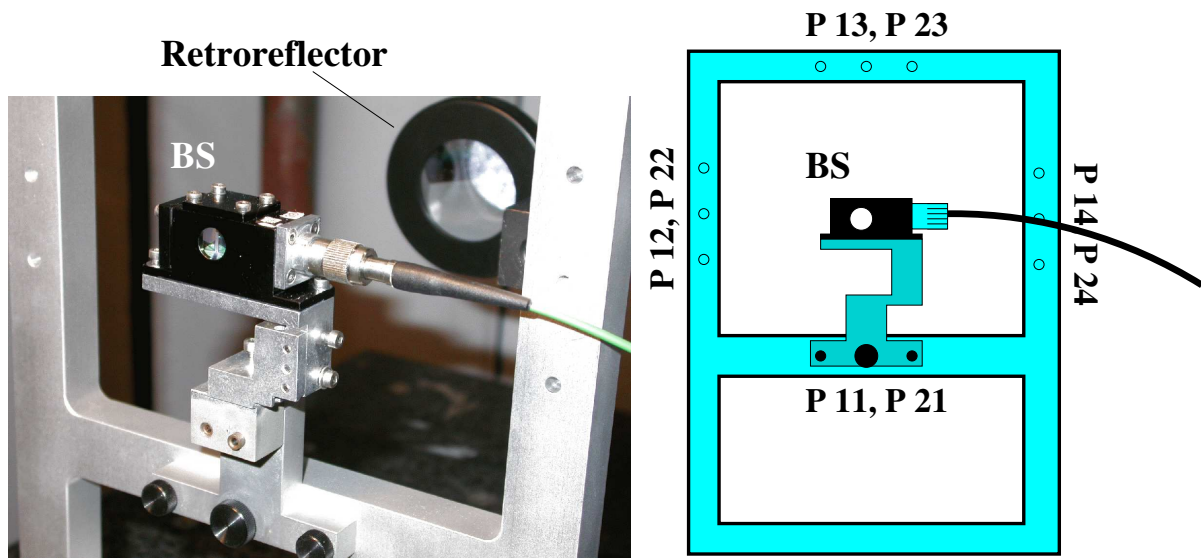
Abbildung 3.8.: Picture of the BS mounting positions for collinearity measurements.

Adjustment screws have been foreseen to be able to adjust both beams from the BS in order to guarantee their detection on every TEC disc.
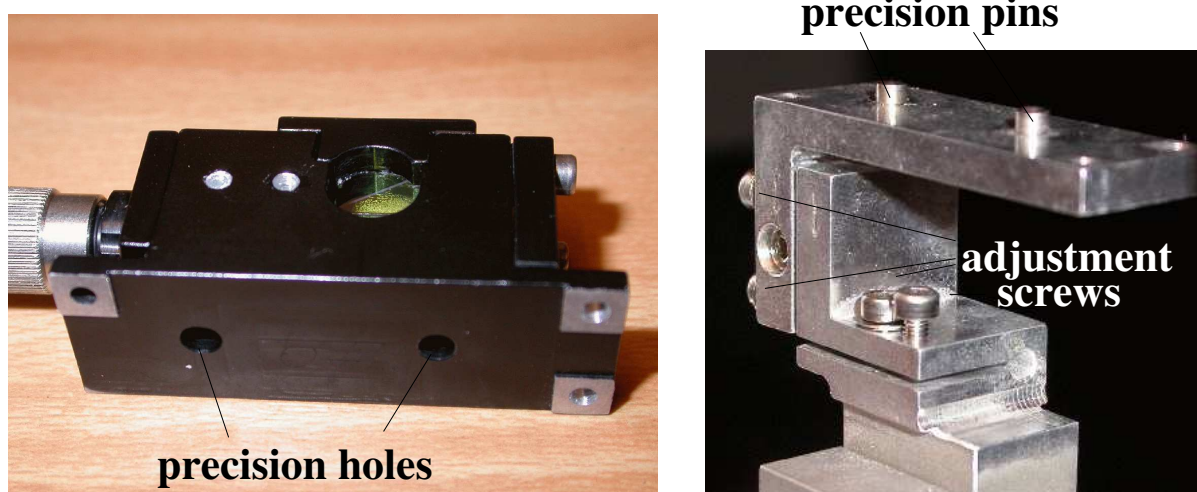

Abbildung 3.9.: The mounting of the BS in the test setup is identical the way it is mounted on TEC D6. It is accomplished via two precision holes on the BS backside matching precision pins on the mounting platform.

A pre-adjustment of the orientation of all BS mounts in D6 was made on a 3D measuring machine before assembly into TEC+ (TEC-). As discussed in appendix G (figure G.2) collinearity was checked qualitatively by moving an indicator card along the normal of D6, thus simulating the transparent 10 mm diameter area of the silicon sensor backplane. This procedure helped to define the approximate beam direction to within 2 $mrad$ and formed the basis for a fast integration of the BS into the TEC.

3.2.2. Results

Every beamsplitter was put into the collinearity setup and measured in all mounting positions. The results are 8 data points for θ_C as well as for θ_P and the RMS of these measurements gives the angle measurement accuracy $\Delta\theta$.

	Δ beam12, X	
χ^2 / ndf		2.953 / 5
p0		0.7133 ± 0.001735
p1		$-0.0004632 \pm 7.76\text{e-}06$

	Δ beam12, Y	
χ^2 / ndf		3.712 / 5
p0		0.4937 ± 0.001732
p1		$-0.0004482 \pm 7.747\text{e-}06$
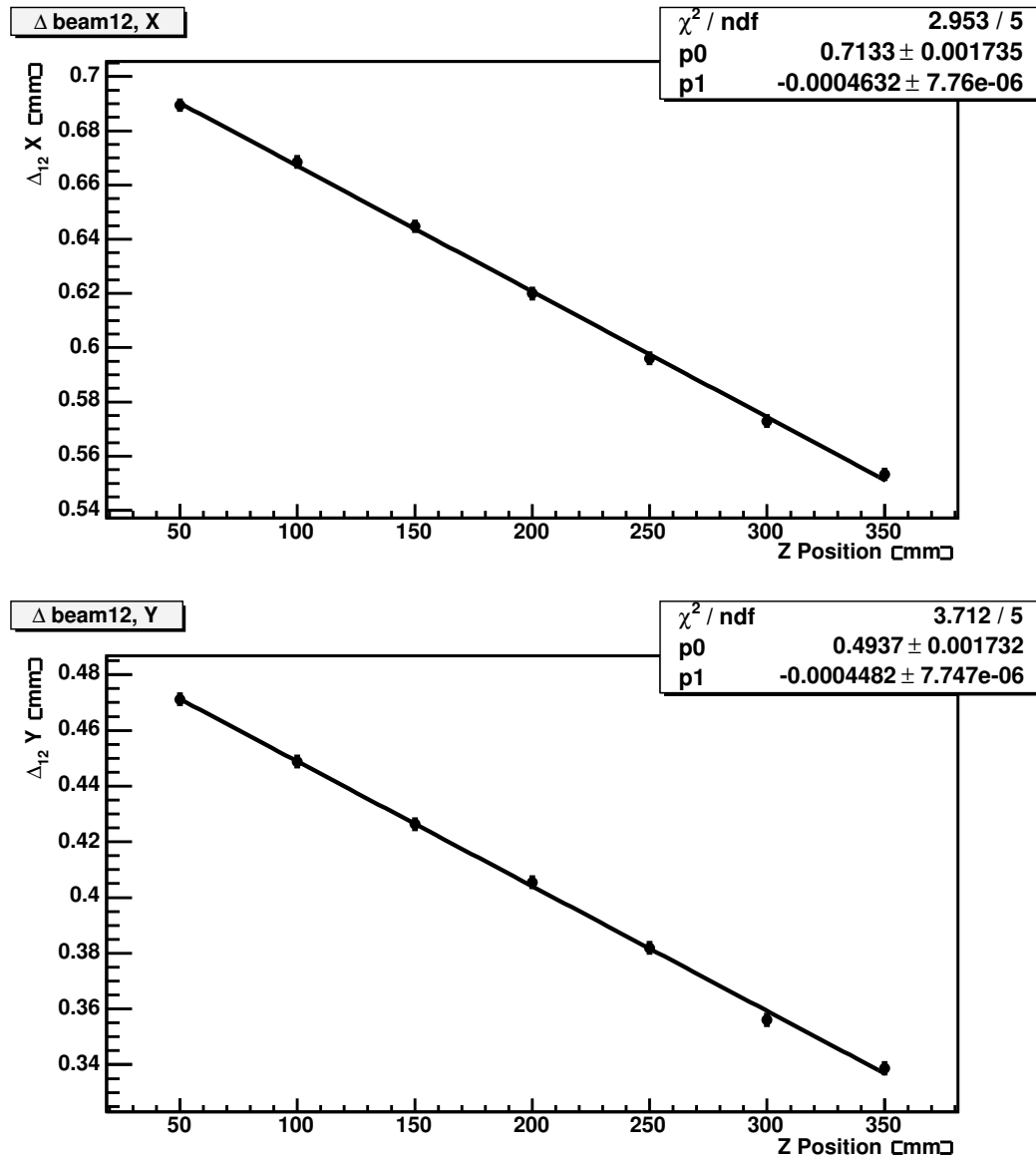
Abbildung 3.10.: The CCD camera measures both beam spots originating from one BS. At several distances the difference of beam 1 with respect to beam 2 in the x (*upper diagram*) and y coordinate (*lower diagram*) was determined. For each run a straight line was fitted to the data points to obtain θ_P and θ_C.

Figure 3.10 shows as an example the x and y difference between beam 1 and beam 2 as measured by the CCD camera for one BS orientation. A straight line was fitted to the data, with point errors $\Delta x = 2\ \mu m$ and $\Delta y = 2\ \mu m$ given by the precision of the

3. Beamsplitters

servomotor and $\Delta z = 1\ mm$. The linear behaviour is obvious for both beams and the slope of the fits gives the collinearity angles $\theta_P = -0.463\ mrad$, $\theta_C = -0.448\ mrad$.

The error on θ_P and θ_C was obtained from the distributions of the 8 independent measurements. These are shown for one beamsplitter in figure 3.11 and result in $\Delta\theta_P = 35.1\ \mu rad$, $\Delta\theta_C = 29.4\ \mu rad$.
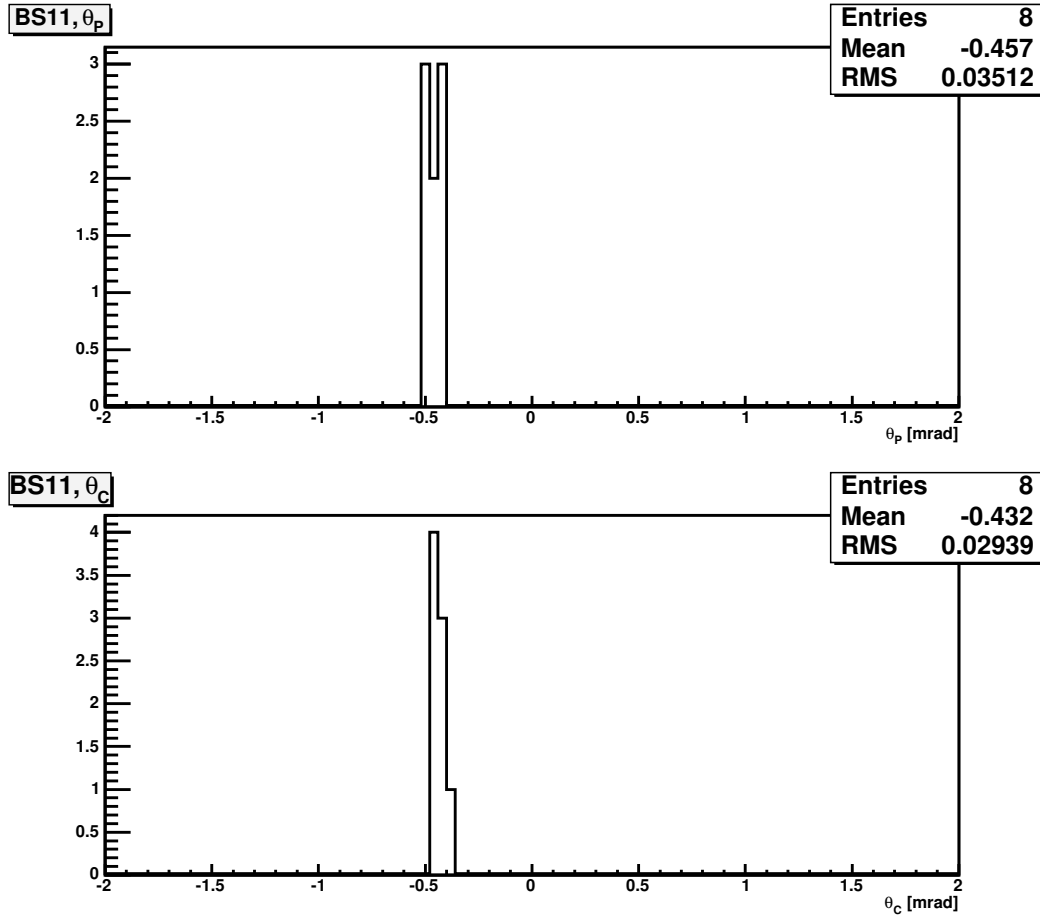
Abbildung 3.11.: Distribution of all 8 independent angle measurements (figure 3.8). The RMS value is a measure for the reproducibility and gives the uncertainty $\Delta\theta_C$ ($\Delta\theta_P$) for the collinearity angle θ_C (θ_P).

Emphasis has been put on the development and creation of a beamsplitter calibration device. A few BS were tested, as shown exemplarily above (figures 3.10 and 3.11). In total, 32 beamsplitters were calibrated [66] and found to be within the specifications, as confirmed by the distribution in figure 3.12. Detailed information about each BS (tables G.1, G.2), as well their assignment to the endcap sectors is summarized in appendix G.

At room temperature all BS fulfill the requirements $\theta_C < 3\ mrad$ with $\Delta\theta_C < 50\ \mu rad$. Still to be proven is their performance in the tracker working environment at $-10^o C$, which is the subject of the next section.
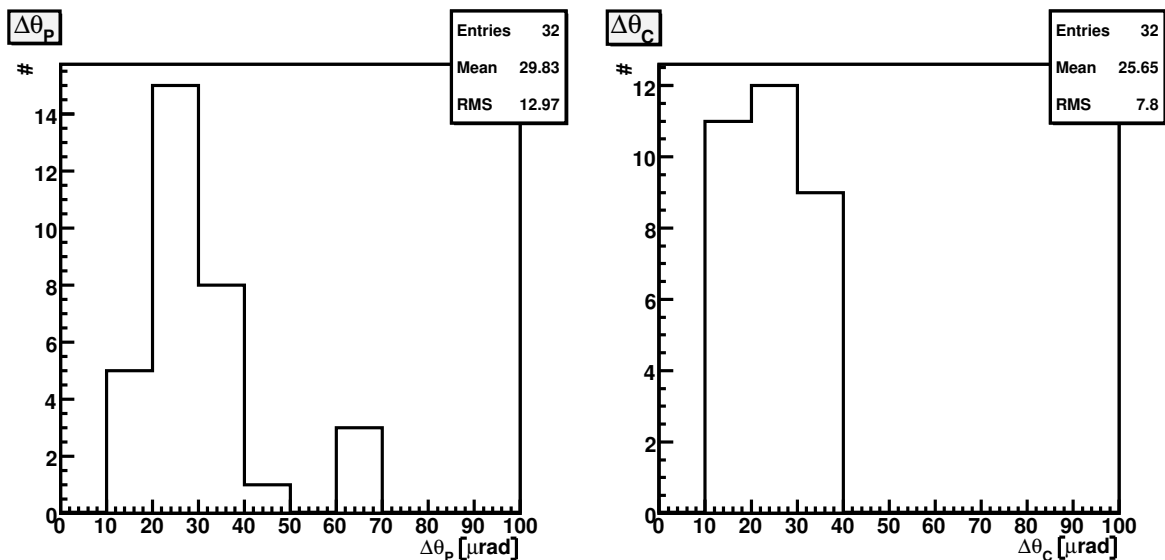
Abbildung 3.12.: The histograms show the $\Delta\theta_C$, $\Delta\theta_P$ distributions for all BS integrated in the endcaps [66]. The required precision $\Delta\theta_C < 50$ μrad is fulfilled by all beamsplitting devices.

3.2.3. BS Collinearity at Low Temperature

Since the tracker will be operated at low temperature ($\approx -10^o C$) the BS collinearity angle should be stable not only in time but also as a function of temperature. During production and assembly, each BS has been subjected to more than 20 temperature cycles down to less than $-20^o C$ to remove internal stresses and tensions of the material [60].

To check the time dependence, collinearity data were taken again for selected BS 1, 4 and 6 weeks after the initial measurement. It was found, that there is no change from the first data sets and the measured collinearity angles remain constant within 50 μrad.

A more complex setup was necessary to understand the behaviour as a function of temperature. The optical properties of the LAS components were tested in a special cooling box, developed to examine the electrical properties of silicon modules in the tracker operating environment [65].

As shown in figure 3.13, four R4 alignment modules M1, M2, M3, M4, with a BS in between have been arranged inside the box.

The container and its components, the module housings and the BS mount, are made of aluminium. The modules are fixed on aluminium support plates and the beamsplitter mounting interface is made of plastic as shown in figure G.6. A flow of dry nitrogen N_2 in the box keeps the ambient humidity to values of less than 15%.

The ARC test system [65] has been used to read out the silicon modules at a bias voltage of 400 V and each signal histogram has been fitted by a gaussian to determine the laser spot position.

In special runs, the BS has been replaced by a collimator illuminating two modules to study possible movements of the light source and detectors (see figure 5.8).

Starting at $T = +25^o C$ (run $r_p = 1$) the temperature was decreased in $5^o C$ steps down to $T = -25^o C$ ($r_p = 11$). Pedestal and signal data were taken at each temperature
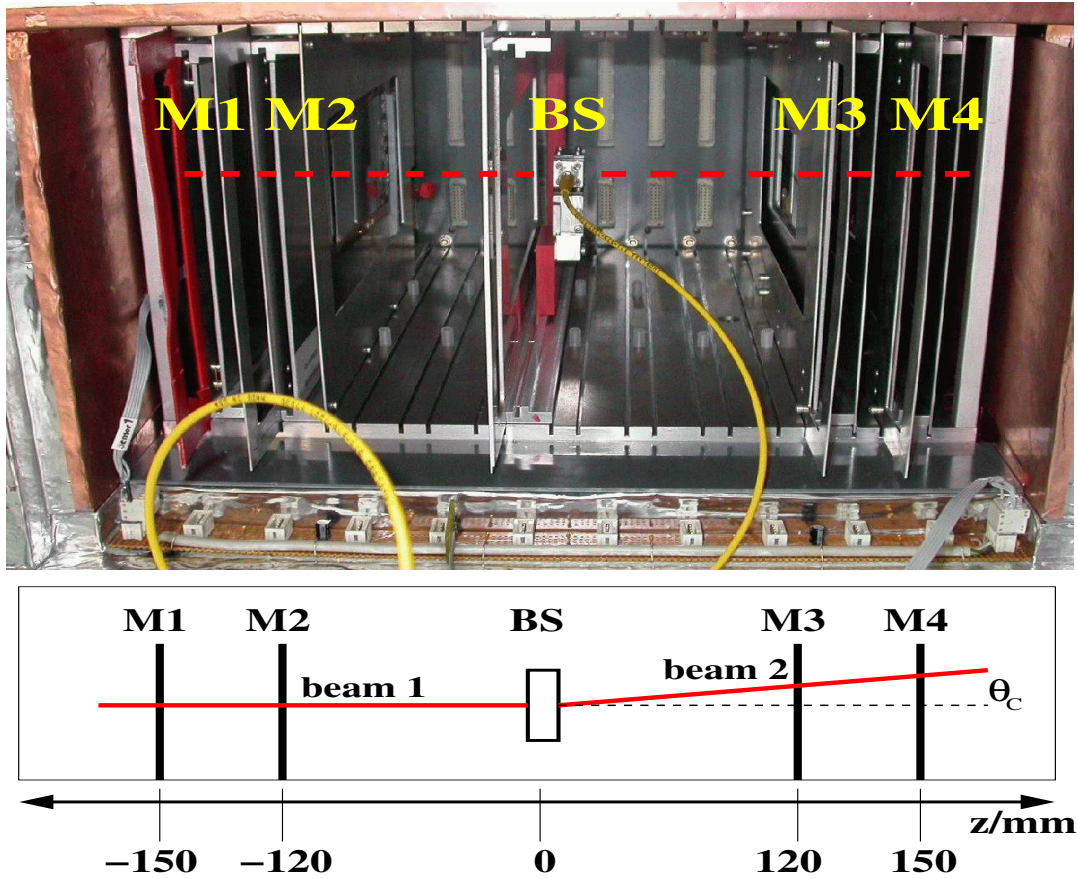
3. Beamsplitters

Abbildung 3.13.: Setup for collinearity measurements of θ_C in a cold environment with two modules M1, M2 on the left and two M3, M4 on the right side of the BS. A picture of the BS mounting is shown in G.6.

setting. Finally, the system was warmed up and the last three runs ($r_p = 12, 13, 14$) were taken at $T = +20^oC, +15^oC, +20^oC$.

In figure 3.14 laser beam positions measured on all four modules are shown. In the following the data are discussed in terms of different scenaria of relative position changes of the modules and the BS due to the cooling.

1. Modules remain fixed, the laser beams can move.
   The maximal deviation between beam 1 and beam 2 would result in an angle error $\Delta\theta_C \approx 1 \; mrad$. This is obtained from the outermost modules M1 (displacement of the beam spot by 60 μm) and M4 (displacement by $-80 \; \mu m$), since the spot position changes measured in the modules closer to the BS (M2, M3) are usually less than in M1, M4. This leads to the first interpretation possibility, that on the right side the spot moves down while on the left side it moves up, equivalent to a BS rotation perpendicular to the z axis.
   Figure 3.15 shows the result for the orientation of the left side (θ_L) and right side (θ_R) beams determined from the slope of straight lines fitted to the BS position and to the laser spot position measured by the modules M1, M2 and to BS, M3, M4. The collinearity angle $\theta = \theta_L - \theta_R$ is also plotted and shows variations up to 500 μrad
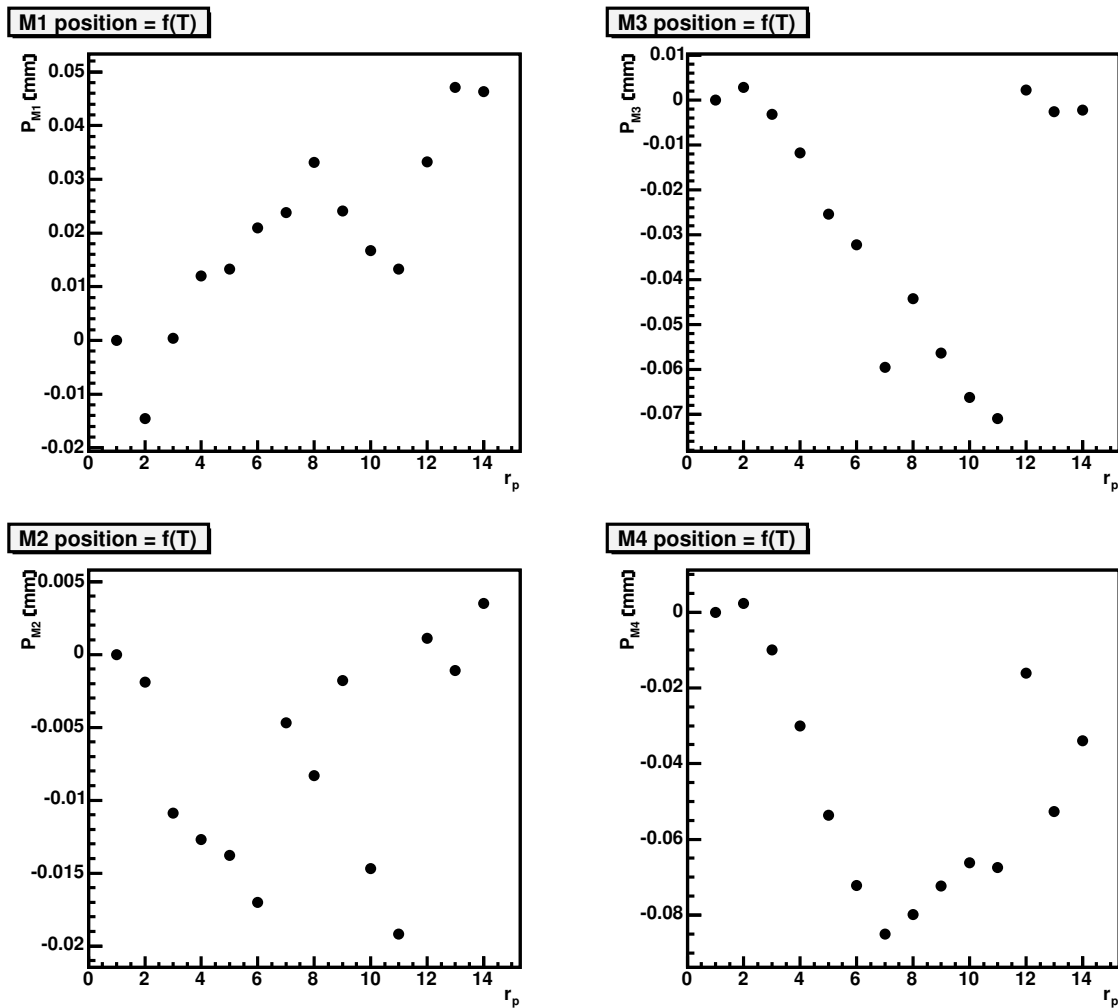
Abbildung 3.14.: The reconstructed laser spot position on each module is given as a function of the temperature run r_p. All variations have been defined with respect to the initial position. Cooling down corresponds to $r_p \leq 11$, while the last three points show the behaviour after warming up.

during the temperature cycle, i.e. 10 times larger than allowed. By comparison, for room temperatures at the beginning and the end of the cycle (points $r_p = 1$ and $r_p = 12, 13, 14$), the variation in θ is less than 100 μrad.

However, it cannot be distinguished between changes in the beam orientation θ_C caused by movement of the BS as a whole and changes brought about by shifts in the position of the components inside the BS.

This is investigated by taking data with the same setup, where the beamsplitter including its mount interface, has been exchanged by a collimator (see figure 5.8) illuminating two alignment modules. One temperature cycle was taken with a pair of R4 modules, while three cycles were recorded with a R6 pair.

3. Beamsplitters
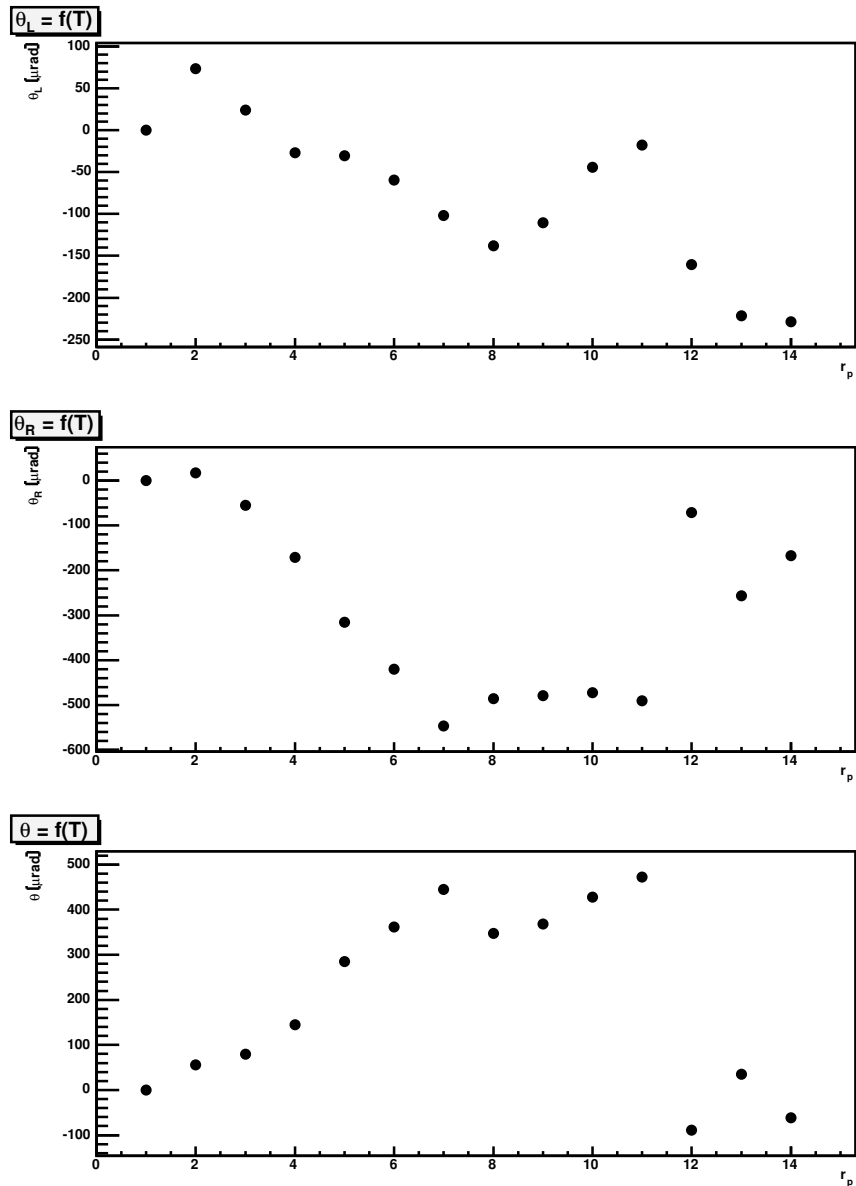
Abbildung 3.15.: Variations during the temperature cycle in θ_L and θ_R (*first two diagrams*) and in their difference $\theta = \theta_L - \theta_R$ (*third diagram*). θ_L is obtained by a left side straight line fit (M1, M2, BS) and θ_R by a right side fit (BS, M3, M4).

As above, the beam orientation θ was obtained from the slope of a straight line fitted to the position of the collimator and the measured beam spot positions on the two modules. From the results shown in figure 3.16 it is clear that large movements from 500 μrad to 1400 μrad occur also in this setup. This suggests, but does not confirm, that the BS mount is moving during temperature cycling.
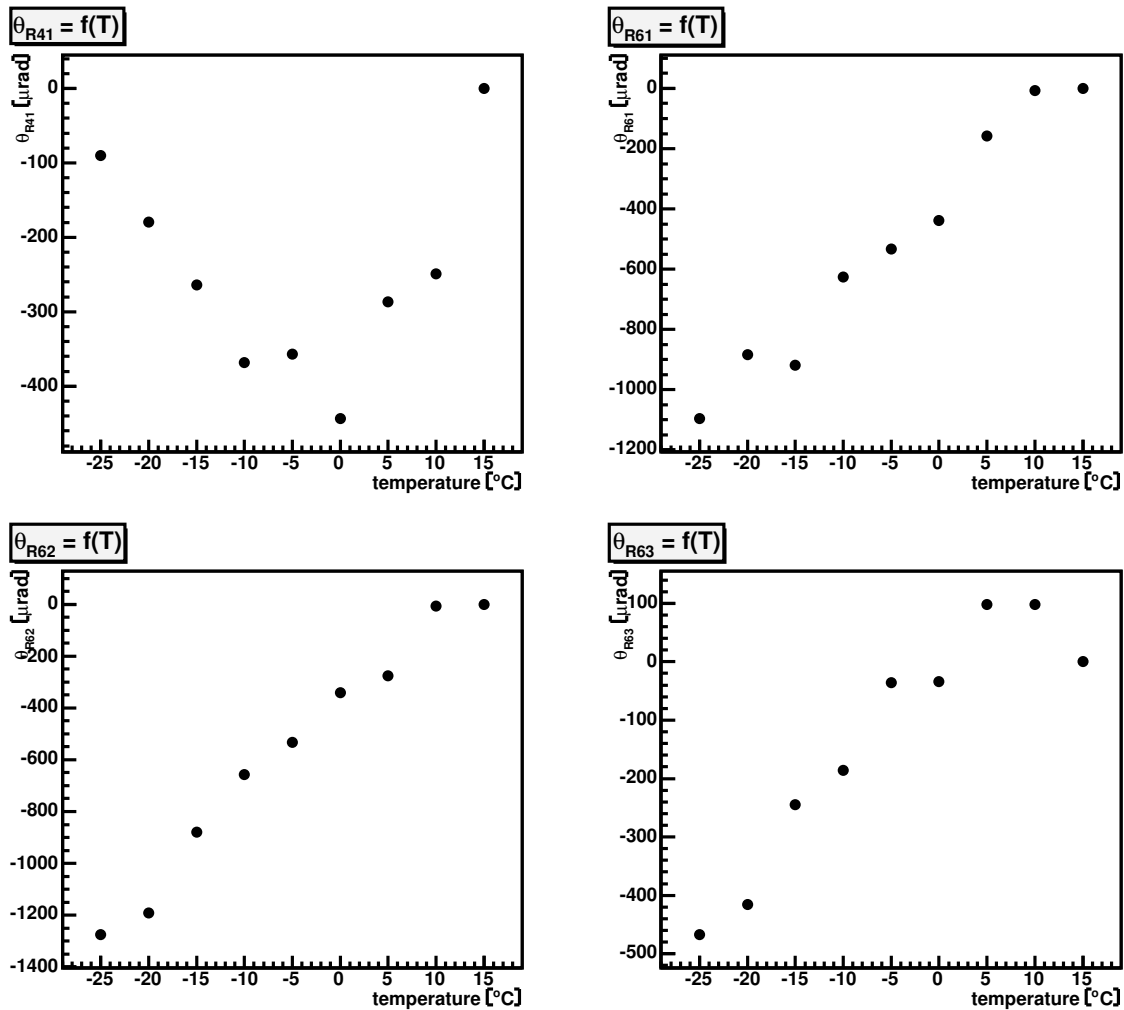
Abbildung 3.16.: The setup with the BS replaced by a collimator illuminating two alignment modules (figure 5.8) also leads to large beam spot position variations during cooling.

2. The collinearity remains constant although both the BS as a whole and the modules can move.

   To check whether this assumption is consistent with the data of figure 3.14, a linear fit was performed for each temperature setting to the measurements on modules M1 to M4 including the position of the beamsplitter in between. Before the fit, the data were corrected for the collinearity angle measured at room temperature for the particular BS used. Figure 3.17 shows the distribution of the residuals calculated for each module.

   The RMS values of these distributions do not exceed 15 μm, which is of the same order as the module resolution. Thus the assumption above might be a reasonable explanation for the beamsplitter temperature data. However, it does not guarantee that the calibration of the collinearity angle θ_C will remain constant within the required accuracy of 50 μrad.

3. Beamsplitters
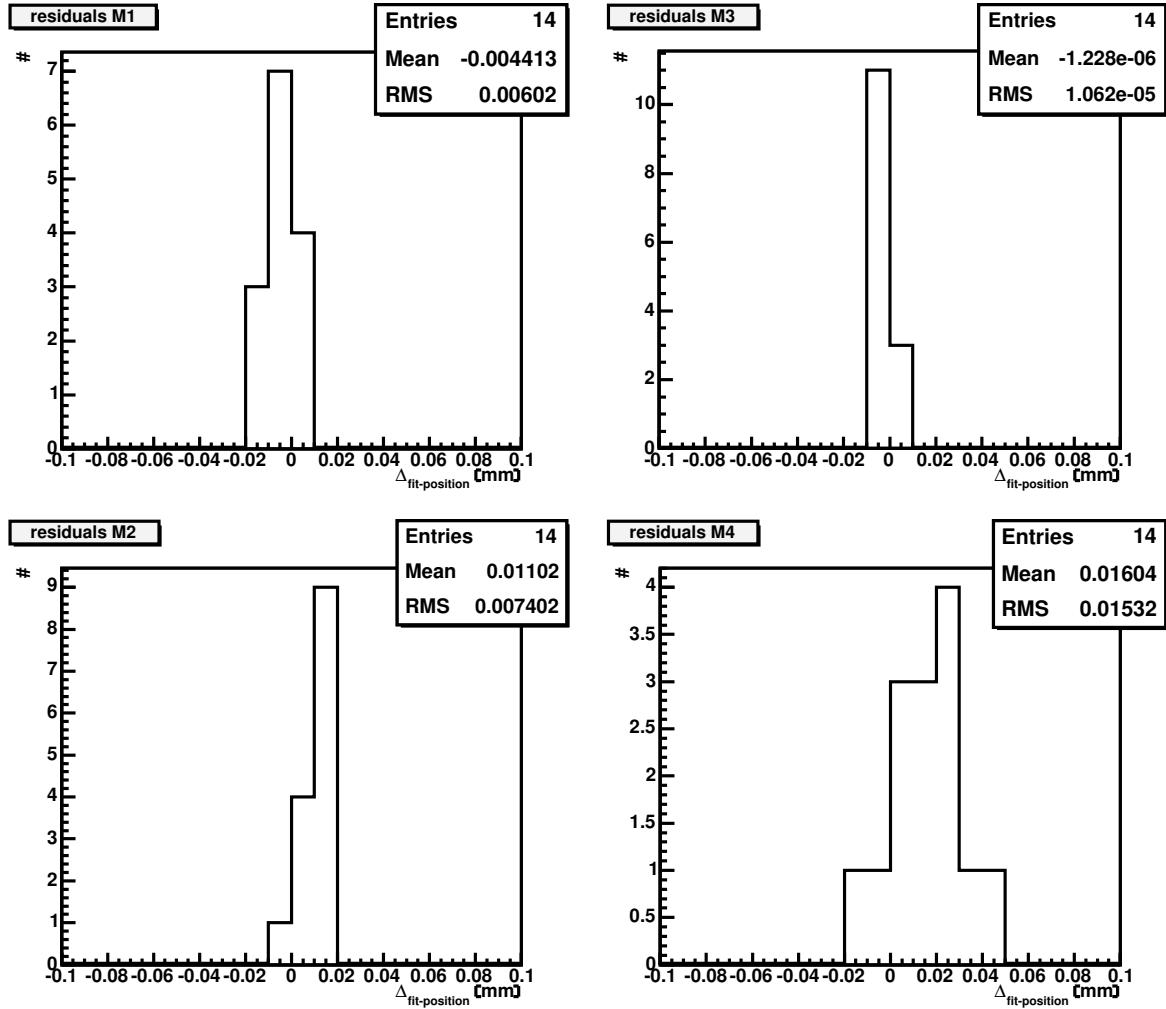
Abbildung 3.17.: With the assumption of a constant θ_C the residuals ($\Delta_{fit-position}$) between the linear fit from module M1 to M4 and the measured laser position on each module have been calculated. The residuals for all modules (M1, M2, M3, M4) are shown in the distributions above.

3. To examine the limits within which the collinearity calibration of the BS remains constant, the setup of figure 3.6 was used again to measure the collinearity as a function of a large locally applied temperature gradient.

As illustrated in figure 3.18, the most sensitive part on the beamsplitter is the FC fibre coupling device, which defines the collinearity for a focal length $f = 10\ mm$. For a temperature change $\Delta T = 20\ K$, an upper limit of the change in beam orientation can be estimated assuming fixation of the fibre coupling via an M2 screw and taking the thermal expansion coefficient of aluminium $\alpha_{Al} = 25\ \mu m\ m^{-1}K^{-1}$ into account:

$$\Delta L = \alpha\ \Delta T\ d_{M2} \approx 1\ \mu m \qquad \Delta\theta_C = \frac{\Delta L}{f} = 100\ \mu rad \qquad (3.3)$$

The worst case variation would then be $3\theta_C = 300\ \mu rad$, exceeding the required accuracy by a factor of six.
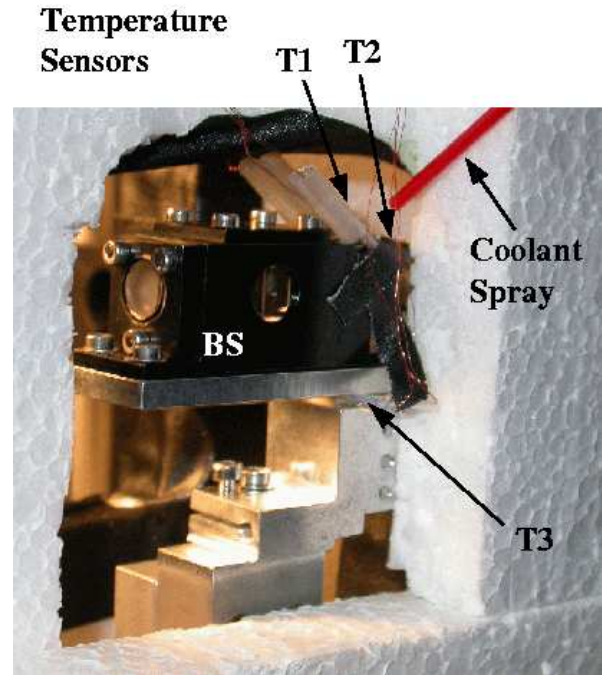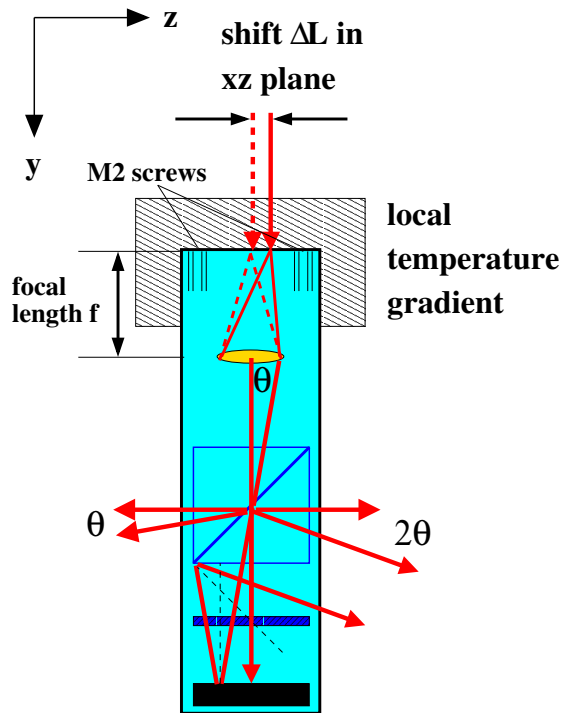
Abbildung 3.18.: Application of a local temperature gradient on the most sensitive part of the BS, the fibre coupling. The relative orientation of the two outgoing beams is defined by the position of the incoming beam in the xz plane.

Although the assumption of a local temperature difference of 20 K on the BS is extreme, experimental data were taken under such conditions by cooling the fibre coupling area with a coolant spray, as illustrated in figure 3.18.

Three temperature sensors were used to monitor the BS temperature. Sensors T_1 and T_2 were attached to the fibre coupling area, while T_3 was glued on the BS aluminium mount. For every z position between the BS and the CCD camera, the fibre coupling area was cooled down to $T_1 \approx T_2 \approx -30^oC$ for a few seconds with these temperatures saturating to -5^oC and T_3 was constant, $T_3 \approx 0^oC$, during the measurement. Statistics at each point were limited by water condensation on the outer glass surface. The result of one measurement is shown in figure 3.19. Deviations from the straight line up to 10 μm are visible, but the overall behaviour is clearly linear and the distribution of the residuals confirms the stability of the BS collinearity under a local temperature gradient.

χ^2 / ndf	114.9 / 5
p0	-1.424 ± 0.001938
p1	$-0.001118 \pm 8.668\text{e-}06$

χ^2 / ndf	56.03 / 5
p0	0.02952 ± 0.001718
p1	$0.0003574 \pm 7.682\text{e-}06$
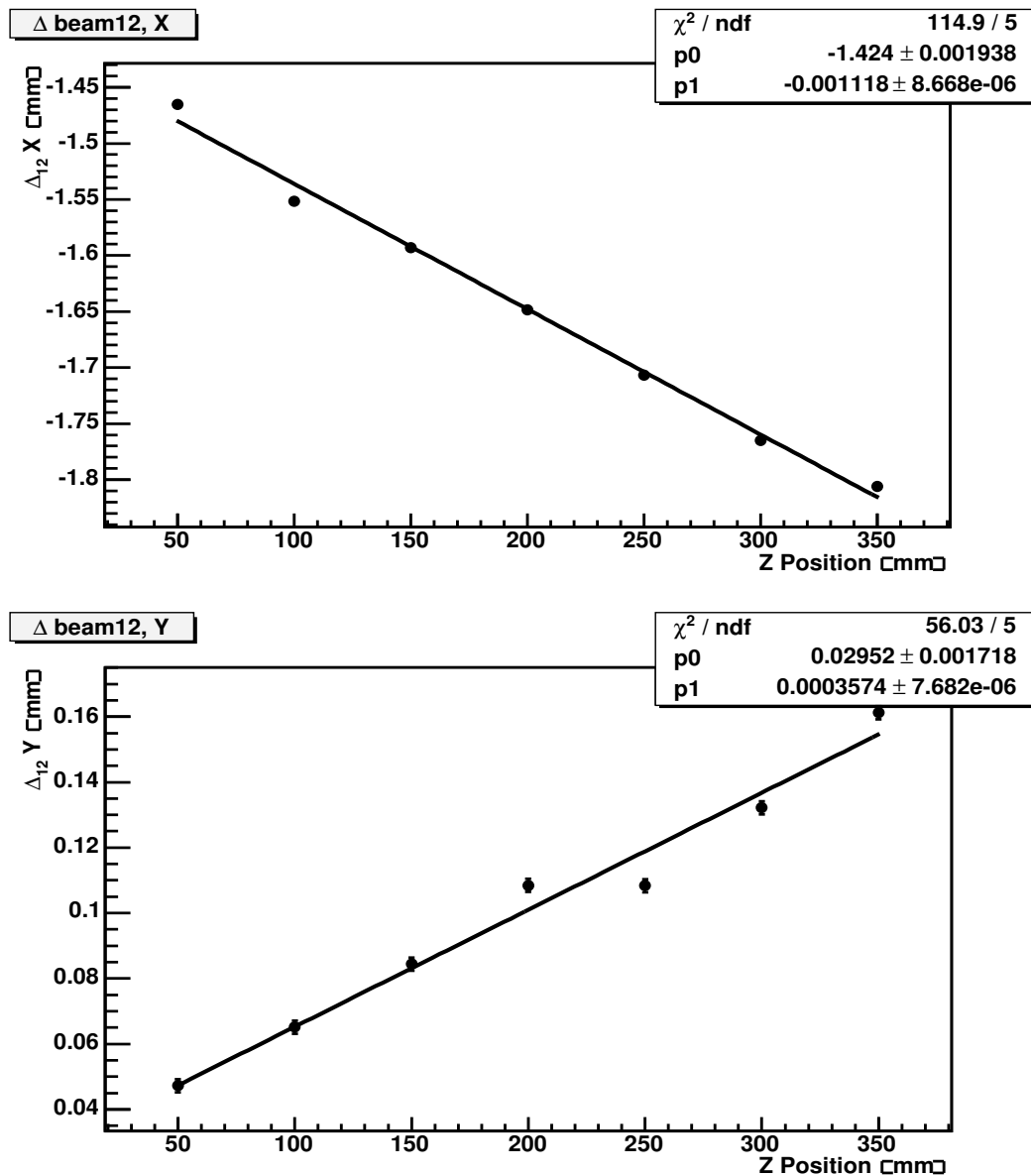
Abbildung 3.19.: The same collinearity measurement procedure explained in section 3.2.1, was used after applying a local temperature gradient on the fibre coupling part of the BS. The angles θ_P and θ_C were obtained from the slope of straight line fits to the data, compare figure 3.10.

The distribution of 11 independent data samples including the measurements at room temperature is shown in figure 3.20. It is seen that the collinearity does not change before, during and after the temperature cycle and the RMS value of the distribution is compatible with the required accuracy of 50 μrad. The variations with temperature of the beam position are caused by movements of the BS mount interface and/or the silicon modules and the calibration of the beamsplitters in the laboratory (tables G.1 and G.2) remains valid for their operation inside the CMS tracker.
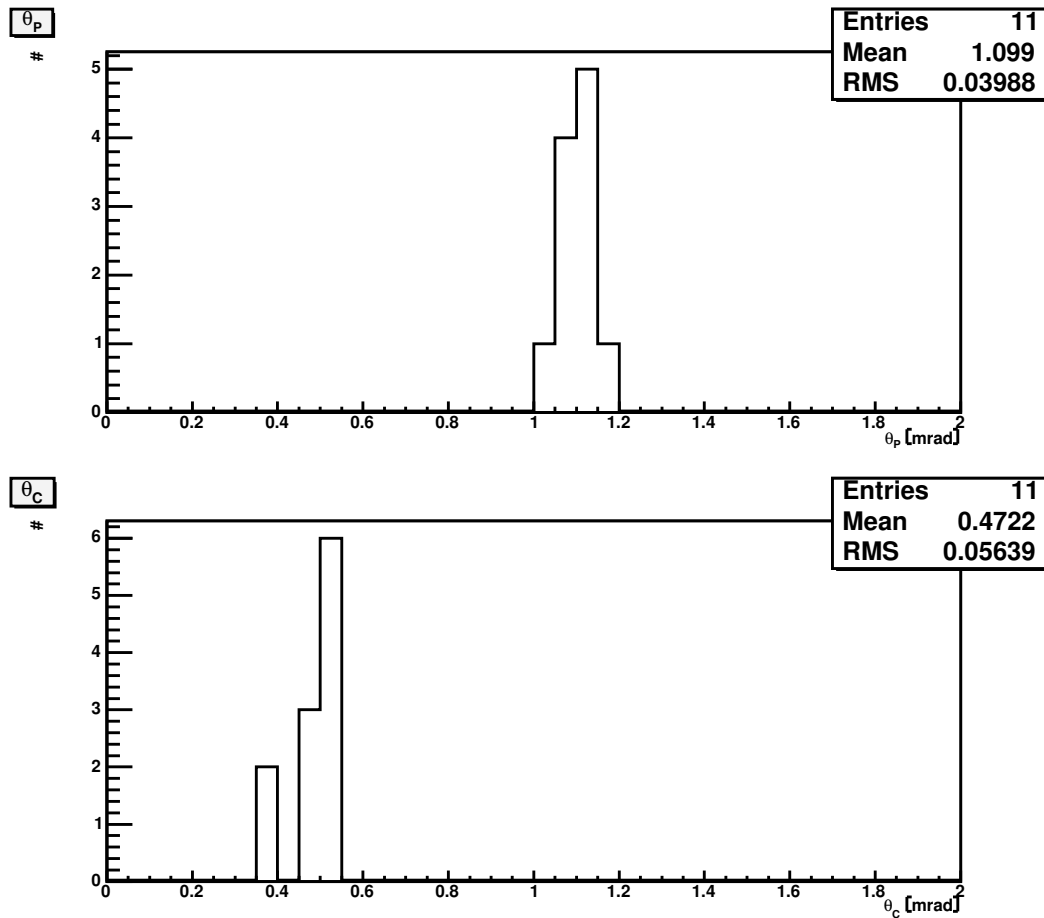
Abbildung 3.20.: The distribution of 11 independent data samples show BS performance constant within 50 μrad under extreme conditions.

A LAS calibration at room temperature as well as a possible re-calibration under the tracker operating conditions allow an absolute positioning of the structure. If relative movements have to be monitored than changes in the BS mounting should be negligible, which is the case for measurements at temperatures constant to $\pm 5^o C$.

3.2.4. Conclusions of the Beamsplitter Measurements

Several optical and mechanical constraints have been taken into account during the development of a beam splitting device. Investigations of the BS characteristics under tracker working conditions have shown that all requirements, namely

- Radiation hardness.

- Use of non-magnetic materials.

- Incorporation in TEC D6 within the geometric constraint given by the 16 mm disc thickness.

- Collinearity $\theta_{P,C} \leq 3\ mrad$.

- Variations of collinearity $\sigma_{\theta_{P,C}} \leq 50\ \mu rad$.

- No changes of the BS properties with temperature and with time: $\theta_{P,C} \neq f(T)$, $\theta_{P,C} \neq f(t)$

have been fulfilled and allow therefore a stable performance during 10 years of LHC.

3.3. Alignment Tube

3.3.1. Requirements and Layout

The alignment tubes serve to provide a light path connecting the tracker subdetectors, TIB, TOB and the two TECs. They are fixed within an annular region of 16 mm along the inner envelope of the TOB. Alignment tubes are arranged on both the $+z$ and $-z$ sides.

Their (r, φ) position is shown in figure 2.7 and beamplitters are put on all $+z$ tubes. Each individual tube has to send 3 beams to the TOB and 3 to TIB (figure 3.21).
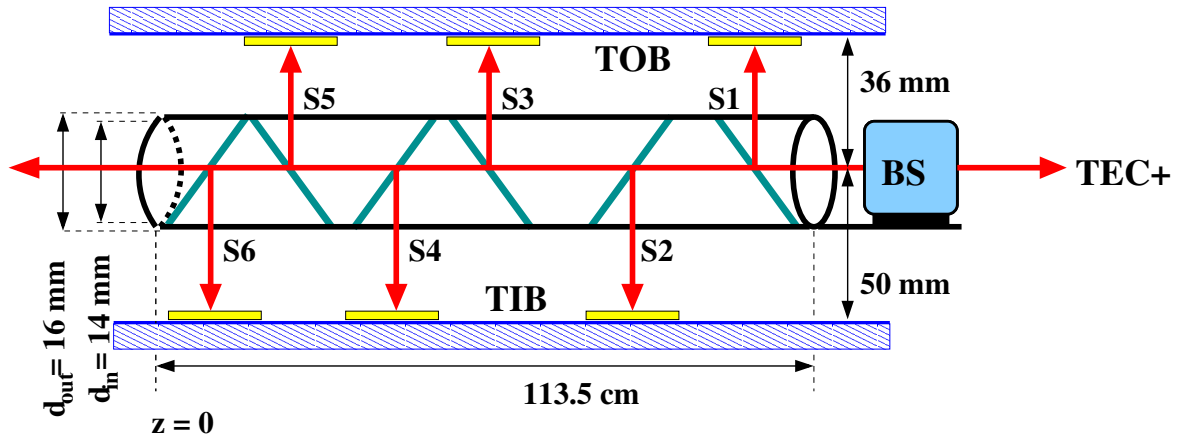
Abbildung 3.21.: Layout of the AT on the $+z$ side. The BS is fixed on the AT and is located in the area between the TOB and TEC+.

The distance to the TIB outer modules is 50 mm and to the TOB inner layer 36 mm. Since these distances are short compared to those in the TEC and only the first module layers are hit by the laser beams, the relative orientation between the rays going up to the TOB and those going down to the TIB must be known with an accuracy $\sigma_\varphi = 1.5\ mrad$.

Taking the TOB as an example, rods (modules) are placed with a precision of 50 μm with respect to a precision pin on the TOB wheel. Since the distance of this pin to the center of the AT is 30 mm, the orientation of the AT with respect to the TOB modules is known to $\frac{50\ \mu m}{30\ mm} \approx 1.5\ mrad$.

3.3.2. Properties

Experience with low thermal conductivity materials shows, that the existence of temperature gradients perpendicular to the direction of the laser beam may cause losses in resolution, since the refractive index is a function of temperature, $n = f(T)$.
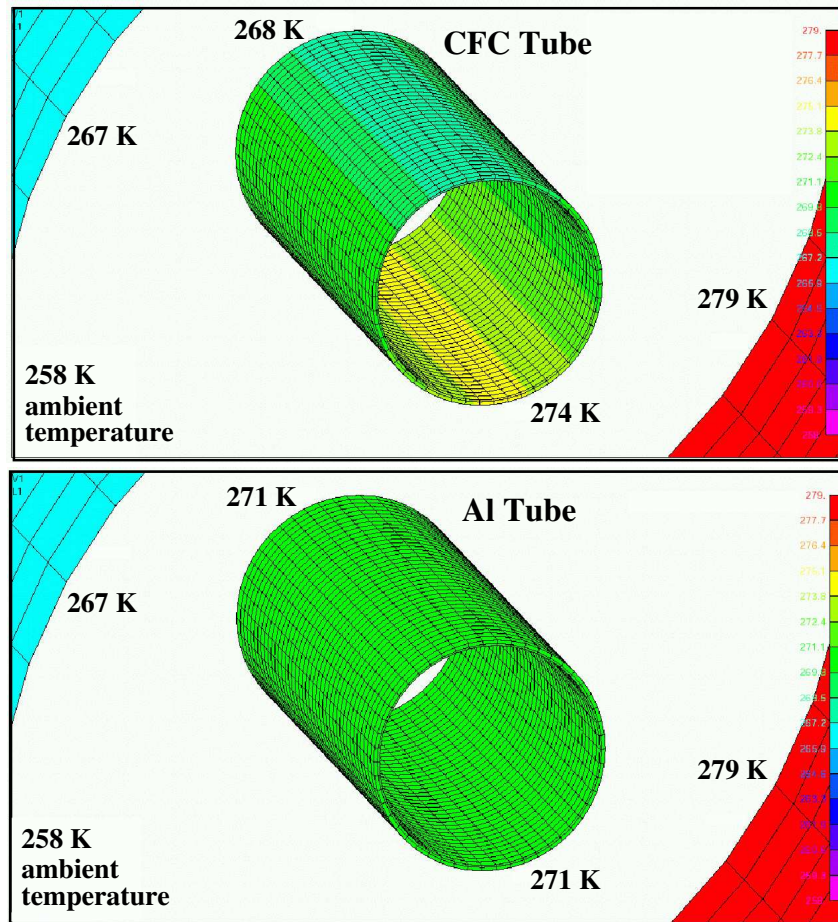
Abbildung 3.22.: The results of FEM calculations for alignment tubes of different materials placed inside a temperature gradient of $\Delta T = (279 - 267)\ K = 12\ K$ [67]. The CFC tube has a diagonal gradient of 6 K, whereas a uniform distribution can be seen when aluminium is chosen.

FEM[1] calculations [67] have been done to simulate the temperature field distribution inside an AT placed in a temperature gradient of $\Delta T = T_{up} - T_{down} = 12\ K$.

As seen in figure 3.22, the effect can be large, depending on the material of the AT, carbon fibre composite (CFC) or aluminium (Al).

There is a uniform temperature distribution inside the aluminium tube, whereas in a CFC tube no inner temperature balance can be achieved. With the laser spot deviation y due to a temperature gradient $\frac{dT}{dy}$ across the beam travel distance L given by

$$y = k\ \frac{dT}{dy}\ L^2 \tag{3.4}$$

a deviation $y = 1.1\ mm$ is obtained for $\Delta T = 6.0^o C$ along the inner tube diameter $d = 14\ mm$, with $L_{barrel} = 2.2\ m$ and $k_{air} = 5.4 \cdot 10^{-7}/^o C$. Though carbon fibre is a rigid material having a low thermal expansion coefficient, it is not suitable for the alignment

---

[1]finite element method

tubes, since beam position changes in the range of $\approx 1\ mm$ exceed the required precision of 100 μm.

Choosing aluminium has the advantage, that the much larger thermal conductivity leads to temperature balance inside the AT, so that no changes in the beam position are expected. Longitudinal (along the z axis) expansion of the tube itself up to 0.5 mm is possible, but such changes are parallel to the strip direction of the TIB and TOB modules.

The layout of the AT is shown in figure 3.21. The TIB and TOB laser beam positions are summarized in table 3.1.

	TIB [*mm*]			TOB [*mm*]		
z+	180	380	620	220	580	1040
z-	100	340	540	140	500	860

AT beam positions

Tabelle 3.1.: Position of laser rays to the TIB and TOB.

Reflection on mirrors depends on the polarization of the incoming light and can be calculated by using the Fresnel equations in appendix H. The plot in figure 3.23 shows the dependence of s, p polarized light on the angle of incidence, which is 45° for the AT mirrors.
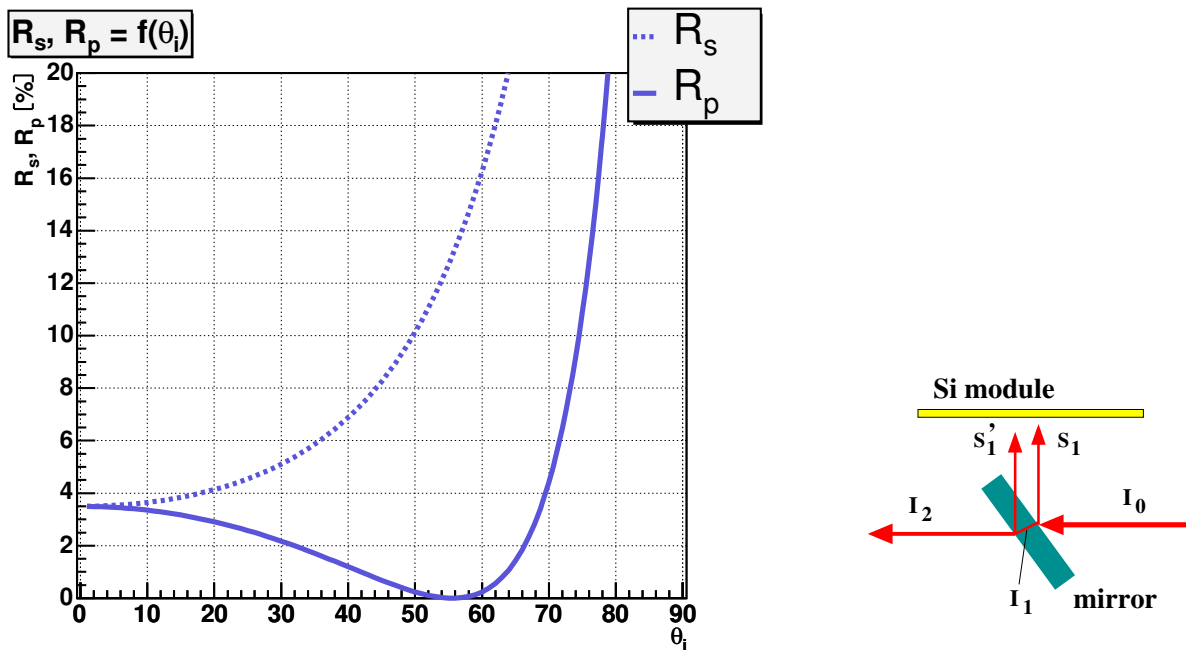
Abbildung 3.23.: The dependence of the reflection of polarized light on the angle of incidence can be calculated by using the Fresnel equations (appendix H). For incidence at 45°, the fraction of s and p-polarized light is $8:1$. To avoid a secondary reflection S_1' on the mirror backside, s-polarized light has to be used.

Since the polarization definition is with respect to the plane of incidence and for the BS this plane is rotated by 90° relative to that for the AT mirrors, the s-polarized output of the BS has p-polarization for the AT mirrors. However, as explained in the following, the light incident on the AT mirrors must have s-polarization.

An anti-reflex-coating has been applied on the surface of the second mirror-air interface to minimize a second reflection S_1', as illustrated in figure 3.23.

S_1' is a defined fraction (≤ 1 %) of the incoming intensity I_1. If p-polarized light is used, then I_1 is of the same order as I_0, because the reflected intensity S_1 is ≈ 1 % (compare figure 3.23). Thus the second reflection S_1' is appreciable and has been observed in experiments with p-polarized light as shown in the right diagram of figure 3.24.

By using circular or s-polarized light for the AT mirrors, the S_1' signal becomes negligible in comparison to S_1. In first studies, a $\frac{\lambda}{4}$-plate has been inserted between the BS and the AT generating circularly polarized light on the AT mirrors. The result is shown in the left diagram of figure 3.24, where the second reflection is hardly visible.

Improvements can be achieved by replacing the $\frac{\lambda}{4}$-plate with a $\frac{\lambda}{2}$-plate resulting in s-polarized light on the AT mirrors. The experimental setup and the measurement for all 6 AT mirrors are described in [66].
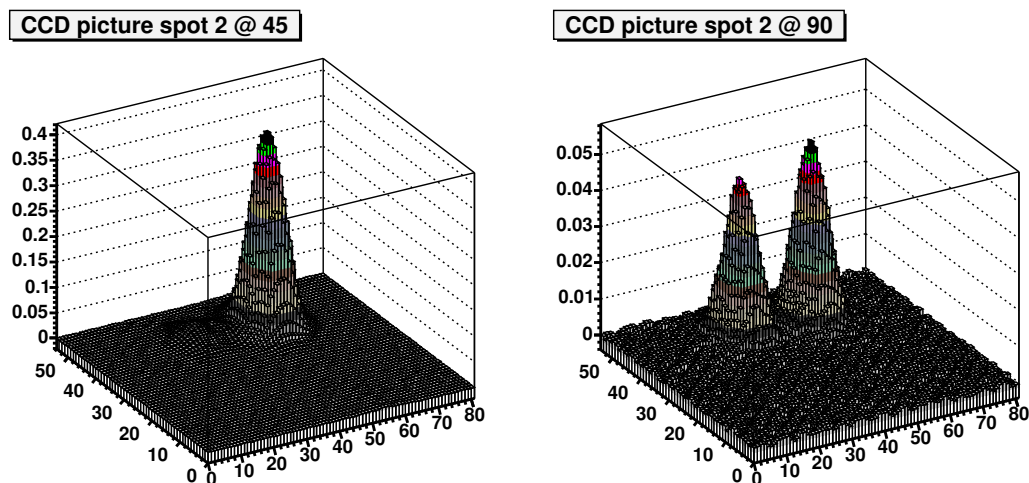
Abbildung 3.24.: Experimental verification of the influence of polarization on the reflection behaviour of the AT mirrors [66]. The left diagram shows the case for circularly polarized light, whereas the right diagram is the result for p polarization.

The radiation hardness of the optical components has been tested together with those for the BS (section 3.1.2). The results are identical and it can be concluded that all mirrors are suitable for the laser alignment system of the CMS tracker.

3. Beamsplitters

4. Alignment Sensors

The same modules, which detect particle tracks, are also used to read out the signal induced by the laser beams. In addition to the modification of the silicon sensor aluminium backplane, as already shown in figure 2.12, the light transmission of the alignment sensors has to be optimized.

In particular the LAS sensors should provide:

1. Sufficient light transmission to reach the next sensor layer.

2. Uniform transmission and thus absorption (signal generation) over the area transparent to laser light (figure 2.12).

3. Minimal reflection losses or effects from back-reflection on subsequent modules.

The application of an additional anti-reflex-coating (ARC) on the sensor surface was the key to satisfy the above list of requirements. To optimize the ARC it was necessary to understand the optical properties of the silicon sensor and the influence of the coating on laser light reflection (R), transmission (T), and absorption (A).

With the help of the matrix formalism of appendix H, a model to calculate T,R,A for the silicon sensors has been developed. The model is explained in the first part of this chapter, including the effects of the diffraction grating formed by the sensor strips, and describes the influence of the ARC. Finally, the results of the model are compared to transmission and reflection measurements.

4.1. Sensor Coating

Standard alignment sensors have been delivered by Hamamatsu [68]. These are uncoated sensors with an aluminium free zone on their backplane. Their optical properties have been measured for $\lambda = 1064 \ nm$ with transmission and reflection data taken by scanning the backside of the sensor in a direction perpendicular to the strips. T and R data have been measured separately and are shown in figure 4.1. No care was taken for the reproducibility of the positioning of the sensor in the setup and hence the anticorrelation of T and R is not evident.

From figure (4.1) it can be seen that both T and R values are very sensitive to the particular position on the sensor. Interference effects result in large variations, e.g. changes in R from 15 % to 50 %. This can be understood by calculating the interference between laser rays reflected at the front and back of the silicon layer. It is found that the reflected

4. Alignment Sensors
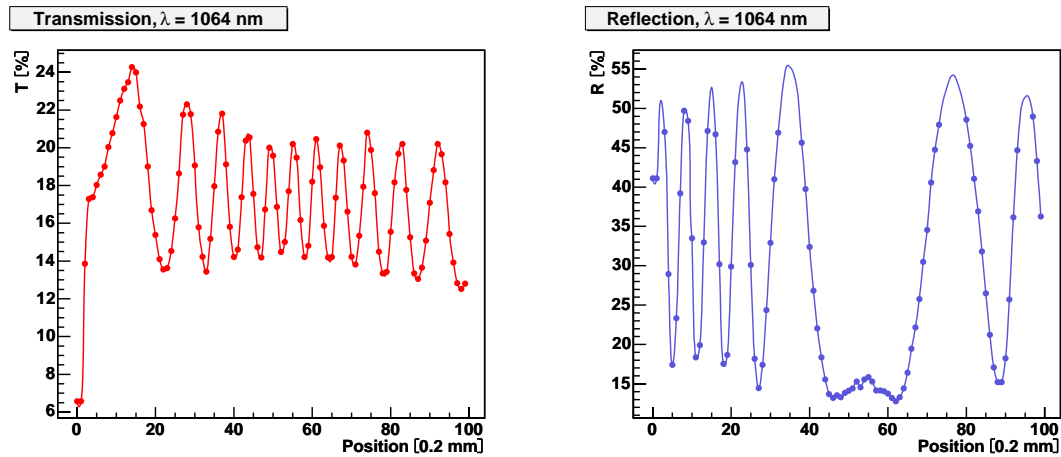
(a) Uncoated R4 sensor, transmission varia-
tions.

(b) Uncoated R4 sensor, reflection variations

Abbildung 4.1.: Reflection R and transmission T of laser light for an uncoated R4 alignment sensor as a function of the laser spot position.

intensity is sensitive to thickness variations of the silicon layer of the order of $\frac{\lambda}{4 \cdot n_{Si}} \approx$ 100 nm [44].

The specification on the sensor flatness requires that bending over the total length should be less than 100 μm [52]. Thus the surface quality of approximately 1 μm over 1 mm is not adequate for LAS purposes and interference patterns can be observed.

Operating a LAS with sensors having large differences in T,R,A would be very difficult, since each beam would require separate tuning for each layer and small beam movements would result in large intensity variations. In addition, back-reflections from downstream sensor layers could disturb the laser signal in the module being read out.

To improve the optical properties of the alignment sensors an anti-reflex-coating has been applied in the transparent backplane area by mso jena [69].

Attempts to coat both the ohmic and the strip sides resulted in large changes of the intrinsic properties of the silicon sensors. In particular, the interstrip resistance R_{int} is lowered by several orders of magnitudes, so that the electrical separation between the strips is severely reduced, making the sensor useless for tracking purposes.

With backside coating alone (see figure 4.2), the electrical properties stay within the allowed range ($R_{int} > 1.5$ $G\Omega$, 1 $M\Omega < R_{poly} < 2.2$ $M\Omega$) and remain stable.

In this respect, precautions were taken regarding the handling of the sensors during the coating process to avoid any charge accumulation effects. The electrical stability of the coated sensors was controlled by measuring R_{int}, R_{poly} and by comparing their IV-curves before and after coating (see figure 4.3).

The coating on the transparent area of the sensor backplane consists of a 95 nm Ta$_2$O$_5$ layer followed by a 94 nm SiO$_2$ (see figure 4.2) [69].

In total 560 R4 and 320 R6 sensors have been subjected to this procedure.
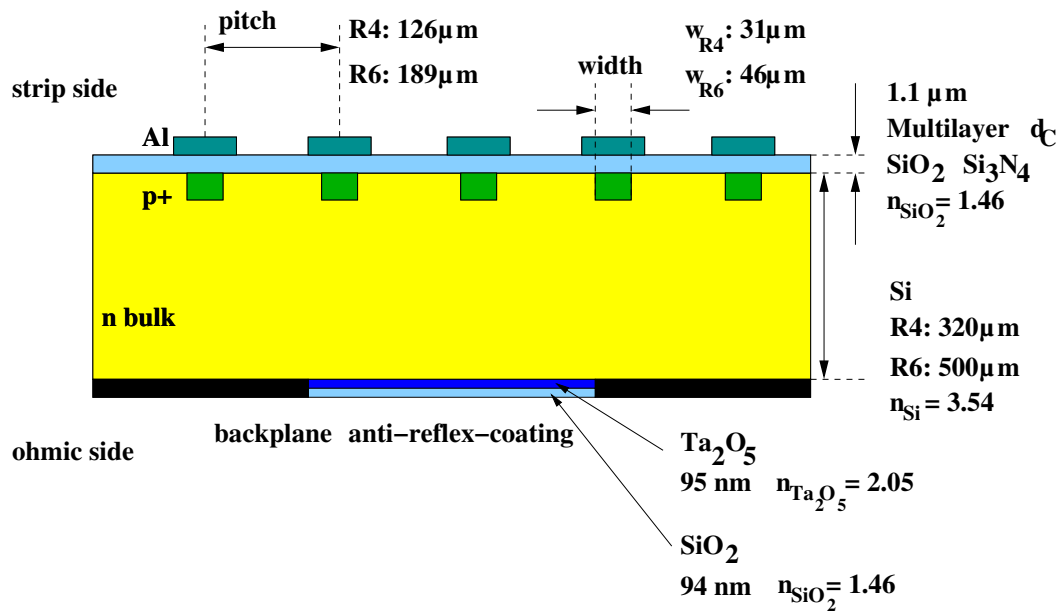
Abbildung 4.2.: Cross section of an alignment sensor with anti-reflex-coating. The sensor layout has been taken from [51], [52] and the given parameter values have been used for all theoretical calculations. The backplane coating consists of two layers, 95 nm Ta$_2$O$_5$ and 94 nm SiO$_2$.
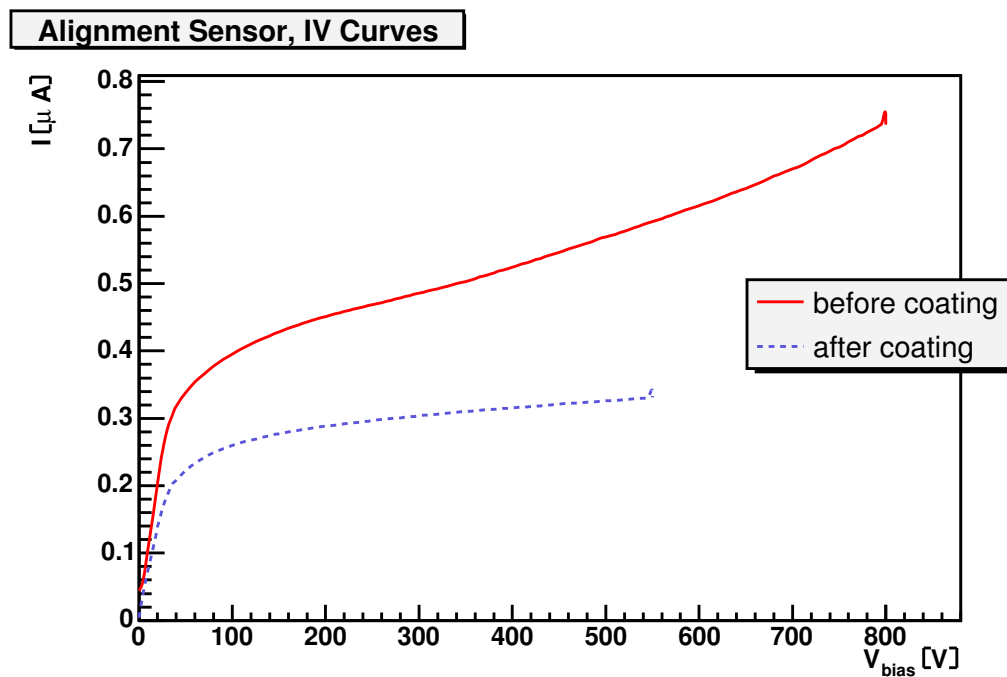

Abbildung 4.3.: A typical IV-curve from the quality control of an alignment sensor before and after anti-reflex-coating.

67

4.1.1. Absorption Coefficient

The amount of infrared laser light absorbed in the alignment sensors must be sufficient to generate the signal, but enough light has to traverse the silicon to reach the next module layer.

A first approximation of light absorption is to neglect reflection and calculate the intensity loss[1] according to

$$I(d) = I_0 \, e^{-\alpha d}, \tag{4.1}$$

where d is the silicon thickness. The absorption coefficient α was taken to be $10 \; cm^{-1}$. For R4 (R6) sensors 27.4 % (39.3 %) of the incident intensity is absorbed.

A more detailed theory describing light absorption in silicon is given by [70]. Several contributions to the interaction between light and silicon have been taken into account and are calculated as function of the wavelength at different temperatures. Using this model, figure 4.4 shows that less absorption is expected at lower temperatures, e.g. for the tracker operating conditions.
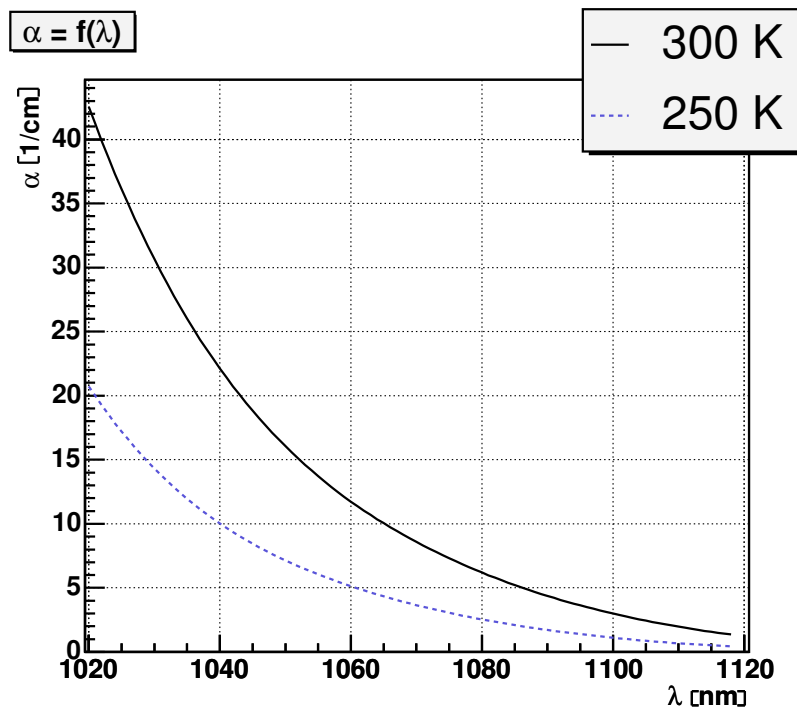
Abbildung 4.4.: Absorption coefficient α as function of the wavelength λ for temperatures 250 K and 300 K [70].

---

[1] same as equation (H.21) from appendix H

4.1.2. Diffraction Grating Influence and Applied Matrix Model

The aluminium strips of the sensors act as a diffraction grating for the laser beam. The intensity I varies as a function of the angle θ according to

$$I(b, p) = I_0 \cdot \frac{\sin^2\left(\frac{\pi b \sin(\theta)}{\lambda}\right)}{\left(\frac{\pi b \sin(\theta)}{\lambda}\right)^2} \cdot \frac{\sin^2\left(\frac{N \pi p \sin(\theta)}{\lambda}\right)}{\sin^2\left(\frac{\pi p \sin(\theta)}{\lambda}\right)} \tag{4.2}$$

where p is the strip pitch ($p_{R4} = 126 \ \mu m$, $p_{R6} = 189 \ \mu m$), b the slit width ($b_{R4} = 86 \ \mu m$, $b_{R6} = 128 \ \mu m$) and N the amount of strips covered by the laser beam ($N_{R4} = 10$, $N_{R6} = 6$).

The diffraction patterns for R4 and R6 sensors are shown in figure 4.5. Due to the larger pitch the first order maxima are closer to the main peak for R6 than for R4. As the distance of the light source from the sensor decreases, the separation of the main peak (zero order maximum) from secondary maxima becomes more difficult. This contributes to the module resolution of the laser spot, as described in chapter 5.

When measuring T,R,A the distances were choosen so that only the intensity of the central maximum was detected by the CCD camera. This was also taken into account in the calculations and therefore the sum $T + R + A$ is less than one, both for experimental and for simulated data.

$$T + R + A < 1 \tag{4.3}$$

The intensity contributing to the interference pattern is the fraction g_{alu} of light passing the strips:

$$g_{alu} = \left(1 - \frac{w}{p}\right) - \frac{w}{p} \cdot 2 \cdot 0.15 = 0.675 \tag{4.4}$$

This factor includes the constant strip width to pitch ratio $\frac{w}{p} = \frac{1}{4}$ as well as the metal overhang of 15 % on each side of the strip (see figure 4.2).

The ratio of the integral over the main peak of the diffraction pattern (figure 4.5) to the total intensity passing the grating[2] leads to a factor of $g_{int} = 0.6$, both for R4 and for R6 sensors.

Therefore a maximum value for transmission is given by

$$g_{int} \cdot g_{alu} \approx 0.4 \tag{4.5}$$

---

[2]integration from $-\pi/2$ to $\pi/2$

4. Alignment Sensors

The T,R,A characteristics of the alignment sensors mainly depend on

- Wavelength λ, $T, R, A = f(\lambda)$.

- Surface quality, in particular the unevenness Δd_{Si}.

- Thickness of the dielectric SiO_2 layer, d_C.

- Thickness of the silicon, d_{Si}.

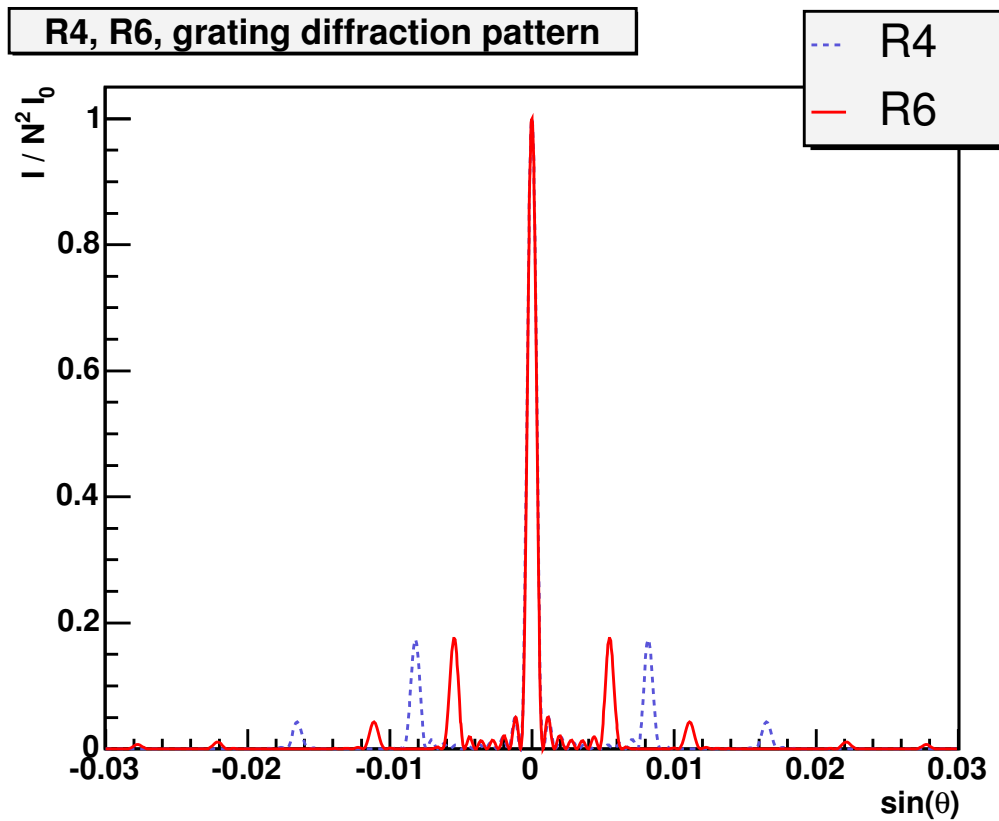The differences between coated (C) and uncoated (UC) sensors are discussed in the following subsections.

Abbildung 4.5.: Comparison of both diffraction patterns, R4 (blue, dashed line) and R6 (red). Due to the larger pitch of R6, the secondary maxima are closer to the main peak than for R4, which becomes important for the resolution.

The applied matrix model of appendix H is based on wave propagation through layered media. Each separate layer including its optical properties, is described by a matrix M . Since the light transfer calculation through a multilayer system is factorized, transmission and reflection amplitudes are obtained by multiplication of the corresponding matrices (see figure H).

Starting with the definition of matrices and optical parameters, preliminary values for T,R,A are calculated. The model takes into account the influence of diffraction caused by the sensor strips and leads to a theoretical prediction of the optical properties of the alignment sensors. The different steps of the calculation are briefly outlined below.
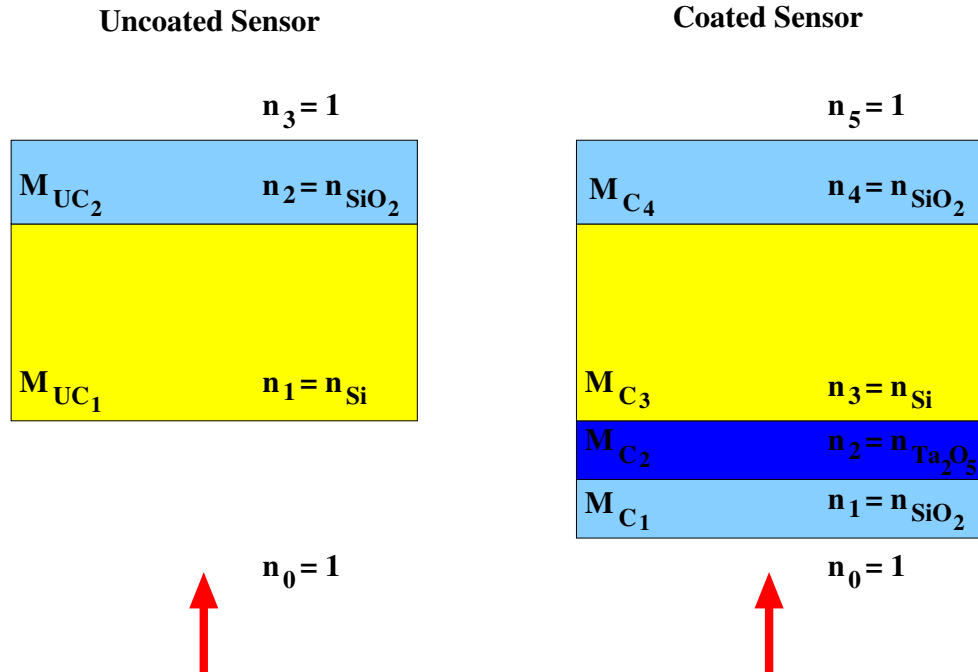
Abbildung 4.6.: Every layer is described in optics theory by a separate matrix M.

1. Definition of the matrices according to equation (H.49) and figure 4.6:

$$\mathbf{M_{UC}} = \mathbf{M_{UC_1}} \cdot \mathbf{M_{UC_2}} \tag{4.6}$$
$$\mathbf{M_C} = \mathbf{M_{C_1}} \cdot \mathbf{M_{C_2}} \cdot \mathbf{M_{C_3}} \cdot \mathbf{M_{C_4}} \tag{4.7}$$

and of all parameters used in the calculations:

- Silicon thickness:
  $d_{Si_{R4}} = 320 \ \mu m$
  $d_{Si_{R6}} = 500 \ \mu m$

- Dielectric (SiO$_2$) thickness:
  $d_C = 1.1 \ \mu m$

- Coating layer (SiO$_2$, Ta$_2$O$_5$):
  $d_{Ta_2O_5} = 95 \ nm$
  $d_{SiO_2} = 94 \ nm$

- Refraction indices:
  $n_{Si} = 3.54$
  $n_{SiO_2} = 1.46$
  $n_{Ta_2O_5} = 2.05$

- Temperature:
  $T = 300 \ K$

4. Alignment Sensors

2. Preliminary values T_p, R_p, and A_p (equation H.48) are determined for vertical beam incidence by neglecting the sensor strips. The calculations take into account the dependence of the absorption coefficient α on the wavelength, as given in figure 4.4.

$T_p = |t|^2$
$R_p = |r|^2$
$A_p = 1 - T_p - R_p$

3. The transmitted intensity has to be corrected for the part reflected back by the aluminium strips, which is assumed to be completely absorbed in the silicon due to diffuse scattering.

$T_p' = T_p \cdot g_{alu}$
$A_p' = A_p + T_p \left(1 - g_{alu}\right)$

The reflected and transmitted intensity is multiplied by the factor g_{int} to account for the fact that only the main peak of the diffraction pattern is detected.

The calculation of the transmission, reflection, and absorption of the alignment silicon sensors finally leads to:

$T = T_p \cdot g_{alu} \cdot g_{int}$
$R = R_p \cdot g_{int}$
$A = A_p'$

4.1.3. T,R,A as Function of Wavelength

Application of the theory leads to the following results for R4 and R6 alignment sensors. Diagrams on the left side refer to uncoated sensors, while those on the right side to sensors with anti-reflex-coating.
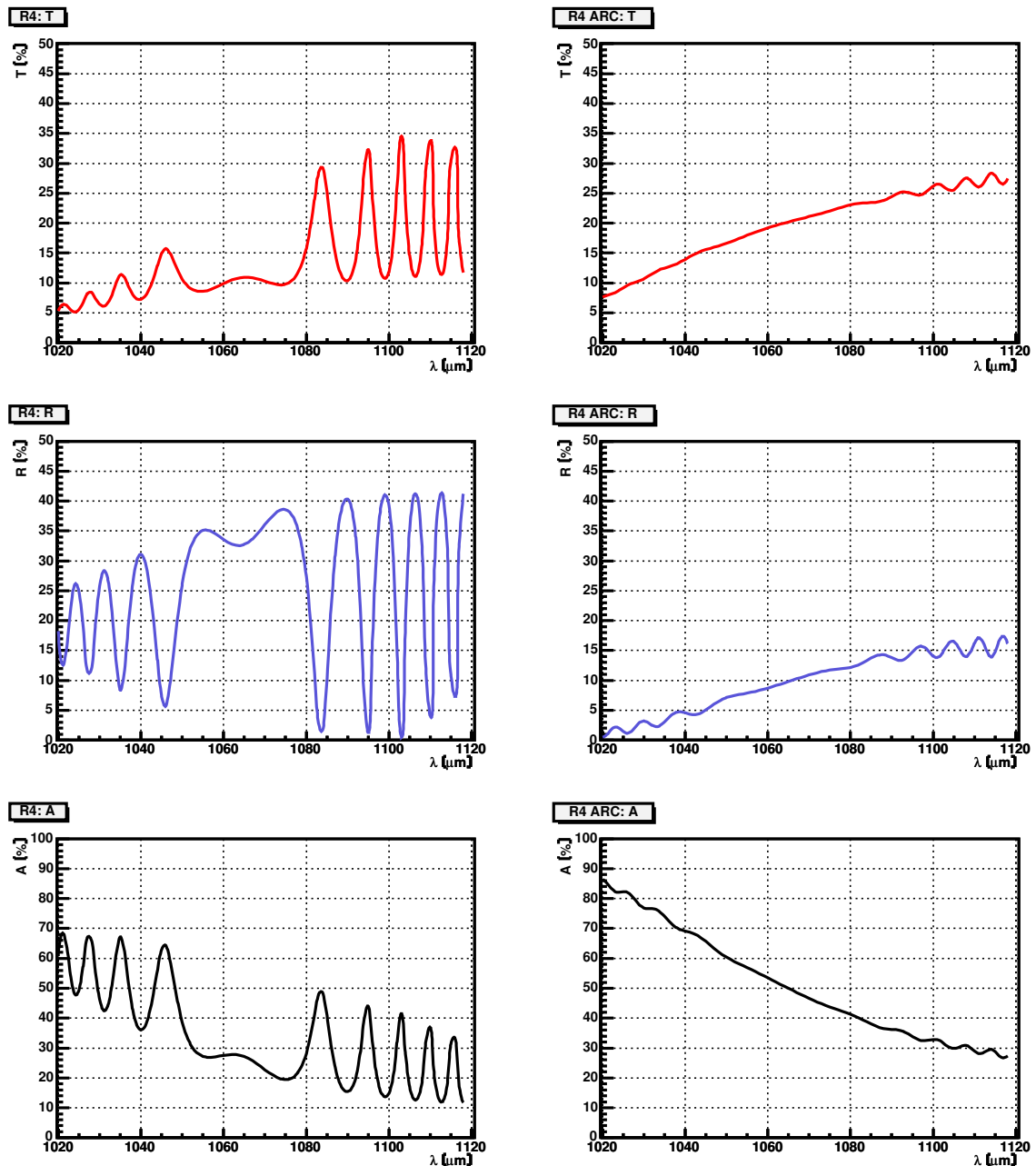
Abbildung 4.7.: Simulation: T,R,A as functions of wavelength λ, for uncoated (UC) *left* and coated (C) *right* R4 sensors. By application of an ARC layer on the sensor backplane large T,R,A variations are reduced and show a smooth behaviour as functions of λ.

73
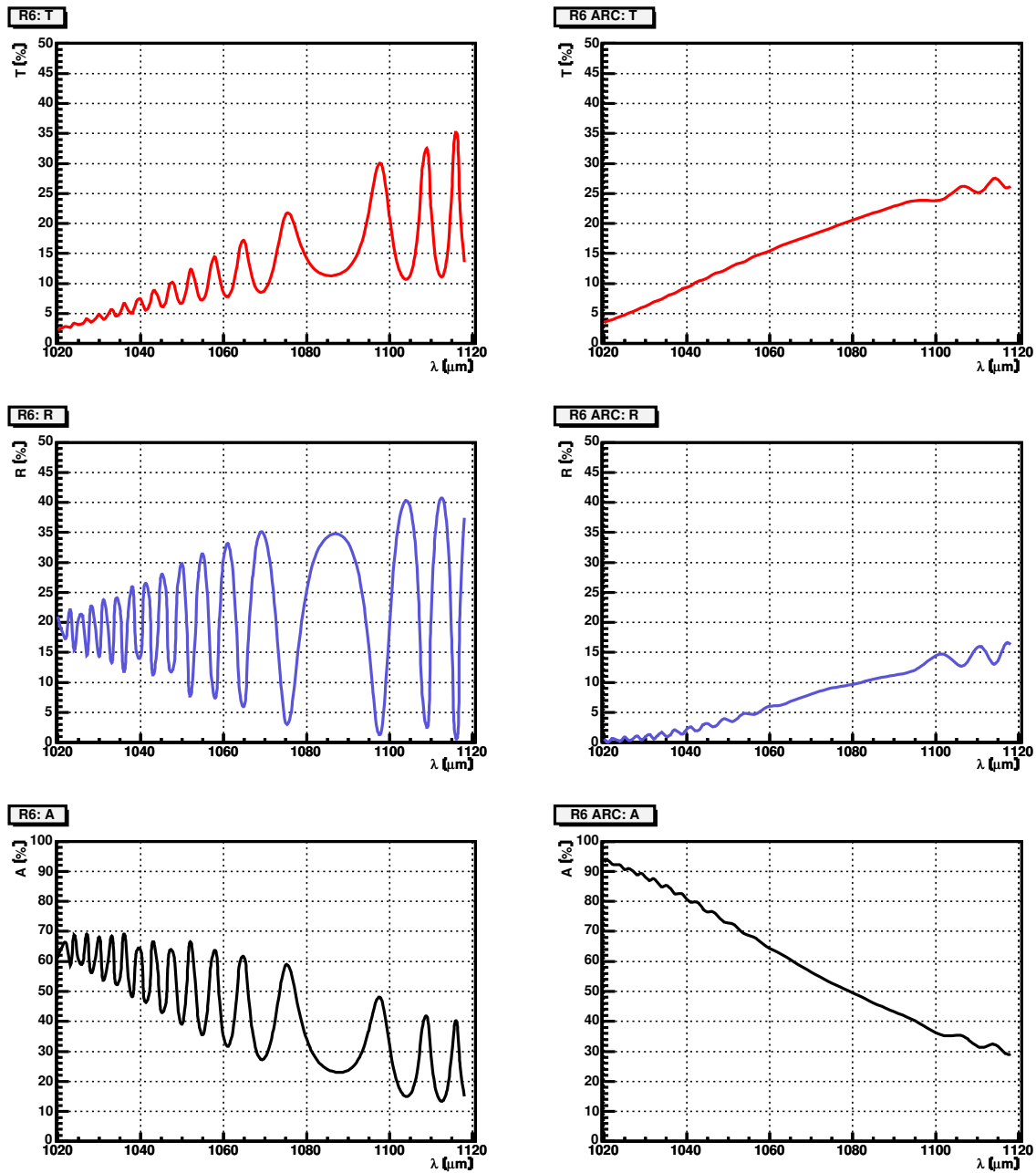
Abbildung 4.8.: Simulation: T,R,A as functions of wavelength λ, for UC *left* and C *right* R6 sensors. The same improvement as for R4 can be seen also for R6.

It is obvious, that large variations in T,R,A as a function of wavelength exist due to interference effects. The latter disappear after application of the ARC and T,R,A become smooth functions of the wavelength.

The data of T,R,A for uncoated and coated R4 and R6 sensors as functions of wavelength are combined in figure 4.9. Here and in the follwing subsections transmission is the solid, reflection the dashed and absorption the dotted line.
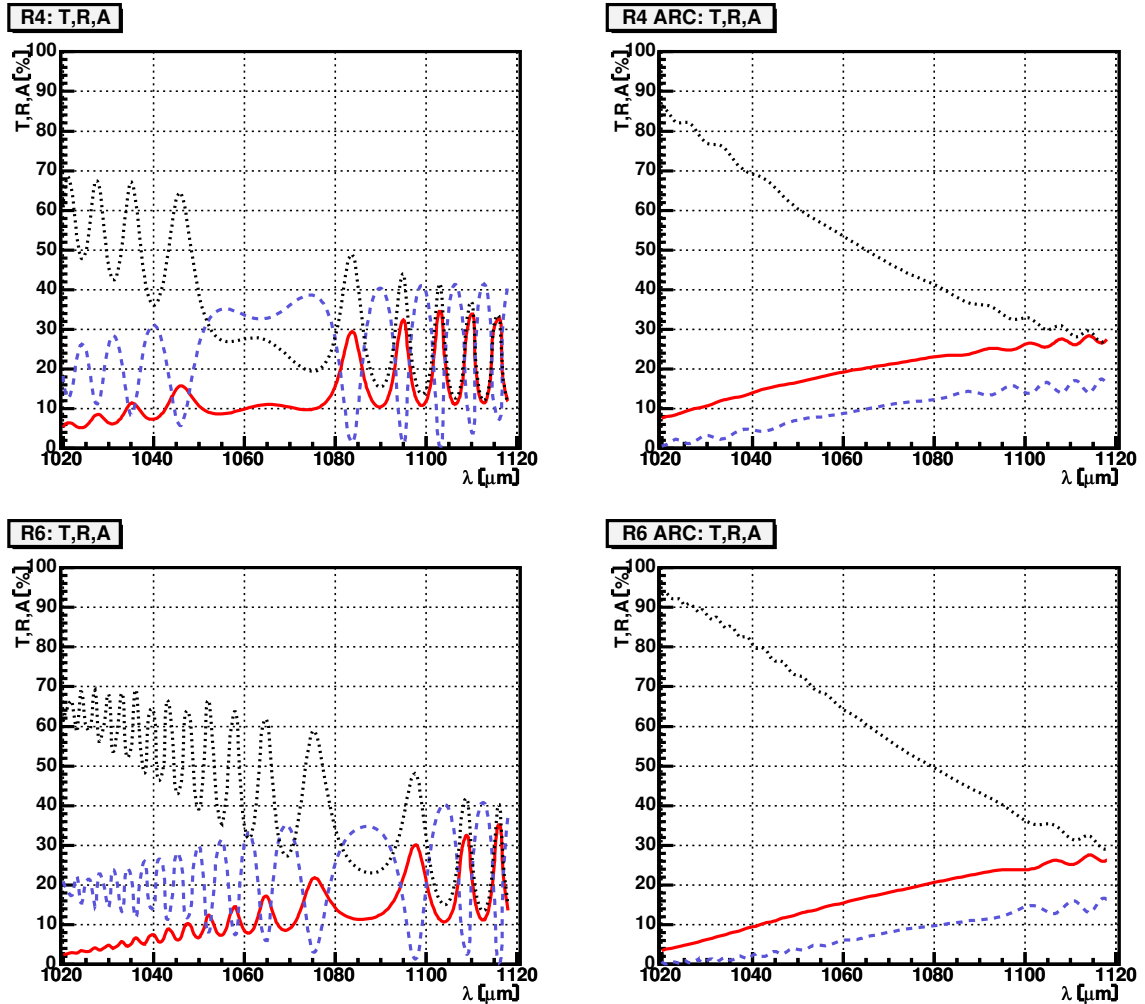
Abbildung 4.9.: Combination of T, R, and A simulations for R4, R6, as function of wavelength λ for UC *left* and C *right* sensors. The infrared region optimized ARC minimizes reflection and interference caused by different layers of same optical thickness. The result is an increased transmission, more for R4 than for R6 due to their sensor thickness.

Since reflection and interference are minimized by the ARC, transmission is increased, with the increase being greater for the thinner (R4) than for the thicker (R6) sensors, see also figure 4.12.

4.1.4. Dielectric Thickness Variations

Figure 4.10 shows the sensitivity of T,R,A on the SiO_2 thickness d_C for $\lambda = 1064\ nm$ and for d_C in the range $0.8\ \mu m$ to $1.8\ \mu m$.

Even after application of the ARC, a sinusoidal behaviour is seen. Unfortunately the sensor design has been frozen to include a $1.1\ \mu m$ SiO_2 layer, resulting in a transmission minimum and therefore in a reflection maximum. This is still valid in the infrared region used by the LAS, $\lambda = 1075 \pm 3.5\ nm$.

Small variations in the thickness of the dielectric ($\approx 100\ nm$) lead to changes in transmission and reflection of $\approx 3\ \%$. This can be a reason for the large variations in T and R of all measured sensors, independent of the delivery batch.
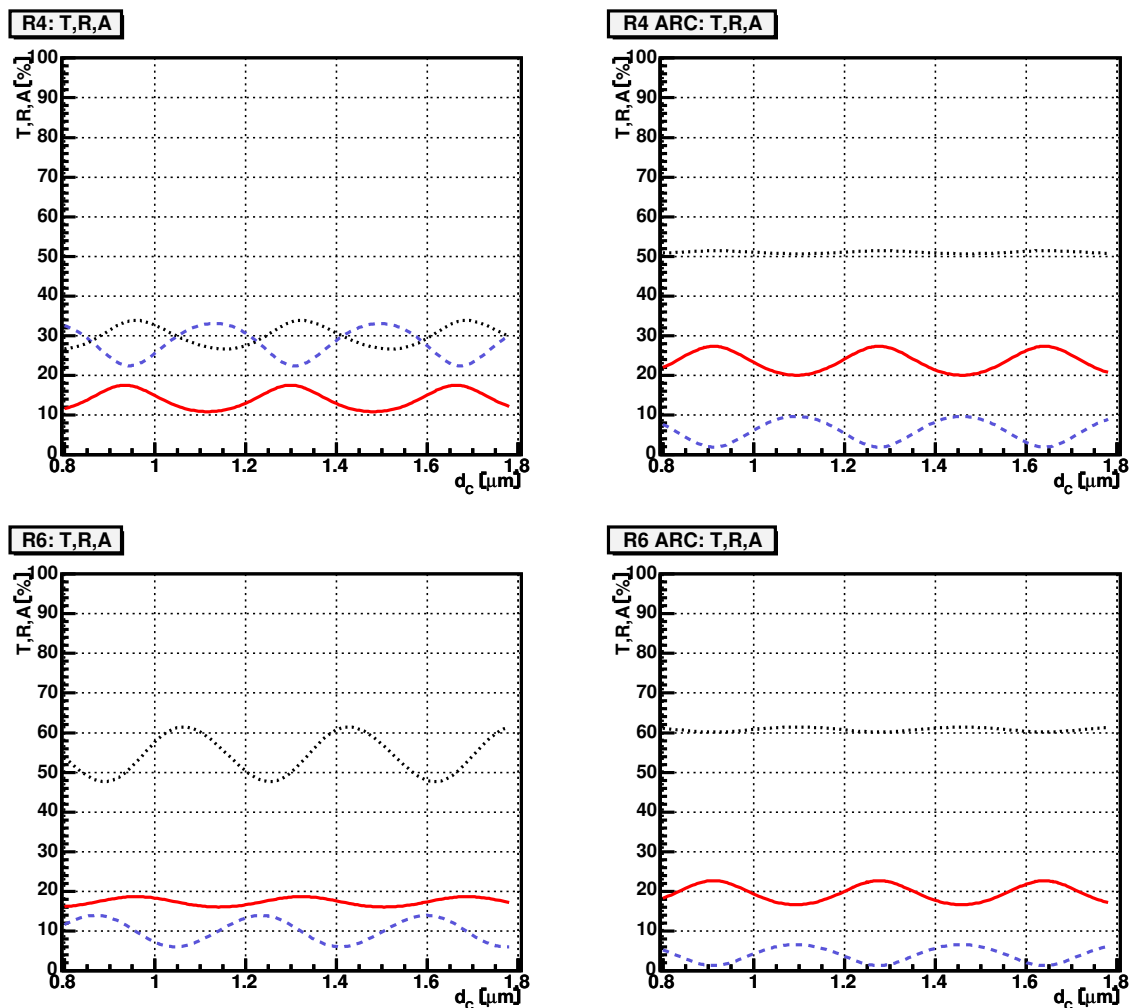
Abbildung 4.10.: Simulation: T,R,A dependence on capacitor thickness d_C, for UC *left* and C *right* R4 and R6 sensors. Enhancement in T and A has been achieved by the coating.

4.1.5. Silicon Surface Quality

As observed with the first measurements of uncoated sensors, minimal sensor thickness variations result in large changes of transmission. Calculation reproduces the effect, as shown in figure 4.11 for $\lambda = 1064\ nm$.

Unlike the dependence on the dielectric thickness, this can be completely eliminated by anti-reflex-coating.
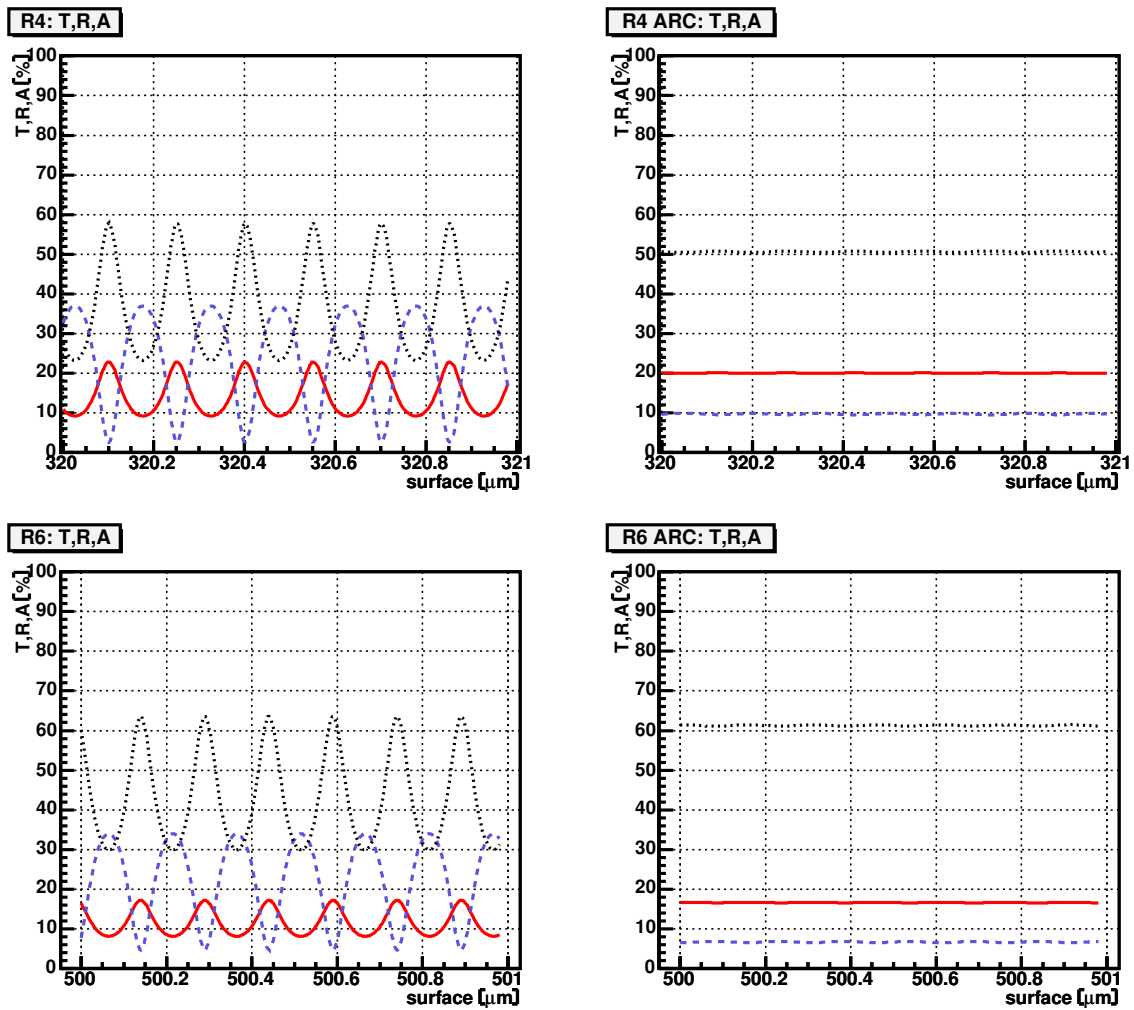
Abbildung 4.11.: Simulation: T,R,A dependence for R4 and R6 sensors on surface quality, i.e. thickness variations Δd_{Si} of the silicon sensors (R4: $d_{Si} = 320\ \mu m$, R6: $d_{Si} = 500\ \mu m$). UC *left* and C *right*.

4.1.6. Dependence on Silicon Thickness

As expected from equation (4.1) and shown in figure 4.12 for a wavelength of $\lambda = 1064\ nm$, absorption increases for a larger silicon thickness. Due to the interference effects mentioned before, T,R,A data for uncoated sensors show large variations, which are completely eliminated by ARC.
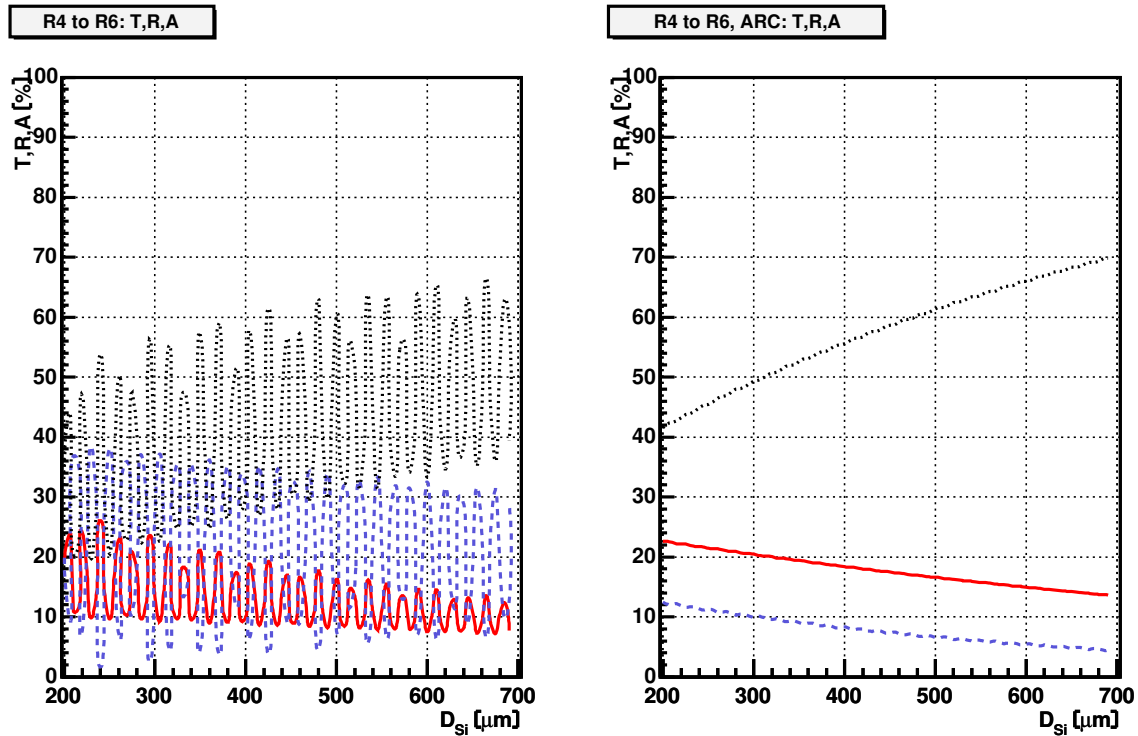
Abbildung 4.12.: T,R,A dependence on sensor thickness. Simulated thickness D_{Si} changes from R4, $d_{R4} = 320\ \mu m$ to R6, $d_{R6} = 500\ \mu m$ are shown. As expected, an increase in A and at the same time a decrease in T and R are observed.

4.2. Transmission and Reflection Measurement

In the previous section it has been described theoretically, how anti-reflex-coating can improve the optical properties of the alignment sensors. Differences between coated and uncoated sensors can be studied experimentally by scanning the relevant areas on their backside, as shown in figure 4.13.
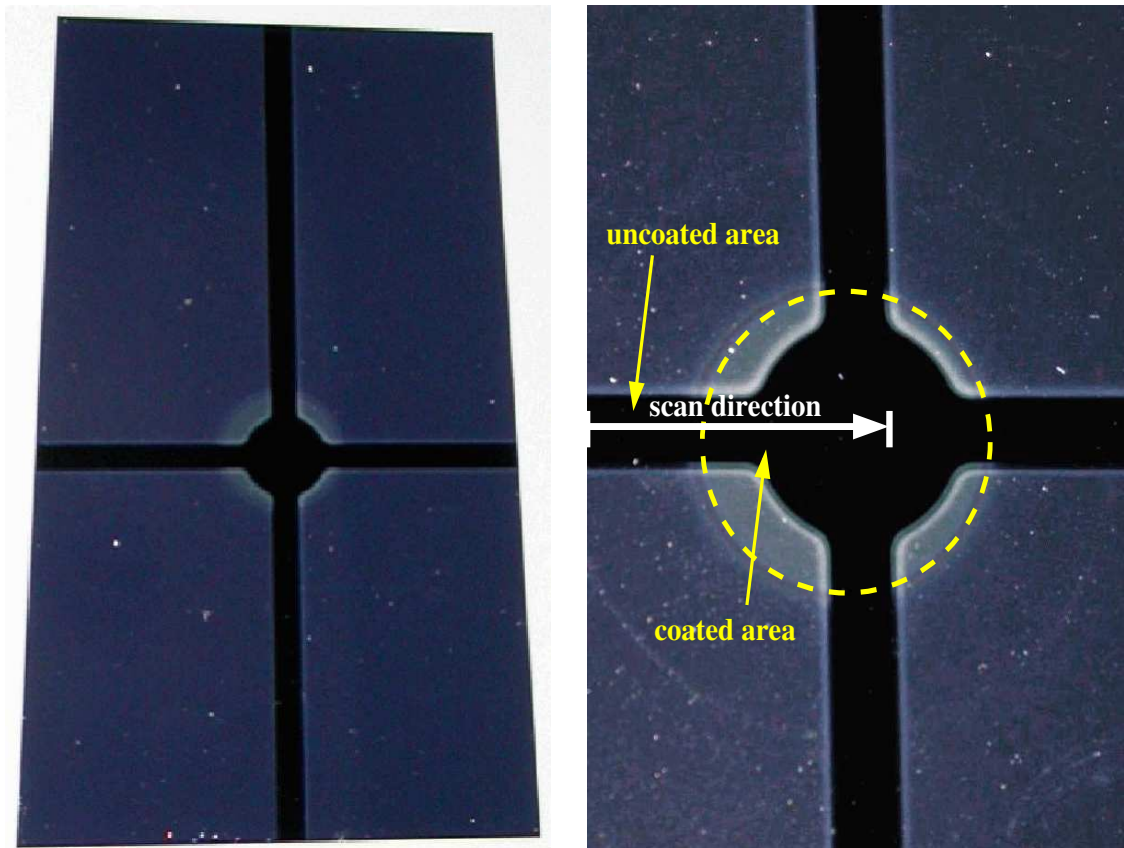
(a) Coated R4 sensor.

(b) Scan direction on the sensor backplane (white arrow) in the transition region from the uncoated to the coated area (dashed circle). The direction is perpendicular to the sensor strips.

Abbildung 4.13.: Backside scanning to measure the difference between the uncoated and the coated area. ARC has been applied only in the central part of the sensor backplane.

4. Alignment Sensors

4.2.1. Experimental Setup

The test setup has been designed to provide easy handling of R4 as well as R6 sensors and simultaneous measurement of T and R.

In the setup (figure 4.14) the sensor is mounted on an aluminium support with a teflon surface to prevent scratches on the silicon. Mounting pins, as marked in picture 4.15, define the positions of R4 (figure 4.16(a)) and R6 (4.16(b)) sensors and an area of constant low pressure is generated via a venturi nozzle to guarantee a stable sensor fixation during data taking.

Two CCD cameras, CCD T and CCD R, are arranged at distances $d_T = 45$ cm and $d_R = 40$ cm to detect the main peak of the diffraction pattern of the transmitted and reflected laserlight. The diameter of the beam spot on the sensor surface is 1.2 mm.
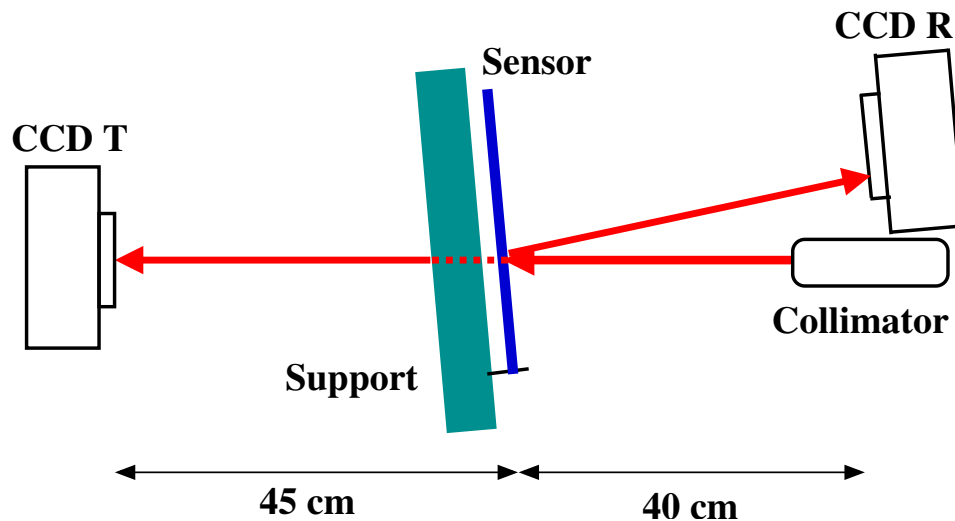
Abbildung 4.14.: Simultaneous measurement of transmission (CCD T) and reflection (CCD R)
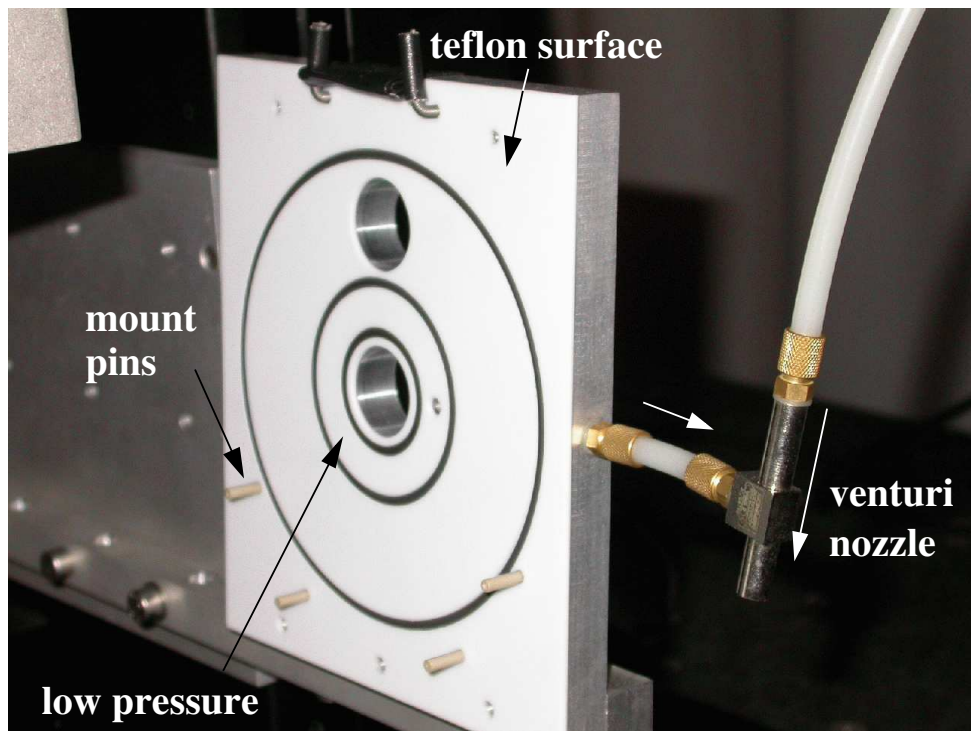
Abbildung 4.15.: Picture of the sensor support. Mounting pins are used to position the sensor and a venturi nozzle generates a circular low pressure area to keep the sensor in place during data taking.
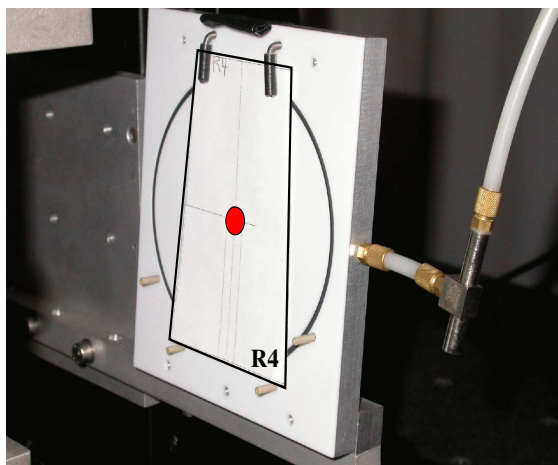
(a) R4 sensor placement
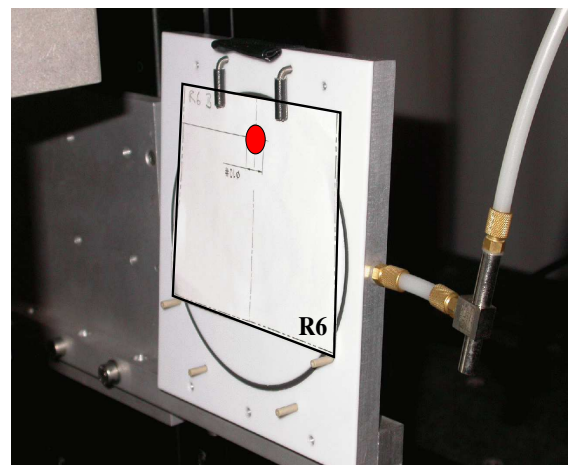
(b) R6 sensor placement

Abbildung 4.16.: The sensor support device has been designed so that both sensor geometries fit into the same experimental setup.

4. Alignment Sensors

The data taking procedure was divided into two steps.

1. Measurement of the intensity without sensor (figure 4.17), both for CCD T and CCD R.

2. Simultaneous measurement of the transmitted and reflected intensity (an example is shown in figure 4.19) over the area indicated in figure 4.13(b). Data has been taken at three different wavelengths: $\lambda_1 = 1050\ nm$, $\lambda_2 = 1064\ nm$, and $\lambda_3 = 1083\ nm$.

As already mentioned in chapter 3 the CCD chip has an overall size of $6.4 \times 4.8\ mm^2$. To be able to detect the transmitted and reflected laser spots at distances of $40\ cm$ and $45\ cm$, precise adjustment of the CCD camera and stable fixation of the silicon sensor were essential.

In the data analysis a 2D gaussian fit procedure has been applied to determine the transmitted and reflected intensity as well as the intensity without sensor. The advantage of the fit procedure was that beam spots partially covering the CCD chip could also be analyzed. The data were analyzed online and several steps were taken to guarantee stability of the fitting method.

Starting with a transformation of the CCD picture into a 800×520 2D histogram, a rebinning procedure was applied to gain two 2D histograms of size 80×52:

- h_{data}: A rebinned 2D histogram including all entries, as shown in figures 4.17 and 4.19

- h_{mf}: To determine the mean values in h_{data}, only entries exceeding 25% of the maximum value are included; all others are set equal to 0.

For h_{mf} the mean values m_x and m_y are calculated and the fit ranges in x (y) are defined by moving either side of m_x (m_y) and counting the number of bins in x (y) until the value 0 is reached.

To gain good starting values for a 2D gaussian fit, the previous values have been used in h_{data} to generate 8 slice histograms in x and y symmetrically distributed around m_x and m_y. These were 8 1D vertical and horizontal histograms. By application of 1D gaussian fits over the previously defined ranges, the two histograms $h_{1D,x}$ and $h_{1D,y}$ having the largest amplitude ($a_1 \approx a_2 = a$) of the gaussian function were chosen (see figures 4.18 and 4.20). These represent a horizontal ($h_{1D,x}$) and vertical ($h_{1D,y}$) slice in h_{data}.

Both fitted widths σ_x and σ_y as well as the maximum height a have been used as starting values for the 2D gaussian fit of h_{data}.

$$I\left(x, y\right) = a \cdot e^{-\frac{1}{2}\left(\left(\frac{x-m_x}{\sigma_x}\right)^2 + \left(\frac{y-m_y}{\sigma_y}\right)^2\right)} \tag{4.8}$$

The integral of (4.8)

$$P = a \cdot \int\int e^{-\frac{1}{2}\left(\left(\frac{x-m_x}{\sigma_x}\right)^2 + \left(\frac{y-m_y}{\sigma_y}\right)^2\right)} dx\, dy = a\ 2\pi\sigma_x\sigma_y \tag{4.9}$$

is a measure of the laser spot intensity and was calculated both for CCD T and CCD R for each position of the laser spot on the alignment sensor. The fraction to the intensity values without sensor result in the measured transmission and reflection.
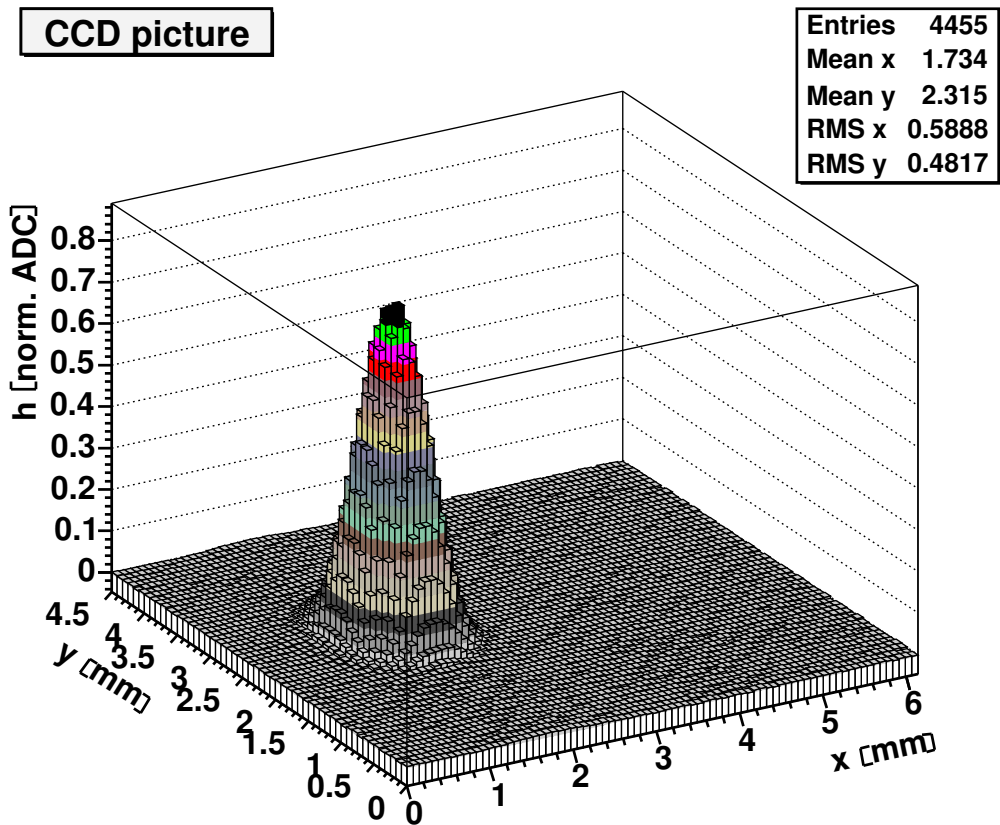
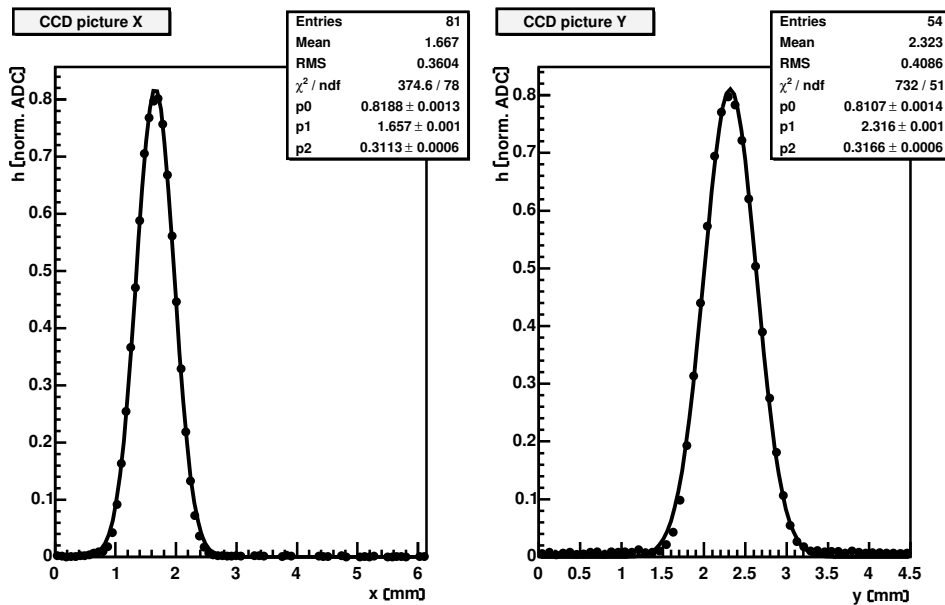Abbildung 4.17.: CCD picture of the laser spot without sensor.

Abbildung 4.18.: Without sensor: horizontal $h_{1D,x}$ and vertical slice histogram $h_{1D,y}$ with the 1D gaussian fit.
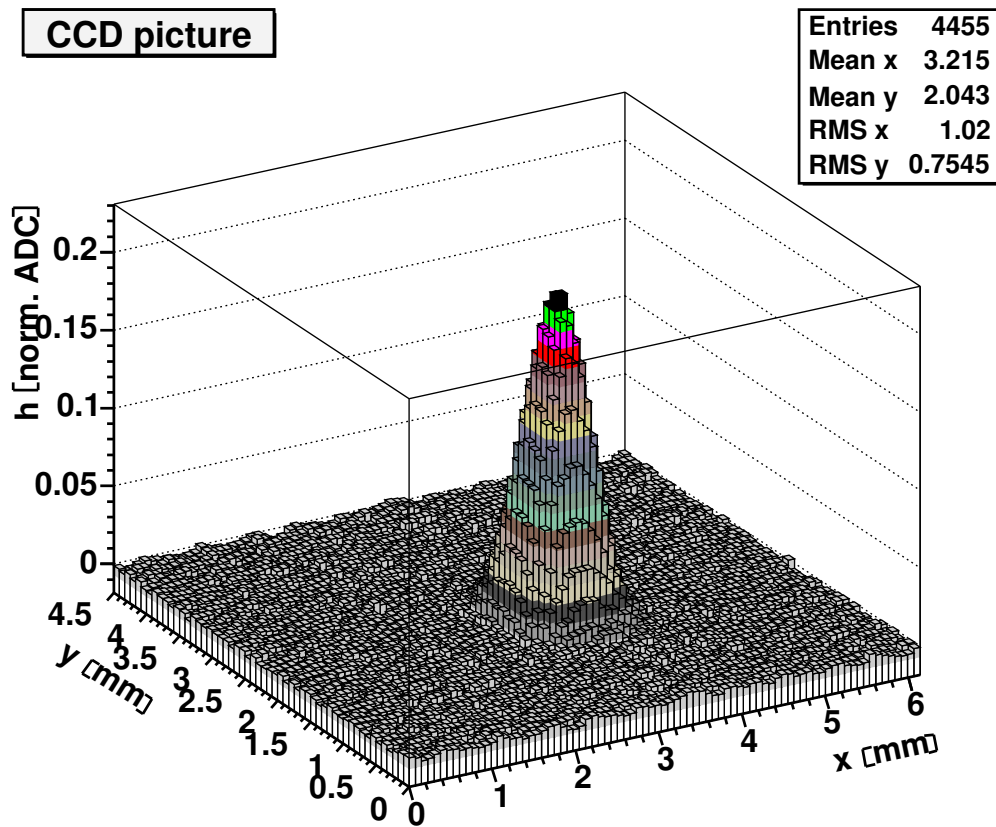
4. Alignment Sensors

Abbildung 4.19.: CCD picture of the laser spot with a sensor in front. Since the intensity is smaller, the CCD noise is also visible (rough surface).
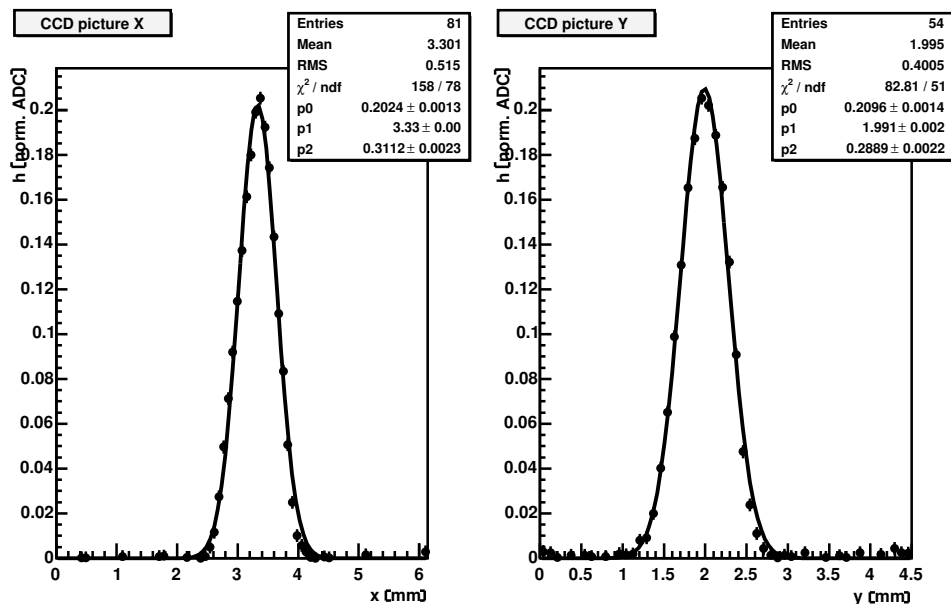

Abbildung 4.20.: With sensor: horizontal $h_{1D,x}$ and vertical slice histogram $h_{1D,y}$ with the 1D gaussian fit.

84

4.2.2. Results

Each R4 and R6 sensor has been measured at $\lambda_1 = 1050\ nm$, $\lambda_2 = 1064\ nm$ and $\lambda_3 = 1083\ nm$. The scan started in the uncoated region and the sensors were moved by a servomotor so that the transition to the coated zone was detected by the T and R CCD cameras. The absolute position of the sensor mount on the servomotor was precise in the range of 5 mm, thus in the following diagrams the transition region lies between 40 and 50 on the x-axis in units of 0.2 mm.
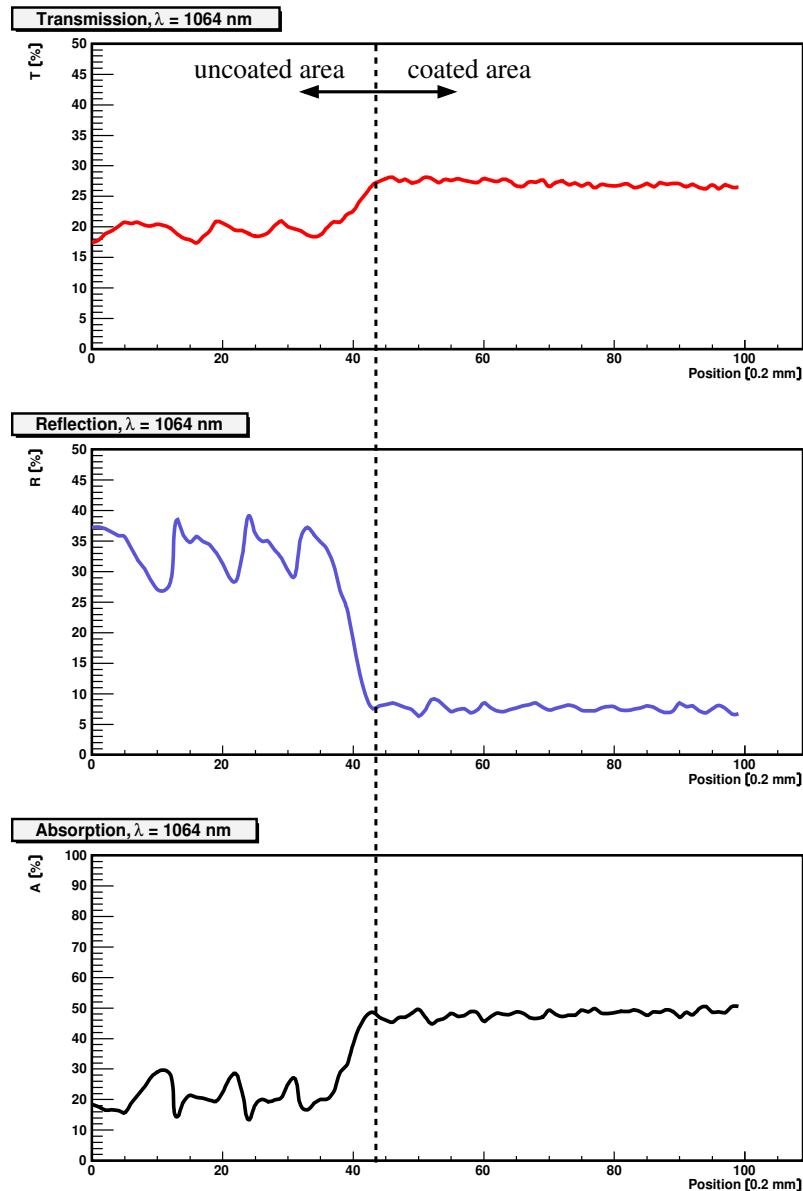
Abbildung 4.21.: R4 sensor: T,R,A data at $\lambda = 1064\ nm$.

4. Alignment Sensors

To resolve the surface pattern a few reference sensors have been measured using a small servomotor step of 0.2 *mm*. The results are shown in figures 4.21 and 4.22. In the coated area an increase in transmission and absorption as well as an decrease in reflection is obvious. Also the large variations in the uncoated area are much reduced. To speed up the measurement it was sufficient to use a 1 *mm* step for all other sensors.
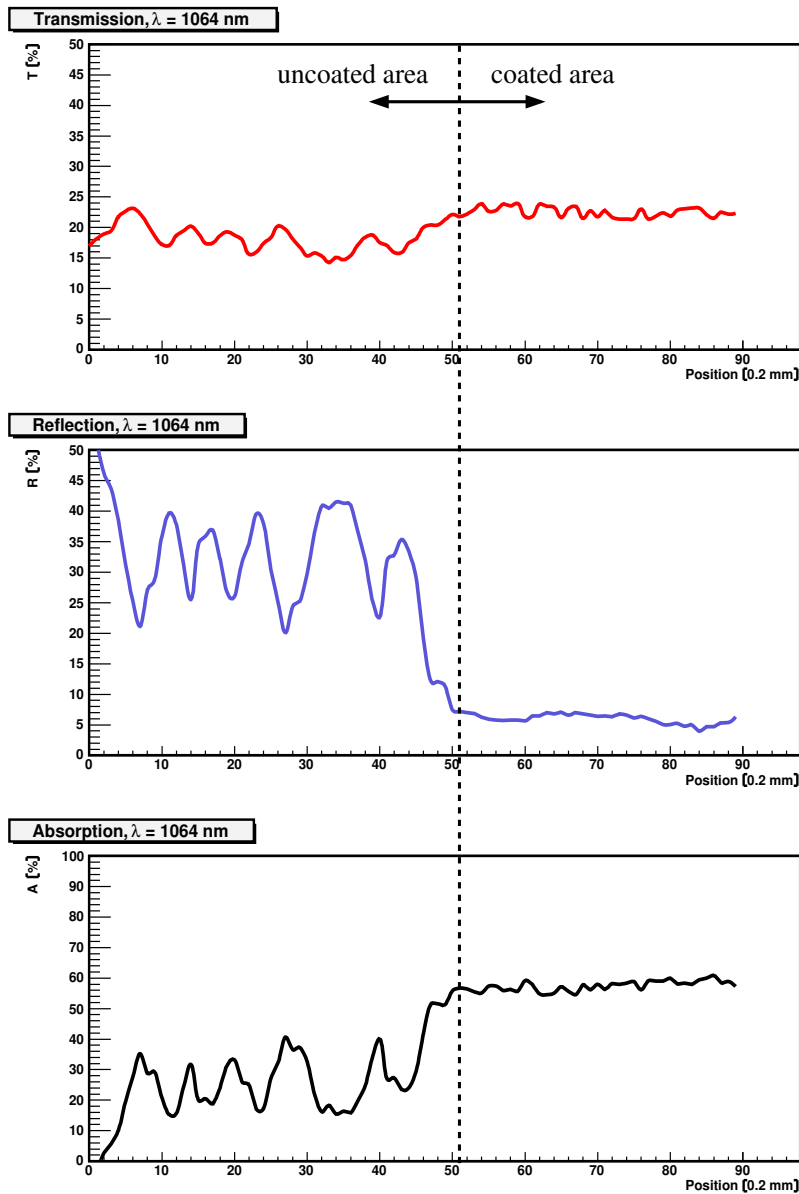

Abbildung 4.22.: R6 sensor: T,R,A measurement at $\lambda = 1064\ nm$.
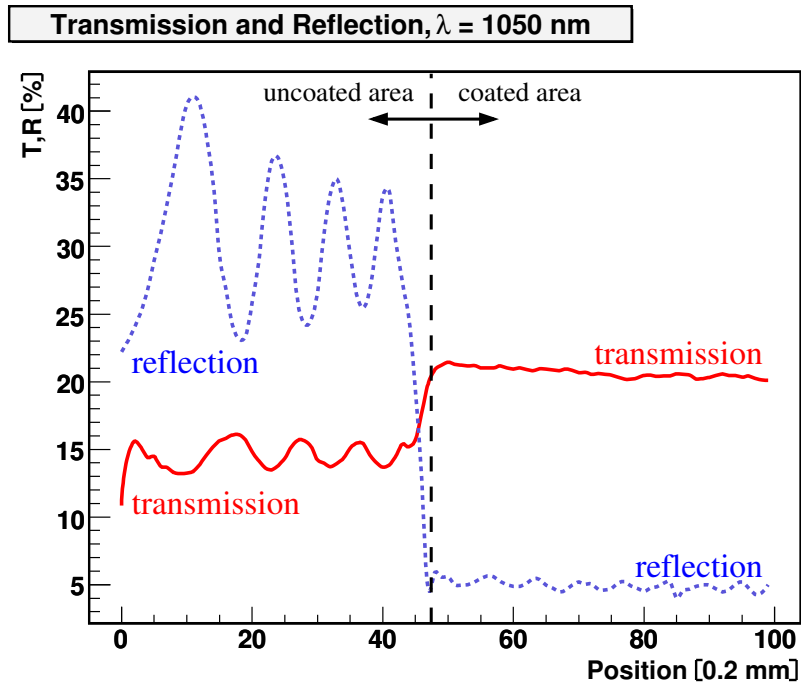
Abbildung 4.23.: R4 sensor: Transmission T (*solid line*) and reflection R (*dashed line*) data at $\lambda = 1050 \ nm$. Clearly visible is the anticorrelation between T and R as a function of the laser position on the sensor.

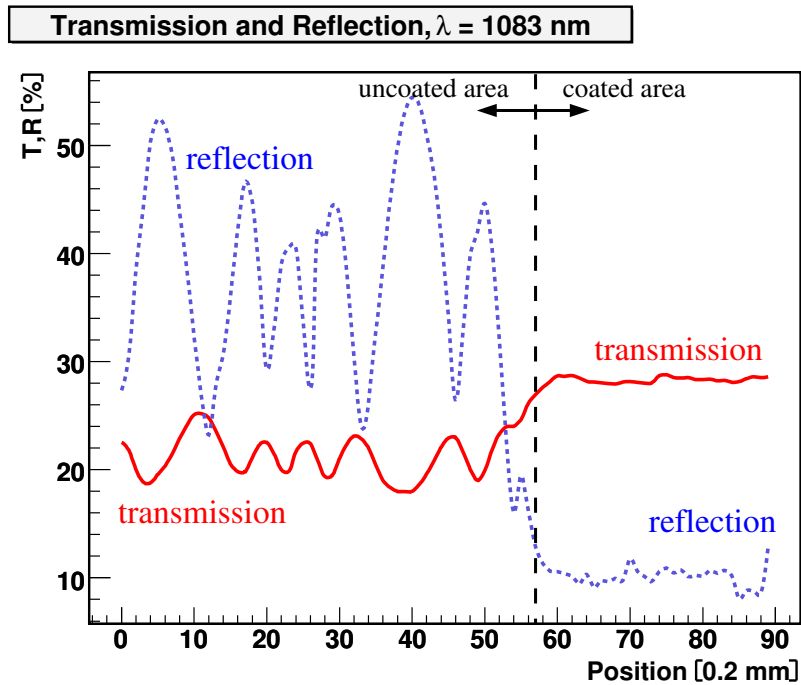Abbildung 4.24.: R6 sensor: T(*solid line*) and R (*dashed line*) data at $\lambda = 1083 \ nm$.

4. Alignment Sensors

Approximately 50 R4 and R6 sensors have been measured at three different wavelengths. In figures 4.23 and 4.24, where transmission (solid line) and reflection (dashed line) are shown in one diagram, the anticorrelation between T and R values is evident, high transmission corresponding to small reflection and vice versa.

To get a mean value of T and R the data in the uncoated and coated region have been separately fitted to a constant. This is of course an approximation for the UC region, where large variations are observed, but is quite reasonable for the C region. The distribution of the mean values obtained at $\lambda = 1064\ nm$ are shown in figure 4.25 for all R4 sensors and in figure 4.26 for all R6 sensors.
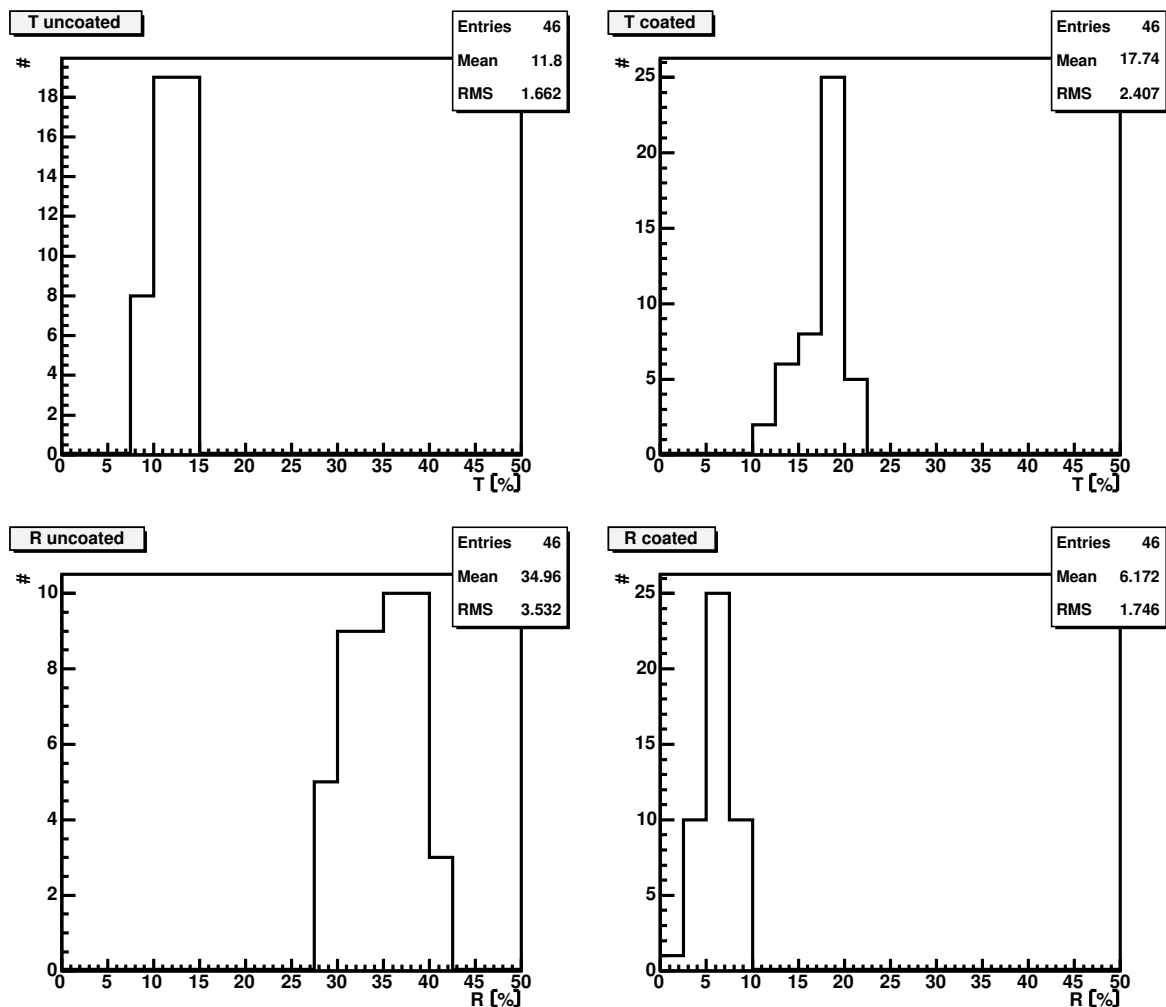

Abbildung 4.25.: R4 sensors: T,R distribution at $\lambda = 1064\ nm$. Transmission improvement: 11.8 % → 17.7 %; reflection minimization: 35 % → 6.2 %.

For the R4 sensors the transmission was improved from 11.8 % to 17.7 %, while at the same time reflection was reduced from 35 % to 6.2 %. Similar results were obtained for the R6 sensors, namely transmission improvement from 11.1 % to 16.1 % and reflection reduction from 30.5 % to 3.7 %.
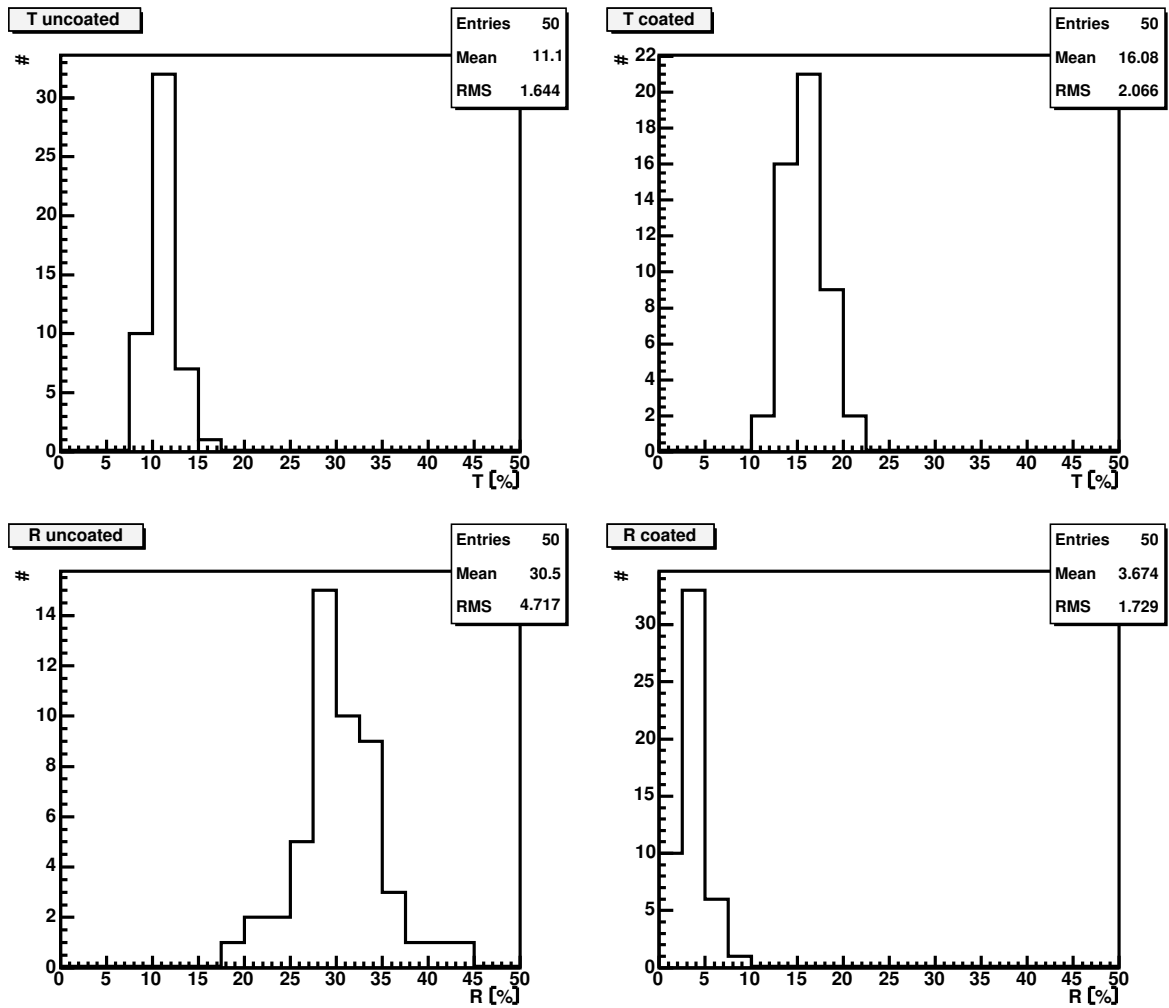
Abbildung 4.26.: R6 sensors: T,R distribution at $\lambda = 1064\ nm$. Transmission improvement: 11.1 % $\rightarrow$ 16.1 %; reflection minimization: 30.5 % $\rightarrow$ 3.7 %.

All alignment sensors show similar T,R,A distributions (e.g. figure 4.21) in the observed wavelength range, but even after coating the absolute values of transmission and reflection at a specific wavelength vary by a few percent. Thus these variations belong to intrinsic properties of each individual sensor and can be explained by differences of $\approx 100\ \mu m$ in the thickness of the dielectricum layer d_C (compare figure 4.10). Since the variation in d_C is not known exactly, the RMS values of the transmission and reflection distributions (figures 4.25 and 4.26) have been taken as the experimental error on T and R.

4.   *Alignment Sensors*

The results of the T and R measurements are summarized in tables 4.1 and 4.2, where the values predicted from the theoretical model as well as their difference to the results obtained for coated sensors (expressed in terms of the standard deviation σ), are also included. Comparison shows good agreement (within $\approx 2\sigma$) between measured and predicted values for both R4 and R6 alignment sensors.

Ring 4 Transmission and Reflection Distribution								
wavelength	uncoated		coated		theoretical		deviation	
λ [nm]	T [%]	R [%]	T [%]	R [%]	T [%]	R [%]	ΔT [σ]	ΔR [σ]
1050	9.0±1.3	31.3±2.3	13.5±1.9	3.9±1.5	16.6	7.1	1.6	2.1
1064	11.9±2.0	34.9±3.5	17.9±2.8	6.2±1.7	20.0	9.6	0.8	2.0
1083	13.9±2.3	32.8±4.7	20.9±3.3	7.4±2.9	23.4	13.0	0.8	1.9

Tabelle 4.1.: Experimental data and theoretical prediction for R4 transmission and reflection. Comparison of measured and predicted values for coated sensors is given in units of the experimental error σ.

Ring 6 Transmission and Reflection Distribution								
wavelength	uncoated		coated		theoretical		deviation	
λ [nm]	T [%]	R [%]	T [%]	R [%]	T [%]	R [%]	ΔT [σ]	ΔR [σ]
1050	7.9±1.2	34.7±2.0	11.5±1.5	2.2±4.3	12.6	3.7	0.7	0.3
1064	11.1±1.6	30.5±4.7	16.1±2.1	3.7±1.7	16.6	6.5	0.2	1.7
1083	14.3±2.1	35.9±4.2	20.5±2.6	5.1±2.7	21.3	10.2	0.3	1.9

Tabelle 4.2.: Experimental data and theoretical prediction for R6 transmission and reflection. Comparison of measured and predicted values for coated sensors is given in units of the experimental error σ.

In figure 4.27 the transmission and reflection properties of alignment sensors are shown as a function of wavelength before and after coating demonstrating again the significant improvement.

In conclusion, the alignment sensors are of high optical quality, achieved by application of an anti-reflex-coating. The goals of

- Minimization of reflection.

- Improvement of transmission and enhancement of signal (absorption).

- Reduction of interference effects.

- High surface quality, uniform transmission distribution in the center of the sensor backplane region.

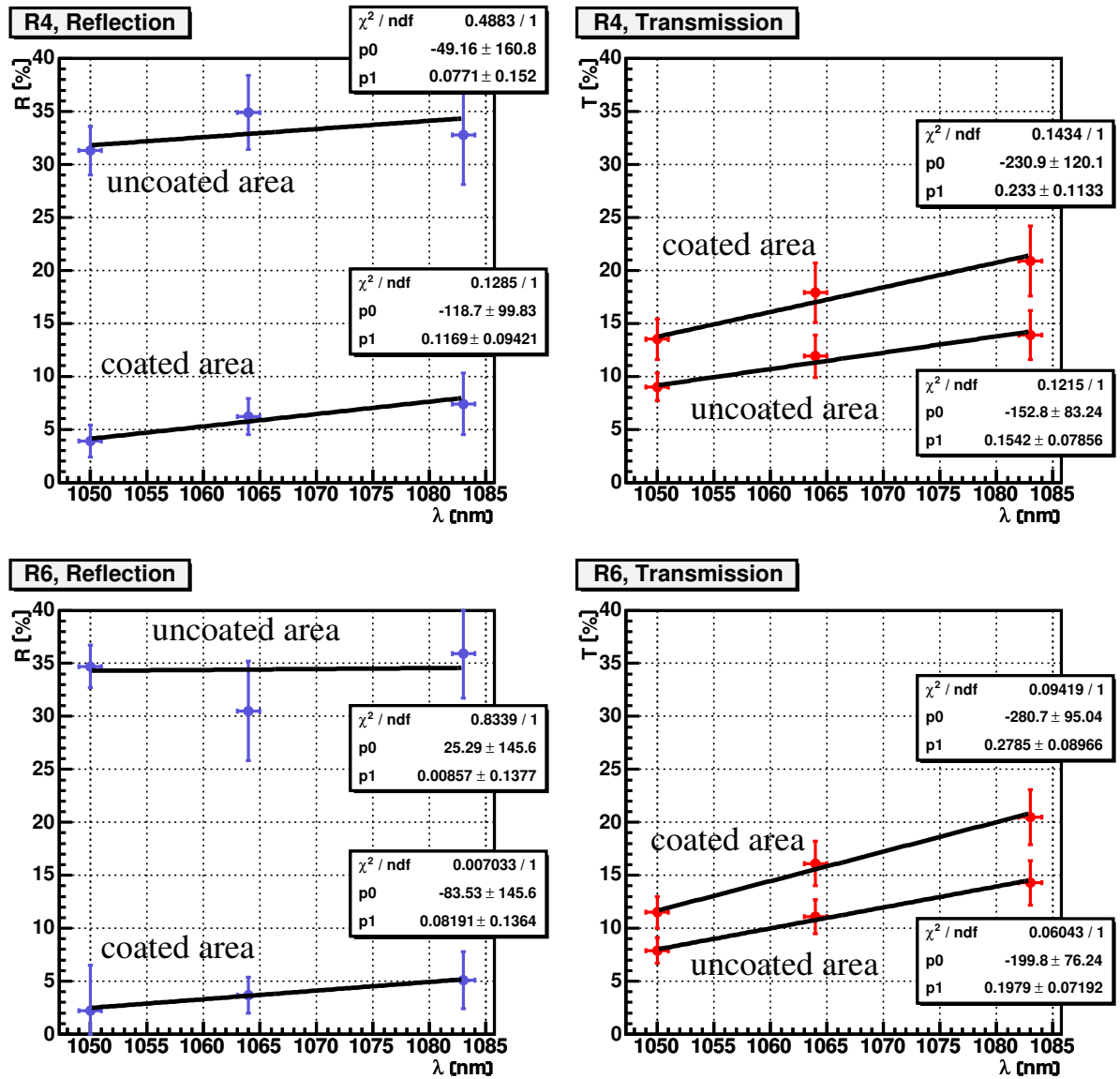- No change in the performance of the sensors as charged particle detectors.

Abbildung 4.27.: T,R of the C and UC area of R4 and R6 alignment sensors as functions of wavelength.

have been achieved, leading to optimization of the positional resolution of the laser spot. The latter is the subject of the next chapter.

4. Alignment Sensors

5. Laser Light Detection

Precise reconstruction of the laser signal in each module layer is essential for absolute and relative position measurements with the LAS. A setup with a geometry closely approximating that of the TEC has been developed in order to study experimentally the laser signal reconstruction and geometry monitoring performance of the optical system.

After verification of the LAS design measurements of the beam spot resolution and studies of the influence of refraction effects were carried out. Finally, the assembly precision of the TEC+ was determined by analysis of laser alignment data and compared to survey measurements.

5.1. Laser Signal Readout

5.1.1. The Operating System

A block diagram of the test setup is given in figure 5.1. It can be divided into a geometry and a readout part.

Module Readout

The readout of the alignment modules was based on the APV Readout Controller System (ARC)[1]. This has been developed for module testing and quality assurance during mass production [65].

Laser pulses are generated by a laser diode (LD), which is connected via a singlemode fibre to a BS. The signal of the laser light incident on an alignment module is read out by the ARC system. A DC low voltage (LV) supply provides $\pm 5\ V$ to the ARC board as well as to the control unit of the LD. High voltage (HV) is used to bias the silicon sensor and has been set to $300\ V$. In addition, a frequency generator (FG), NIM electronics, and an oscilloscope have been integrated to control the trigger signals, defining the time at which the laser is fired and that at which the module is read out. Finally a PC is used to control the system via the ARC software and to analyze the data.

To replicate the LHC bunch crossing interval of 25 ns, the ARC board provides a 40 MHz clock. To initiate module readout a binary trigger pattern synchronous to the ARC clock is sent by the board to the APVs (time t_0 in figure 5.1). The trigger pattern is used to set a programmable delay up to 375 ns in steps of 25 ns, after which the modules

---

[1]The development, maintenance as well as implementation of additional test procedures has been done by the III. Physikalisches Institut B, RWTH Aachen [65]. For LAS purposes it was sufficient to operate the basic system.
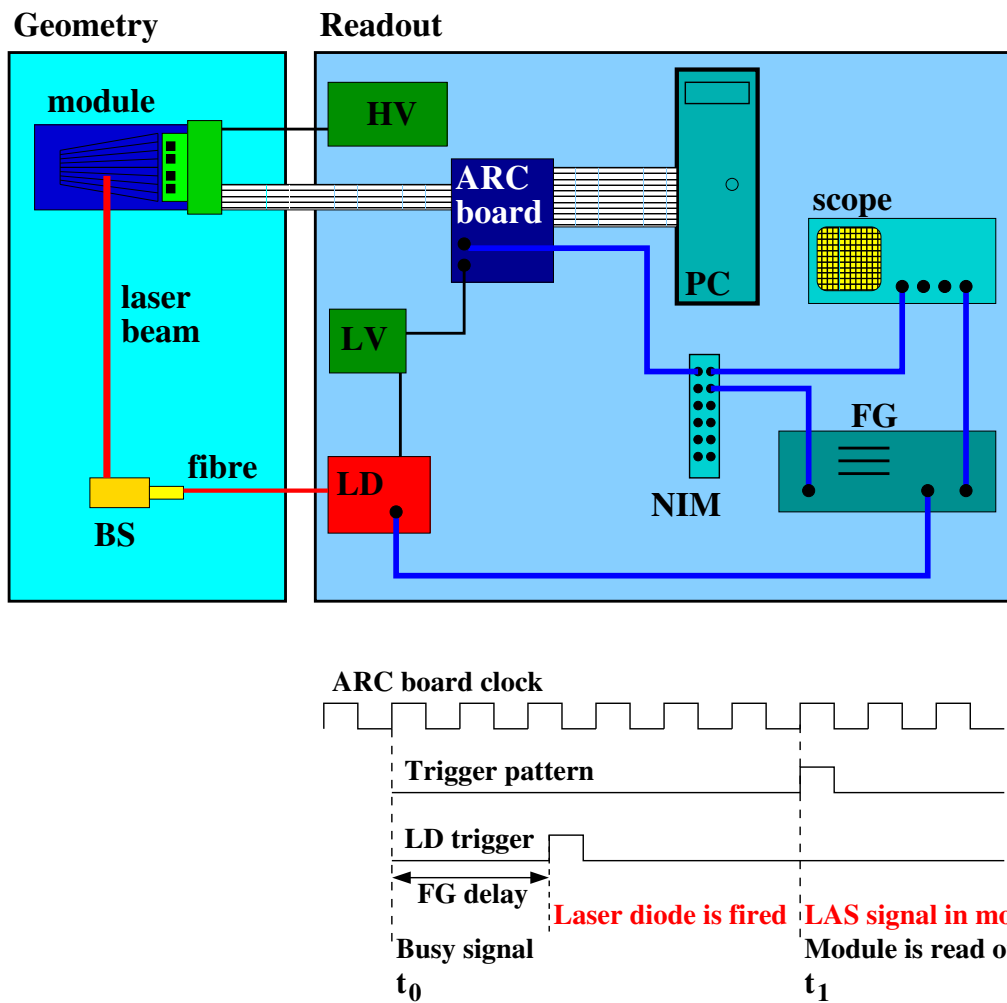
Geometry   **Readout**

Abbildung 5.1.: Block diagram of the LAS test setup. The laser signal readout is triggered and controlled by the ARC board. The time between the busy signal at t_0, firing the laser in an adjustable delay to t_0, and reading out the laser signal in the module at t_1 is optimized by several delay stages for best matching of light generation and detection.

are read out (t_1). At t_0 the ARC board also generates a busy signal, which is used to fire the LD following an adjustable delay. The timing was optimized by fine tuning of the trigger delay in the FG and by varying the latency parameter for the APVs.

The modules were read out by standard ARC software in deconvolution mode, the same mode, that will be used for the tracker readout[2]. For a defined number of events n the output was converted to ROOT files [71], containing ADC histograms (signal or pedestal) as well as noise distribution.

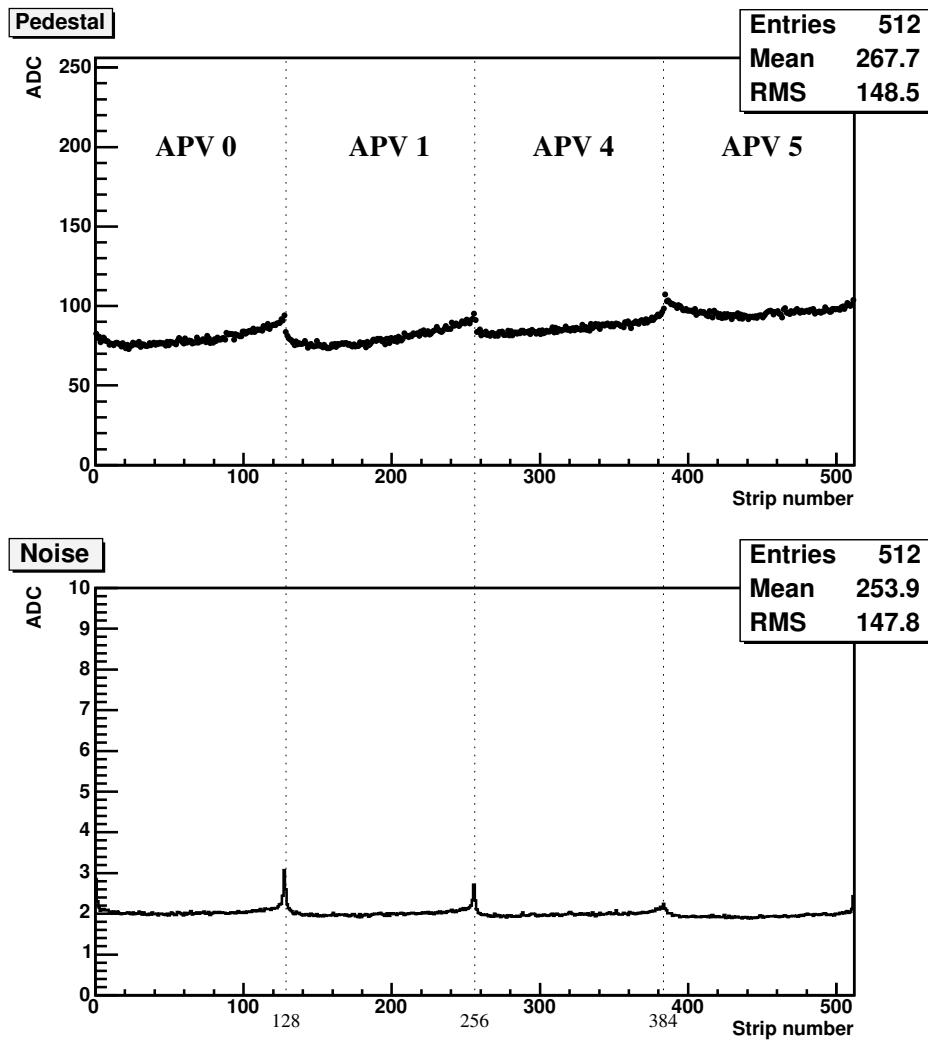
[2]More details can be found in [65]

Abbildung 5.2.: Pedestal and noise distribution of an alignment module used to measure the resolution of the laser beam spot.

For each strip a mean value $\bar{x}$, noise σ_x and error on the mean $\sigma_{\bar{x}}$ have been calculated according to

$$\bar{x} = \frac{1}{n}S_x \qquad \sigma_x = \sqrt{\frac{1}{n-1}\left(S_{xx} - \frac{1}{n}S_x^2\right)} \qquad \sigma_{\bar{x}} = \frac{\sigma_x}{\sqrt{n}} \qquad (5.1)$$

where

$$S_x = \sum_{i=1}^{n} x_i \qquad S_{xx} = \sum_{i=1}^{n} x_i^2 \qquad (5.2)$$

Pedestal data were taken before each laser run and the pedestal values subtracted from all laser signals S. All strip signal data S were divided by the appropriate noise value N (σ_x), without taking common mode corrections into account.

A typical example of the pedestal and noise values obtained with 10000 events for one of the alignment modules is shown in figure 5.2. Common for all tracker modules is the

larger noise of strips belonging to the APV borders (strip numbers 128, 256, 384). For R4 as well as for R6 modules the nominal laser spot position is located in the transition region from APV 1 to APV 4 (see figure 5.2). As will be pointed out later, there is a correlation between strip noise and laser spot resolution.

As displayed in figure 5.3, modules being integrated in the tracker have a smoother noise distribution. Comparison of figures 5.2 and 5.3 shows that resolution measurements were not carried out under optimal conditions.
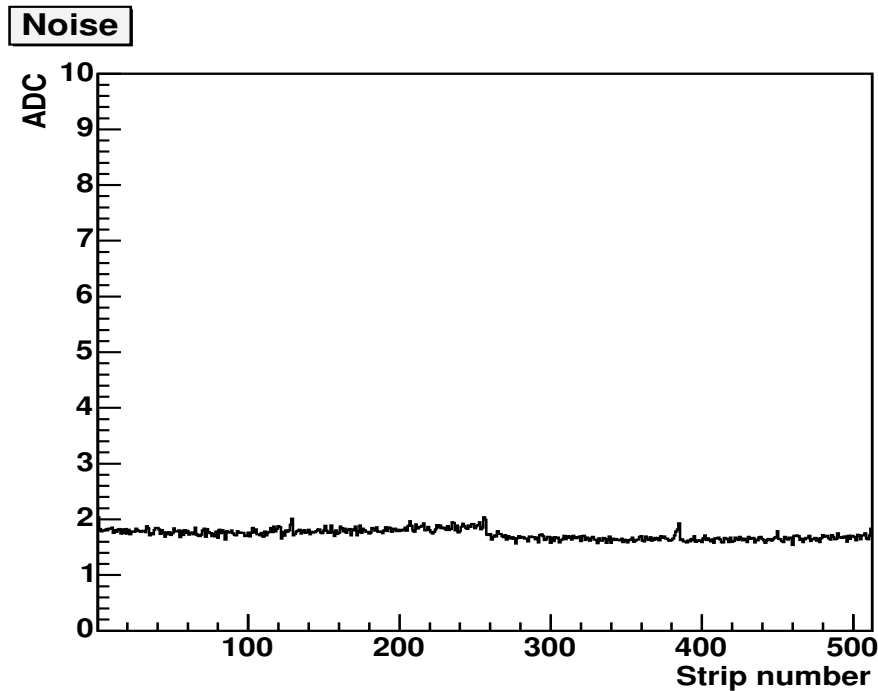
Abbildung 5.3.: Noise distribution of a module integrated in the TEC. In comparison to figure 5.2 the noise of the strips on APV borders is particularly improved.

Module Geometry

A beamsplitter and a set of modules were arranged on a granite table according to the TEC geometry, as shown in figure 5.4.

Reading out a module at a time, this setup was used to verify the LAS design by measuring the beam profile at the position of each module (TEC disc).

With the help of the online display the intensity was optimized for each module position so that the baseline of the APVs was kept stable but also the signal was clearly visible. It follows then that the power provided by the LD is sufficient to reach every layer.

It was shown that after traversal of up to four R4 or R6 modules the laser beam profile is significantly distorted. Nevertheless it was possible to determine the laser spot position precisely. The results for 1000 events recorded per layer are shown in figures 5.5, 5.6, and 5.7. The main peak of each spectrum was fitted by a gaussian

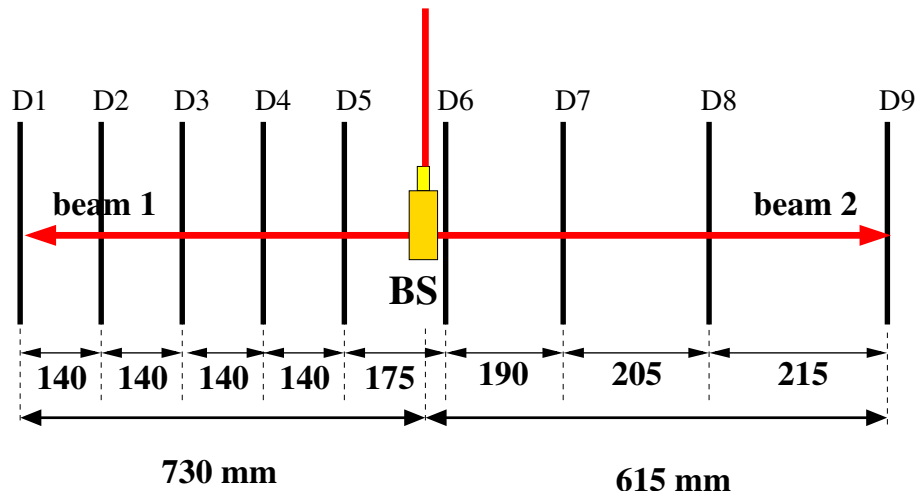$$f(x) = a_0 + a_1 \cdot e^{-\left(\frac{x-x_0}{2\sigma}\right)^2} \tag{5.3}$$

Abbildung 5.4.: Setup according to the TEC geometry to verify the LAS working principle.

in a small range around the maximum. The values obtained for a_0, a_1, x_0, and σ are indicated by p_0, p_1, p_2, p_3 respectively. Although the χ^2-values for the fits are bad, resulting from the beam profile and the very small strip errors obtained for 1000 events from relations (5.1) and (5.2), the results show that in each case the central maximum is detected and its position on the module reconstructed. Thus confirming that the LAS works for the TEC geometry. A quantitative discussion is given in section 5.2.
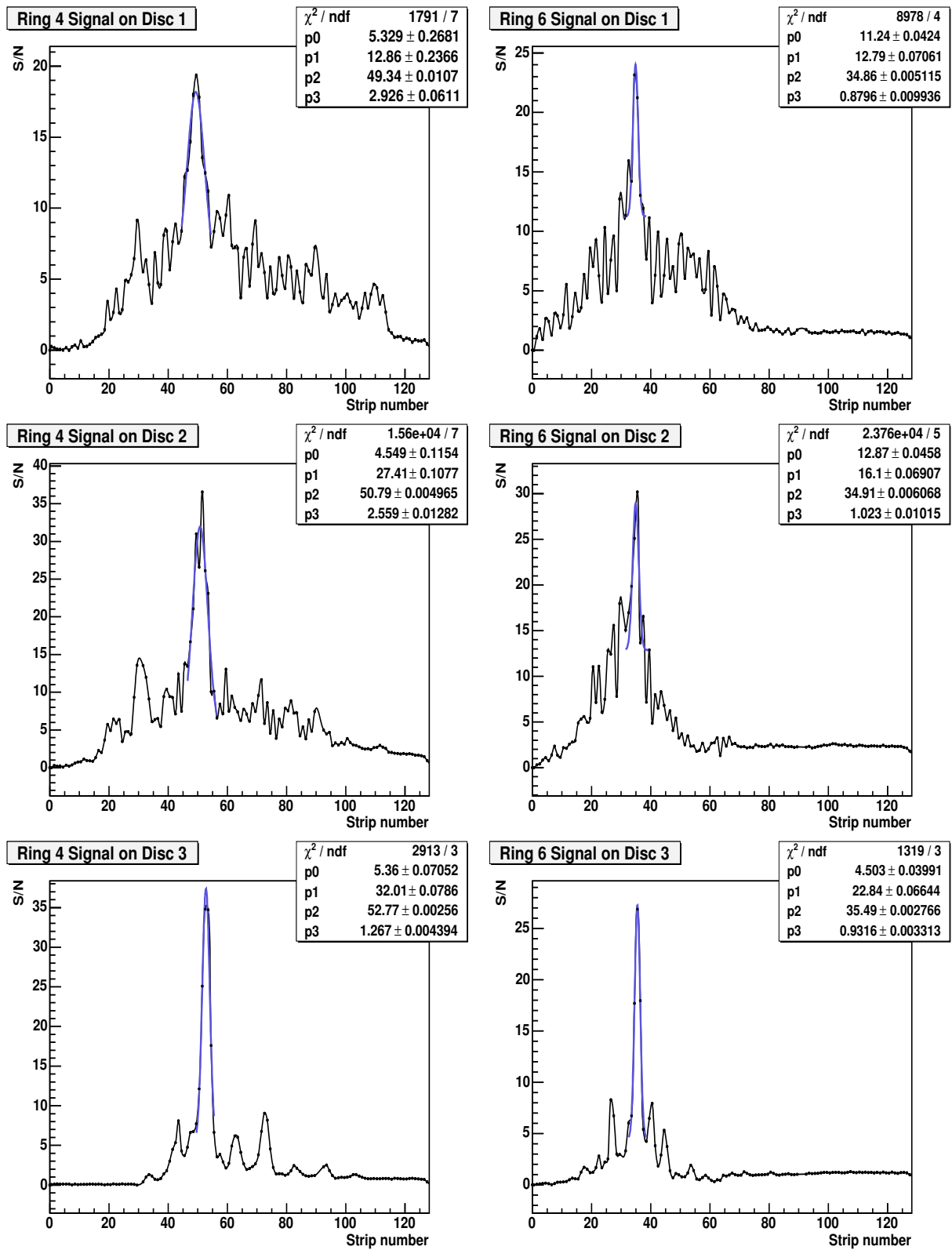
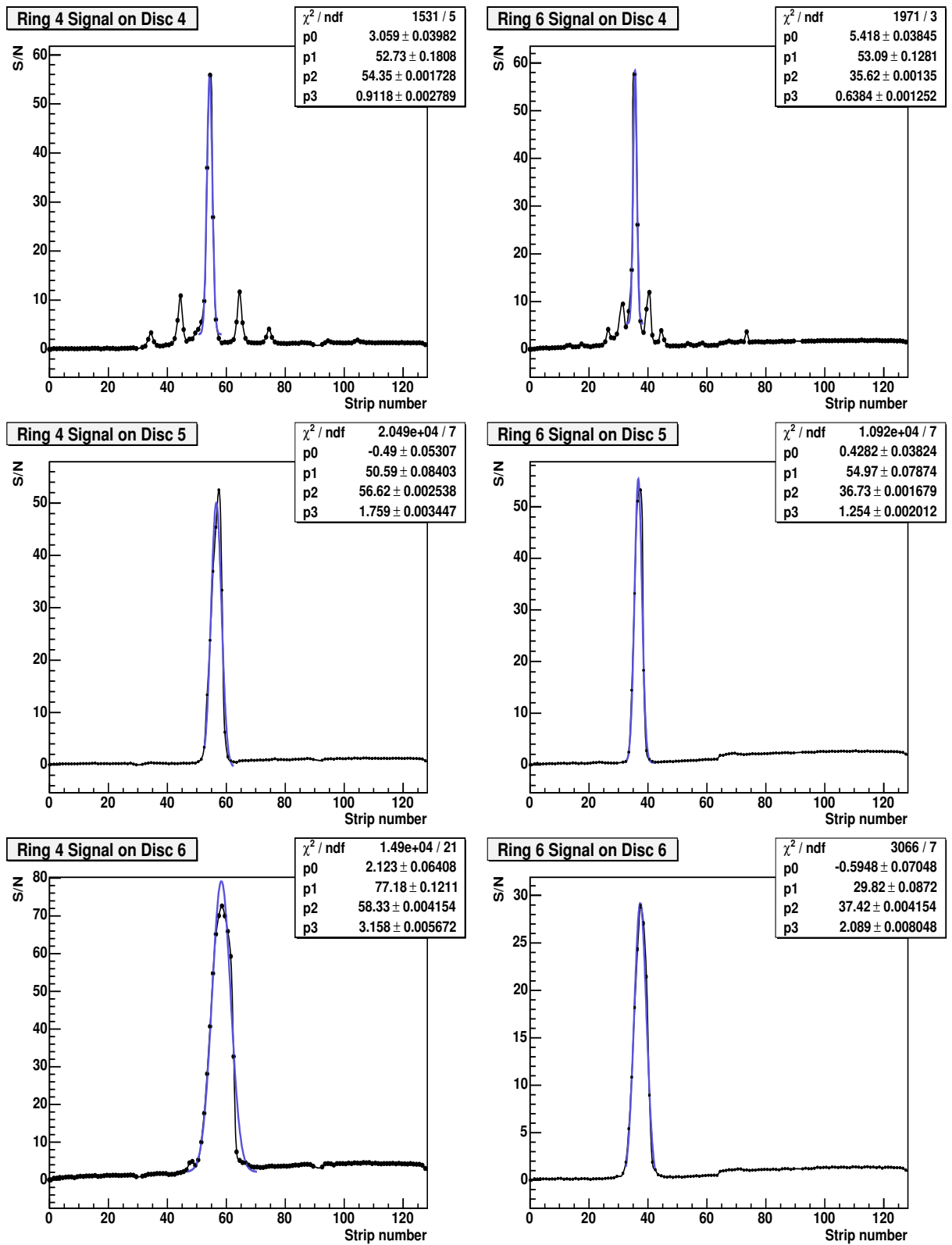Abbildung 5.5.: TEC D1-D3 signal-to-noise (S/N) plots for R4 (*left*) and R6 (*right*).

Abbildung 5.6.: TEC D4-D6 signal-to-noise (S/N) plots for R4 (*left*) and R6 (*right*).
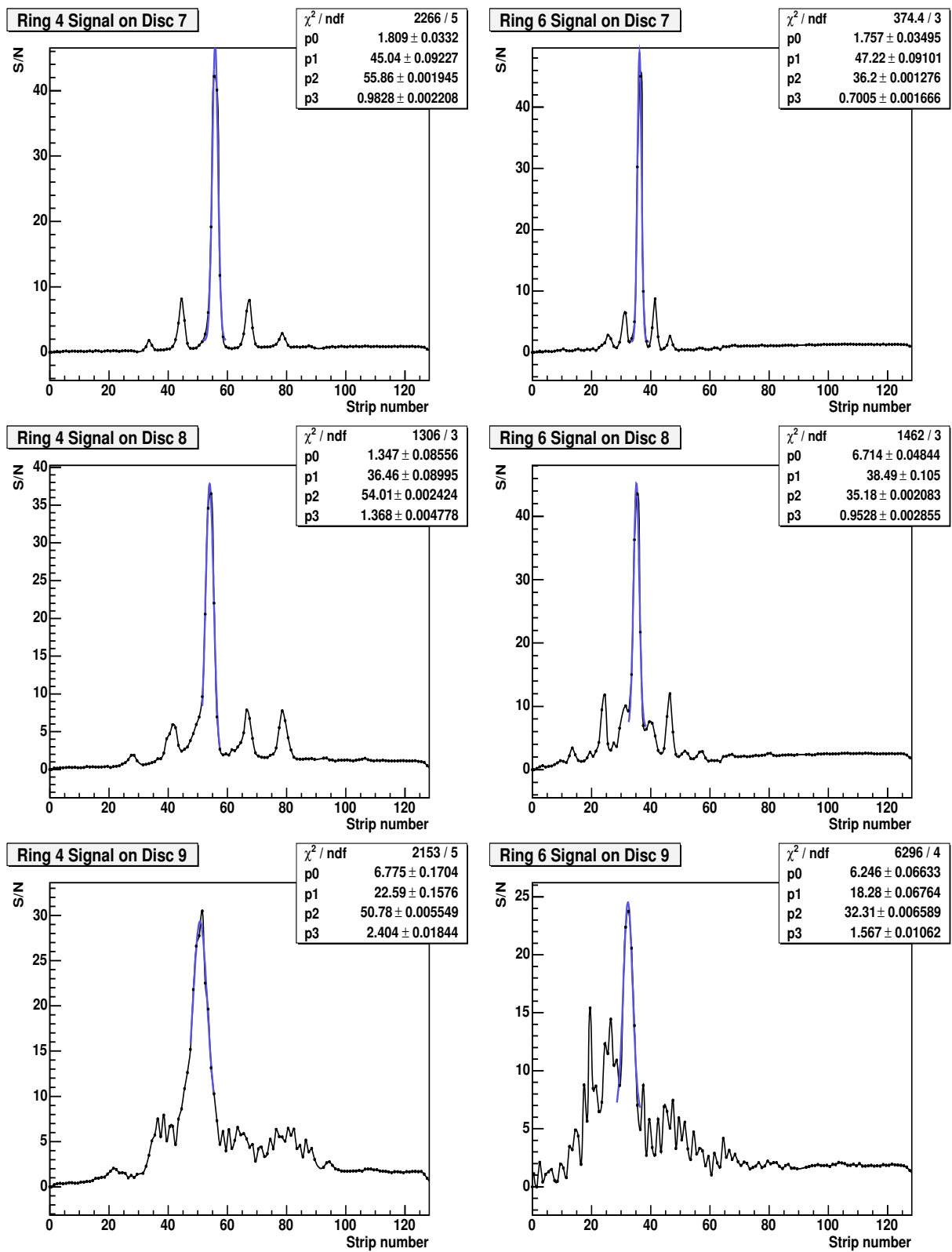
Abbildung 5.7.: TEC D7-D9 signal-to-noise (S/N) plots for R4 (*left*) and R6 (*right*).

5.1.2. Temperature Effects

As it is known from theory and experiments, the absorption coefficient of silicon decreases at lower temperatures, as shown in figure 4.4. Since the working environment of the tracker modules will be at $\approx -10\ ^oC$ in a dry nitrogen (N_2) atmosphere, studies on the transmission of laser light at low temperatures and on the temperature dependence of laser signals were carried out.

Experimental Setup

In the same cooling device (figure 3.13), as described in chapter 3, two modules, either R4 or R6, and a collimator were placed inside the box as indicated in figure 5.8. The collimator housing material was made of plastic and it was mounted in one of the aluminium module holders (see figure 5.8). A constant N_2 flow through the box kept the relative humidity to values less than 15 %.

A bias voltage of 150 V (300 V) was applied to R4 (R6) modules. A laser diode prototype was used to produce laser pulses of constant intensity I_0 with $\lambda \approx 1075\ nm$. Starting at $+15^oC$ the temperature was decreased to -25^oC in 5^oC steps. Since the pedestals generally depend on temperature [65], they were recalculated at each step before taking laser data.
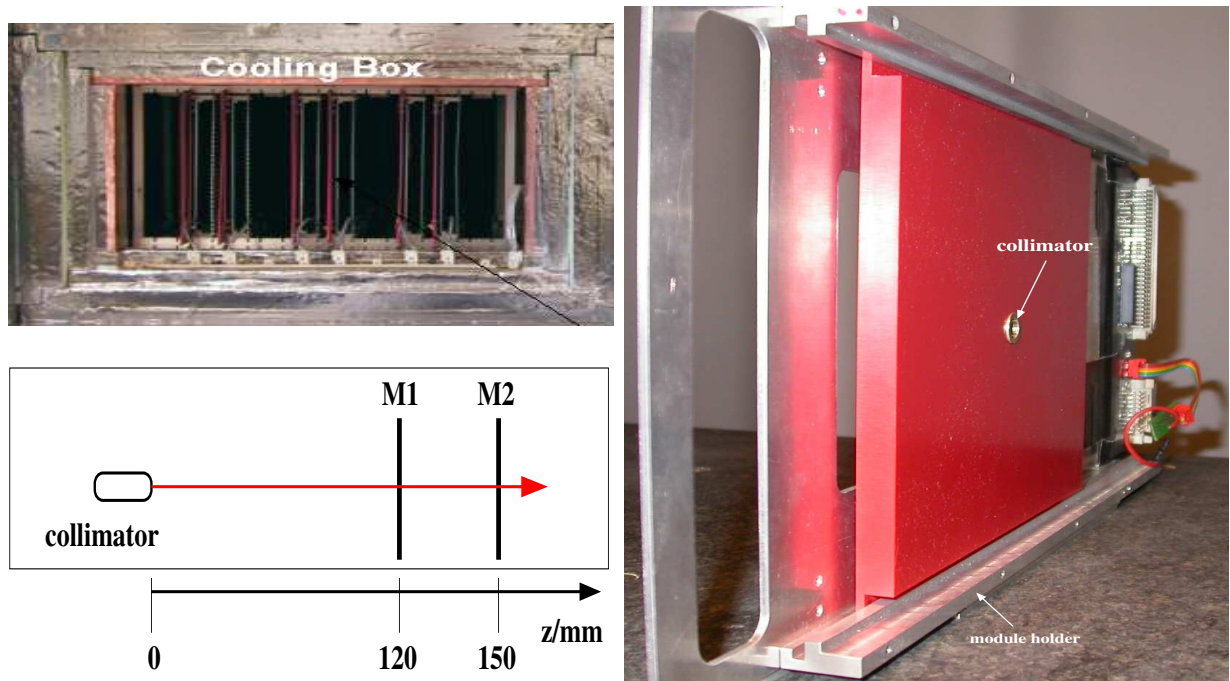

Abbildung 5.8.: Setup (*left*) to measure the laser signals in TEC alignment modules as a function of temperature. A special device has been built to fix a collimator inside the cooling box (*right*).

5. Laser Light Detection

Results

The figure 5.9 shows the laser signal of two R6 modules, placed at positions M1 and M2 of figure 5.8, measured at two different temperatures: $+15^oC$ and -25^oC. The corresponding strips belong to the border region between two APVs (APV1 - APV4). In both diagrams, the larger signal belongs to the first module M1 and the smaller is the one of M2. The decrease with temperature of the M1 signal is obvious, but the much lower M2 signal also decreases.
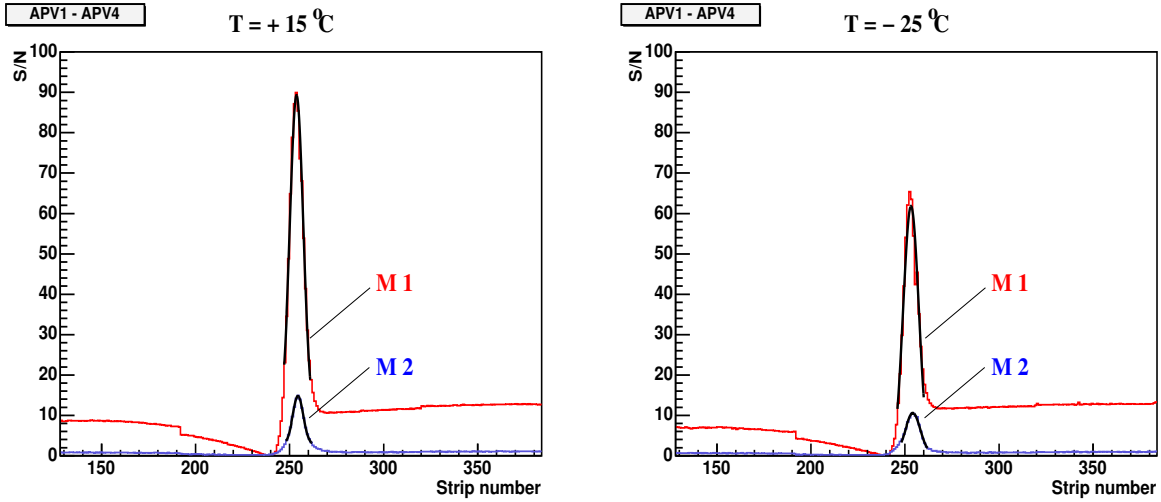

Abbildung 5.9.: S/N plots for R6 modules M1 and M2 at $T = +15^oC$ (*left*) and $T = -25^oC$ (*right*).

Such a decrease is of course expected since the signal depends on the absorption. As seen in figure 4.4 the absorption coefficient α drops to $\approx \frac{\alpha}{2}$ for $\lambda = 1075~nm$ when changing the temperature from $300~K$ to $250~K$.

The increase in transmission T can be approximated by using (H.21), with $\alpha = 1.0~mm^{-1}$, $d_{R4} \approx \frac{1}{3}~mm$, and $d_{R6} \approx \frac{1}{2}~mm$.

$$T = \frac{I}{I_0} = e^{-\left(\alpha d_{R4,R6}\right)} \qquad (5.4)$$

By setting the reflection R equal to zero, the absorption can be obtained as

$$A = 1 - T = 1 - e^{-\left(\alpha d_{R4,R6}\right)} \qquad (5.5)$$

Calculation of the absorption change with temperature leads to

$$f_{\Delta A,R4} = \frac{1 - e^{-\frac{1}{6}}}{1 - e^{-\frac{1}{3}}} = 0.54 \qquad f_{\Delta A,R6} = \frac{1 - e^{-\frac{1}{4}}}{1 - e^{-\frac{1}{2}}} = 0.55 \qquad (5.6)$$

Thus the absorption behaviour of R4 and R6 modules is nearly the same. This is not true for the change in transmission

$$f_{\Delta T,R4} = \frac{e^{-\frac{1}{6}}}{e^{-\frac{1}{3}}} = e^{\frac{1}{6}} = 1.18 \qquad f_{\Delta T,R6} = \frac{e^{-\frac{1}{4}}}{e^{-\frac{1}{2}}} = e^{\frac{1}{4}} = 1.28 \qquad (5.7)$$

which is slightly larger for R6 than for R4. The difference is proportional to $e^{\alpha/2(d_{R6}-d_{R4})}$. The factors of the strip influence g_{alu}, equation (4.4), as well as the diffraction pattern g_{int} cancel out.

The experimental results are shown for R4 and R6 modules in figure 5.10. Due to the decrease in absorption, the intensity for module M1 decreases for both geometries as a function of temperature. M2 shows the same behaviour, but the rate of decrease is much smaller because of the increase in intensity transmitted through M1.
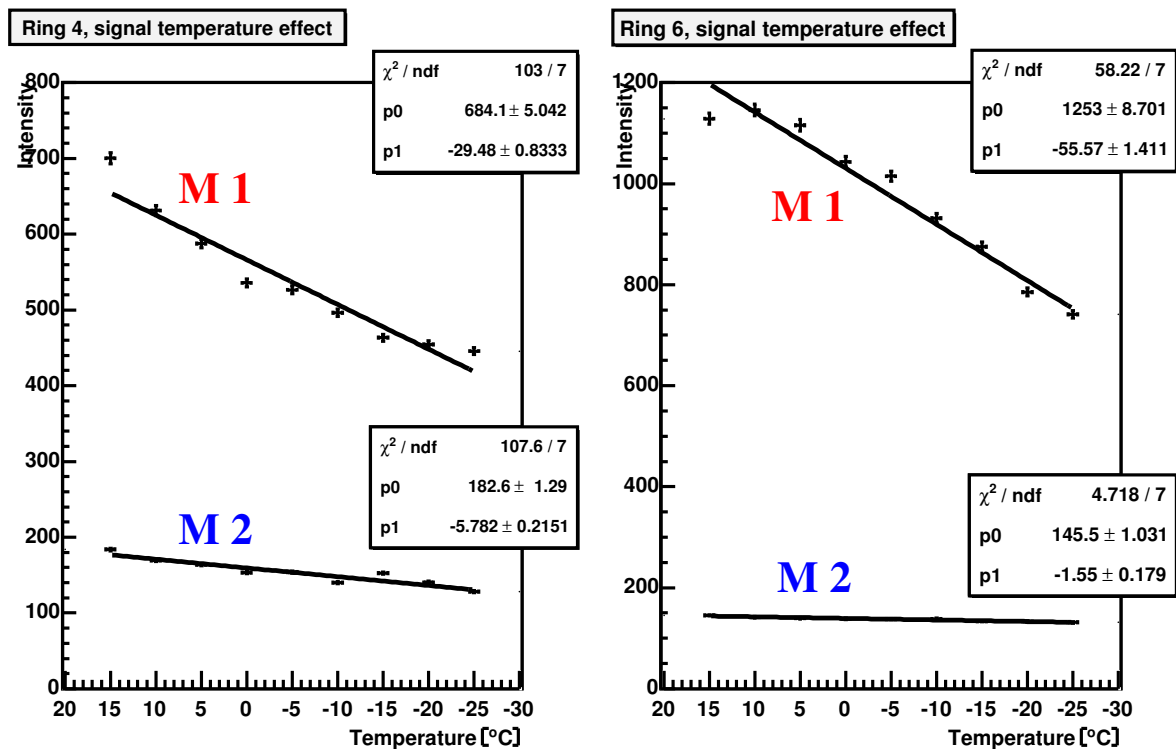

Abbildung 5.10.: S/N dependence on temperature for R4 (*left*) and R6 (*right*) modules. In both diagrams the upper curve belongs to the first module M1, whereas the lower one belongs to M2 (figure 5.8).

Figure 5.11 shows the signal ratio $\frac{I_{M2}}{I_{M1}}$, which is the transmission T through module M1 assuming the same absorption in both modules. In the temperature range from $+15^oC$ to -25^oC the overall gain in transmission for R4 is $f_{R4} = 1.2$ and for R6 $f_{R6} = 1.5$, in agreement with the values previously computed.

In conclusion, even at the lowest tracker temperatures enough laser light is absorbed in the silicon modules to generate laser signals. Transmission factors in the range of $f = 1.2 - 1.5$ have to be taken into account in optimizing the signal readout in the cold environment.

Ring 4, temperature effect on transmission

Ring 6, temperature effect on transmission

χ^2 / ndf	62.68 / 7
p0	26.18 ± 0.3668
p1	0.5356 ± 0.06526

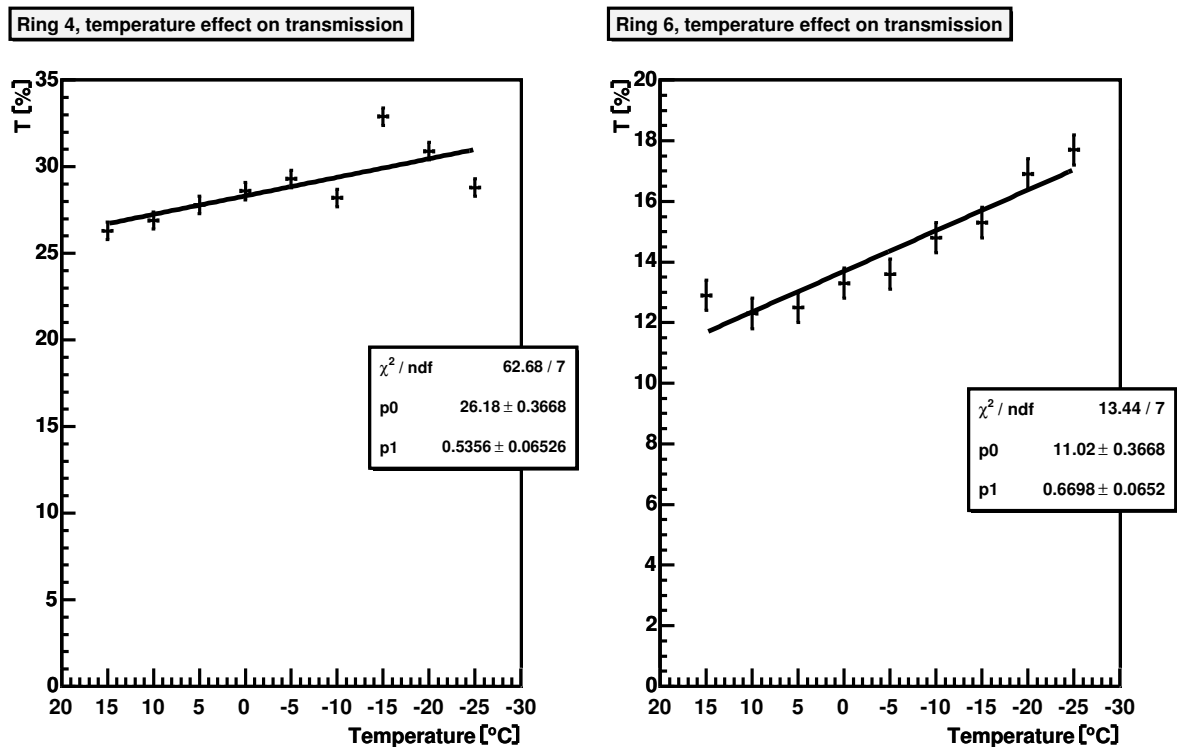| χ^2 / ndf	13.44 / 7
p0	11.02 ± 0.3668
p1	0.6698 ± 0.0652

Abbildung 5.11.: Module transmission as a function of temperature.

5.2. Resolution

The precision obtained by the optical alignment system for the relative positions of the tracker subdetectors is eventually determined by the accuracy with which the laser spot on the silicon modules can be reconstructed.

This depends on the width (7 to 10 strips) as well as on the form of the beam profile and on the influence of the diffraction pattern caused by crossing consecutively arranged sensors. In addition, beam refraction effects, resulting in variations of the position of the laser spot center (mean value), can contribute to the error in reconstructing the optical signal.

5.2.1. Experimental Setup and Data Taking

To determine the laser spot position resolution for the LAS, the setup described below (figure 5.12) was used to arrange the modules according to the TEC geometry (figure 5.4). The alignment module being read out was moved via a servomotor in a direction perpendicular to the strips over a distance of 20 mm in steps of 0.2 mm.

The detection of the laser spot started approximately at strip number 167, belonging to APV 1, and finished at 322, belonging to APV 4. The starting point was arbitrary, since only relative position changes were measured. Important for resolution studies was to include the data from traversing the strips at the APV readout border (strip number 256) to analyze the influence of the larger strip noise in that region.
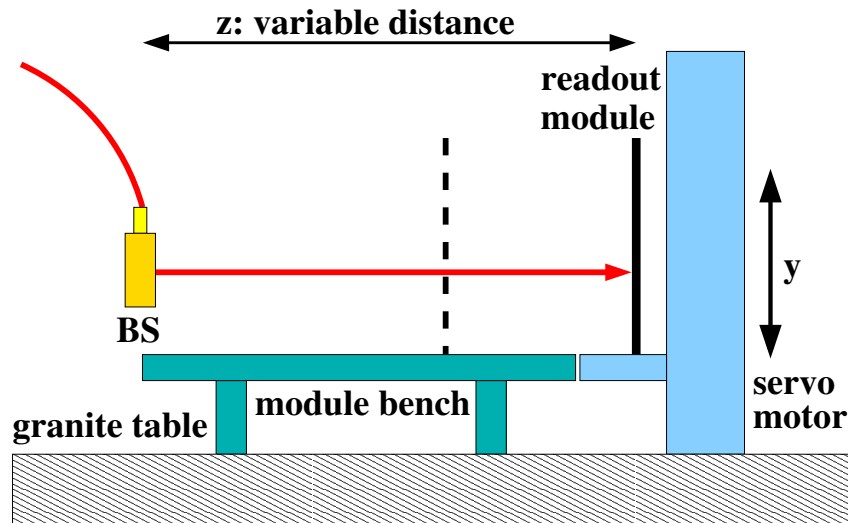
Abbildung 5.12.: Setup to measure the module resolution. The dashed line symbolizes n modules ($n = 0, .., 4$) in front of the module being read out and moved by the servomotor. The distance z to the BS was set according to the TEC disc position (figure 5.4).

The reconstructed laser spot position P_L is plotted versus that of the servomotor P_S in figure 5.13. A linear relation is expected, thus deviations from the straight line are equivalent to the LAS resolution, since other error contributions are negligible (compare section 3.2). The inverse of the slope is the module pitch and gives for R4 $p_{R4} = 126 \ \mu m$ and for R6 $p_{R6} = 189 \ \mu m$, which is in agreement with the known sensor geometry. With the pitch p the residuals can be calculated by:

$$r = P_L \cdot p - P_S = P_M - P_S \tag{5.8}$$

The procedure to take and analyse resolution data is summarized below.

- Define a geometry (e.g. R4 module on TEC D3) and place the module being read out by the ARC system on the servomotor at the corresponding distance from the BS. In addition, according to the geometry, mount n modules between the BS and the module read out.

- Take pedestal data by reading 10000 events.

- Take laser data. At each motor position:

  - Read out 1000 laser signal events and calculate the mean $\bar{x}$, noise σ_x and error on the mean $\sigma_{\bar{x}}$ (equation (5.1) and (5.2)).

  - Subtract the pedestals and remove the data of strips declared to be faulty [65] (see also figure 5.14).

  - Apply a gaussian fit (equation (5.3)) to the data and record the reconstructed laser spot position on the module P_M (mean value) as well as the servomotor position P_S.
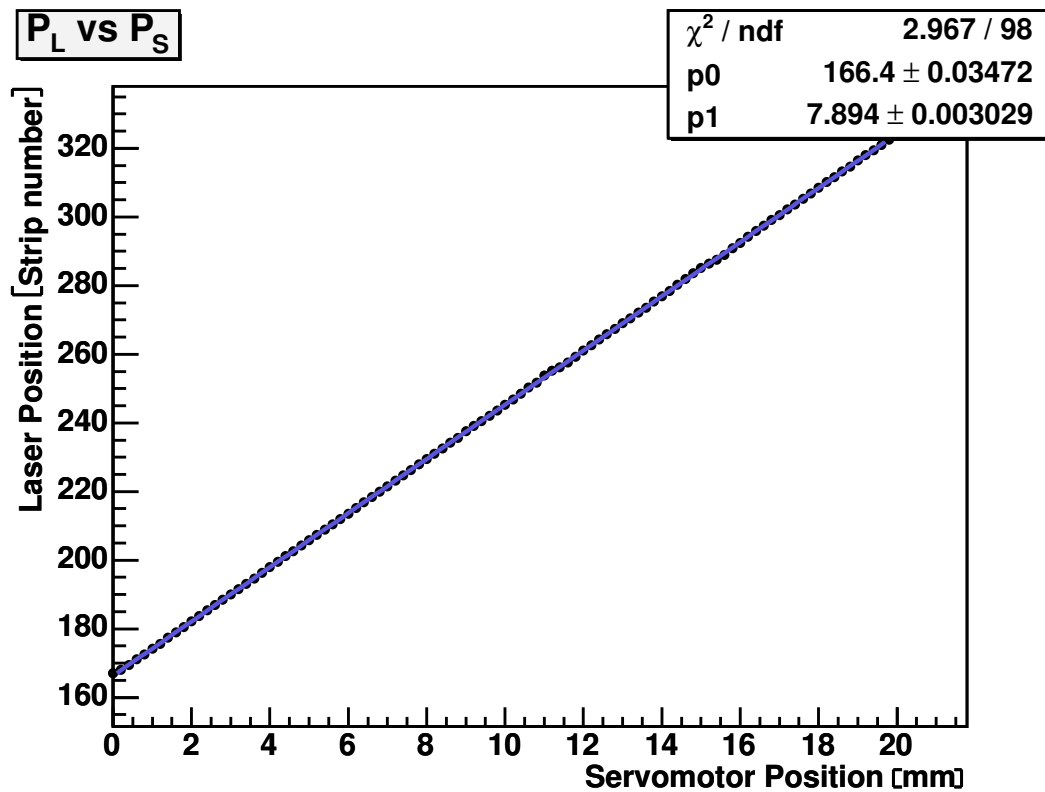
Abbildung 5.13.: Laser spot versus servomotor position shown for the TEC D1 R4 geometry. The pitch is determined by the inverse of the slope p_1^{-1}.

- Determine the residuals $r = P_M - P_S$ and plot their distribution (figures 5.16, 5.17 and 5.18). The resolution is given by the width σ of a gaussian fitted to the residuals distribution.

5.2.2. Results

Figure 5.14 shows in the upper diagram the noise distribution of the R4 module at TEC position D1 and in the lower one the residuals r as a function of the scan position on the module.

By using a R4 module with several defective strips it was possible to study the contribution of faulty strips to the resolution. A correlation between large residuals and anomalous noise values is obvious. Although the entries of those strips declared as faulty have been removed before fitting the laser spot signal, their influence cannot be compensated completely.

By far the largest effect is seen for the strips at the APV readout border, which is also true for R6 modules as illustrated in figure 5.15.

For the TEC D1 position the laser beam traverses the largest number of silicon sensors and also the separation in z between successive discs is minimal. Hence the worst resolution is expected at this position. Comparing the corresponding distributions for R4 (figure 5.14)
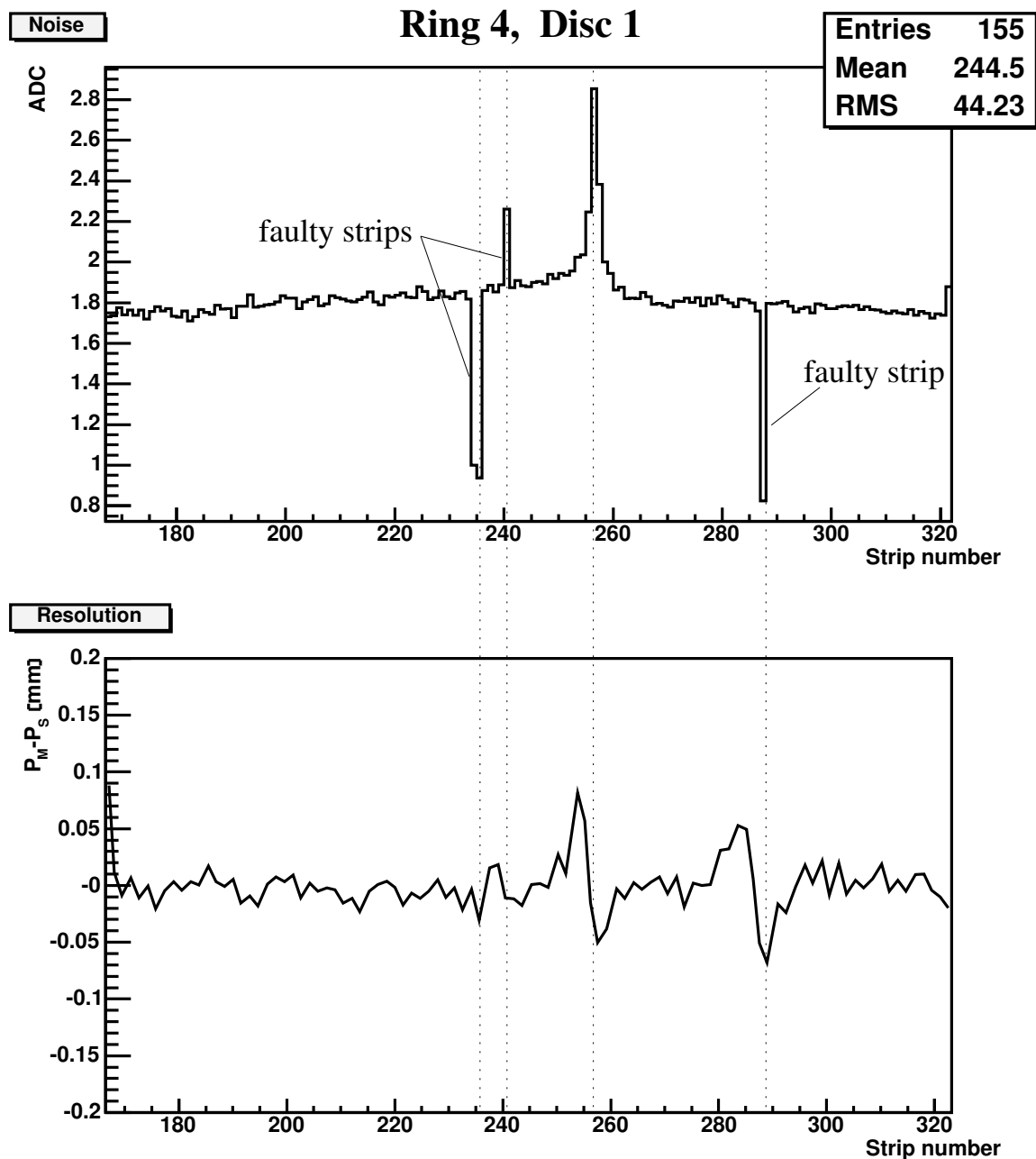
Abbildung 5.14.: Comparison of strip noise and measured residuals. A correlation between resolution and faulty strips is evident.

and R6 (figure 5.15) large variations of the residuals are visible for R6 even in the absence of faulty strips, whereas the variations are small for R4.

This effect can be explained by the module geometry. Since the number of traversed sensors and the TEC discs is the same for R4 and R6, the only difference is their pitch with $p_{R6} > p_{R4}$. As a result of equation (4.2), the overlap of higher order diffraction maxima with the main peak becomes more important for the laser spot reconstruction in R6 modules (compare the R4 and R6 signals in figures 5.5, 5.6, 5.7) and tends to deform
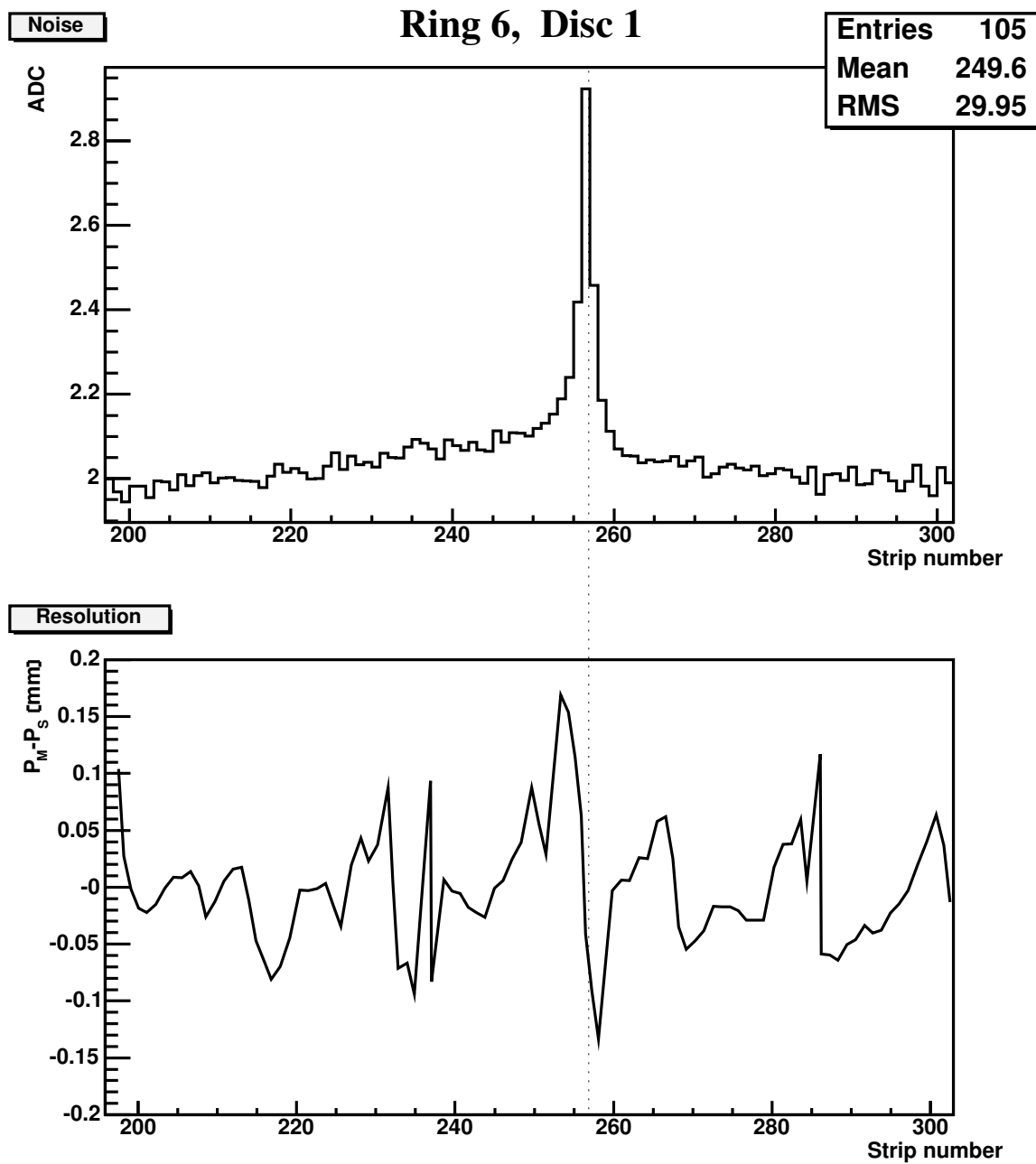
Abbildung 5.15.: Strip noise and measured residuals for an R6 D1 module at the TEC D1 position.

the central maximum. Thus the precise determination of the laser spot position is limited by the silicon sensor geometry.

Figures 5.16, 5.17 and 5.18 show the resolution histograms at all TEC disc positions for both the R4 modules (diagrams on the left) and the R6 ones (diagrams on the right). The gaussian fits to the residual distributions are also displayed.
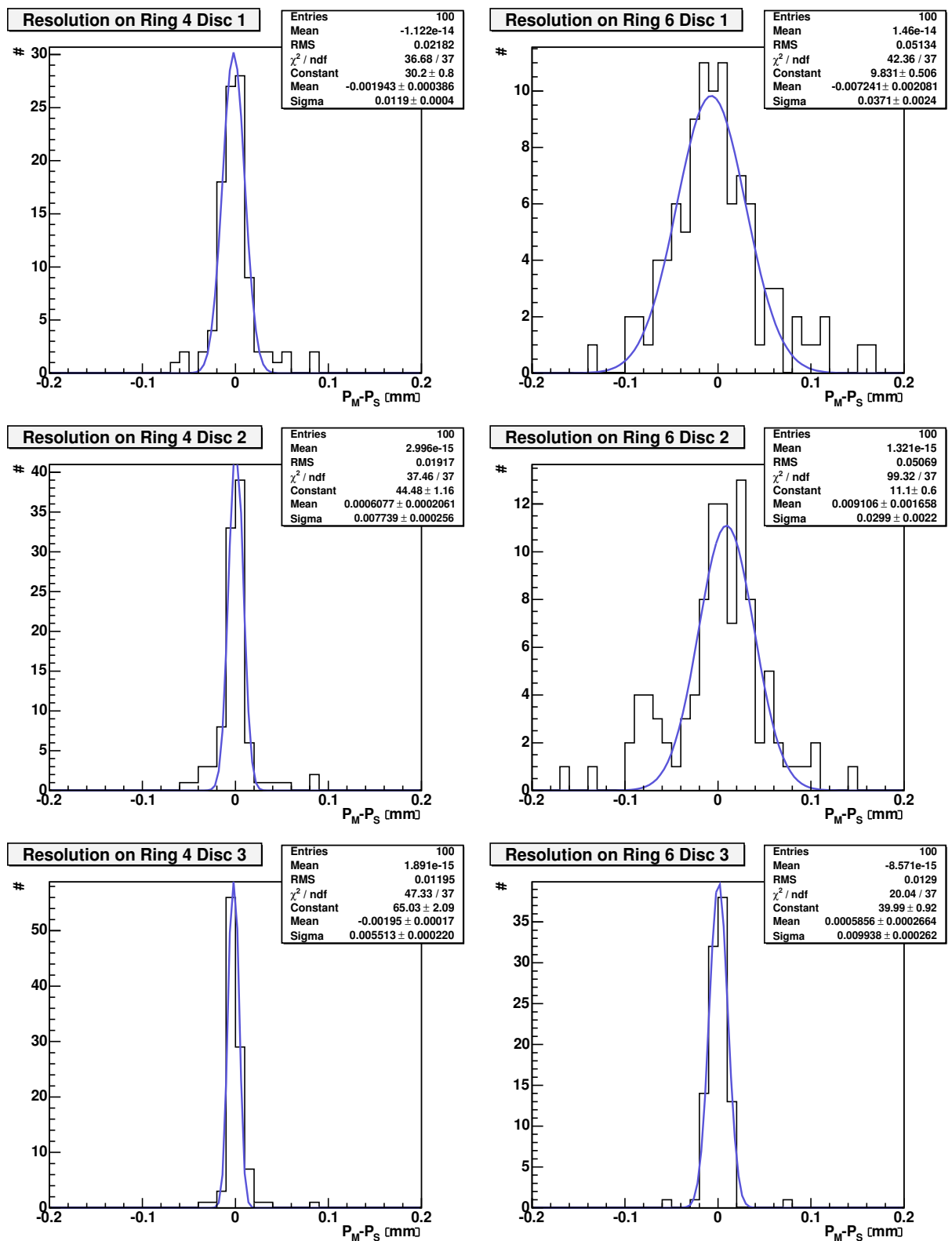
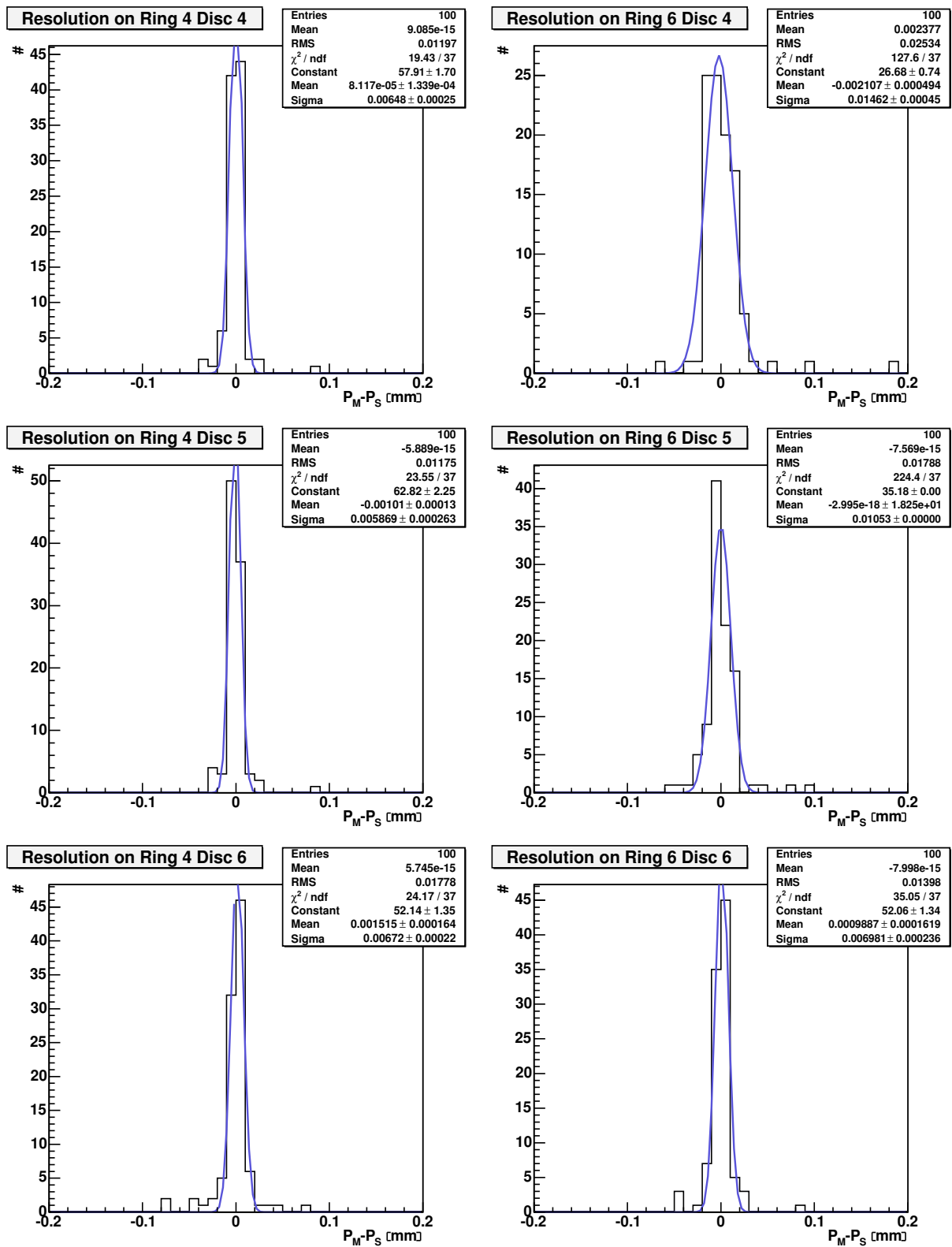Abbildung 5.16.: TEC D1-D3 resolution histograms for R4 (*left*) and R6 (*right*).

Abbildung 5.17.: TEC D4-D6 resolution histograms for R4 (*left*) and R6 (*right*).
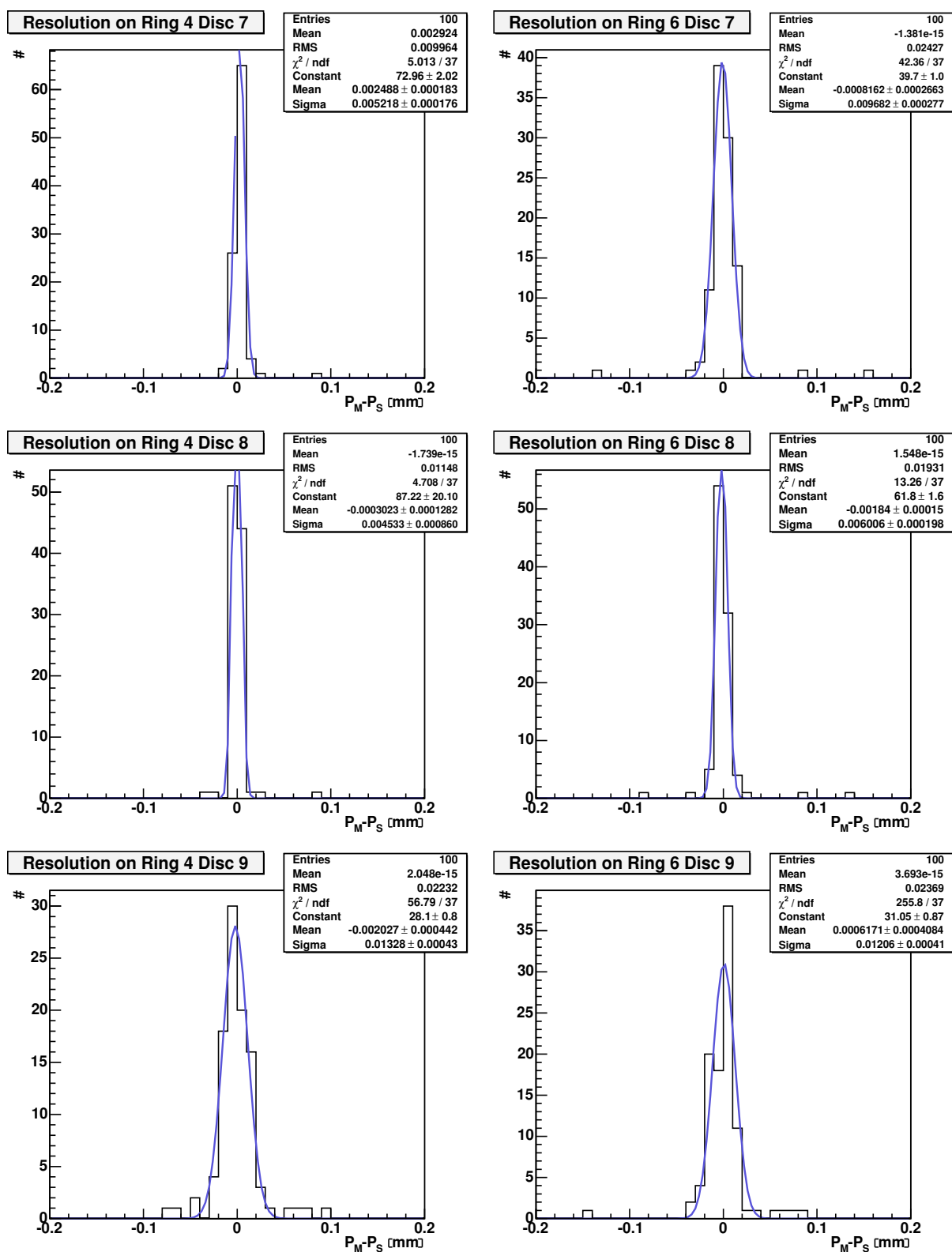
Abbildung 5.18.: TEC D7-D9 resolution histograms for R4 (*left*) and R6 (*right*).

The width of the fitted gaussian represents the measurement accuracy under optimal module performance. The effects of noisy and faulty strips result in non-gaussian tails. As a measure of their effect, the RMS value of the distributions is listed in the table below together with the fitted gaussian width σ.

Laser Alignment Resolution				
disc	Ring 4		Ring 6	
	σ [μm]	RMS [μm]	σ [μm]	RMS [μm]
1	11.9	21.8	37.1	51.3
2	7.7	19.2	29.9	50.7
3	5.5	12.0	9.9	12.9
4	6.5	12.0	14.6	25.3
5	5.9	11.8	9.6	17.9
6	6.7	17.8	7.0	14.0
7	5.2	10.0	9.7	24.3
8	4.5	11.5	6.0	19.3
9	13.3	22.3	12.1	23.7

Tabelle 5.1.: Ring 4 (left), Ring 6 (right) resolution values for all TEC disc positions.

From this overview it is evident that most of the distributions are narrow, except for R6 on D1 and D2, as already discussed.

In conclusion, the requirement that the laser spot be reconstructed with a resolution of $\approx 10\ \mu m$ has been fulfilled for all locations of the alignment modules except for R6 modules on D1 and D2. Since there are redundant LAS measurements, the monitoring of the TEC D1 and D2 by R4 data should be sufficient.

5.3. Refraction

Refraction causes a shift in the position of the laser spot. Such a shift does not influence the performance of the LAS, as long as it is significantly smaller than the 100 μm accuracy required for absolute position measurements. However, its value should be stable with variations being of the same order as the module resolution, thus leading to no additional contribution to the error in the determination of the laser spot position. The effects of refraction were studied in a setup similar to that used for resolution measurements.

5.3.1. Experimental Setup

As seen in figure 5.19, in the startup geometry s_0 the laser light was divided into two beams by a beamsplitter and detected by the two modules (either R4 or R6) on the D1 and D9 positions. Beams 1 and 2 were measured separately with the readout module moved by the servomotor over a distance of 20 mm in steps of 0.2 mm.

With the z position of the BS relative to the readout modules on D1 and D9 being constant, the effect on refraction of adding alignment modules in between could be studied (change of the setup configuration from s_i to s_{i+1}).
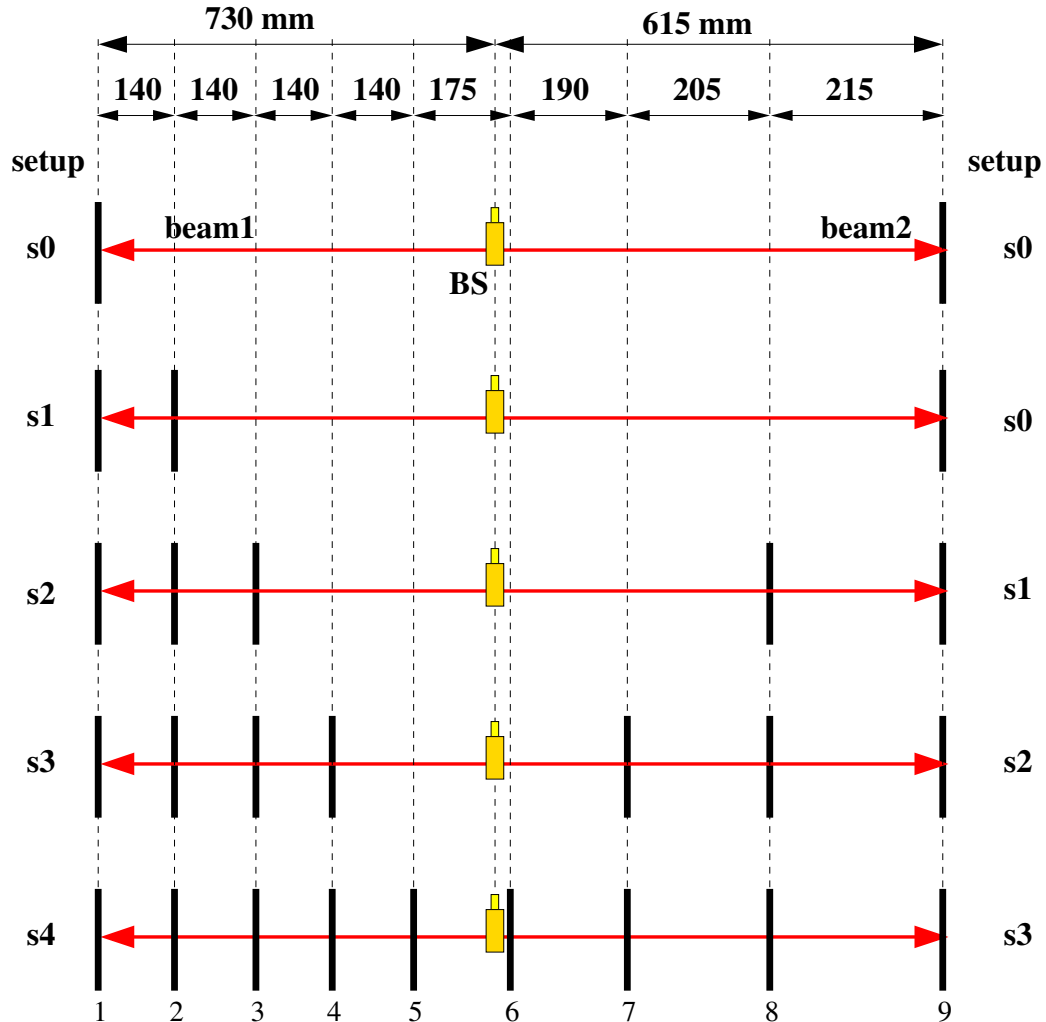

Abbildung 5.19.: Setup to measure refraction effects.

5.3.2. Results

For each configuration s_i the difference $\Delta m_{0,i} = P_{s_0} - P_{s_i}$ in the position of the laser spot with respect to its original position P_{s_0} was determined and is shown in figures 5.20 and 5.21. Since setup s_i always contains the previous one s_{i-1}, each successive plot in figures 5.20 and 5.21 shows the effect of inserting one additional alignment module.

The mean values of all distributions are all less than 35 μm, so that the required accuracy for absolute LAS position measurements (better than 100 μm) is not affected by refraction.
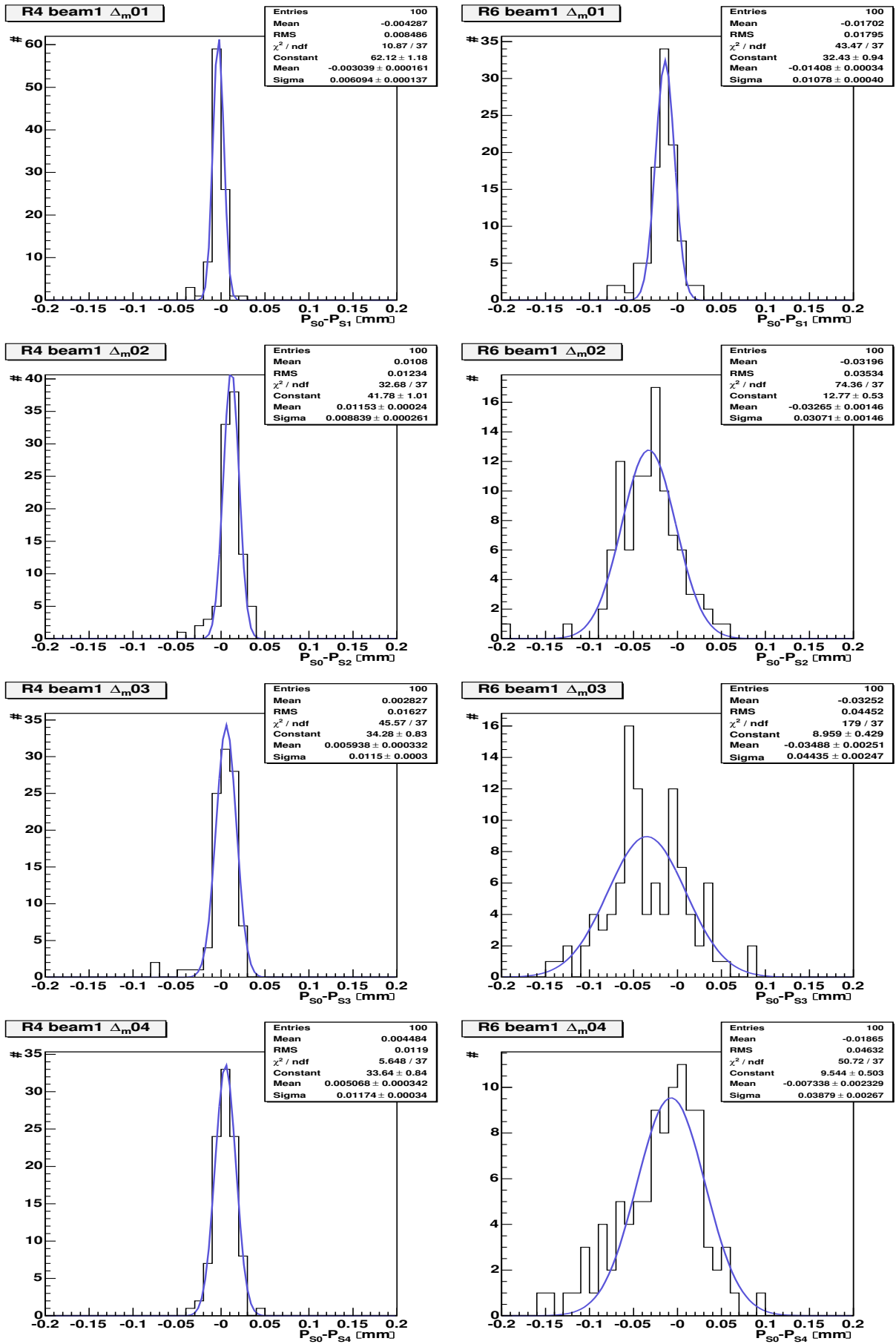
Abbildung 5.20.: Beam 1 TEC refraction studies for R4 (*left*) and R6 (*right*). Distributions of the difference of each reconstructed position ($\Delta m_{0,i} = P_{s_0} - P_{s_i}, i = 1, \ldots, 4$) after addition of 1, 2, 3 and 4 modules into the laser path.
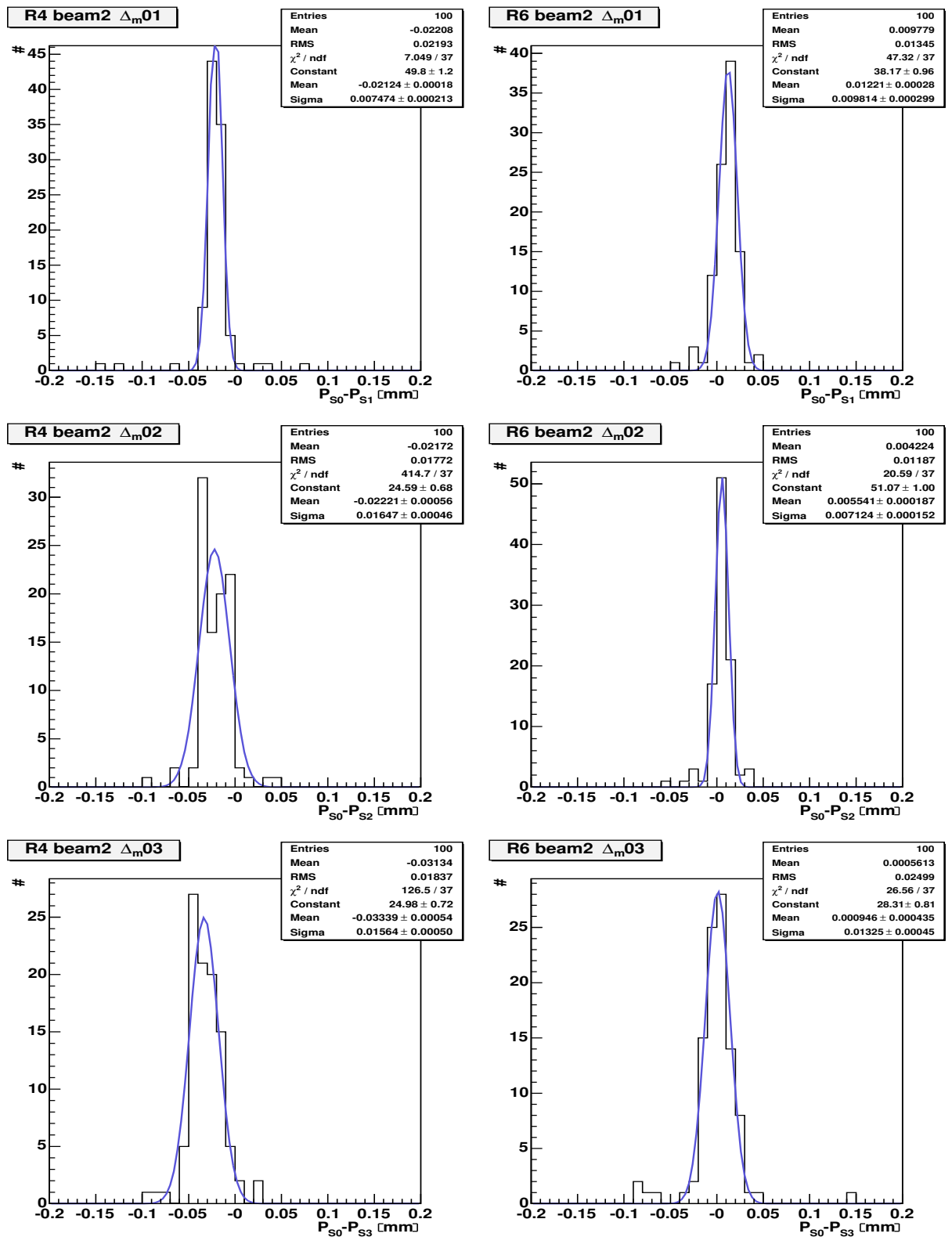
Abbildung 5.21.: Beam 2 TEC refraction studies for R4 (*left*) and R6 (*right*). Distributions of the difference of each reconstructed position after addition of 1, 2 and 3 modules into the laser path.

5. Laser Light Detection

To check the stability of possible refraction effects, it was examined whether the width of the distributions in figures 5.20 and 5.21 can be explained just by the measured resolution in reconstructing the laser spot (σ_{s_0} and σ_{s_i}) without an additional contribution from refraction variations (σ_{ref}).

From the distributions of the residuals shown in figures 5.22, 5.23 and 5.24 the resolution σ_{s_i} was determined for each individual configuration s_i following the method described in section 5.2.

The magnitude of possible refraction variations σ_{ref} was evaluated from the quadratic sum of errors

$$\sigma_{\Delta m_{0,i}} = \sigma_{s_0} \oplus \sigma_{s_i} \oplus \sigma_{ref} \tag{5.9}$$

For example, for beam 1 through R4 in configuration s_4 the above equation gives

$$11.7^2 = 6.2^2 + 11.9^2 + \sigma_{ref}^2 \tag{5.10}$$

leading to $\sigma_{ref} \approx 0$.

All results are summarized in the following table:

Laser Alignment Refraction		
configuration	Ring 4	Ring 6
	σ_{ref} $[\mu m]$	σ_{ref} $[\mu m]$
beam 1		
s01	0	0
s02	0	7.2
s03	0	13.7
s04	0	0
beam 2		
s01	0	0
s02	8.3	0
s03	0	0

Tabelle 5.2.: Ring 4 (left), Ring 6 (right) refraction variations.

Most of the values are consistent with zero. The three cases, for which values comparable to the 10 μm resolution required for LAS monitoring were obtained, are consistent with the statistical expectation.

It is probable, that the smooth sensor surface achieved by application of the anti-reflex-coating has made refraction effects insignificant for LAS purposes.
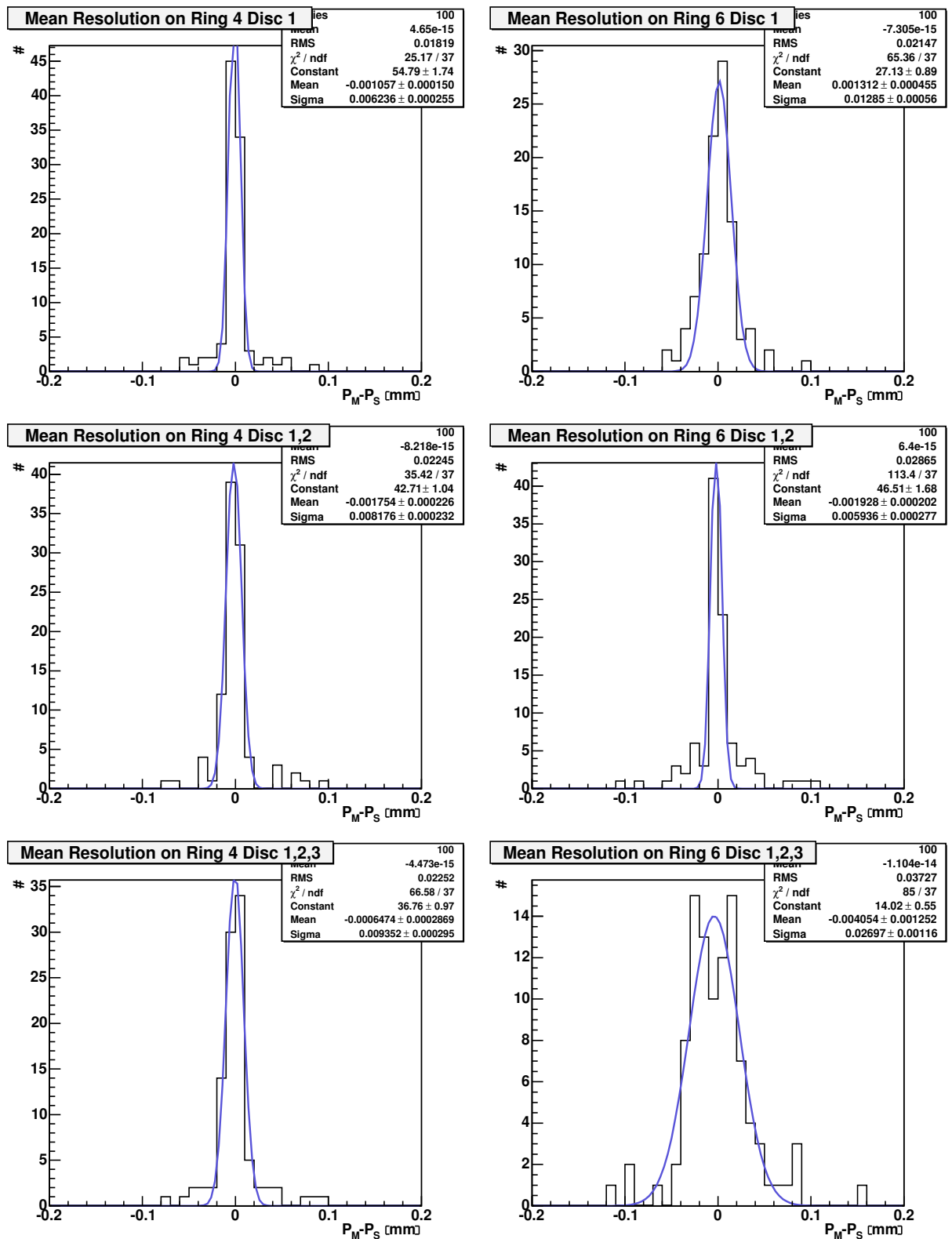
Abbildung 5.22.: Distributions of residuals for beam 1 TEC refraction studies for R4 (*left*) and R6 (*right*). 0, 1 and 2 additional modules added into the laser path.
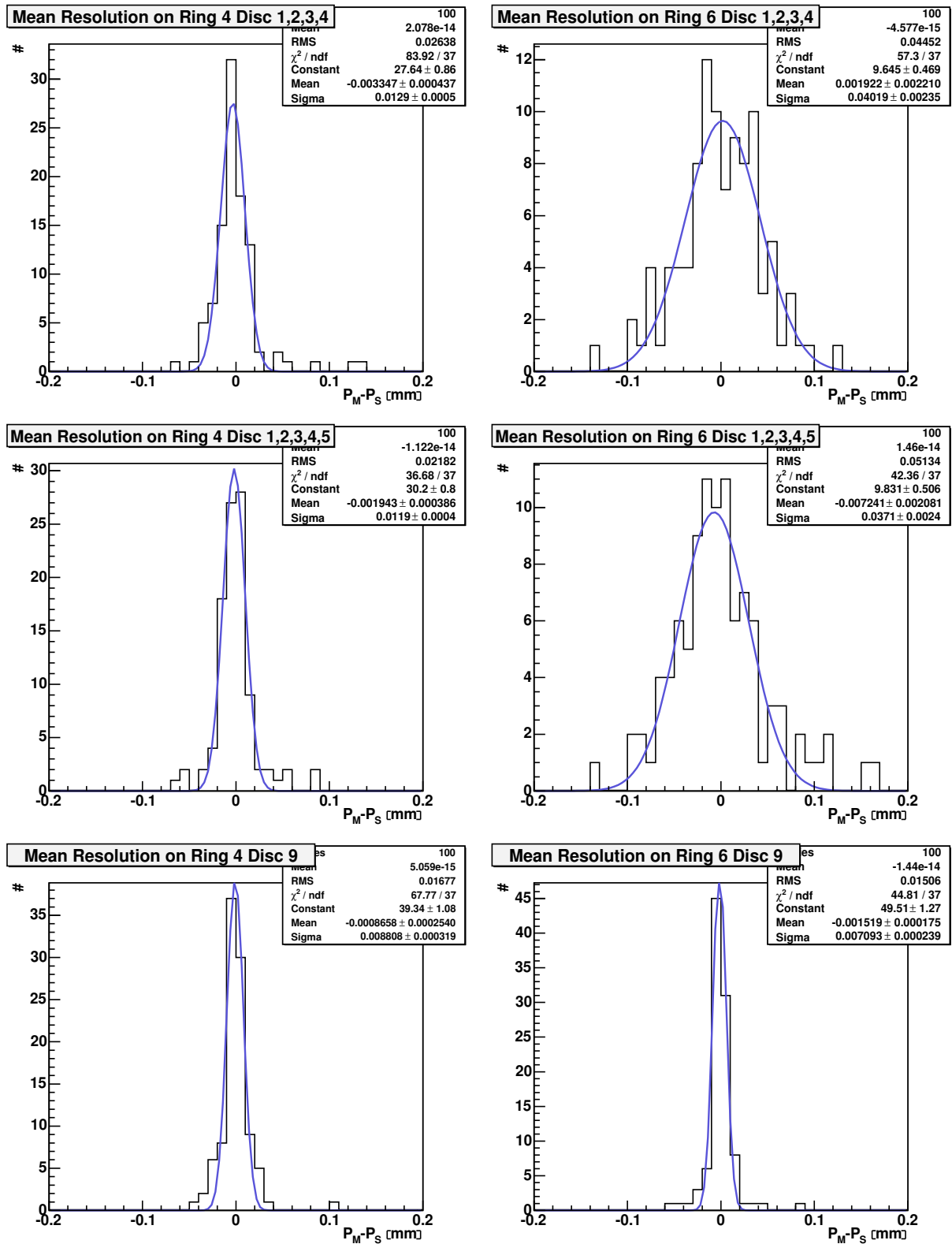
Abbildung 5.23.: Distributions of residuals for TEC refraction studies for R4 (*left*) and R6 (*right*). Beam 1 (first four diagrams): 3 and 4 additional modules added into the laser path. Beam 2 (last two diagrams on the bottom): no additional modules.
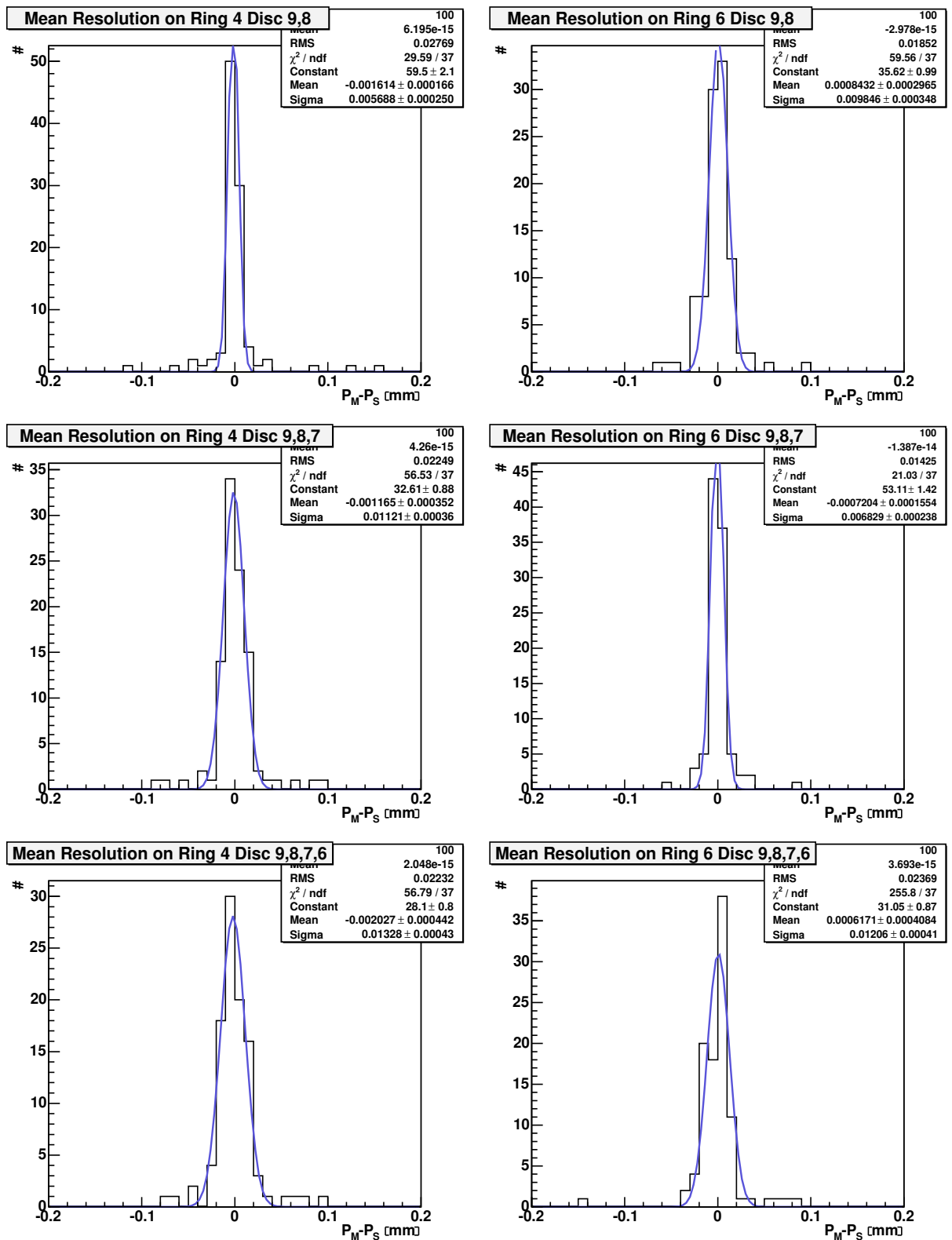
Abbildung 5.24.: Distributions of residuals for beam 2 TEC refraction studies for R4 (*left*) and R6 (*right*). 1, 2, and 3 additional modules added into the laser path.

5.4. First Sector TEC Data

5.4.1. Laser Beam Reconstruction

After petal integration into the first sector of TEC+ (see figure 5.25) and system commissioning, laser pulses of 50 ns width were generated by the laser diodes at a rate of $\approx 100\ Hz$ and read out by all R4 and R6 alignment modules in deconvolution mode.
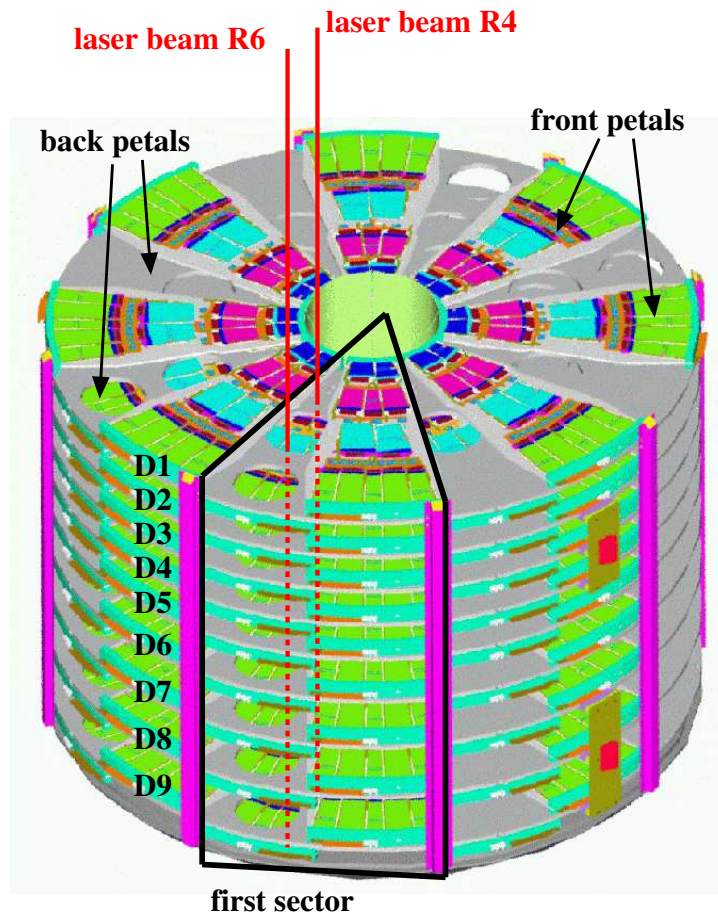

Abbildung 5.25.: Subdivision of TEC+ into 8 sectors, each consisting of 9 front and 9 back petals. The R4 and R6 laser beams for the first sector are also indicated.

All laser signals are shown in figures 5.26, 5.27, 5.28, 5.29, 5.30, and 5.31, where the signal S is plotted versus the strip number of the corresponding module.

These are the first LAS signal measurements in the TEC structure including the final readout components. Common-mode noise was subtracted by performing a straight line fit to the segments of groups of 64 strips without a laser signal. The result was used to correct the entries of all 64 strips in the group thus leading to a uniform baseline distribution. This procedure helped to recover apparent displacements in the position of the laser spot caused by baseline shifts from APV 1 to APV 4.
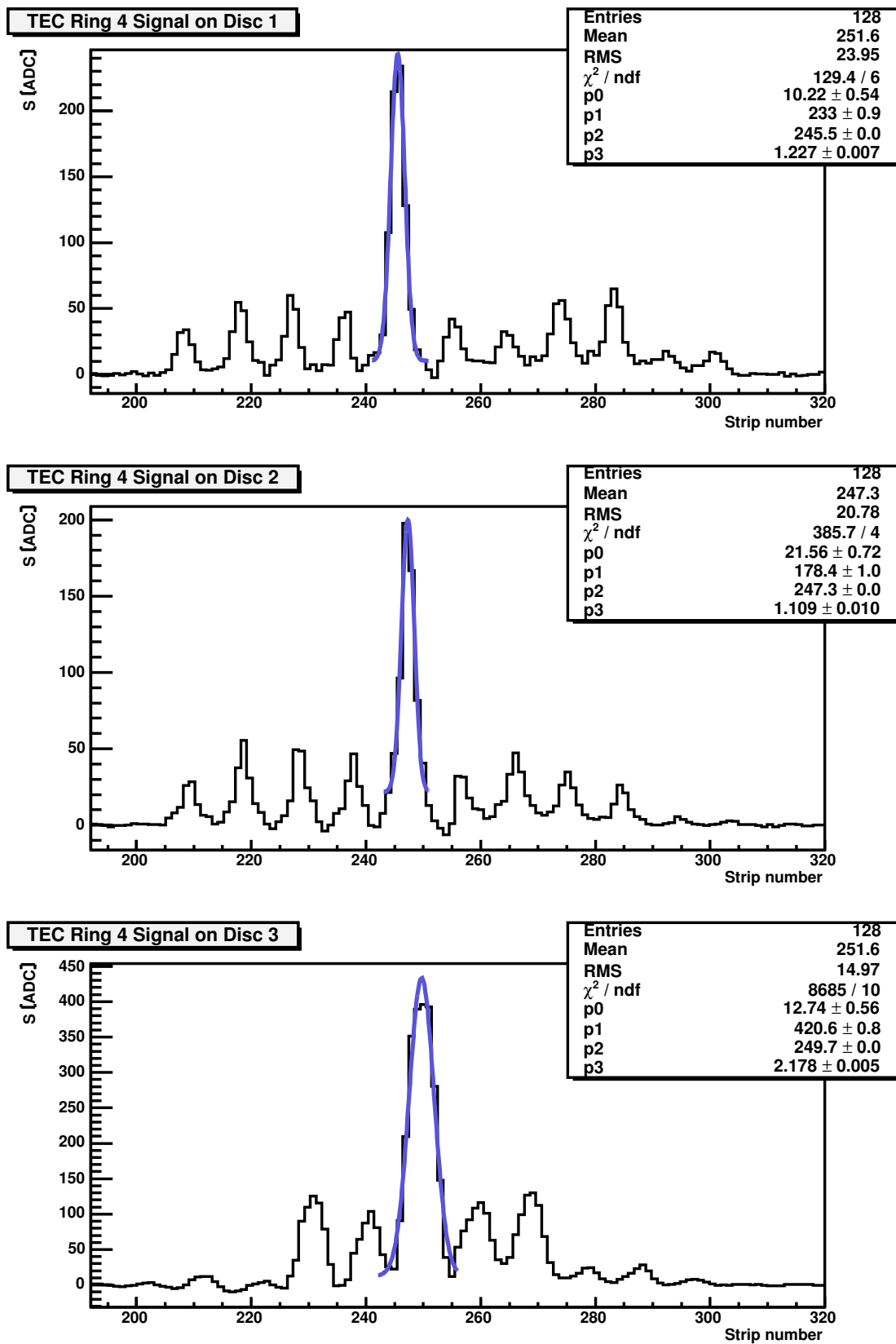
TEC Ring 4 Signal on Disc 1		Entries	128
		Mean	251.6
		RMS	23.95
		χ^2 / ndf	129.4 / 6
		p0	10.22 ± 0.54
		p1	233 ± 0.9
		p2	245.5 ± 0.0
		p3	1.227 ± 0.007

TEC Ring 4 Signal on Disc 2		Entries	128
		Mean	247.3
		RMS	20.78
		χ^2 / ndf	385.7 / 4
		p0	21.56 ± 0.72
		p1	178.4 ± 1.0
		p2	247.3 ± 0.0
		p3	1.109 ± 0.010

TEC Ring 4 Signal on Disc 3		Entries	128
		Mean	251.6
		RMS	14.97
		χ^2 / ndf	8685 / 10
		p0	12.74 ± 0.56
		p1	420.6 ± 0.8
		p2	249.7 ± 0.0
		p3	2.178 ± 0.005

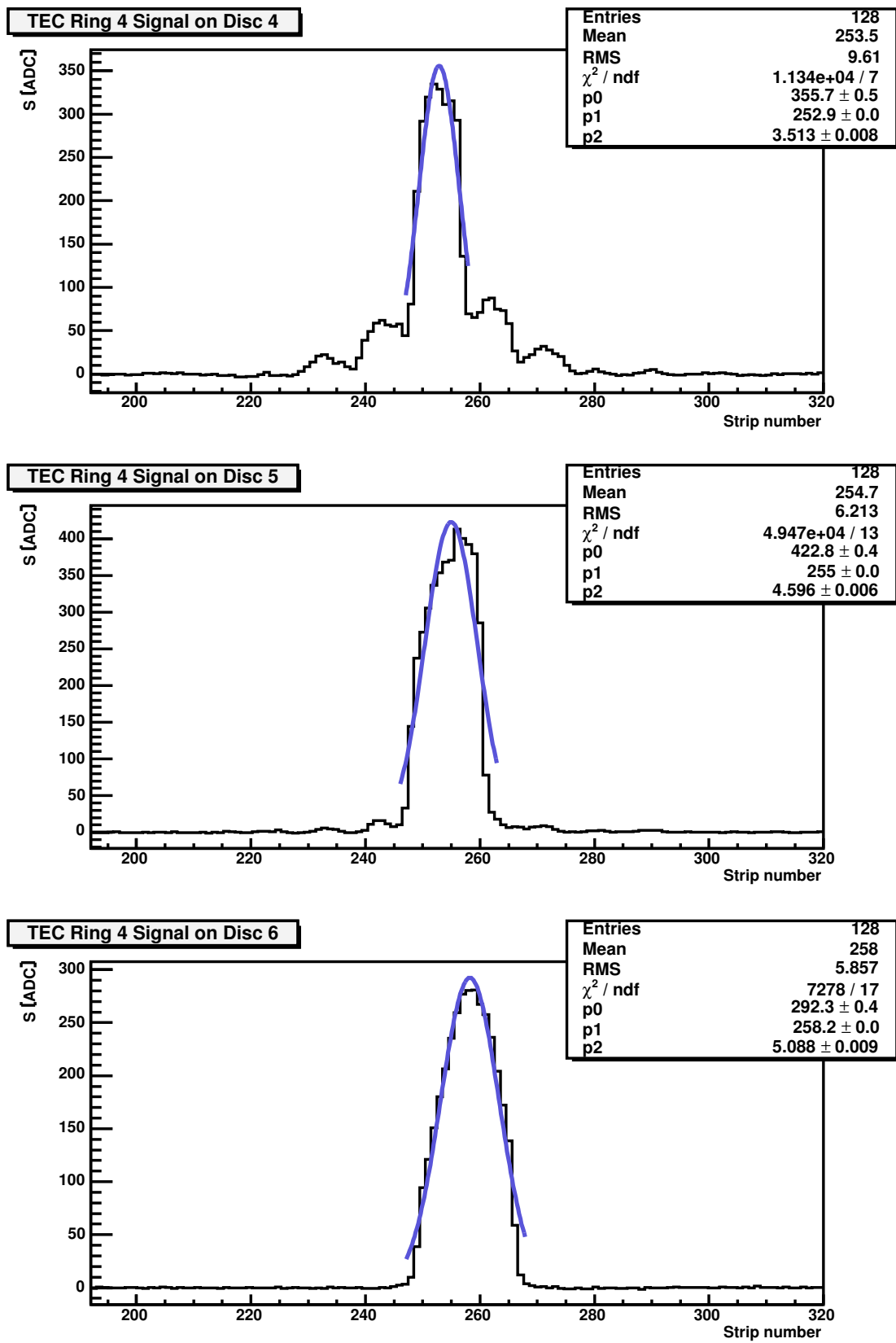Abbildung 5.26.: TEC R4 signals from D1 to D3 and laser spot reconstruction.

Abbildung 5.27.: TEC R4 signals from D4 to D6 and laser spot reconstruction.
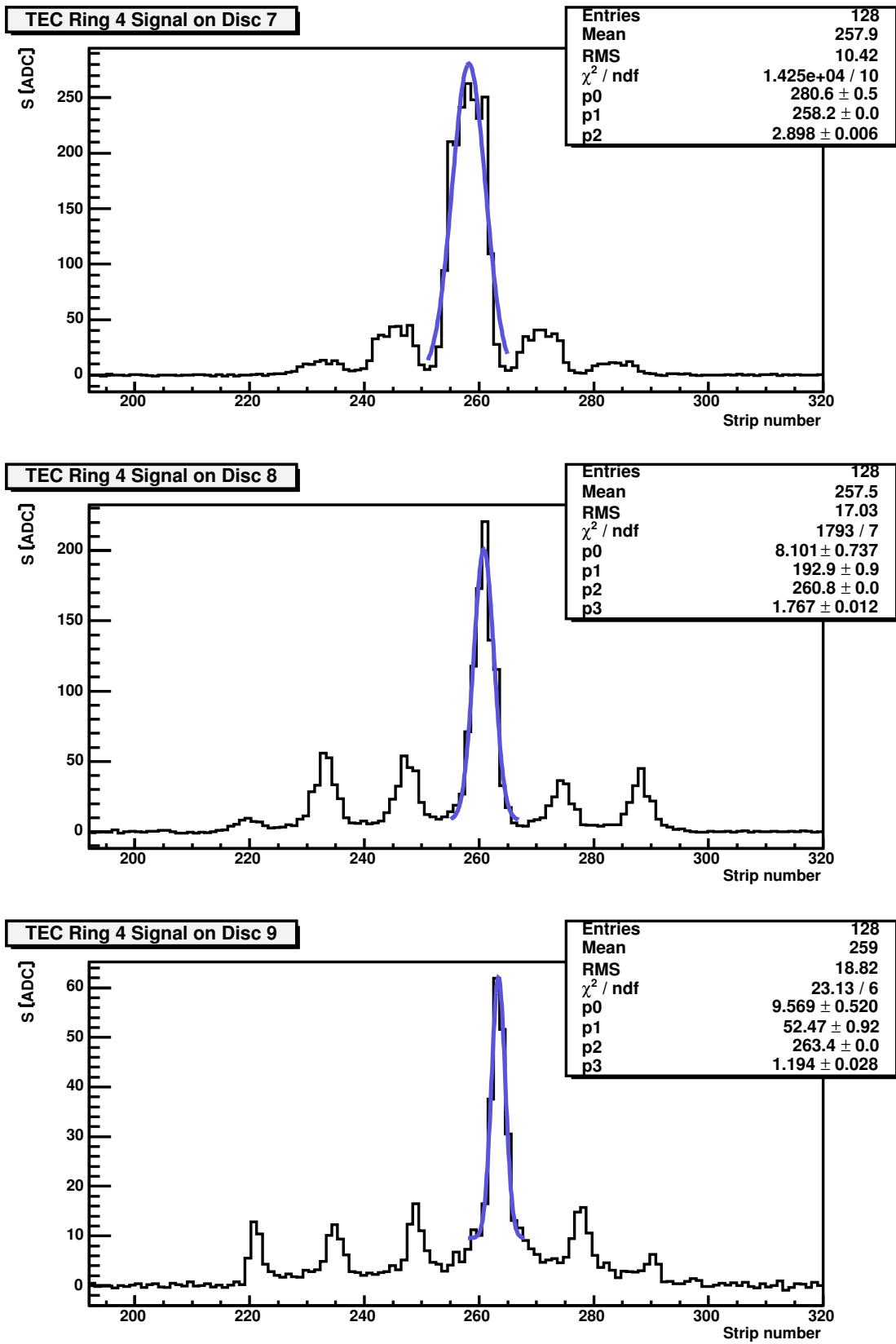
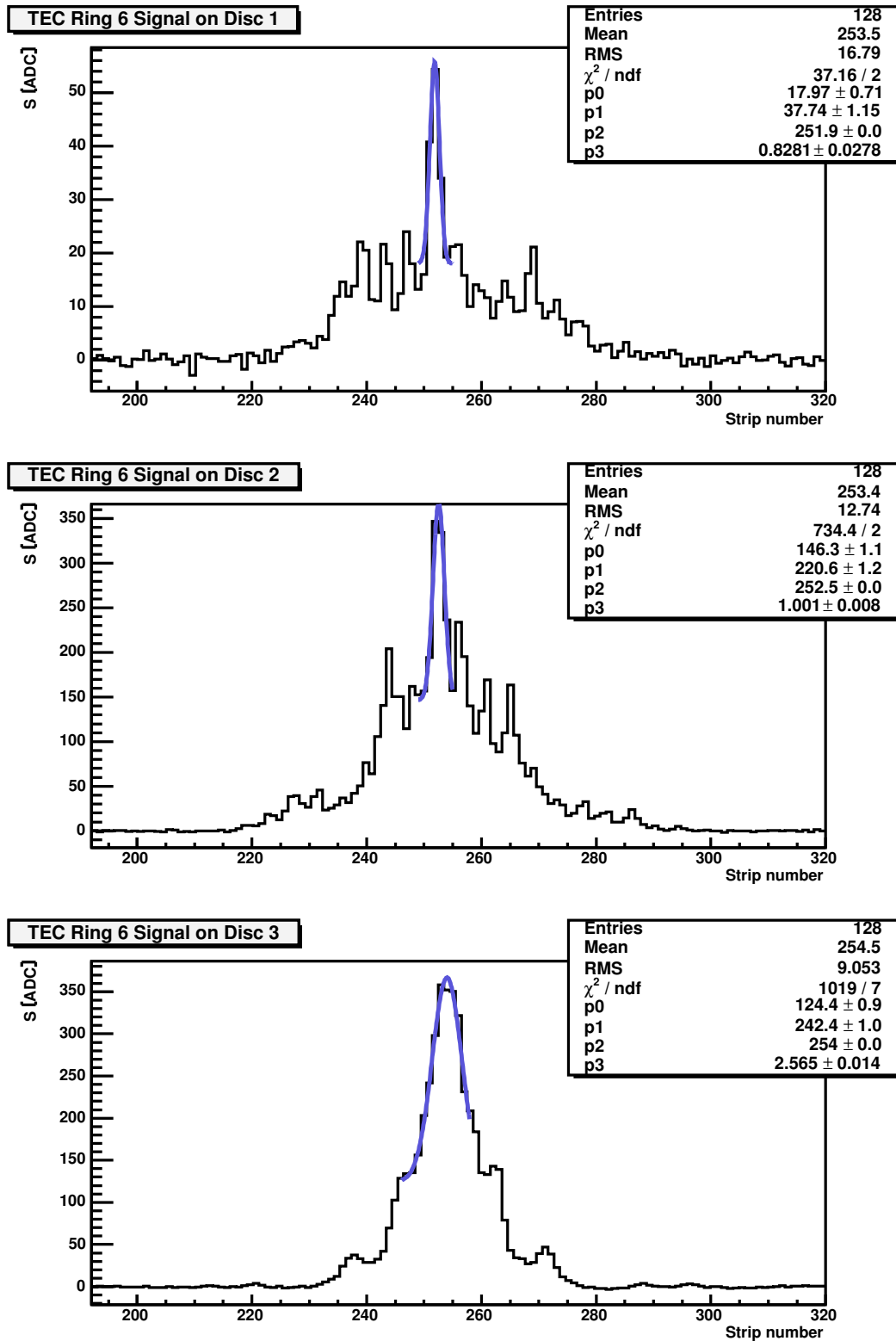Abbildung 5.28.: TEC R4 signals from D7 to D9 and laser spot reconstruction.

Abbildung 5.29.: TEC R6 signals from D1 to D3 and laser spot reconstruction.
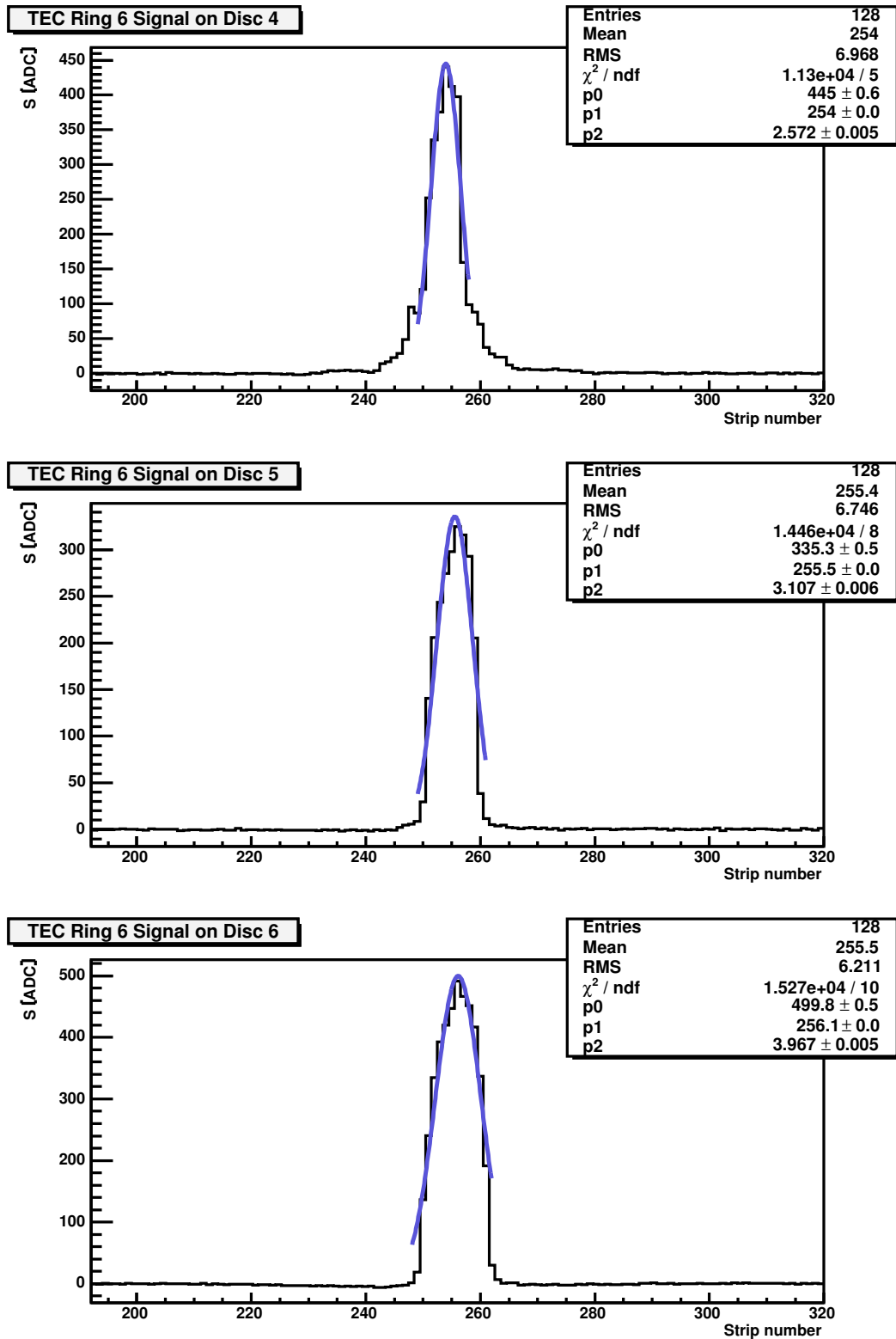
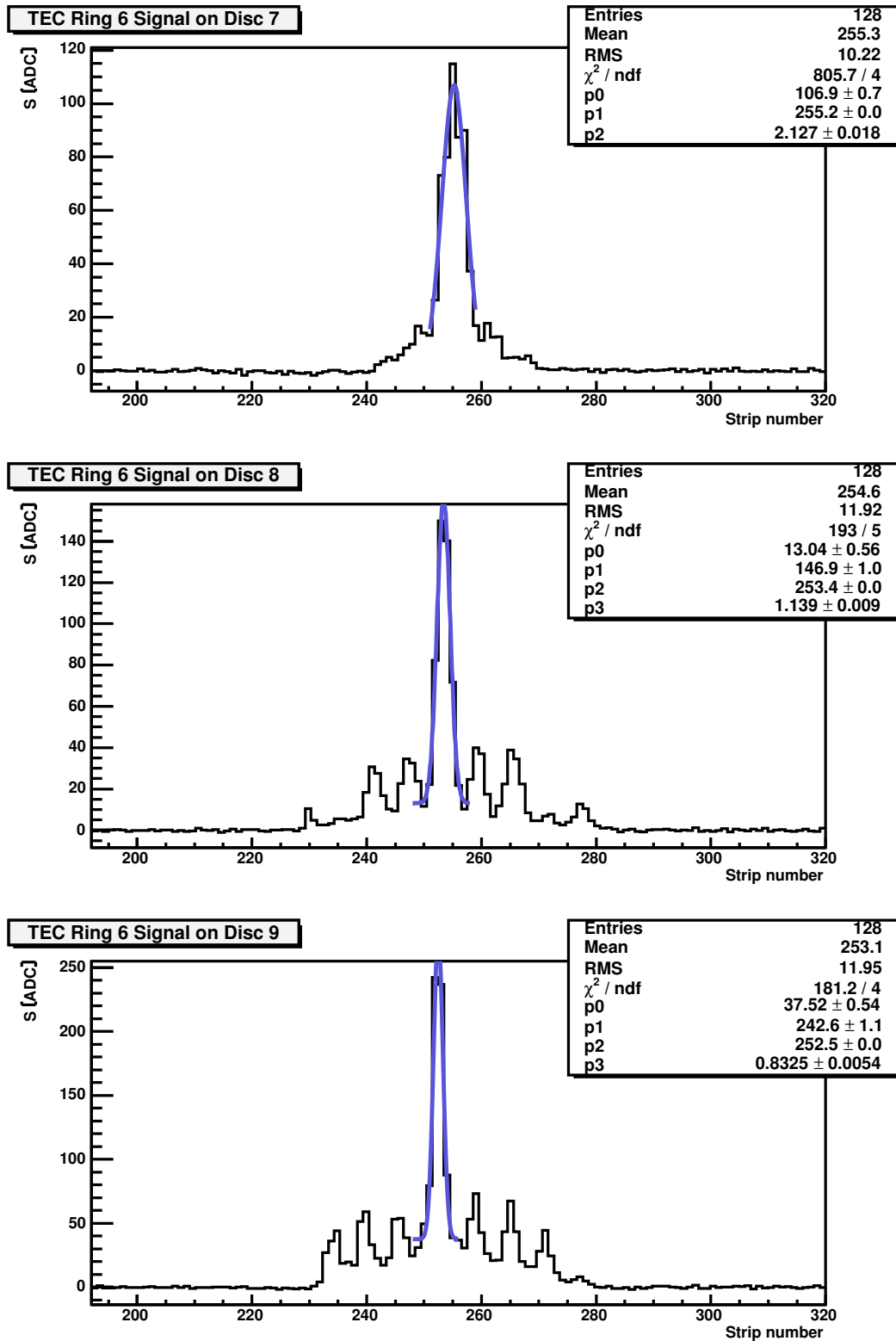Abbildung 5.30.: TEC R6 signals from D4 to D6 and laser spot reconstruction.

Abbildung 5.31.: TEC R6 signals from D7 to D9 and laser spot reconstruction.

In comparison to signal shapes measured in the laboratory (see figures 5.5 - 5.7), the spectra show the same diffraction pattern with higher order maxima tending to overlap with the central maximum for R6 in D1 and D2 as before.

The mean value of the position of the laser spot on each disc was obtained by fitting a gaussian to the beam profiles over the region of the central maximum. Only three parameters were fitted, the fit performance being considerably better by omitting the offset a_0 in the function (5.3).

The reconstructed positions of the laser spot in R4 and R6 are shown in figure 5.32 for all nine discs D1 - D9. The kink at the position of the beamsplitter on D6 is clearly visible.
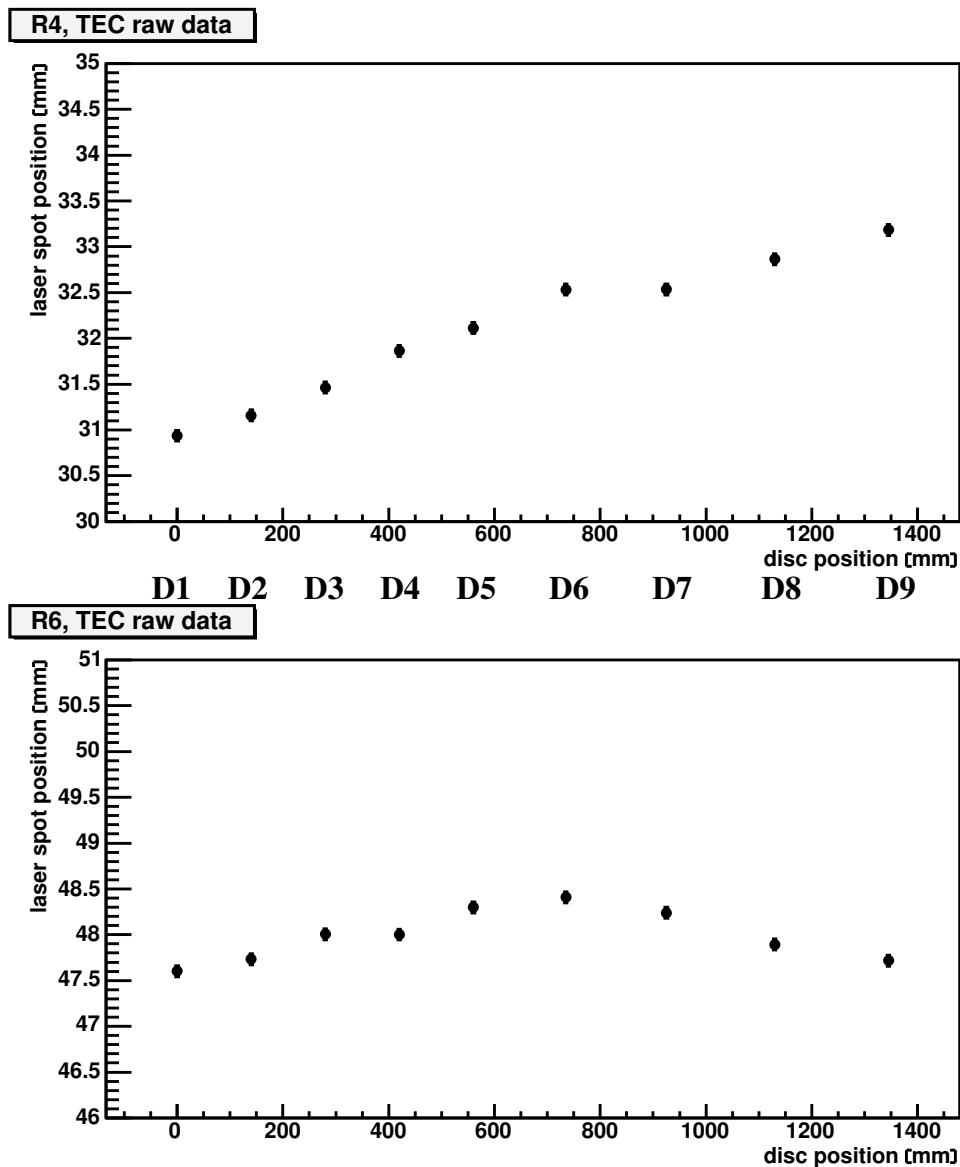

Abbildung 5.32.: Reconstructed laser spot position in R4 and R6, without BS corrections.

5. Laser Light Detection

Since the beamsplitter collinearity angles are known (see table G.1)

- $\theta_{C,R4} = -1.399\ mrad$

- $\theta_{C,R6} = -2.532\ mrad$

it was possible to apply corrections to the raw laser spot positions of figure 5.32. After correction a straight line fit to all nine points (D1 - D9) was performed and the residuals were calculated.
Details about the procedure are given below.

1. The BS is integrated in D6 right in front of the backpetal (see figure 5.4), dividing the TEC into a left (D1 - D5) and right (D6 - D9) part. Separate linear fits are shown in 5.33.
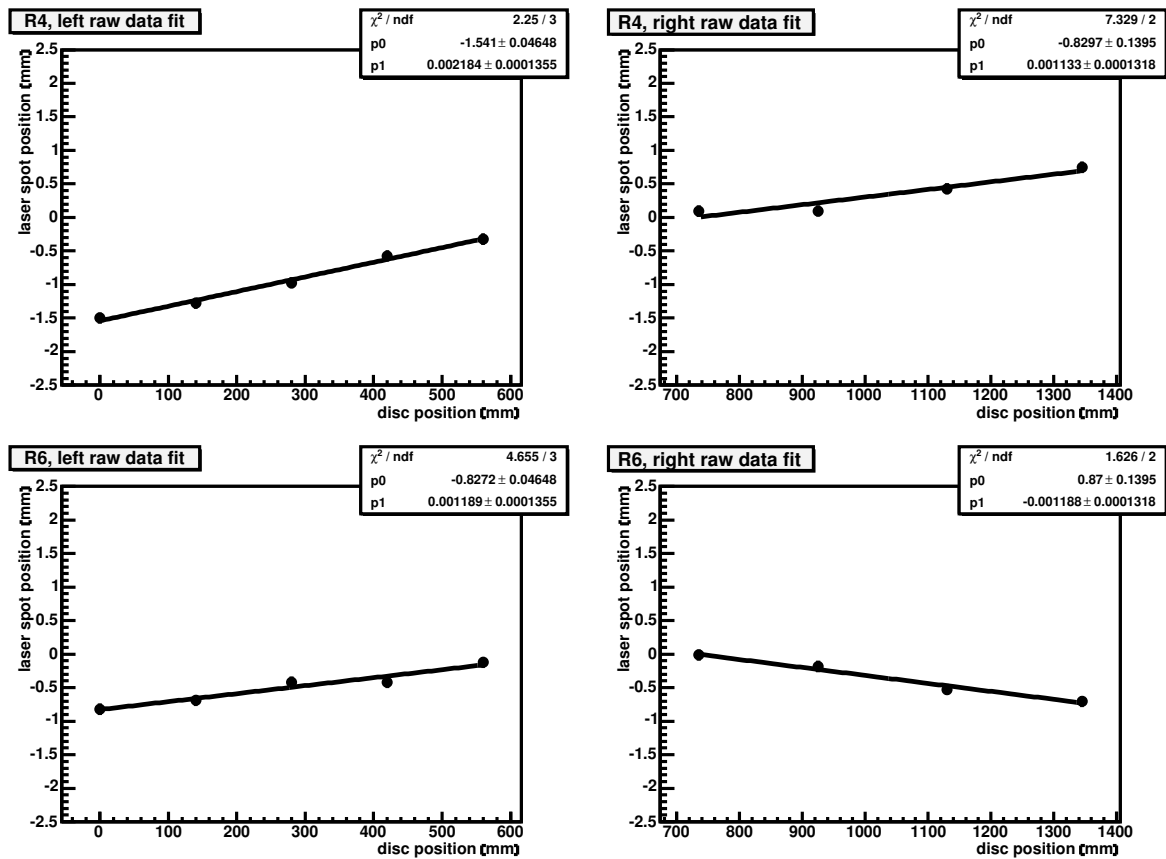

Abbildung 5.33.: Separate fit of beam 1 (D1 - D5) (*left*) and beam 2 (D6 - D9) (*right*) of R4 (*top*) and R6 (*bottom*).

2. Since the BS is located in D6 at $z_{BS} = 732\ mm$, the right side linear fit functions f_{R4} and f_{R6} were evaluated at z_{BS} to obtain the vertical BS position: $f_{R4}(z_{BS}) = 32.437\ mm$, $f_{R6}(z_{BS}) = 48.422\ mm$.

3. The BS collinearity angle θ_C is used to apply angular corrections to the right part (dashed line) by rotation around the vertical BS position determined above (e.g. for R4 by $p_{1,R4_{mod}} = (1.133 + 1.399)\ mrad$) and results in the corrected positions shown in figure 5.34.

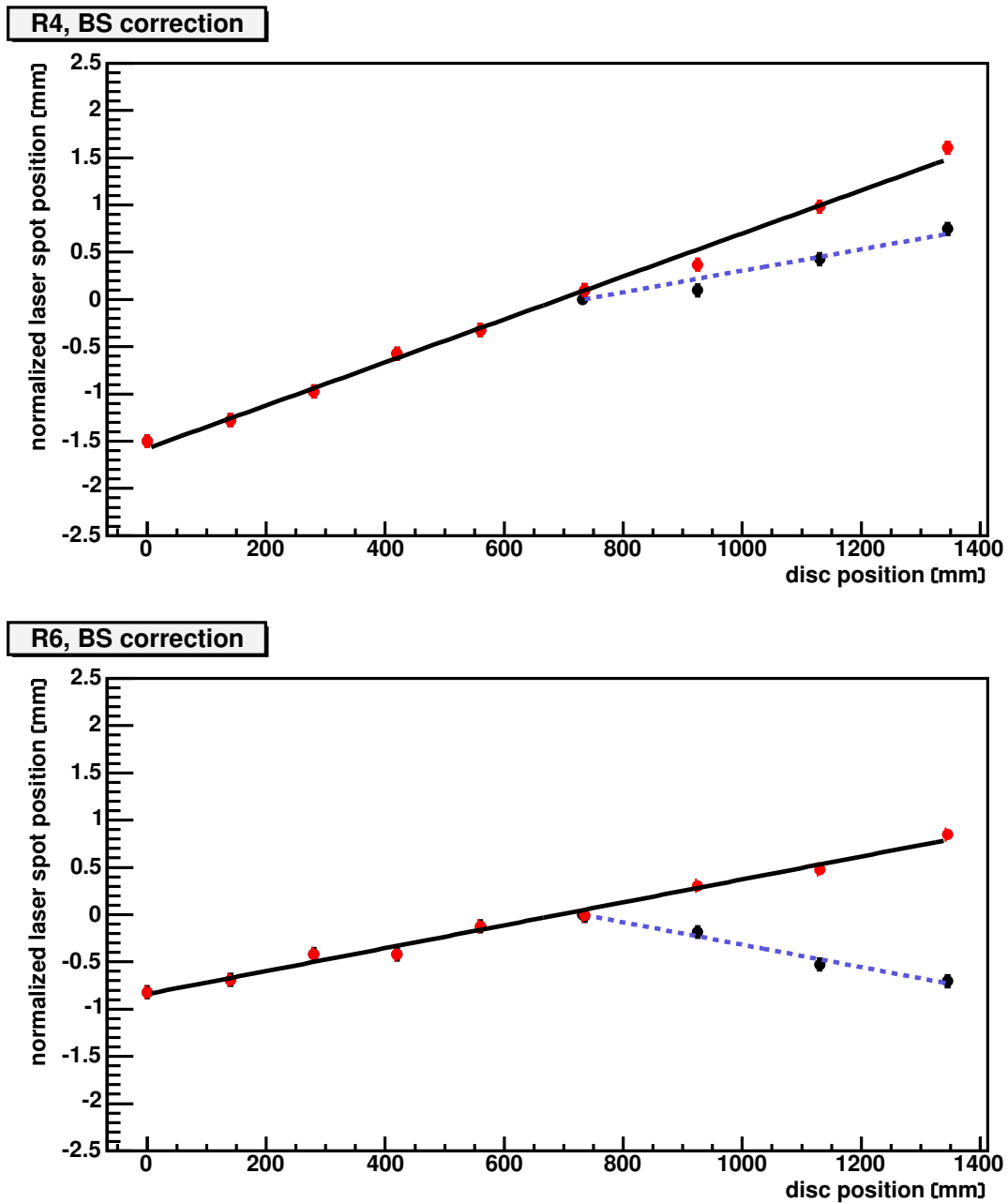Abbildung 5.34.: Comparison of the data before (dashed line) and after (solid line) the BS collinearity correction. The BS position is taken to be at (732,0).

4. Figure 5.35 shows the results of a linear fit to the corrected points from D1 to D9. The distribution of the fit residuals is given in figure 5.36, separately for R4 and R6 as well as combined for both.
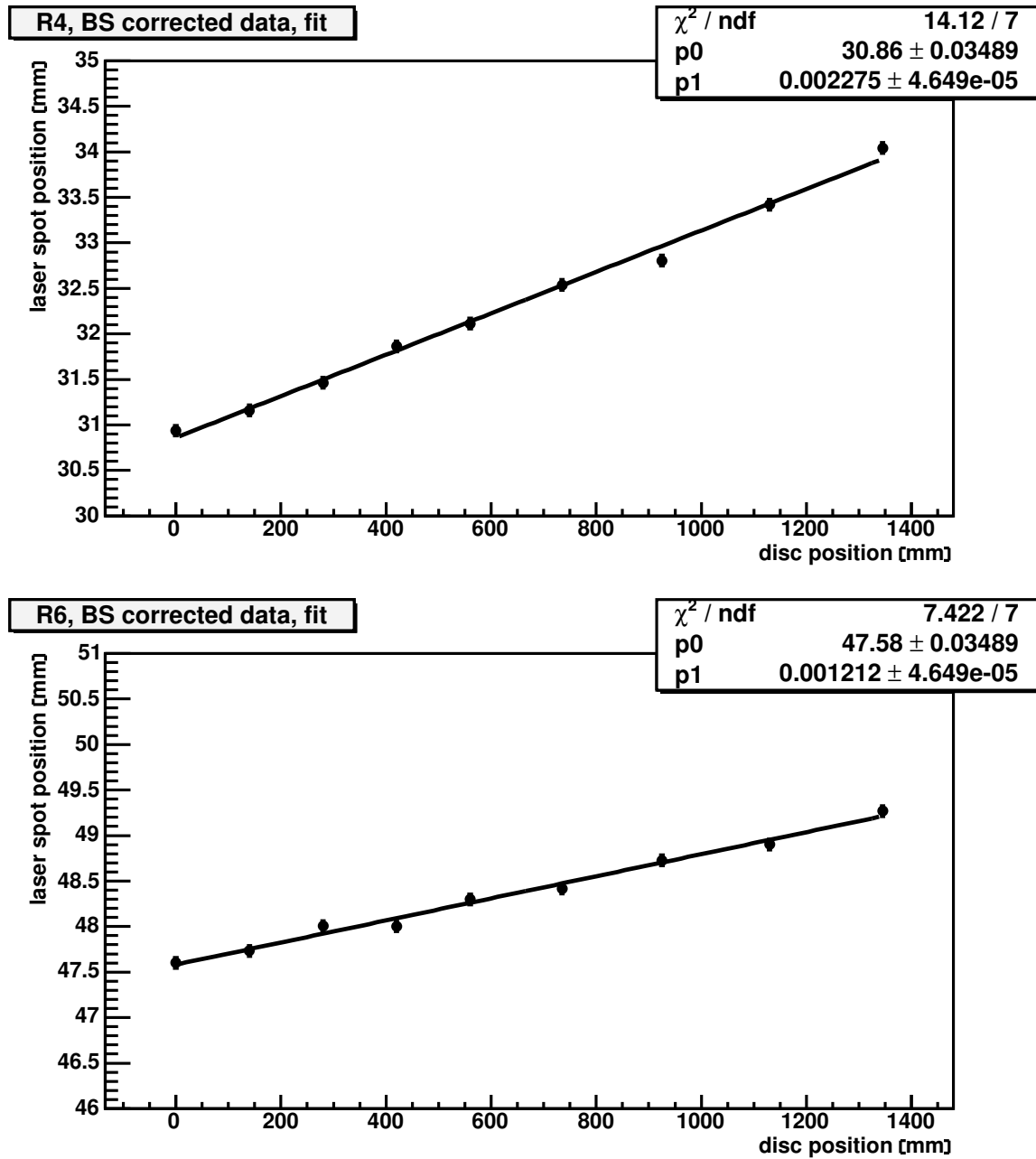

Abbildung 5.35.: Single fit from D1 to D9 after the BS correction.
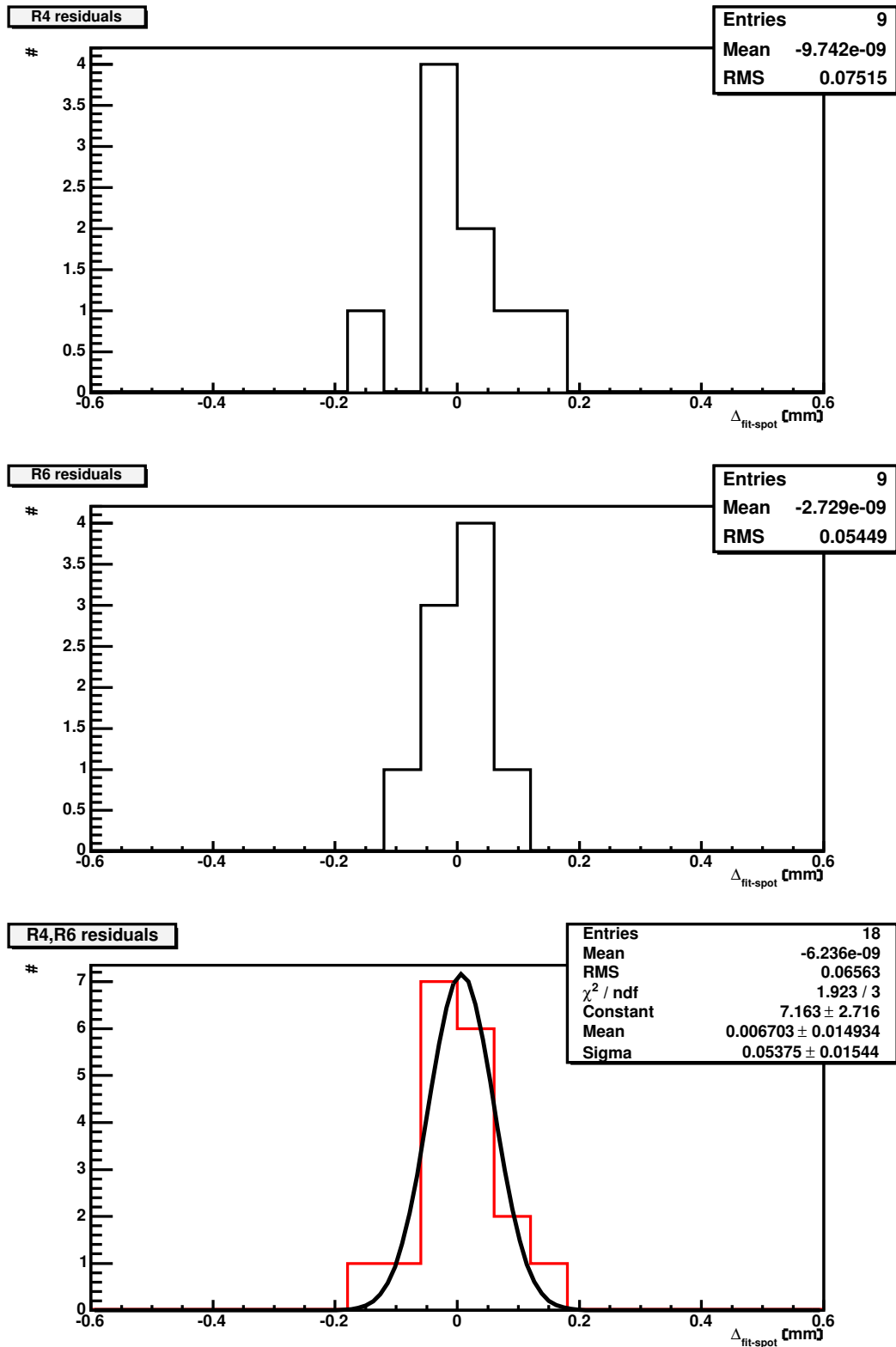
Abbildung 5.36.: First TEC+ sector residuals. Combination of data from the two laser beams, R4 and R6, give an absolute TEC+ reconstruction precision of 54 μm, which is approximately twice better than required.

The combined result for R4 and R6 is

$$\sigma_{R4,R6} = 54 \ \mu m \qquad RMS_{R4,R6} = 66 \ \mu m$$

and demonstrates that the LAS allows checking the assembly accuracy of the first TEC+ sector to much better than 100 μm. Hence it follows that one of the main goals mentioned in chapter 2, has been already achieved with the data of one TEC sector. These results can be improved by taking information from the optical alignment of further sectors into account, since additional redundancy and constraints are then provided. At the same time alignment using cosmic muon tracks can be used to calibrate the LAS.

Studies on relative position changes, e.g. comparison of LAS sector data at room temperature with data in a cold environment, as well as effects of common-mode noise correction and FED operation modes will be discussed in [66], [54].

5.4.2. Survey Measurements

Quantitative validation and justification of the LAS results can be achieved by comparing to an independent external disc reference frame. Survey measurements are based on the
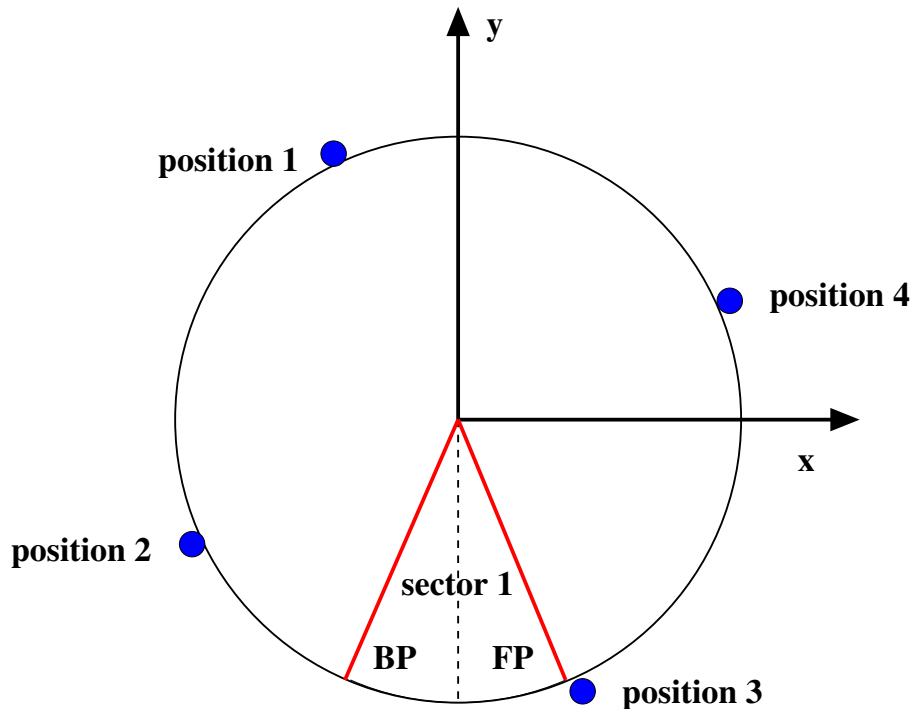
Abbildung 5.37.: Survey measurements coordinate system. Due to the larger lever arm, $\Delta\varphi$ changes in the azimuthal orientation φ are more sensitive to changes Δx of the x-coordinate at positions 3 and 1. Conversely, the sensitivity of $\Delta\varphi$ is greater to changes Δy for positions 2 and 4.

reconstruction of four well defined reference targets on each TEC disc and on the TEC back flange (see picture I.2), leading to a total of 40 data points. The measurements were

analyzed by considering the TEC as a sheared rigid cylinder, neglecting any torsion effects [41]. The residuals computed in this model for the 36 positions measured on the nine TEC discs are shown in figures 5.38 and 5.39. As it is illustrated in figure 5.37, the first sector is closer to survey position 3 and therefore the results for this position are emphasized below.
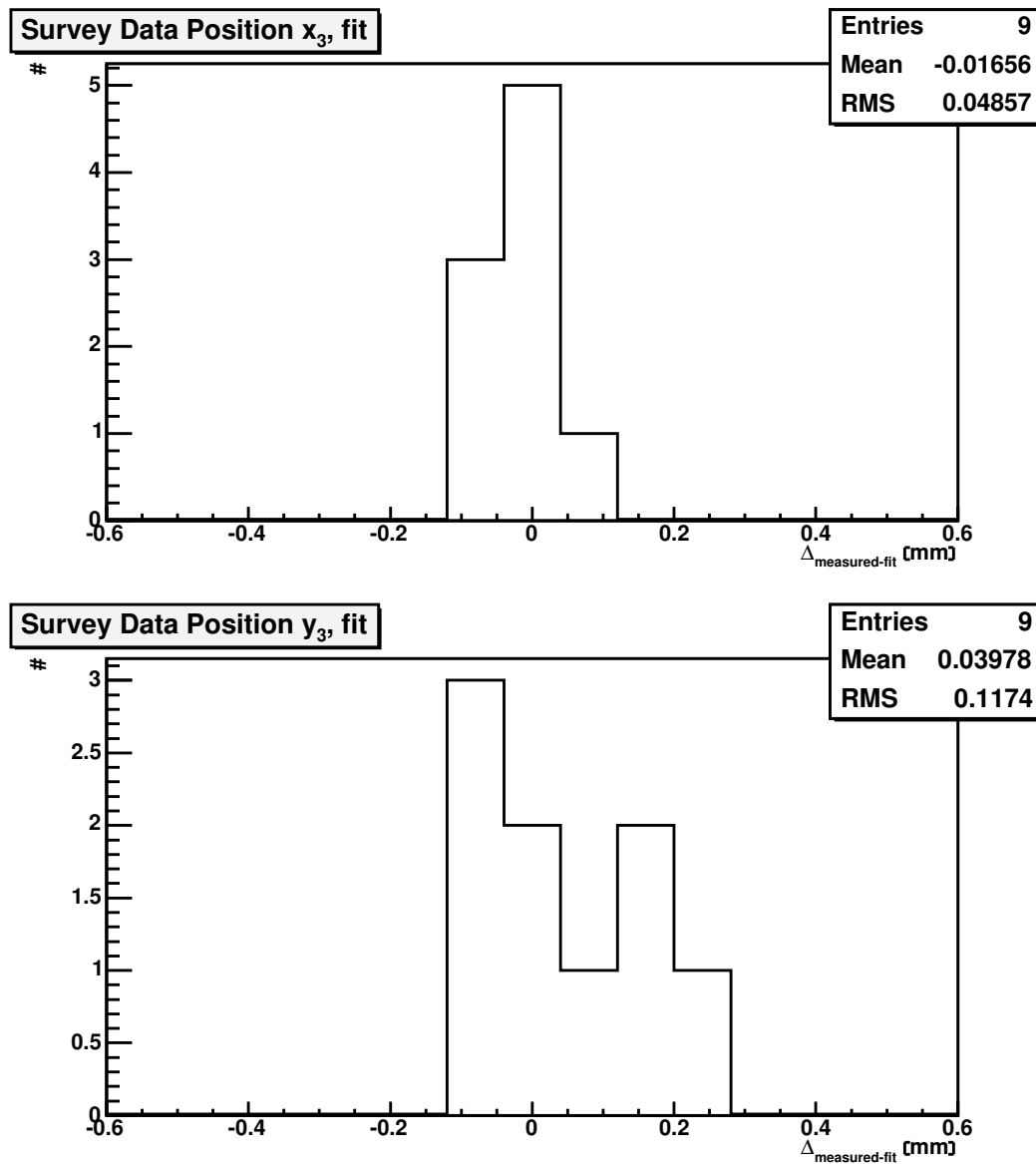

Abbildung 5.38.: Residuals at position 3. The reconstruction model was more sensitive to changes in $r\varphi$, explaining the difference between both RMS values.

Survey Data Position x₁, fit

Entries	9
Mean	0.02022
RMS	0.05818

Survey Data Position y₁, fit

Entries	9
Mean	-0.04856
RMS	0.1402

Survey Data Position x₂, fit

Entries	9
Mean	-0.004667
RMS	0.1168

Survey Data Position y₂, fit

Entries	9
Mean	-0.001889
RMS	0.04837

Survey Data Position x₄, fit

Entries	9
Mean	0.006111
RMS	0.1017

Survey Data Position y₄, fit

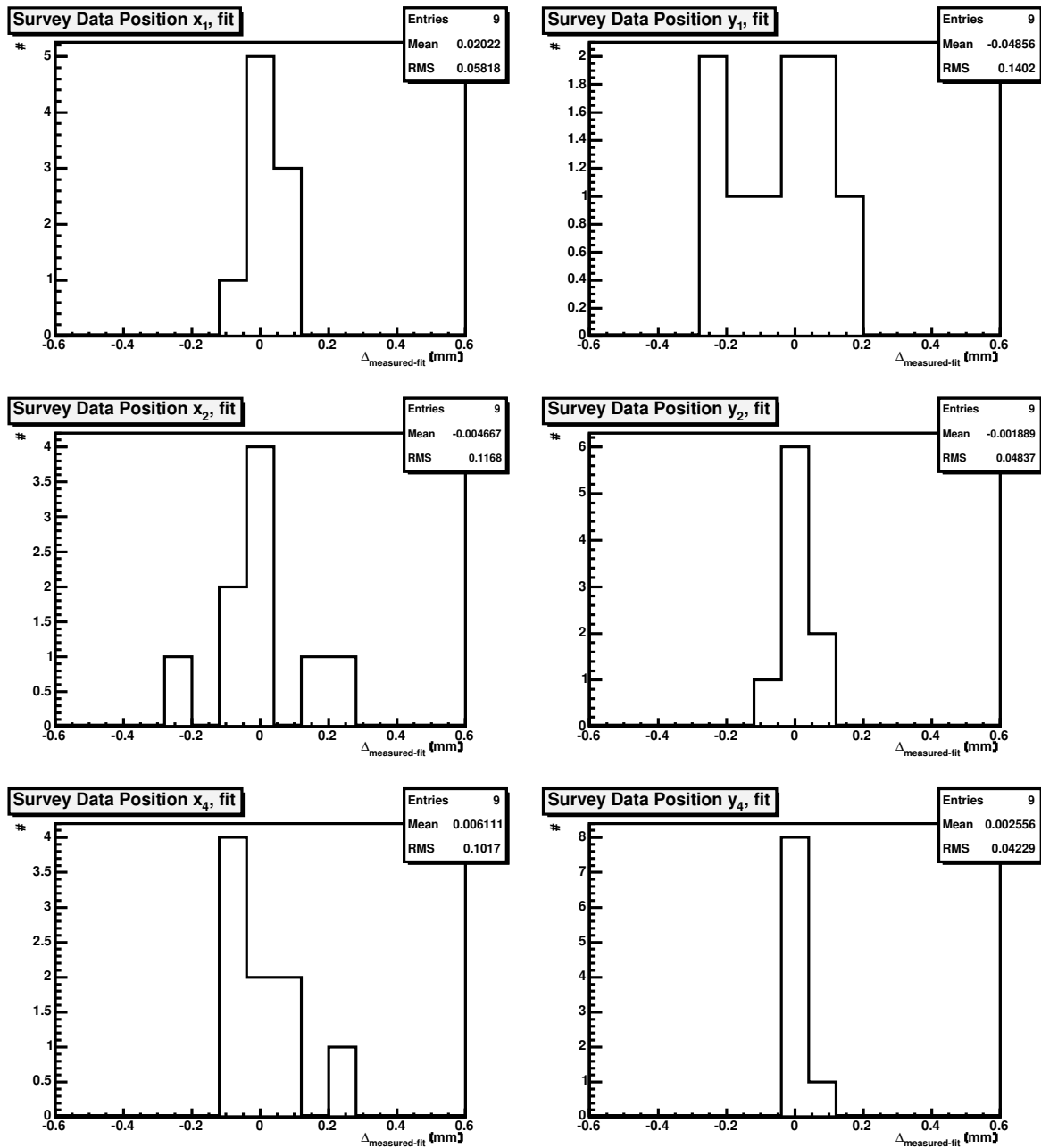| Entries	9
Mean	0.002556
RMS	0.04229

Abbildung 5.39.: Residuals at positions 1, 2, and 4. Also here the $\Delta_{r\varphi}$ sensitivity is obvious.

The mounting precision of the reference targets on each disc was $\Delta_r^{target} = 100 \ \mu m$ and $\Delta_{r\varphi}^{target} = 20 \ \mu m$, so that the reconstruction model was more sensitive to $\Delta_{r\varphi}$, principally to changes in x_1, y_2, x_3, y_4, named $S_{1,2,3,4}$ (see figures 5.38 and 5.39).

Figure 5.40 shows the distribution of the residuals for the coordinates x_1, y_2, x_3 and y_4. The distribution is well described by a gaussian and the result for the mechanical precision in assembling TEC+ is in the order of

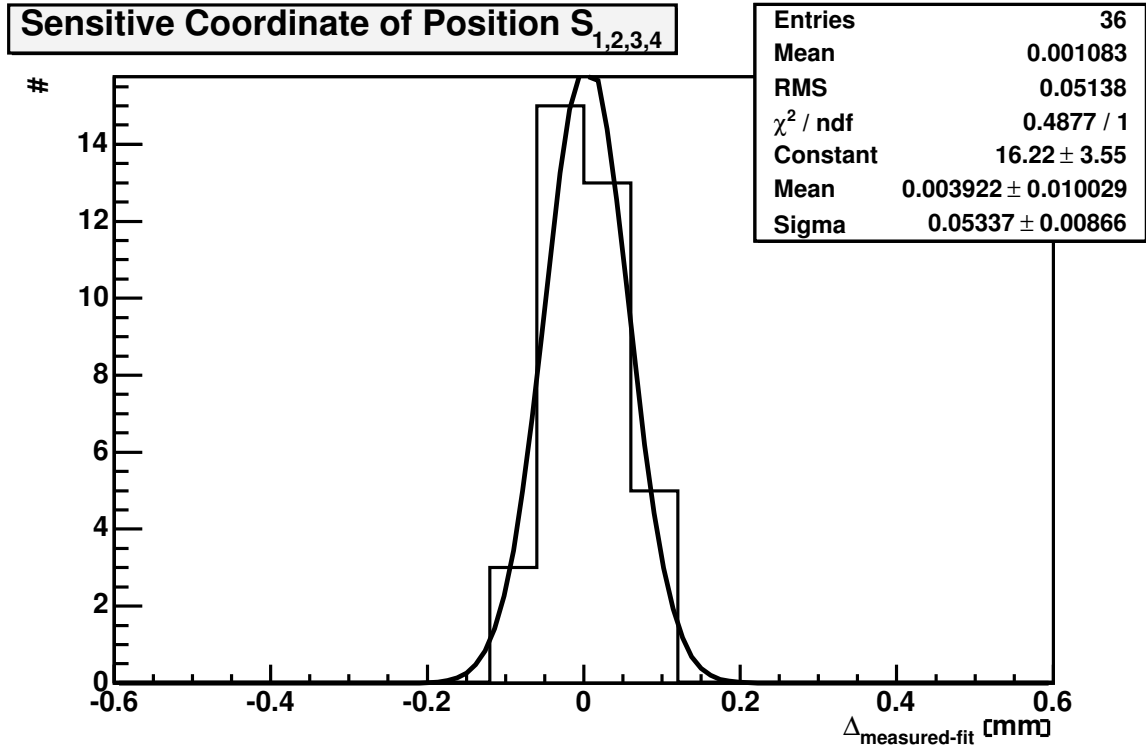$$RMS_{disc} = \Delta_{r\varphi}^{disc} = 50 \ \mu m$$

Abbildung 5.40.: Distribution of the residuals for the coordinates x_1, y_2, x_3, y_4.

5.4.3. Comparison with the Laser Alignment System

The petal mounting precision has been measured to be $\Delta_{petal} = 60 \ \mu m$ and the disc to disc assembly precision of the TEC+ structure is $\Delta_{disc} = 50 \ \mu m$, as described above. Both beams of the LAS are detected by modules on the petals, which have a placement accuracy of $20 \ \mu m \ll 60 \ \mu m$.

Assuming independent contributions to the total error budget, the results of the survey measurements should be confirmed by the LAS within $\Delta_{petal} \oplus \Delta_{disc} \approx 78 \ \mu m$.

The distribution of the difference of LAS residuals for R4 and R6 (figure 5.36) and the residuals of the survey data (figure 5.40) is shown in figure 5.41. It has an RMS of $72 \ \mu m$, fully consistent with the expectation of $78 \ \mu m$:

$$\Delta_{theo} = 50 \oplus 60 \approx 78 \ \mu m \qquad \Leftrightarrow \qquad \Delta_{exp} = 72 \ \mu m$$

This confirms that the LAS reconstruction of the first TEC+ sector is in good agreement with the survey measurements.
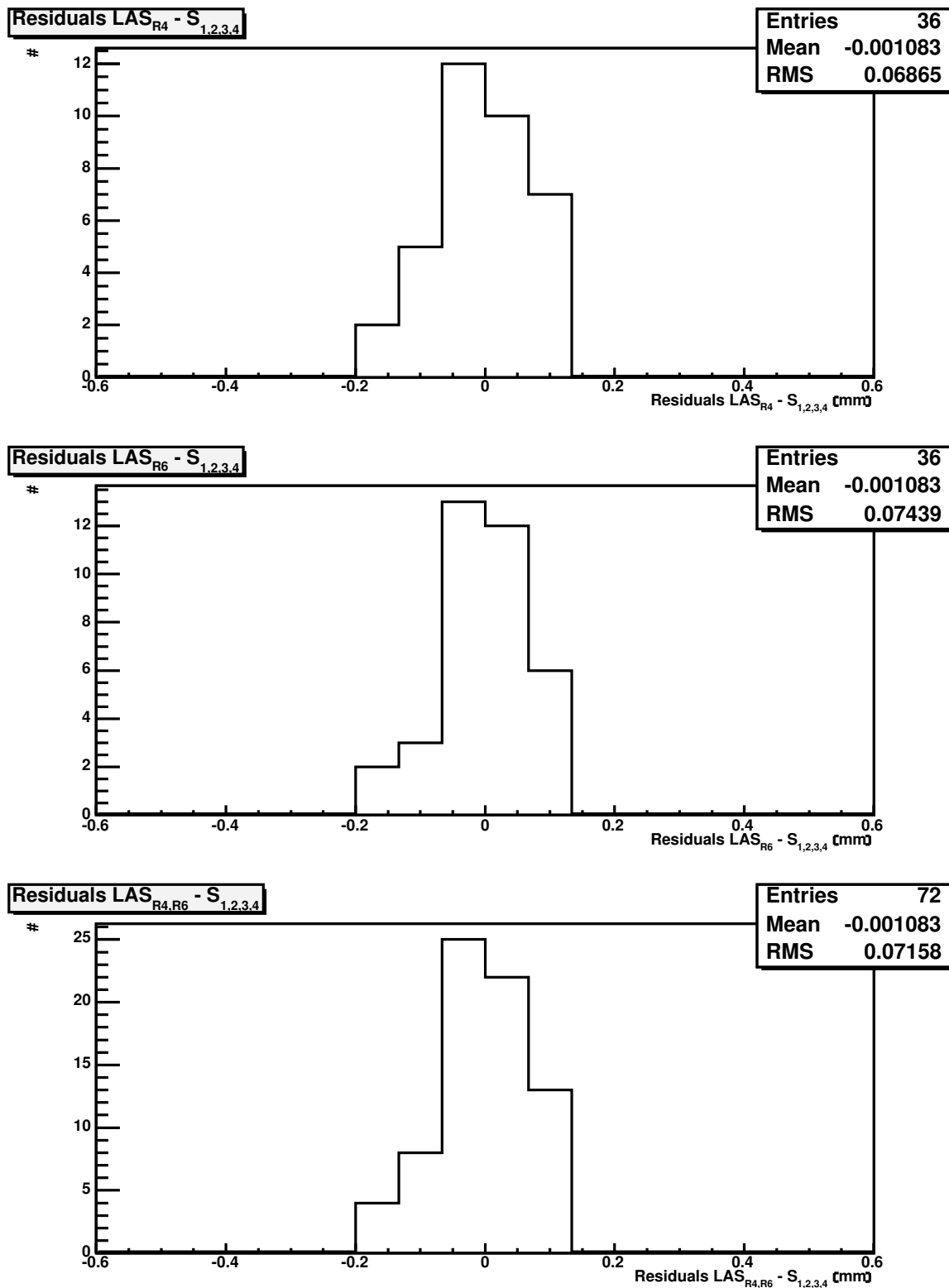
Abbildung 5.41.: Comparison of all LAS R4, R6, and metrology data residuals. The RMS value of the residuals is a measure of the TEC reconstruction precision determined by both independent systems.

Implementation of a possible torsion of the TEC structure into the theoretical survey model as well as LAS data from additional sectors should improve the determination of the disc positions with respect to each other.

Further understanding of the performance of the LAS can be reached through additional investigations, e.g. studies of:

- Noise behaviour
  Different methods of base line corrections should be tried for common-mode noise subtraction.

- Intensity variation at one layer
  Dependence of the reconstruction of the laser beam profile on laser intensity.

- FED operation modes
  Application of different FED readout modi (e.g zero suppression mode) and analysis of the corresponding optical signals.

- Temperature dependence
  Comparison of LAS data at room temperature with data in a cold environment. It has to be tested, whether these are any BS mount movements and whether a common reference system is valid for both environments.

- Resolution data
  The different laser spot resolutions measured in the laboratory for each disc position must be implemented in the analysis. Monitoring of relative position changes of the assembled TEC can be checked by recording precise displacements of an additional BS mounted separately on an external structure.

- Fit performance and reconstruction
  Alignment information from all sectors has to be combined in the reconstruction model. Possible contributions of badly determined points have to be analyzed and appropiately treated.

- Track alignment
  Calibration of the LAS using cosmic muon data for each sector in warm as well as in the cold environment.

5.   Laser Light Detection

6. Conclusions

6.1. Summary

This thesis presents the design, research and development and validation through laboratory tests of an optical alignment system for the CMS tracker. First data following integration of the system into the first sector of the tracker endcap TEC+ have also been analyzed.

The laser alignment system (LAS) employs a number of laser beams generated by diodes and detected by the same silicon sensors used as tracking detectors. These sensors were made transparent to laser light by omitting the backplane metalization over the small area crossed by the beams. It has been verified that their electrical and charged particle detecting properties were not affected by this modification.

For a series of consecutively arranged module layers light absorption inside each module should be enough to create a useful signal, but transmission should be also sufficient in order to reach the next layer. It was found possible to link up to five module layers with a single beam, but to be able to align all nine discs of the TEC structure a beamsplitting device had to be used.

The beamsplitter (BS) is described in detail in chapter 3. In order to satisfy the geometrical constraints it is based on the polarization principle and to fulfill the alignment requirements it should provide two back-to-back beams whose collinearity is known and stable to within 50 μrad. The stability of the beamsplitter collinearity was checked as a function of time and as a function of temperature in the range $+15^oC$ to -25^oC, since the CMS tracker operating environment will be $\approx -10^oC$. It was shown to satisfy the 50 μrad requirement stated above. All beamsplitters to be built into the laser alignment sytem were calibrated by measuring their collinearity at room temperature in the laboratory.

Chapter 4 deals with the optical properties of the silicon sensors. To minimize reflection, and thus increase transmission and absorption, an anti-reflex-coating was applied on the ohmic side of the silicon sensors over the area transparent to the laser beams. The improvement in surface quality also led to uniformity of transmission and absorption and to a minimization of interference effects. The increase in transmission through application of the anti-reflex-coating was measured to be 18 % and 20 % for ring 4 (R4) and ring 6 (R6) sensors respectively.

The resolution in reconstructing the laser spot on each of the TEC discs is discussed in chapter 5. It was checked that beam refraction effects are negligible and that relative movements of the detector structure can be resolved at the 10 μm level. Laser data from the first sector integrated in the TEC, involving 2 laser beams and 18 petals, were used to reconstruct the absolute positions of the 9 TEC discs with an accuracy of 50 μm, much

better than the 100 μm required for the laser alignment system. This result has been confirmed by comparison with survey measurements.

6.2.   Future Plans

The beamsplitters have been installed in both tracker endcaps and integration of petals in TEC sectors is proceeding.

The measurements performed for the first sector have to be repeated for all other sectors separately and a full reconstruction of the tracker endcap has to be done by combining all experimental information. The improvement expected from the redundancy of the optical alignment can be verified. In addition alignment using cosmic muon tracks should be used to calibrate the LAS.

More understanding in monitoring relative subdetector movements is needed. Detailed studies regarding module noise behaviour, procedures for its subtraction, intensity variations and beam profile changes per layer are in preparation.

The alignment tubes have to be qualified and integrated into the tracker outer barrel (TOB) envelope and the alignment of the endcap and barrel substructures has to be studied.

Implementation of the LAS into the CMS DAQ has to be completed. The performance of the optical link to the muon system is being evaluated during the ongoing CMS magnet test.

A. Tracker Pictures

In the following, a few pictures of the silicon strip tracker are collected [36].
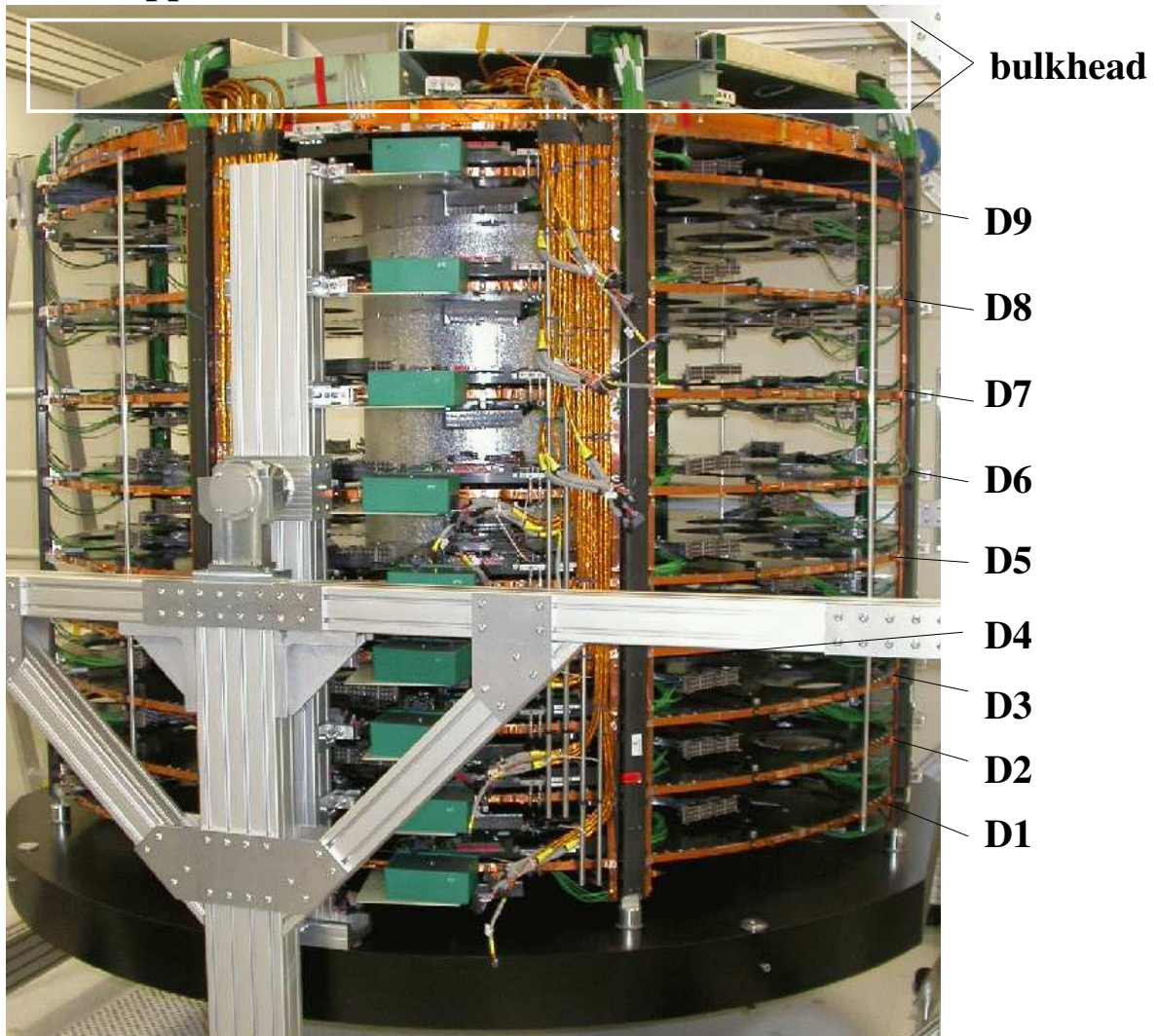
A.1. Endcap

TEC support structure

Abbildung A.1.: TEC support structure.

A.2. Inner Barrel/Disc

TIB halfbarrel layer 4
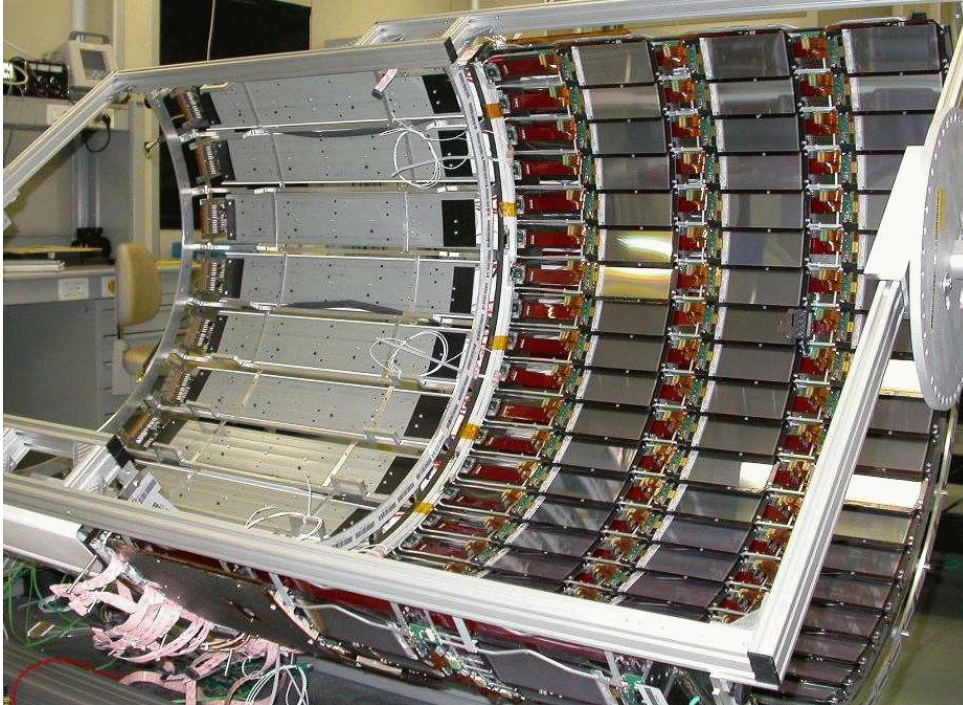

Abbildung A.2.: TIB support structure. Halfshell of outermost TIB layer with mounted modules.
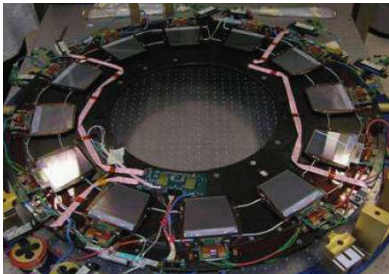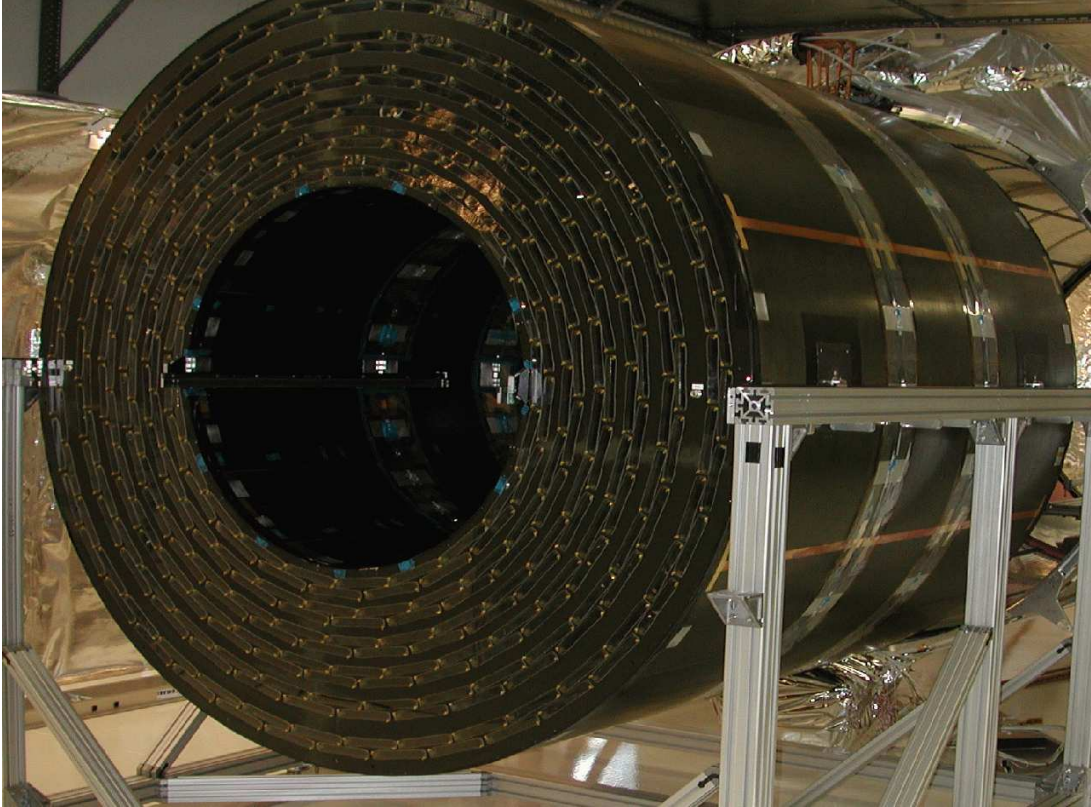
TID R1

TID R3

TID R2

TID Disc = R1+R3+R2

Abbildung A.3.: TID support structure. Combination of three layers to one disc.

A.3. Outer Barrel

TOB support structure

rod top view

Abbildung A.4.: TOB support structure and front side of a TOB rod with three modules.

A.   Tracker Pictures
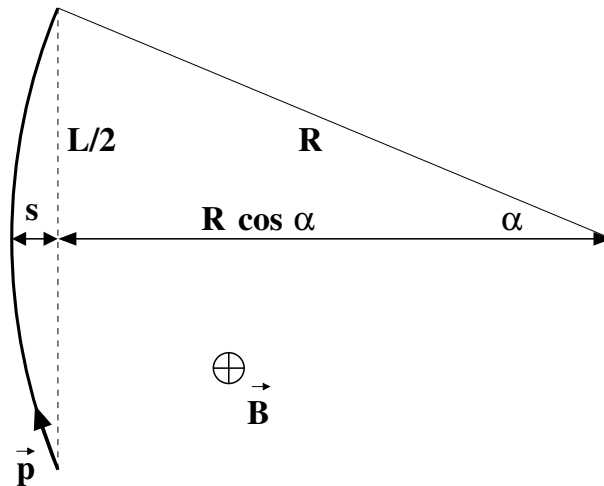
B. Momentum Resolution

Abbildung B.1.: Track curvature bending in presence of a magnetic field.

From figure B.1 the following geometrical relations can be derived:

$$\alpha = \frac{L}{2R} \qquad S = R \, (1 - \cos(\alpha)) \approx R \, \frac{\alpha^2}{2} = \frac{L^2}{8 \, R}$$

The sagitta S, deviation from a straight line, is proportional to the square of the travel distance inside the tracker. The bending radius R scales with the transverse momentum, if p $\perp$ B.

$$R = \frac{p_T}{0.3 \, B} \qquad p_T = q \, R \, B_z \qquad \text{p} \perp \text{B}$$

Hence it follows that for constant length L and magnetic field B the sagitta S is inversely proportional to p_T.

$$S = \frac{0.3 \, B \, L^2}{8 \, p_T} \qquad S \approx \frac{150 \, mm}{p_T/GeV}$$

This limits the tracker resolution for large particle momenta.

B.   Momentum Resolution

C. Laser Diode Power Estimation Studies

In first design studies the power of laserdiodes has been estimated. Starting from the assumption of 20 % transmission through a silicon sensor, two possible TEC scenaria have been calulated and experimentally verified.

1. Starting from the collimator, the laserbeams pass 8 consecutive modules before hitting the last layer. This leads to an intensity variation by six orders of magnitude, but has the advantage of having a single beam.

$$\left(\frac{1}{5}\right)^8 = \frac{1}{390625} = 2.56 \cdot 10^{-6} \tag{C.1}$$

2. Splitting the incoming beam into two collinear beams on disc 6, only four module layers are traversed, but an additional optical device (beamsplitter) is needed.

$$\left(\frac{1}{5}\right)^4 = \frac{1}{625} = 1.6 \cdot 10^{-3} \tag{C.2}$$

The LD power has been estimated for both options. With the help of known attenuation factors the calibration of a laser of $1\ mW$ output power in terms of signal-to-noise $\left(\frac{S}{N}\right)$ units of the APV readout chip lead to $1\ mW \,\hat{=}\, 3000\ \frac{S}{N}$ (see plot C.1). By assumption of a ratio of $\frac{S}{N} \approx 10$ to generate enough signal in the silicon sensor, the following results were obtained.

In the first option, a power of $10 \cdot 5^8 \approx 4 \cdot 10^6$ in $\frac{S}{N}$ units is required to generate sufficient signal in the last layer. This corresponds to laser diodes with an output power in the order of $1 - 2\ W$ and such diodes are not available.

Therefore, the second solution to integrate a beamsplitter inside the tracker, leads to $10 \cdot 5^4 \approx 6 \cdot 10^3$, which is equivalent to a diode power of a few mW. Taking some attenuation losses into account, e.g. fibre coupling, the calculations resulted in the use of 40 laser diodes, one per ray, each having a power $\geq 10\ mW$.
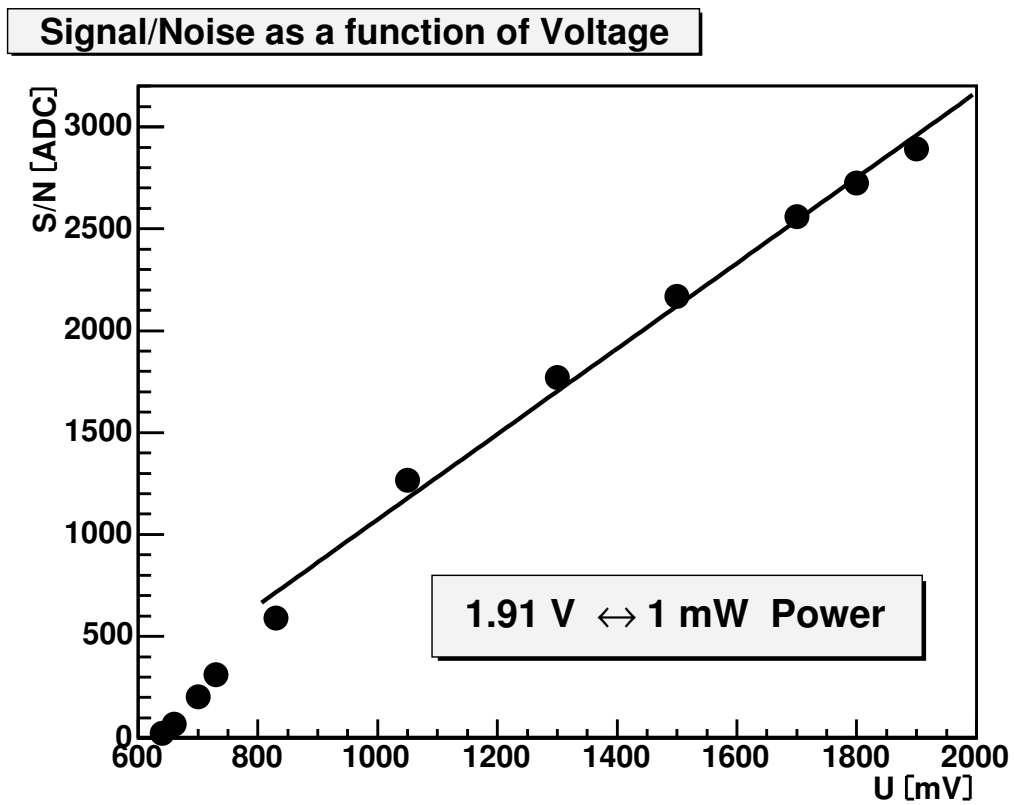
Abbildung C.1.: With a calibration at 1.91 $V \equiv 1$ mW a laser diode power estimation was possible.

D. Light Distribution

Various control components of the experiment are placed inside a separate hall USC55. In a so-called Laser Barrack the laser diode light generation units are integrated in VME crates and send the signals via cables to the experiment. Since only the $+z$ AT are equipped with BS, cable sharing is asymmetric between $+z$ and $-z$ sides. Enough spare cables are included on both sides.

USC55
Laser Barrack

Laser Crate

20 cables, 100m
−Z Tracker bulkhead

30 cables, 100m
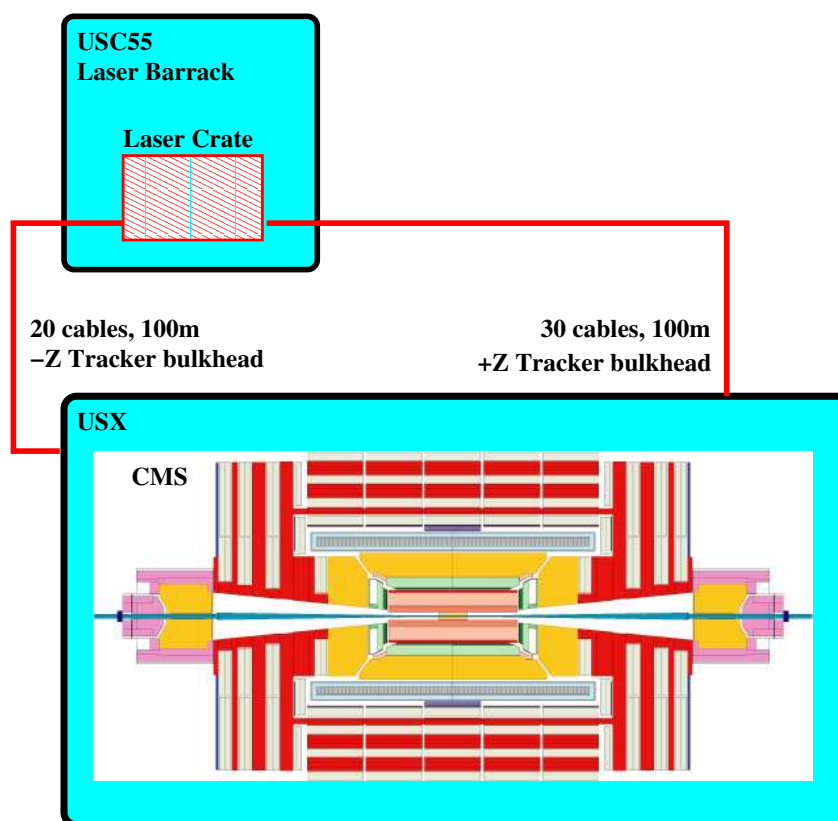**+Z Tracker bulkhead**

USX

CMS

Abbildung D.1.: Scheme of light distribution from the laser source to both tracker bulkheads.

D.   *Light Distribution*

E. Fibres and Connectors

An optical cable is formed by a fibre enclosed in polyethylene for mechanical stability. The single mode fibre, with a core diameter of 8.3 μm, is attached to a standard FC/PC connector (id: IEC 60874-7, CECC 86115-801). The cladding diameter of 125 ± 0.2 μm defines the bore diameter in the ZrO_2 ferrule.

The fibre used here is Corning HI 1060 Flex [46] and the cable has been produced by Ericsson [47]. Special connectors of type FC/PC were made of non-magnetic material (called ARCAP [49]), at Euromicron [48], where also the cable termination has been performed. The spring inside the connectors is produced of stainless steel, DIN 1.4401 (X5CrNiMo1712, AISI 316).

fibre
– cutoff wavelength, λ < 980 nm
– phosphor free
– attenuation < 1 dB/ km
– CERN specification: TF 1176

cable
– material: polyethylene
– halogen free
– flame retardant
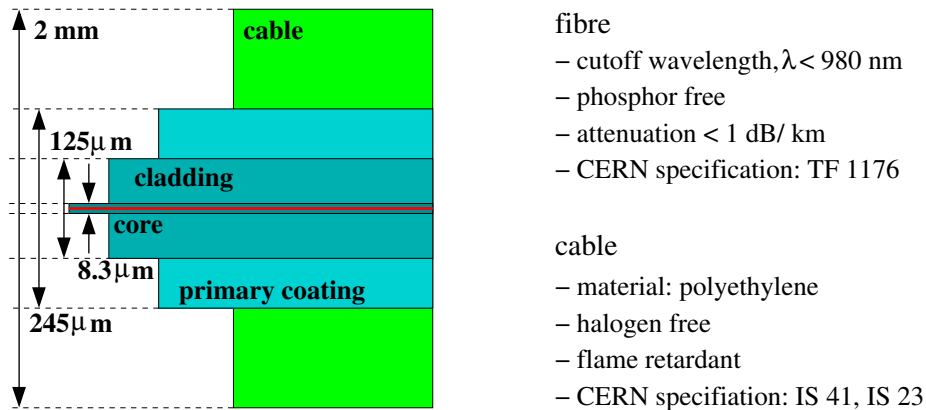– CERN specifiation: IS 41, IS 23

Abbildung E.1.: Cross-section of an optical cable.
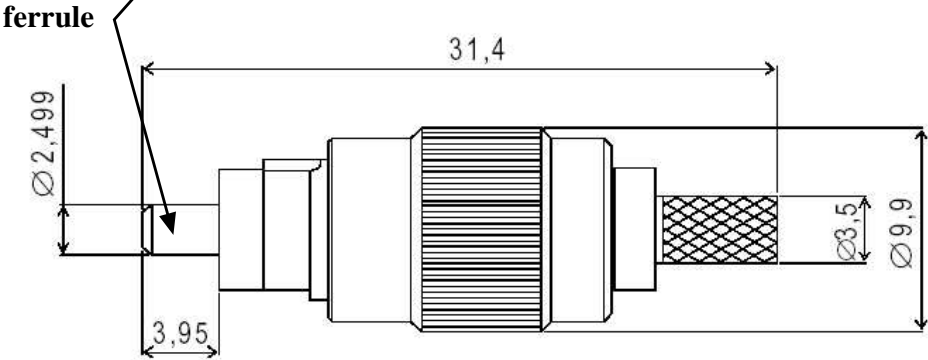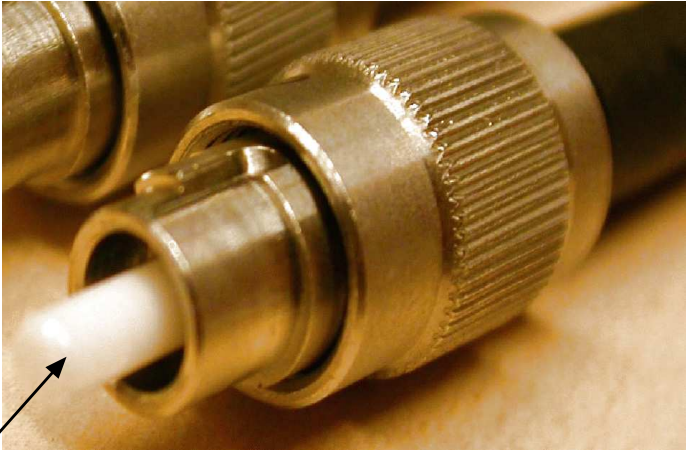
FC/PC connector

Abbildung E.2.: The non-magnetic FC/PC fibre connector.

F. Simulation

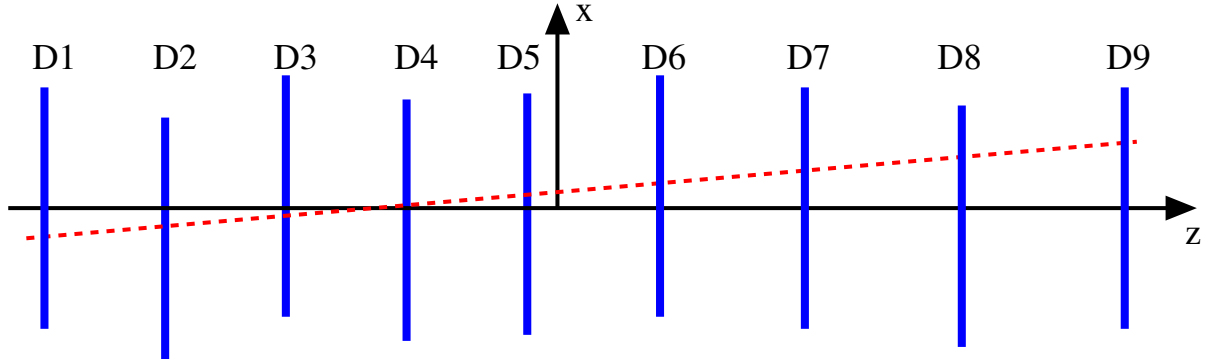In a simplified 2-dimensional example R_{exp} and R_{th} are illustrated:

Abbildung F.1.: A laserbeam (dashed line) traverses $m = 9$ discs and its spot position is measured on each of them.

The experimental readings are all x_i values and the theoretical prediction is given by the applied linear model $az_i + b$, with the two parameters a and b. The resolution with which the spot position on each disc is measured is σ_i.

With χ^2 defined as follows:

$$\chi^2 = \sum_{i=1}^{m} \left(\frac{x_i - (az_i + b)}{\sigma_i} \right)^2 \tag{F.1}$$

two different approaches can be employed. First, by calculation of derivatives, a set of two equations is obtained:

$$\frac{\partial \chi^2(a,b)}{\partial a} = 0, \qquad \frac{\partial \chi^2(a,b)}{\partial b} = 0 \tag{F.2}$$

In this example they can be solved analytically by assuming $\sigma_i = \sigma$ for all discs i and defining the origin of the coordinate system by the center of gravity in z: $\sum_i z_i = 0$:

$$b = \frac{\sum x_i}{m}, \qquad a = \frac{\sum x_i z_i}{\sum z_i^2} \tag{F.3}$$

Second, starting with some values for a and b, e.g. $a_0 = 0$ and $b_0 = 0$, the value χ_0^2 is calculated and minimized in an iterative procedure by $\chi_{j+1}^2 < \chi_j^2$ until reaching some cutoff condition, where the changes in χ^2 are insignificant.

F. Simulation

Regarding again the system of 9 discs in F.1 and taking the first and last disc to be fixed (reference) as done in the simulation of TEC alignment described in chapter 2 the coordinates (readings) of the laser beam spot are given by:

$$x = \frac{x_9 - x_1}{z_9 - z_1} \cdot (z - z_1) + x_1 \qquad \text{(F.4)}$$

and the residuals for D2 - D8 can be calculated by:

$$\Delta x_i = \frac{x_9 - x_1}{z_9 - z_1} \cdot (z_i - z_1) + x_1 - x_i \qquad \text{(F.5)}$$

If more laser beams are assumed, then the system is redundant, with the number of measurements (readings) greater than the number of parameters. By minimization of the χ^2 in (2.2), with the residuals for each beam expressed by (F.5), a set of disc parameters is finally obtained, describing the system geometry with a certain precision.

G. Beamsplitter Pictures and Data

G.1. Design Studies
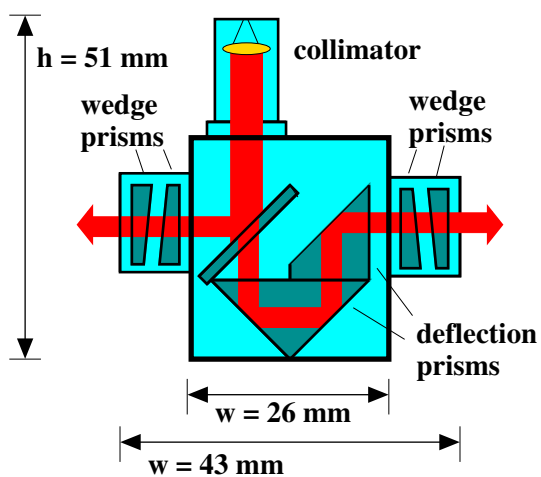
(a) Layout of deflection type BS.

(b) Picture of BS deflection prototype

Abbildung G.1.: First design studies of beamsplitter layout and working principle. The width of the model exceeds the 16 mm allowed by the thickness of TEC D6 and was therefore abandoned in favour of a BS based on the polarization principle.

G.2.   Beam Direction Adjustment

A pre-alignment of all BS mounts in D6 of both endcaps helped to define the optimal beam direction. The line of sight for the beams starting at the BS is defined by the area of 10 mm diameter on the backplane of the alignment sensors, which is transparent to laser light. The adjustment of the BS beam direction to lie within this line of sight was done by using a 3D measuring machine. Moving the indicator card (IC) from the beamsplitter along the normal TEC D6 (z-axis) resulted in qualitative collinearity data better than 2 $mrad$.

This adjustment was important for BS integration in the complete structure, because only fine-tuning of the beam direction was left to be done by the adjustment screws, shown in figure 3.9.
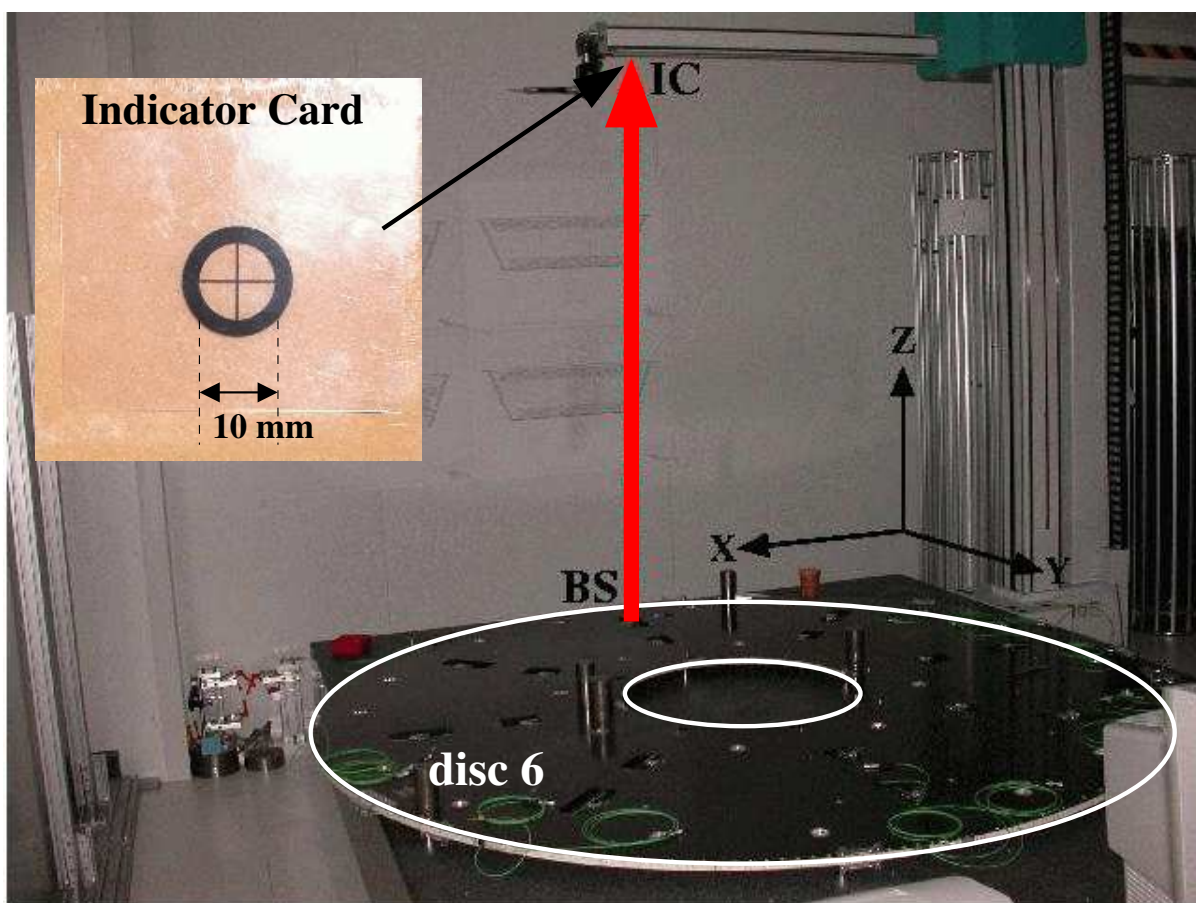

Abbildung G.2.: Pre-alignment of the BS mount interfaces.
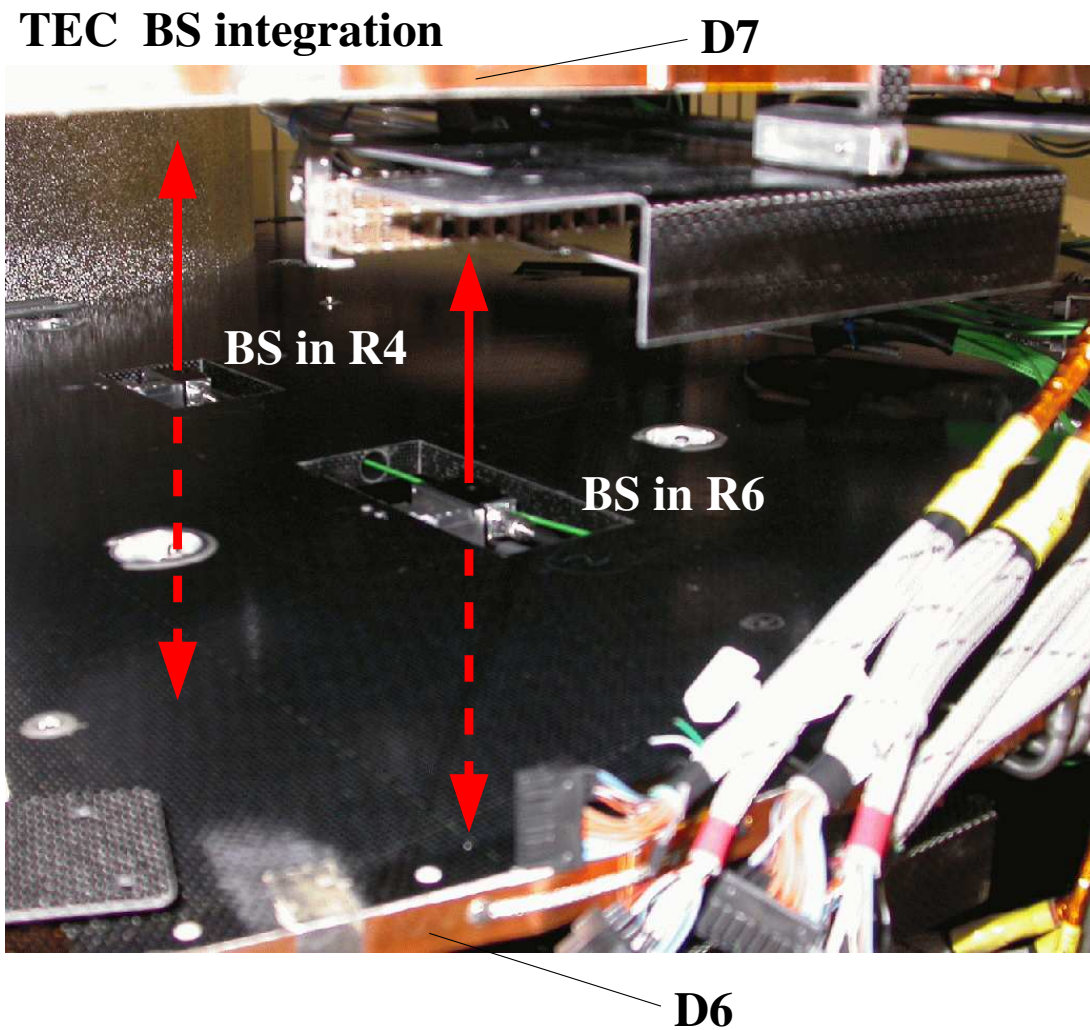
G.3. BS TEC Integration

Abbildung G.3.: Before petal insertion, all BS positions in TEC D6 (picture 2.6) are equipped with BS.

BS and fibres are identified by bar codes ($30260010000XXX$ and $30260020000XXX$ respectively) with each BS uniquely linked to its fibre via the corresponding codes.
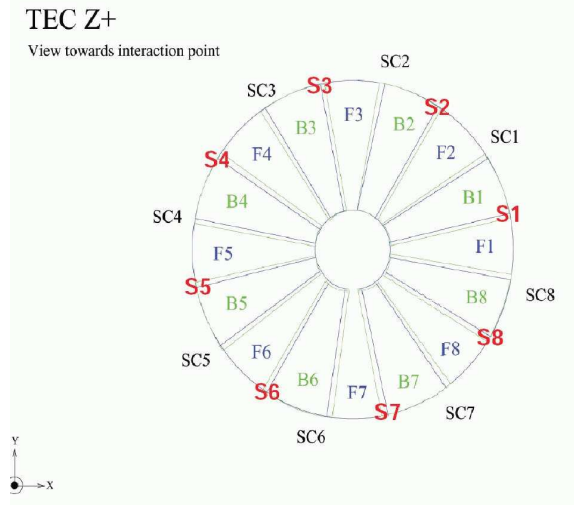
G. Beamsplitter Pictures and Data

Abbildung G.4.: TEC+ sector plan. Each sector (S_i, $i = 1, .., 8$) consists of 9 front and 9 back petals. SC_i denotes the service channels, which are longitudinal carbon fibre bars connecting the TEC discs.

Beamsplitter Collinearity Angle Distribution TEC+						
position		BS	fibre	θ_P	$\Delta\theta_P$	θ_C	$\Delta\theta_C$
sector	ring	barcode	barcode	$mrad$	μrad	$mrad$	μrad
S1	R4	105	060	0.196	20.4	-1.399	31.4
S1	R6	131	073	-0.167	35.2	-2.532	11.5
S2	R4	113	049	-1.356	21.9	-0.796	18.6
S2	R6	107	022	1.112	31.0	-0.274	19.1
S3	R4	150	034	0.823	13.5	0.397	14.7
S3	R6	137	046	0.291	31.7	-2.072	16.1
S4	R4	118	002	2.424	67.8	-1.260	27.0
S4	R6	138	041	-0.827	21.7	-1.195	26.3
S5	R4	114	100	-0.373	27.0	0.160	17.3
S5	R6	122	024	1.359	63.4	-1.983	39.7
S6	R4	126	096	1.079	34.1	0.068	28.9
S6	R6	135	035	1.795	28.6	0.816	18.9
S7	R4	141	025	2.824	18.0	-0.632	20.5
S7	R6	145	027	-0.597	21.7	0.693	23.1
S8	R4	147	099	2.175	24.6	0.562	29.5
S8	R6	130	084	1.803	32.6	0.009	24.0

Tabelle G.1.: TEC+ BS collinearity angles. In combination with the TEC+ sector plan all angular corrections can be applied. This has been done for the first sector and is described in detail in chapter 5.
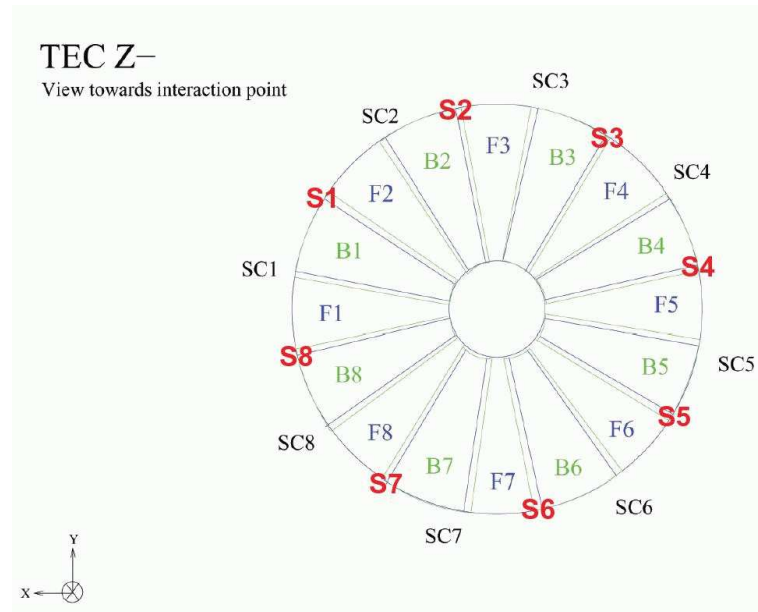
Abbildung G.5.: TEC- sector plan.

Beamsplitter Collinearity Angle Distribution TEC-							
position		BS	fibre	θ_P	$\Delta\theta_P$	θ_C	$\Delta\theta_C$
sector	ring	barcode	barcode	$mrad$	μrad	$mrad$	μrad
S1	R4	119	029	2.019	42.0	1.010	35.1
S1	R6	121	008	1.099	39.9	-0.472	56.4
S2	R4	123	028	-0.972	29.3	0.346	35.7
S2	R6	112	043	1.025	23.8	0.356	34.9
S3	R4	132	019	-2.017	31.7	-2.120	39.9
S3	R6	134	020	0.910	25.3	-2.350	38.3
S4	R4	148	009	-1.198	30.4	0.151	31.8
S4	R6	127	016	-0.457	35.1	-0.432	29.4
S5	R4	146	047	2.257	16.0	1.206	17.9
S5	R6	111	017	0.164	29.8	0.251	17.2
S6	R4	149	003	0.009	25.3	-2.780	17.3
S6	R6	125	018	2.413	64.4	-1.587	26.9
S7	R4	140	033	1.705	22.8	0.313	22.8
S7	R6	124	006	-0.160	19.2	-2.577	29.7
S8	R4	115	021	2.161	18.8	-1.397	32.1
S8	R6	133	001	-1.175	20.4	-0.478	17.3

Tabelle G.2.: TEC- BS collinearity angles.

G.4. BS Coating

S,P - Polarization			
Layer	opt. thickness $n \cdot d$ (Ta$_2$O$_5$) in $\lambda_C/4$ [nm]	Layer	opt. thickness $n \cdot d$ (SiO$_2$) in $\lambda_C/4$ [nm]
1	0.482	2	1.089
3	0.719	4	1.333
5	1.000	6	0.857
7	0.909	8	1.294
9	1.067	10	0.928
11	1.011	12	0.978
13	1.139	14	1.116
15	1.000	16	0.883
17	1.143	18	1.043
19	1.000	20	1.055
21	1.000	22	0.896
23	1.133	24	1.129
25	1.109	26	0.731
27	0.885	28	1.503
29	1.050	30	0.459
31	0.926		

Tabelle G.3.: Optical thickness $n \cdot d$ of beamsplitter s,p-polarization layers for a central wavelength $\lambda_C = 1140\ nm$, given in units of $\frac{\lambda_C}{4}$ so that they can be adjusted according to the application.

- The s,p-polarization coating (table G.3) is on the diagonal surface of the two BS prisms. Thus the angle of incidence is $\theta_0 = \frac{\pi}{4}$ and θ_i for each layer is given by the law of refraction (H.23): $\theta_i = \arcsin\left(\frac{n_{i-1}}{n_i}\right) \cdot \sin\theta_{i-1}$.
$n_0 = n_{\mathrm{SiO_2}} = 1.46$, $n_1 = n_{\mathrm{Ta_2O_5}} = 2.05$, $n_2 = n_{\mathrm{SiO_2}} = 1.46, \ldots, n_{32} = n_0 = 1.46$.

- The high reflection mirror coating consists of 29 layers low ($n_{\mathrm{SiO_2}} = 1.46$) and high ($n_{\mathrm{Ta_2O_5}} = 2.05$) refractive index material.
$n_0 = 1.0$, $n_1 = n_{\mathrm{Ta_2O_5}} = 2.05$, $n_2 = n_{\mathrm{SiO_2}} = 1.46, \ldots, n_{30} = n_{\mathrm{SiO_2}} = 1.46$.

- The two layer coating has been done by $n_0 = n_{\mathrm{SiO_2}} = 1.46$ and $n_1 = n_{\mathrm{Ta_2O_5}} = 2.05$.

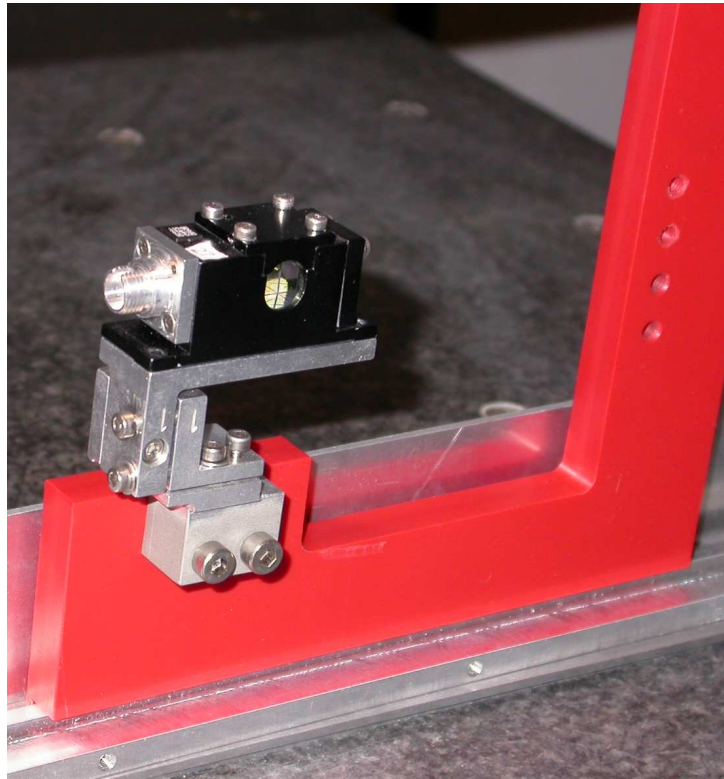## G.5. BS Mount Interface in the Cooling Device

Abbildung G.6.: Structure of the BS mount inside the cold box.

G.   Beamsplitter Pictures and Data

H. Transmission, Reflection, and Absorption Calculation

It is obvious that to describe theoretically the light distribution in the Laser Alignment System, some aspects of optics are needed. In particular the calculation of transmission (T), reflection (R) and absorption (A) for the components used.

During development it was important to understand and to improve especially the T,R,A behaviour of mirror, glas and sensor surfaces. Some basic formulae of optics [59], which have been refered to in the previous chapters, are shortly reviewed here. The matrix theory of wave propagation through a layered medium has been extended to include absorption and is derived in section H.3.

H.1.   Boundary Conditions and Wave Equations

The following boundary conditions at interfaces can be derived from the Maxwell equations:

$$(\mathbf{D}_2 - \mathbf{D}_1) \cdot \mathbf{n} \;=\; 4\pi\rho \tag{H.1}$$

$$(\mathbf{B}_2 - \mathbf{B}_1) \cdot \mathbf{n} \;=\; 0 \tag{H.2}$$

$$\mathbf{n} \times (\mathbf{E}_2 - \mathbf{E}_1) \;=\; 0 \tag{H.3}$$

$$\mathbf{n} \times (\mathbf{H}_2 - \mathbf{H}_1) \;=\; \frac{4\pi}{c}\mathbf{j} \tag{H.4}$$

Assuming vanishing charge density ρ and charge current $\mathbf{j}$, the normal components of $\mathbf{D}$ and $\mathbf{B}$ and the tangential components of $\mathbf{E}$ and $\mathbf{H}$ are continuous.

For a homogeneous nonconductive medium the equations of wave motion are:

$$\nabla^2\mathbf{E} - \frac{\epsilon\mu}{c^2}\frac{\partial^2\mathbf{E}}{\partial t^2} \;=\; 0 \tag{H.5}$$

$$\nabla^2\mathbf{H} - \frac{\epsilon\mu}{c^2}\frac{\partial^2\mathbf{H}}{\partial t^2} \;=\; 0 \tag{H.6}$$

Electromagnetic waves propagate with $v = \frac{c}{\sqrt{\epsilon\mu}}$ and with the definition of refractive index $n = \frac{c}{v}$ of a medium this leads to

$$n = \sqrt{\epsilon\mu} \tag{H.7}$$

Solutions of differential equations (H.5) (H.6) are

$$\mathbf{E}\left(\mathbf{r},t\right) \;=\; \mathbf{E_0}e^{i(k(\mathbf{r}\cdot\mathbf{s})-\omega t)} \tag{H.8}$$

$$\mathbf{H}\left(\mathbf{r},t\right) \;=\; \mathbf{H_0}e^{i(k(\mathbf{r}\cdot\mathbf{s})-\omega t)} \tag{H.9}$$

H.   Transmission, Reflection, and Absorption Calculation

where $\mathbf{s}$ denotes the unit vector in the wave direction $\mathbf{k} = k\mathbf{s}$. The relation between $\mathbf{E}$ and $\mathbf{H}$ is given by

$$\mathbf{E} = -\sqrt{\frac{\mu}{\epsilon}}\mathbf{s} \times \mathbf{H} \tag{H.10}$$

$$\mathbf{H} = \sqrt{\frac{\epsilon}{\mu}}\mathbf{s} \times \mathbf{E} \tag{H.11}$$

and hence it follows by scalar multiplication with $\mathbf{s}$ that $\mathbf{E}$ and $\mathbf{H}$ are perpendicular to the direction of wave propagation ($\mathbf{E} \cdot \mathbf{s} = \mathbf{H} \cdot \mathbf{s} = 0$). For the amplitudes $E = |\mathbf{E}|$ and $H = |\mathbf{H}|$ the expression

$$H = nE \tag{H.12}$$

is valid, if $\mu = 1$.

If wave propagation in a dissipative medium is considered, the wave equation gets an additional damping term proportional to $\frac{\partial \mathbf{E}}{\partial t}$

$$\nabla^2 \mathbf{E} - \frac{4\pi\mu\sigma}{c^2}\frac{\partial \mathbf{E}}{\partial t} - \frac{\epsilon\mu}{c^2}\frac{\partial^2 \mathbf{E}}{\partial t^2} = 0 \tag{H.13}$$

$$\nabla^2 \mathbf{H} - \frac{4\pi\mu\sigma}{c^2}\frac{\partial \mathbf{H}}{\partial t} - \frac{\epsilon\mu}{c^2}\frac{\partial^2 \mathbf{H}}{\partial t^2} = 0 \tag{H.14}$$

and propagating waves are damped by an exponential factor $e^{-\frac{\alpha}{2}(\mathbf{r}\cdot\mathbf{s})}$

$$\mathbf{E}(\mathbf{r}, t) = \mathbf{E_0}e^{-\frac{\alpha}{2}(\mathbf{r}\cdot\mathbf{s})}e^{i(\beta(\mathbf{r}\cdot\mathbf{s}) - \omega t)} \tag{H.15}$$

$$\mathbf{H}(\mathbf{r}, t) = \mathbf{H_0}e^{-\frac{\alpha}{2}(\mathbf{r}\cdot\mathbf{s})}e^{i(\beta(\mathbf{r}\cdot\mathbf{s}) - \omega t)} \tag{H.16}$$

By introduction of complex values, wave number $\hat{k}$, dielectric constant $\hat{\epsilon}$, phase velocity $\hat{v}$

$$\hat{k}^2 = \frac{\omega^2\mu}{c^2}\hat{\epsilon} \qquad \hat{\epsilon} = \epsilon + i\frac{4\pi\sigma}{\omega} \qquad \hat{v} = \frac{c}{\sqrt{\mu\hat{\epsilon}}} \tag{H.17}$$

and a complex refractive index $\hat{n}$

$$\hat{n} = n(1 + i\kappa) \qquad \hat{n} = \frac{c}{\hat{v}} = \sqrt{\mu\hat{\epsilon}} = \frac{c}{\omega}\hat{k} \tag{H.18}$$

where n is the refractive index and κ is the extinction coefficient, the absorptive properties of a medium are described.

Then formally (H.8) (H.9) is identical with (H.15) (H.16) by replacing k by $\hat{k}$

$$\hat{k} = \beta + i\frac{\alpha}{2} \tag{H.19}$$

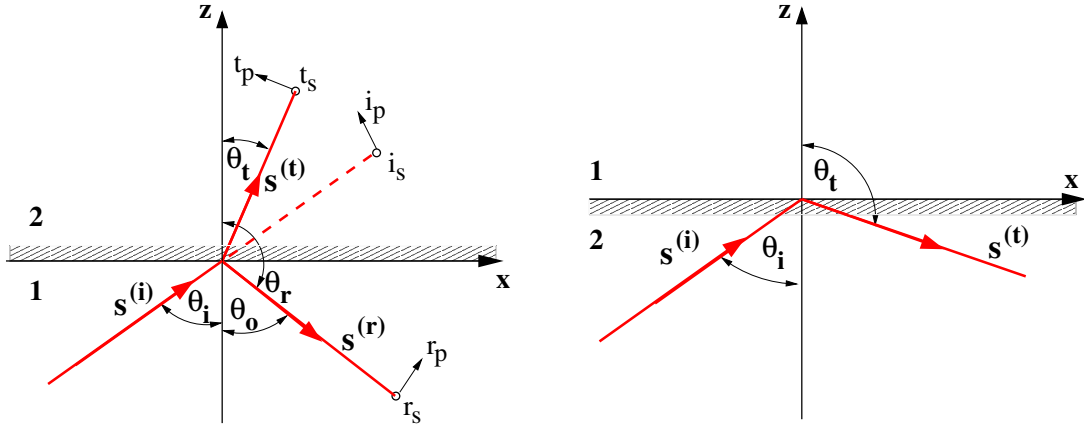with $\beta = \frac{2\pi}{\lambda_0}n$, λ_0 the vacuum wavelength and the absorption coefficient α

$$\alpha = \frac{4\pi}{\lambda_0}n\kappa \tag{H.20}$$

The reciprocal value of $d_A = \frac{1}{\alpha}$ is known as penetration depth for which the intensity $I \sim \mathbf{E}^2$ is decreased to $\frac{1}{e}I_0$. As a function of medium thickness d the transmitted intensity is given by

$$I(d) = I_0\,e^{-\alpha d} \tag{H.21}$$

H.2.   Fresnel Equations

(a) Light propagation at a single boundary.   (b) Total reflection

Abbildung H.1.: Explanation of light propagation at the interface of two materials with refractive indices $n_2 > n_1$.

Regarding a single boundary (H.1(a)), where the plane of incidence is defined by the incoming wave vector $\mathbf{s}^{(i)}$ and the normal to the boundary $\mathbf{e}_b = (0, 0, 1)$, the law of reflection is given by

$$\theta_r = \pi - \theta_i \qquad \theta_i = \theta_o \qquad (H.22)$$

and the law of refraction by

$$n_1 \sin\left(\theta_i\right) = n_2 \sin\left(\theta_t\right) \qquad (H.23)$$

Taking amplitudes of incoming $i_{s,p}$, reflected $r_{s,p}$ and transmitted $t_{s,p}$ waves, using (H.11) as well as the boundary (xy plane) conditions (H.3) and (H.4), a set of four equations (Fresnel equations), which describe the component parallel (p) and perpenticular (s) to the plane of incidence independently, is obtained.

$$t_p = \frac{2 \sin\left(\theta_t\right) \cos\left(\theta_i\right)}{\sin\left(\theta_i + \theta_t\right) \cos\left(\theta_i - \theta_t\right)} \, i_p \qquad (H.24)$$

$$t_s = \frac{2 \sin\left(\theta_t\right) \cos\left(\theta_i\right)}{\sin\left(\theta_i + \theta_t\right)} \, i_s \qquad (H.25)$$

$$r_p = \frac{\tan\left(\theta_i - \theta_t\right)}{\tan\left(\theta_i + \theta_t\right)} \, i_p \qquad (H.26)$$

$$r_s = -\frac{\sin\left(\theta_i - \theta_t\right)}{\sin\left(\theta_i + \theta_t\right)} \, i_s \qquad (H.27)$$

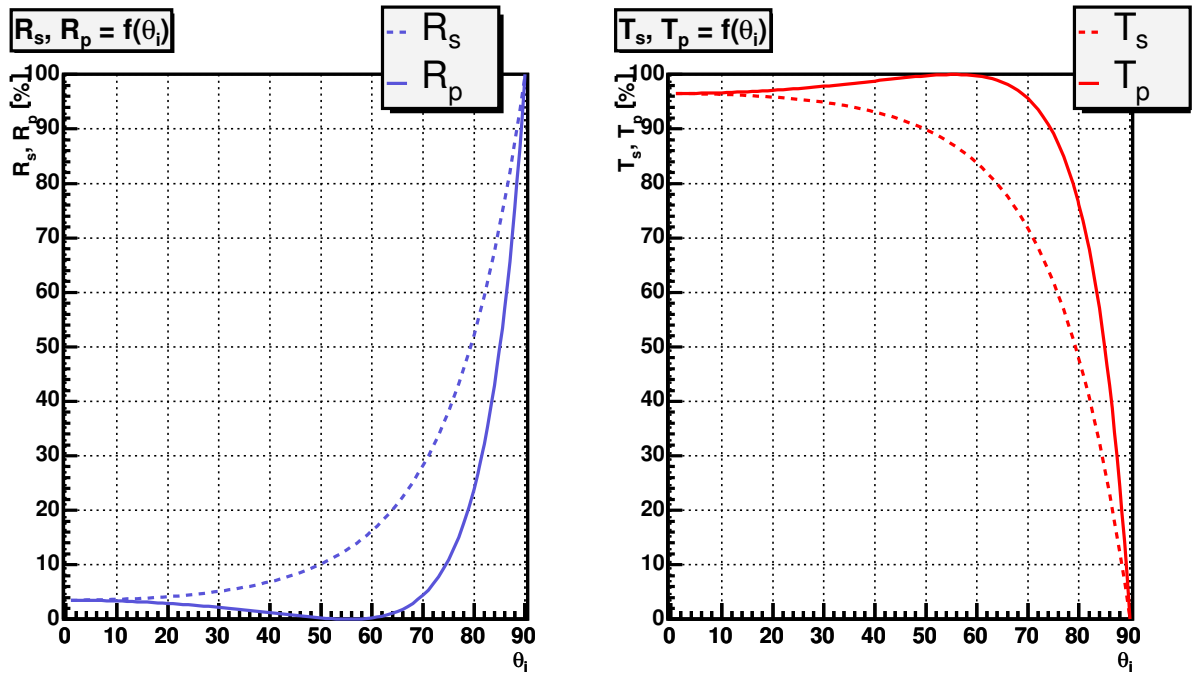The reflected light intensity is then given by

Abbildung H.2.: Calculation of R as function of the angle of incidence, $R_{s,p} = f(\theta_i)$, according to the Fresnel formulae.

$$R_p = \frac{|r_p|^2}{|i_p|^2} = \frac{\tan^2(\theta_i - \theta_t)}{\tan^2(\theta_i + \theta_t)} \tag{H.28}$$

$$R_s = \frac{|r_s|^2}{|i_s|^2} = \frac{\sin^2(\theta_i - \theta_t)}{\sin^2(\theta_i + \theta_t)} \tag{H.29}$$

and the transmitted part is

$$T_p = \frac{n_2 \cos(\theta_t)}{n_1 \cos(\theta_i)} \frac{|t_p|^2}{|i_p|^2} = \frac{\sin(2\theta_i)\sin(2\theta_t)}{\sin^2(\theta_i + \theta_t)\cos^2(\theta_i - \theta_t)} \tag{H.30}$$

$$T_s = \frac{n_2 \cos(\theta_t)}{n_1 \cos(\theta_i)} \frac{|t_s|^2}{|i_s|^2} = \frac{\sin(2\theta_i)\sin(2\theta_t)}{\sin^2(\theta_i + \theta_t)} \tag{H.31}$$

H.3.   Matrix Theory

Derivation of the matrix formalism starts with one homogeneous layer, as shown in figure H.3. For non-normal incidence, both modes, TE (s-polarization) and TM (p-polarization), depend differently on the angle of incidence θ_0.

Using (H.11) with $\mathbf{s} = (cos(\theta_0), 0, sin(\theta_0))^T$ and the boundary conditions (H_z is continous), the relation between $\mathbf{E}$ and $\mathbf{H}$ leads in the TE mode to

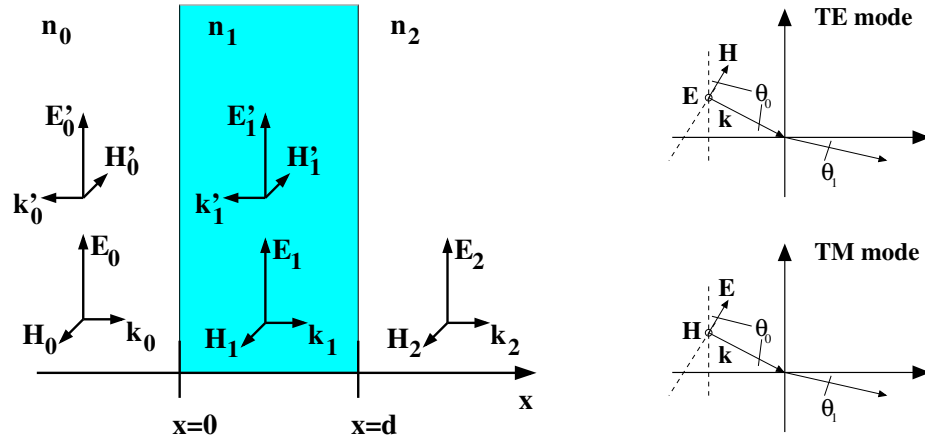$$H_z = n\,cos(\theta_0)\ E_y \tag{H.32}$$

Abbildung H.3.: Illustration of a homogenous layer with refractive index n_1 and thickness d to derive the basic formulas of the Matrix Theory.

and in the TM mode, by using (H.10) and the boundary conditions (E_z is continous), to

$$E_z = -\frac{\cos(\theta_0)}{n} \, H_y \tag{H.33}$$

For normal incidence on a layer i,

$$p_i = n_i \cos(\theta_i) \tag{H.34}$$

and

$$q_i = \frac{\cos(\theta_i)}{n_i} \tag{H.35}$$

are equal and the difference between s- and p-polarization vanishes.

Calculation of propagation of a TE wave in a homogeneous layer gives for E_y (figure H.3)

$$E_y = \begin{cases} E_0 e^{ik_0 x} + E_0' e^{-ik_0 x} & , \quad x < 0 \\ E_1 e^{ik_1 x} + E_1' e^{-ik_1 x} & , \quad 0 < x < d \\ E_2 e^{ik_2(x-d)} & , \quad d < x \end{cases} \tag{H.36}$$

and it follows for H_z

$$H_z = \begin{cases} H_0 e^{ik_0 x} - H_0' e^{-ik_0 x} & , \quad x < 0 \\ H_1 e^{ik_1 x} - H_1' e^{-ik_1 x} & , \quad 0 < x < d \\ H_2 e^{ik_2(x-d)} & , \quad d < x \end{cases} \tag{H.37}$$

It follows for the interfaces at $x = 0$

$$\begin{aligned} E_0 e^{ik_0 x}\big|_{x=0} + E_0' e^{-ik_0 x}\big|_{x=0} &= E_1 e^{ik_1 x}\big|_{x=0} + E_1' e^{-ik_1 x}\big|_{x=0} \\ H_0 e^{ik_0 x}\big|_{x=0} - H_0' e^{-ik_0 x}\big|_{x=0} &= H_1 e^{ik_1 x}\big|_{x=0} - H_1' e^{-ik_1 x}\big|_{x=0} \end{aligned} \tag{H.38}$$

and $x = d$:

$$\begin{aligned} E_1 e^{ik_1 x}\big|_{x=d} + E_1' e^{-ik_1 x}\big|_{x=d} &= E_2 e^{-ik_2(x-d)}\big|_{x=d} \\ H_1 e^{ik_1 x}\big|_{x=d} - H_1' e^{-ik_1 x}\big|_{x=d} &= H_2 e^{-ik_2(x-d)}\big|_{x=d} \end{aligned} \tag{H.39}$$

167

H. Transmission, Reflection, and Absorption Calculation

Finally this leads to four independent equations, including (H.34)

$$
\begin{aligned}
E_0 + E_0' &= E_1 + E_1' \\
p_0 E_0 - p_0 E_0' &= p_1 E_1 - p_1 E_1' \\
E_1 e^{ik_1 d} + E_1' e^{-ik_1 d} &= E_2 \\
p_1 E_1 e^{ik_1 d} - p_1 E_1' e^{-ik_1 d} &= p_2 E_2
\end{aligned}
\tag{H.40}
$$

Elimination of E_1 and E_1' results in

$$
\begin{aligned}
1 + r &= \left(\cos(k_1 d) - i \, {}^{p_2}\!/_{p_1} \, \sin(k_1 d) \right) t \\
p_0 (1 - r) &= \left(-i p_1 \sin(k_1 d) + p_2 \cos(k_1 d) \right) t
\end{aligned}
\tag{H.41}
$$

with the definitions

$$
r := \frac{E_0'}{E_0} \qquad\qquad t := \frac{E_2'}{E_0}
\tag{H.42}
$$

Writing (H.41) in matrix form

$$
\begin{pmatrix} 1 \\ p_0 \end{pmatrix} + r \begin{pmatrix} 1 \\ -p_0 \end{pmatrix} = t \, \mathbf{M} \begin{pmatrix} 1 \\ p_2 \end{pmatrix}
\tag{H.43}
$$

by introducing the transfer matrix $\mathbf{M}$, which describes all properties of the layer between $x = 0$ and $x = d$ uniquely

$$
\mathbf{M} = \begin{pmatrix} \cos(k_1 d) & - \, {}^{i}\!/_{p_1} \sin(k_1 d) \\ - \, i p_1 \sin(k_1 d) & \cos(k_1 d) \end{pmatrix}
\tag{H.44}
$$

the calculation of light transfer is factorized. For a multi layer system $i = 1, \ldots, N$, each component is described by its transfer matrix $\mathbf{M}_i (p_i, d_i)$, where $\mathbf{M}$ is then given by

$$
\mathbf{M} = \mathbf{M_1} \cdot \mathbf{M_2} \cdot \mathbf{M_3} \cdot \ldots \cdot \mathbf{M_N}
\tag{H.45}
$$

The amplitudes of reflection r and transmission t can be calculated by solving (H.41) and can be expressed as functions of the matrix elements $\mathbf{m}_{11}, \mathbf{m}_{12}, \mathbf{m}_{21}, \mathbf{m}_{22}$

$$
r = \frac{p_0 U - V}{p_0 U + V} \qquad\qquad t = \frac{2 p_0}{p_0 U + V}
\tag{H.46}
$$

where

$$
U = \mathbf{m}_{11} + p_{N+1} \mathbf{m}_{12} \qquad\qquad V = \mathbf{m}_{21} + p_{N+1} \mathbf{m}_{22}
\tag{H.47}
$$

Reflection R and transmission T can then be calculated by

$$
R = |r|^2 \qquad\qquad T = \frac{p_{N+1}}{p_0} \cdot |t|^2
\tag{H.48}
$$

To include the absorptive behaviour of a material, k has to be replaced by $\hat{k}$ from (H.19). This is based on the reasonable assumption, that absorption takes place during traversal of the material and not at the infinitesimal border (interface region).

$$
\mathbf{M}_i (p_i, d_i) = \begin{pmatrix} \cos\left(d_i \left(\beta_i + i \, \frac{\alpha_i}{2} \right) \right) & - \frac{i}{p_i} \sin\left(d_i \left(\beta_i + i \, \frac{\alpha_i}{2} \right) \right) \\ - i p_i \sin\left(d_i \left(\beta_i + i \, \frac{\alpha_i}{2} \right) \right) & \cos\left(d_i \left(\beta_i + i \, \frac{\alpha_i}{2} \right) \right) \end{pmatrix}
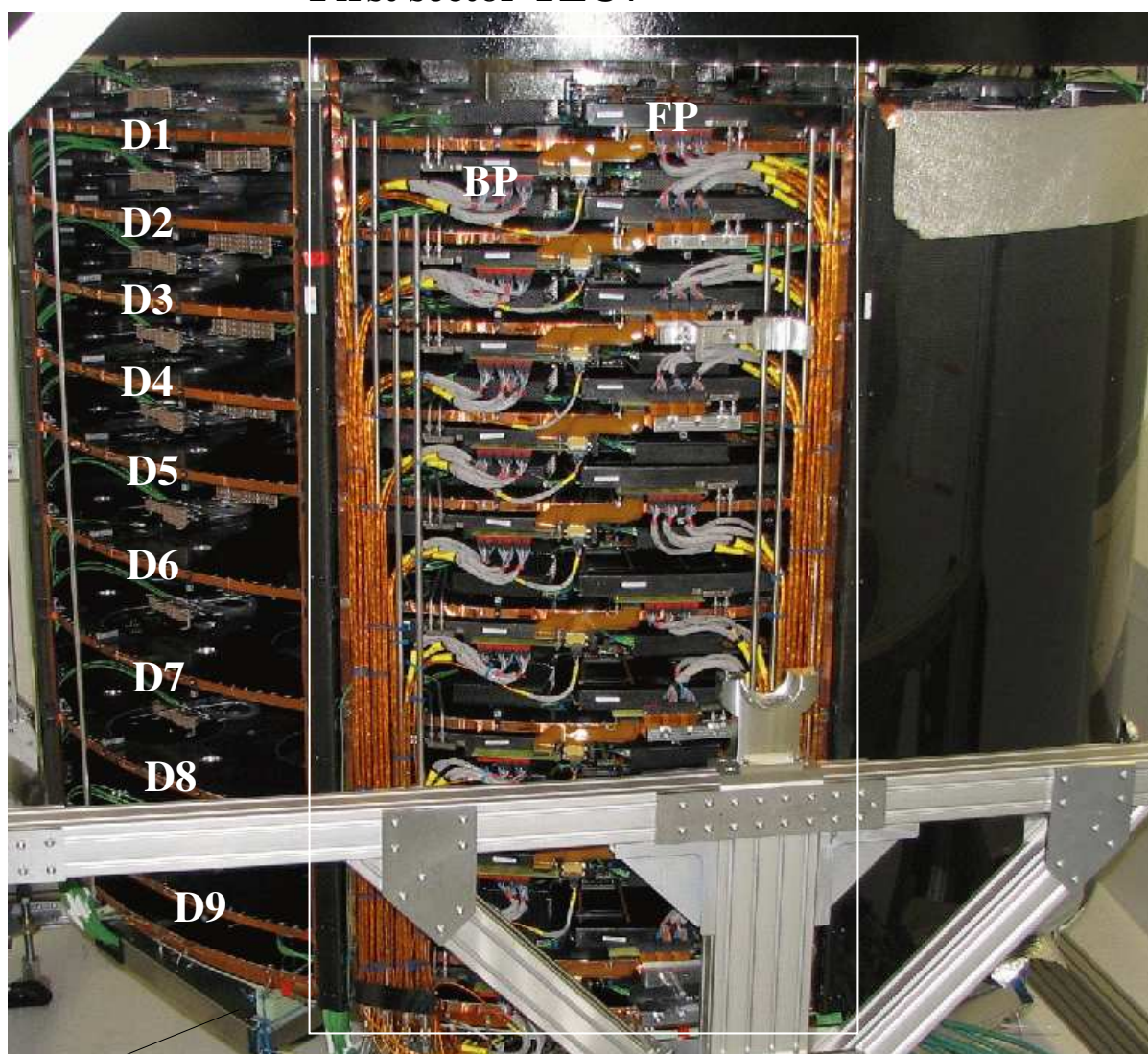\tag{H.49}
$$

For TM waves p_i has to be replaced in all formulas by q_i, which is defined in equation (H.35). The law of conservation of energy is then expressed as

$$
T + R + A = 1
\tag{H.50}
$$

I. TEC First Sector

I.1. TEC Picture

First sector TEC+

D1
D2
D3
D4
D5
D6
D7
D8
D9
FP
BP

bulkhead

Abbildung I.1.: Petal integration in the first sector of TEC+.

I.2. Survey Measurements

TEC+ spherical survey targets

Abbildung I.2.: Spherical survey targets have been fixed on each TEC disc at four positions (figure 5.37). More details can be found in [41].

J. TEC Laser Data

J.1.   Laser Beams of the First Sector

The residuals of R4 plotted versus those of R6 show only a small correlation (J.1). Since the R4 and R6 beams are individually aligned and are provided by different beamsplitters, a large correlation is not expected. A larger effect should occur when monitoring relative movements with respect to a previously defined absolute coordinate system.
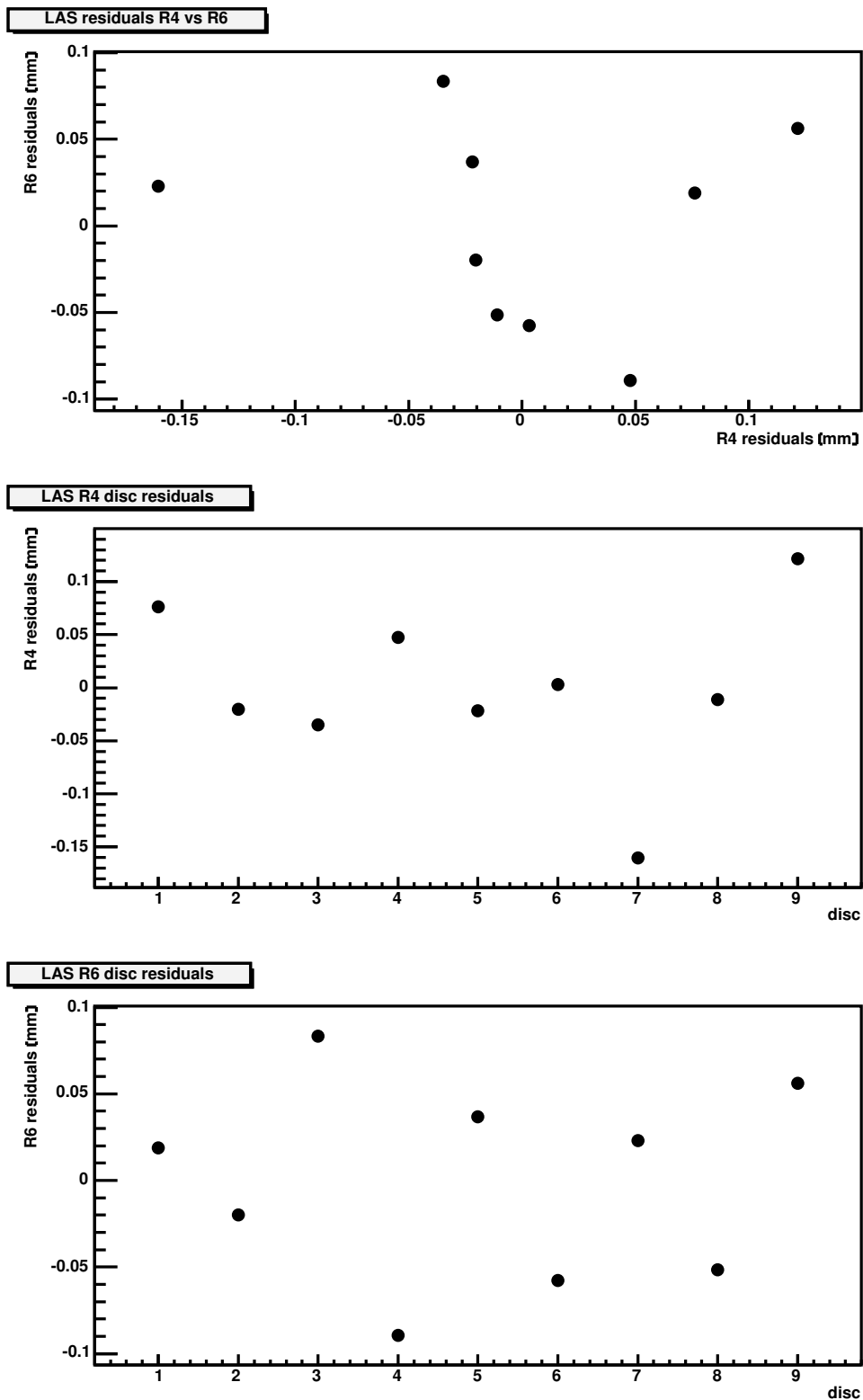
Abbildung J.1.: R4 and R6 beam residuals versus each other and as a function of the TEC disc number. A small correlation can be seen in the first diagram. Because both data sets, R4 and R6, are independent and have been fitted individually without refering to a common (absolute) coordinate system, their correlation is small.

J.2. Determination of the z-Coordinate

In principle the diffraction pattern can be used to determine the disc position in z by applying the formula $n \ \lambda \ = \ p \ \sin{(\theta)}$, where p is the pitch and θ the direction of the observed order n. This can be done at least for R4 for discs D1 - D3 and D7 - D9 (see the patterns in figures 5.26 - 5.31). However, for D8 and D9 as well as for D1, D2 and D3 several diffraction patterns are superimposed and thus the accuracy is worse than the mechanical assembly precision.

As illustrated in figure J.2, reconstruction of the diffraction pattern in R4 D7 gives the distance $\Delta z_{D6-D7} = 189.8 \pm 3.3 \ mm$, in agreement with the assembly value of 190 mm.
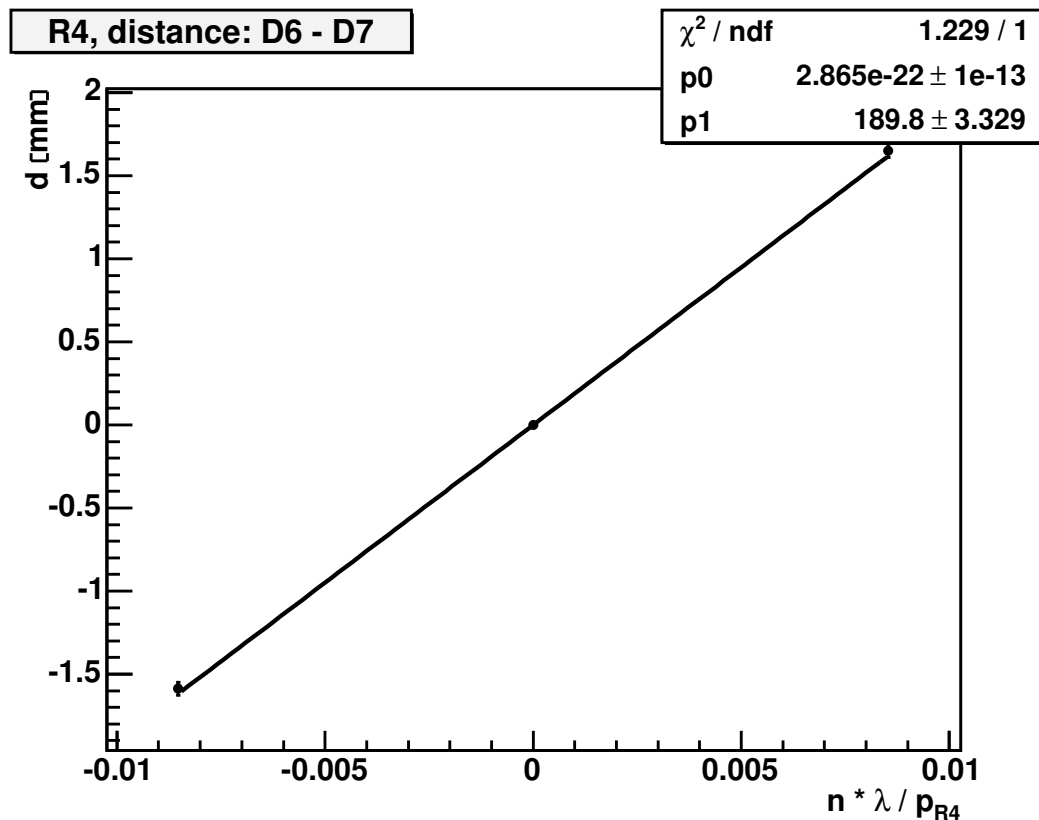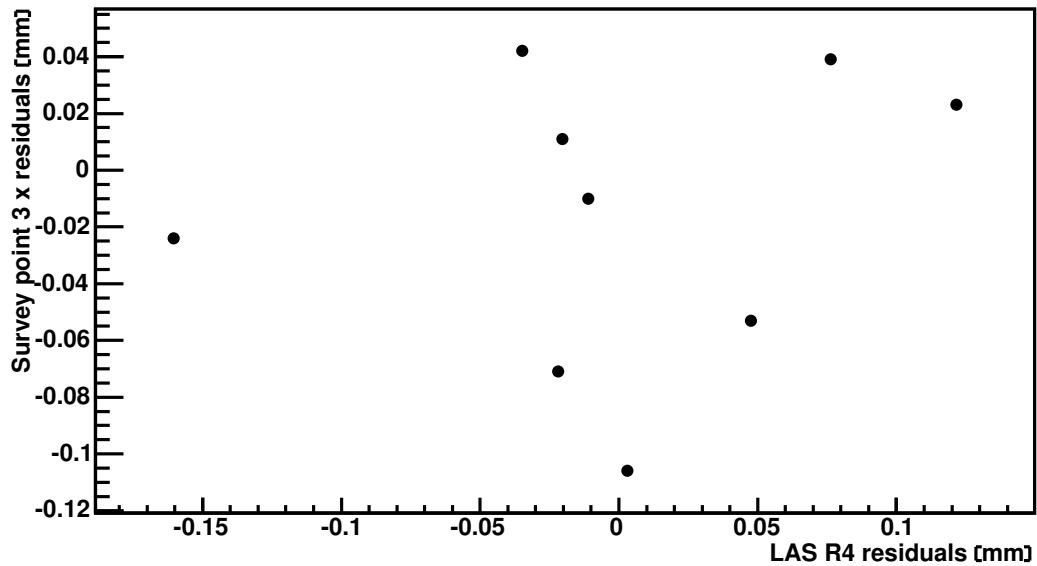

Abbildung J.2.: Diffraction pattern of D6 as seen by D7.

J.3.   Laser Alignment and Survey Measurements

In figure J.3 the residuals for the R4 and R6 beams are plotted versus those of the survey position x_3. A correlation is expected since both methods, LAS and survey, align the same structure TEC+. Only a small correlation is visible.
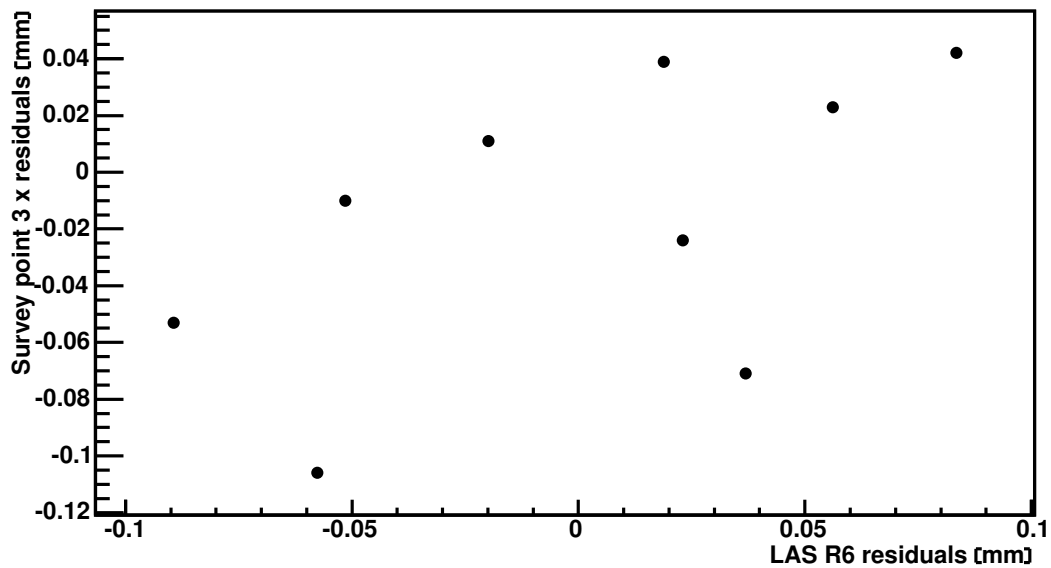

Abbildung J.3.: LAS R4, R6 measured residuals versus those obtained by the survey data at point 3.

The difference of the LAS and survey residuals for position x_3 is shown in figure J.4. Since R6 is closer to x_3, a reconstruction precision of 50 μm can be achieved, while for R4 a value of 80 μm is obtained.
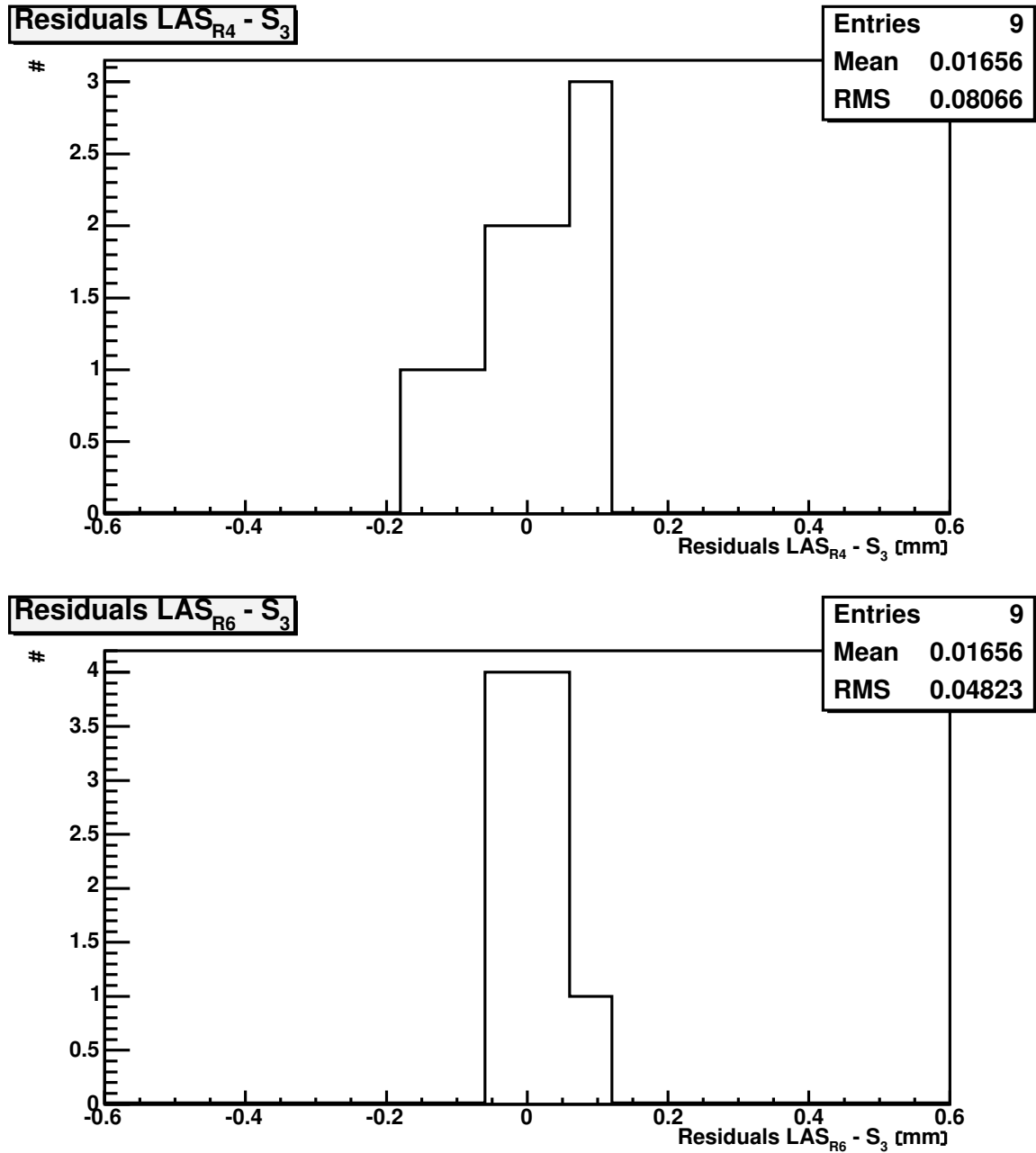

Abbildung J.4.: Difference between the residuals of R4 and R6 with respect to survey data measurements at point 3

J.   TEC Laser Data

Literaturverzeichnis

[1] The LEP Electroweak Working Group *http://lepewwg.web.cern.ch/LEPEWWG/*.

[2] S. Eidelman et al. *Review of Particle Physics*. Phys. Lett. B **592** (2004) 1.
http://pdg.lbl.gov/.
Ch. Berger *Elementarteilchenphysik*. Springer Verlag Berlin Heidelberg, 2002.
P. Schmüser *Feynman-Graphen und Eichtheorien für Experimentalphysiker*. Springer Verlag Berlin Heidelberg, 1995.

[3] H. Fritzsch, M. Gell-Mann, H. Leutwyler *Advantages of the Color Octet Gluon Picture*. Phys. Lett. B **47** (1973) 365.

[4] H. D. Politzer *Reliable Pertubative Results for Strong Interactions?*. Phys. Rev. Lett. **30** (1973) 1346.
D. J. Gross, F. Wilczek *Ultraviolet Behavior of Non-Abelian Gauge Theories*. Phys. Rev. Lett. **30** (1973) 1343.

[5] The ATLAS and CMS Collaborations *High Transverse Momentum Physics at the Large Hadron Collider*. hep-ex/ 0110021

[6] N. Cabibbo *Unitary symmetry and leptonic decays*. Phys. Rev. Lett. **10** (1963) 531.
M. Kobayashi, T. Maskawa *CP-Violation in the Renormalizable Theory of Weak Interaction*. Prog. of Theo. Physics, **B49** (1973) 652.

[7] G. 't Hooft, M. J. G. Veltman *Regularization and renormalization of gauge fields*. Nucl. Phys. **B44** (1972) 189.

[8] P. W. Higgs *Broken symmetries, massless particles and gauge fields*. Phys. Lett. **12** (1964) 132.
P. W. Higgs *Broken symmetries and the masses of gauge bosons*. Phys. Rev. Lett. **13** (1964) 508.
P. W. Higgs *Spontaneous symmetry breakdown without massless bosons*. Phys. Rev. **145** (1966) 1156.
T. W. B. Kibble *Symmetry breaking in non-abelian gauge theories*. Phys. Rev. **155** (1967) 1554.
G. S. Guralnik, C. R. Hagen, T. W. B. Kibble *Global conservation laws and massless particles*. Phys. Rev. Lett. **13** (1964) 585.
F. Englert, R. Brout *Broken symmetry and the mass of gauge vector mesons*. Phys. Rev. Lett. **13** (1964) 321.

J. Goldstone, A. Salam, S. Weinberg *Broken symmetries.* Phys. Rev. **127** (1962) 965.

[9] S. L. Glashow *Partial-Symmetries of Weak Interactions.* Nucl. Phys. **22** (1961) 579.
A. Salam *Weak and electromagnetic interactions.* printed in Svartholm: Elementary Particle Theory, Proceedings of the Nobel Symposium held 1968 at Lerum, Sweden, Stockholm 1968, 367-377.
S. Weinberg *A model of leptons.* Phys. Rev. Lett. **19** (1967) 1264.

[10] Augustin et al. *Discovery of a Narrow Resonance in e^+ e^- Annihilation.* Phys. Rev. Lett. **33** (1974) 1406.
Aubert et al. *Experimental Observation of a Heavy Particle J.* Phys. Rev. Lett. **33** (1974) 1404.

[11] Goldhaber et al. *Observation in e^+ e^- Annihilation of a Narrow State at 1865 MeV/c^2 Decaying to $K\pi$ and $K\pi\pi$.* Phys. Rev. Lett. **37** (1976) 255.

[12] Abachi et al. *Observation of the Top Quark.* Phys. Rev. Lett. **74** (1995) 2632.
Abe et al. *Observation of Top Quark Production in $\bar{p}p$ Collisions with the Collider Detector at Fermilab.* Phys. Rev. Lett. **74** (1995) 2626.

[13] Hasert et al. *Observation of neutrino-like interactions without muon or electron in the Gargamelle neutrino experiment.* Phys. Lett. **46B** (1973) 138.

[14] UA1 Collaboration *Experimental observation of isolated large transverse energy electrons with associated missing energy at $\sqrt{s} = 540$ GeV .* Phys. Lett. **122B** (1983) 103.
UA1 Collaboration *Experimental observation of lepton pairs of invariant mass around 95 GeV/c^2 at the CERN SPS collider.* Phys. Lett. **126B** (1983) 398.

[15] Ch. Berger et al. *Evidence for gluon bremsstrahlung in e^+ e^- annihilations at high energies.* Phys. Lett. **86B** (1979) 418.
S. Wu e^+ e^- *Physics at PETRA - The first five years.* Phys. Rep. **107** (1984) 60.

[16] J. Christenson, J. Cronin, V. Fitch, R. Turlay *Evidence for the 2π decay of the K_2^0 meson.* Phys. Rev. Lett. **13** (1964) 138.
Alavi-Harati et al. *Observation of Direct CP Violation in $K_{S,L} \to \pi\pi$ Decays.* Phys. Rev. Lett. **83** (1999) 22.
The BABAR Collaboration *Measurement of CP-Violating Asymmetries in B^0 Decays to CP Eigenstates.* hep-ex/0102030. The Belle Collaboration *Measurement of CP Violation Parameter* $\sin 2\phi_1$ *in B_d^0 Meson Decays.* hep-ex/0102018.

[17] ALEPH, DELPHI, L3, OPAL, SLD Collaborations, LEP Electroweak Working Group, SLD electroweak, heavy flavour groups *Precision Electroweak Measurements on the Z Resonance.* hep-ex/0509008.

[18] ALEPH, DELPHI, L3, OPAL Collaborations, LEP Working Group for Higgs Boson Searches *Search for the Standard Model Higgs Boson at LEP.* hep-ex/0306033.

[19] D. Kazakov *Beyond the Standard Model.* hep-ph/0012288.
W. de Boer *Grand Unified Theories and Supersymmetry in Particle Physics and Cosmology.* hep-ph/9402266.

[20] The LHC Study Group *LHC - The Large Hadron Collider, Conceptual Design.* CERN/AC/95-05 (LHC) 1995.
LHC - The Large Hadron Collider *http://lhc.web.cern.ch/lhc/.*

[21] The world's largest particle physics laboratory *http://www.cern.ch/.*

[22] ATLAS Collaboration *Technical Proposal.* CERN/LHCC 94-43, LHCC/P2, 1994.
The ATLAS Experiment *http://atlas.ch/index.html.*

[23] ALICE Collaboration *Technical Proposal.* CERN/LHCC 95-71, LHCC/P3, 1995.
The ALICE Experiment *http://aliceinfo.cern.ch.*

[24] CMS Collaboration *Technical Proposal.* CERN/LHCC 94-38, LHCC/P1, 1994.
The CMS Experiment *http://cmsinfo.cern.ch/outreach/.*
C.-E. Wulz *The CMS experiment at CERN.* CMS CR 2005/026, 2005.

[25] LHCB Collaboration *Technical Proposal.* CERN/LHCC 98-4, LHCC/P4, 1998. The LHCb Experiment *http://lhcb.web.cern.ch/lhcb/.*

[26] R. Bailey, P. Collier *Standard Filling Schemes for Various LHC Operation Modes.* LHC Project Note 323, 2003.

[27] F. Pauss, M. Dittmar *Experimental Challenges at the LHC.* CMS CR 1999/008, 1999.

[28] ATLAS Collaboration *Elastic Cross-Section and Luminosity Measurements in AT-LAS at LHC.* hep-ex/0510078.
The TOTEM Experiment *http://totem.web.cern.ch/Totem/.*

[29] CMS Collaboration *CMS Physics, Technical Design Report.*
Volume I: Detector Performance and Software, CERN/LHCC 2006-001, Feb. 2006,
Volume II: Detector Physics Performance, to be published.
CMS Collaboration *Tracker Technical Design Report.* CERN/LHCC 98-6, CMS TDR 5, April 1998.

[30] W. Bernreuther et al. *Top quark pair production and decay at hadron colliders: Predictions at NLO QCD including spin correlations.* hep-ph/0209202.
F. Beaudette *Top physics prospects at LHC.* CMS CR 2005/010, 2005.
A. Giammanco *Top physics studies and perspectives with CMS.* CMS CR 2005/026, 2005.
A. Ghezzi et al. *Precision measurement of the W mass with the CMS detector at the LHC.* CMS IN 2005/034, 2005.

[31] M. Spira *Higgs Production and Decay at Future Machines.* hep-ph/9711394, 1997.

Literaturverzeichnis

[32] F. Gianotti, M. Mangano *LHC physics: the first one-two year(s)....* hep-ph/0504221, 2005.
M. Pieri *Searches for Higgs Bosons at LHC.* CMS CR 2005/031, 2005.
S. Abdullin et al. *Summary of the CMS Potential for the Higgs Boson Discovery.* CMS NOTE 2003/033, 2003.

[33] F.P. Schilling *Prospects for Measuring $B_s^0 \rightarrow \mu^+\mu^-$ with the CMS Detector.* CMS CR 2005/022, 2005.
S. Villa *Discovery Potential for SUGRA/SUSY at CMS.* CMS CR 2003/033, 2003.

[34] CDF Collaboration *http://www-cdf.fnal.gov/.*
http://www-cdf.fnal.gov/images-movies/60selected.html.

[35] P. Paolucci *The CMS Muon System.* CMS NOTE 2006/006, 2006.

[36] CMS Tracker Collaboration *http://cmsdoc.cern.ch/Tracker/Tracker2005/.*
CMS Tracker EndCap (TEC) *http://accms04.physik.rwth-aachen.de/∼cms/TEC.*
J. Fernandez *The CMS Silicon Strip Tracker.* CMS CR 2006/007, Jan. 2006.

[37] St. Koenig *Deformation Studies on CMS Endcap Modules and Misalignment Studies on the CMS Tracker.* PhD thesis, I. Physikalisches Institut B, RWTH Aachen, Germany, July 2003.

[38] A. Bondar et al. *Influence of misalignment on CMS central tracker performance.* CMS IN 1997/016, May 1997.

[39] CMS Collaboration *The TriDAS project, Technical Design Report.*
Volume I: The Trigger Systems, CERN/LHCC 2000-038, Dec. 2000,
Volume II: Data Acquisition and High-Level Trigger, CERN/LHCC 2002-026, Dec. 2002.
http://cmsdoc.cern.ch/cms/TRIDAS/html/tridas.html

[40] I. Belotelov et al. *Simulation of Misalignment Scenarios for CMS Tracking Devices.* CMS NOTE 2006/008, Jan. 2006.

[41] A. Behrens *CMS - Tracker - TEC+, Measurement of the TEC+ in vertical and horizontal position.* CERN EDMS document 616538, July 2005.
A. Ostaptchouk *Measurement of the TEC Geometry.* Tracker engineering meeting, 15. March 2005.
A. Ostaptchouk, I. Physikalisches Institut B, RWTH Aachen, Germany, *Measurement of the TEC Geometry.* private communication.
G. Fiore *Bari status of art.* Tracker gantry meeting, Dec. 2005.

[42] AMS Collaboration *http://ams.cern.ch/.*
J. Vandenhirtz, W. Wallraff, M. Weisgerber *Space flight experience with the AMS infrared tracker alignment system.* Proceedings of the 27th International Cosmic Ray Conference (ICRC), 2001.
J. Vandenhirtz *Ein Infrarot Laser Positions-Kontroll-System für das AMS Experiment.* PhD thesis, I. Physikalisches Institut B, RWTH Aachen, Germany, 2001.

[43] S. Hameed Khan *Specifications for the Alignment Optics.* Presented at the CMS Tracker week, April 2001.

[44] B. Wittmer *The Laser Alignment System for the CMS Silicon Microstrip Tracker.* PhD thesis, I. Physikalisches Institut B, RWTH Aachen, Germany, Feb. 2002.

[45] QPhotonics, LLC *QPhotonics L.L.C., 1435 Crossways Blvd. Ste. 101, Chesapeake, VA 23320, USA; http://www.qphotonics.com*

[46] Corning GmbH *Corning GmbH, Abraham-Lincoln-Str. 30, 65189 Wiesbaden, Germany; http://www.corning.com*

[47] Ericsson Network Technologies *Ericsson Network Technologies AB, Kablevagen 1, 82482 Hudiksvall, Sweden; http://www.ericson.com*

[48] Euromicron GmbH *Euromicron GmbH, Im Seifen 12, 35756 Mittenaar, Germany; http://www.euromicron-fo.de*

[49] Engelhard-CLAL *Engelhard-CLAL Deutschland GmbH, Lise-Meitner-Str.7, 63303 Dreieich, Germany; http://www.clal-msx.com*

[50] CMS Muon Alignment Group *http://cmsdoc.cern.ch/cms/MUON/alignment/.*
The Muon Alignment Group *CMS Muon Alignment - Progress Report.* CMS TN/96-050, Feb. 1996.
CMS Collaboration *Muon Technical Design Report.* CERN/LHCC 97-32, CMS TDR 3, Dez. 1997.
M. Fernandez Garcia *An Alignment System for the CMS Experiment at the Large Hadron Collider.* PhD thesis, Instituto de Fisica de Cantabria, CSIC Universidad de Cantabria, Oct. 2001.

[51] CMS Collaboration *Invitation to Tender: IT-2777/EP/CMS, Technical Specification.* Supply of Silicon Micro-Strip Sensors for the CMS Silicon Strip Tracker (SST), Dez. 2000.

[52] S. Braibant et al. *Investigation of design parameters and choise of substrate resistivity and crystal orientation for the CMS silicon microstrip detector.* CMS NOTE 2000/011, Feb. 2000.
L. Borrello et al. *Sensor design for the CMS Silicon Strip Tracker.* CMS NOTE 2003/020.

[53] A. Ostaptchouk et al. *The Alignment System of the CMS Tracker.* CMS NOTE 2001/053, May. 2001.

[54] M. Thomas *Simulation and Software Integration of the CMS Tracker Laser Alignment System.* PhD thesis, I. Physikalisches Institut B, RWTH Aachen, in preparation.

[55] R. Brauer et al. *Design and Test Beam Performance of Substructures of the CMS Tracker End Caps.* CMS NOTE 2005/025, Dec. 2005.

Literaturverzeichnis

[56] J. Varela. *Timing and Synchronization in the LHC Experiments.* CMS CR 2000/012, Oct. 2000.
http://www.cern.ch/TTC/intro.html
B. G. Taylor for the RD12 Coll., IEEE Trans. Nucl. Sci. **45** 821, 1998.

[57] J. A. Coughlan *The Front-End Driver card for the CMS Silicon Tracker Readout.* Proc. of the 8th Workshop on Electronics for LHC experiments, Colmar, France 2002.

[58] K. W. Bell et al. *User Requirements Document for the Final FED of the CMS Silicon Strip Tracker.* Version 0.53, CMS NOTE 2001/043, May 2003.

[59] M. Born, E. Wolf *Principles of Optics.* 6th edition. Pergamon Press, 1980.

[60] S. Hameed Khan, B. Suleman, J. Akhtar, L. Ali *Optics Laboratories, P.O. Box 1021, Islamabad, Pakistan.*

[61] R. Alemany et al. *Technical Feasibility Studies for the CMS Tracker Position Monitoring System.* CMS NOTE 2001/006, Feb. 2001.

[62] Fraunhofer-Institut für Naturwissenschaftlich-Technische Trendanalysen INT *Fraunhofer INT, Appelsgarten 2, 53879 Euskirchen, Germany;* http://www.int.fraunhofer.de/

[63] OWIS GmbH *OWIS GmbH, Im Gaisgraben 7, 79219 Staufen, Germany;* http://www.owis-staufen.de/

[64] Melles Griot GmbH *Melles Griot GmbH, Lilienthalstrasse 30-32, 64625 Bensheim, Germany;* http://www.mellesgriot.com/

[65] III. Institut B, RWTH Aachen *III Institut B, RWTH Aachen, Physikzentrum, 52056 Aachen, Germany;* http://www.physik.rwth-aachen.de/group/IIIphys/CMS/tracker/en/index.html
M. Axer *Development of a Test System for Quality Assurance of Silicon Microstrip Detectors for the Inner Tracking System of the CMS Experiment.* PhD thesis, III. Physikalisches Institut B, RWTH Aachen, Germany, Dec. 2003.
T. Franke *Development and Evaluation of a Test System for the Quality Assurance during the Mass Production of Silicon Microstrip Detectors for the CMS Experiment.* PhD thesis, III. Physikalisches Institut B, RWTH Aachen, Germany, July 2005.
J. Niehusmann *Entwicklung von Testverfahren für die Ausleseelektronik der CMS-Siliziumstreifendetektoren.* diploma thesis, III. Physikalisches Institut B, RWTH Aachen, Germany, March 2002.
Th. Hermanns *Aufbau eines Systems für Kühltests zur Qualitätsüberwachung von CMS Silizium-Modulen.* diploma thesis, III. Physikalisches Institut B, RWTH Aachen, Germany, Jan. 2004.

[66] M. Henke *Systemintegration des Laser Alignment Systems in den CMS Silizium-Spurdetektor*. diploma thesis, I. Physikalisches Institut B, RWTH Aachen, Germany, in preparation.

[67] A. Schultz v. Dratzig, I. Physikalisches Institut B, RWTH Aachen, Germany, *FEM calculations*. private communication.

[68] Hamamatsu Photonics, (HPK) *http://www.hamamatsu.com*

[69] mso jena *mso jena Mikroschichtoptik GmbH, Carl-Zeiss-Promenade 10, 07745 Jena, Germany; http://www.mso-jena.de/*.

[70] Jr. G. E. Jellison and D. H. Lowndes *Optical absorption coefficient of silicon at 1.152 μ at elevated temperatures*. Appl. Phys. Lett. **41** (7): 594-596, (1982).

[71] R. Brun et al., ROOT *An Object-Oriented Data Analysis Framework; http://root.cern.ch/*.

Acknowledgements

- To my collegues of the Laser Alignment group: Dr. Andrei Ostaptchouk, Dr. Bruno Wittmer, Maarten Thomas and Michael Henke. Many thanks for your fantastic cooperation and support throughout the years.
  Additionally, I wish to thank especially Dr. D. Pandoulas for reading the preprint versions of my thesis very carefully, improving the English and giving important recommendations.

- Also I would like to thank my office collegues Jan Olzem, Henning Gast and Katja Klein for the incredible atmosphere at work. Besides discussions about physics, solving software and hardware problems, we had so much fun during all these years together, that a summary becomes impossible. Thank you very much for the wonderful time and LTBR.

- Of course no single line of this thesis would have been written without the support from my family. I can always count on you in all situations. Many thanks to my parents, my sister and her family.

- The journey is the reward. Gunda, you're the best ever happend to me, thanks for joining my space-time curve.

Curriculum Vitae

Persönliche Daten

Name	Roman Adolphi
Geburtsdatum	22.11.1974
Geburtsort	Adenau
Email	adolphi@physik.rwth-aachen.de

Schule

1981 - 1985	Grundschule Hillesheim
1985 - 1994	Thomas-Morus-Gymnasium Daun
Mai 1994	Abitur

Wehrdienst

1992 - 2000	Ersatzdienst im Katastrophenschutz, Feuerwehr Walsdorf

Studium

1994 - 2001	Physikstudium an der Rheinisch-Westfälischen Technischen Hochschule (RWTH) Aachen
April 1997	Vordiplom
März 2001	Diplom, Thema der Arbeit: "Monte-Carlo-Untersuchungen zum Nachweis eines leichten Higgs-Bosons im CMS Detektor"
Mai 2001	Beginn der Promotion am I. Physikalischen Institut B der RWTH Aachen, Thema der Arbeit: "Construction and Calibration of the Laser Alignment System for the CMS Tracker"
April 2002 - April 2005	Stipendium im Graduiertenkolleg der DFG: "Elementarteilchenphysik an der TeV Skala"
25.08.2006	Einreichen des Promotionsgesuchs
28.11.2006	Promotionsprüfung